Development and application of an innovative method for studying the diffusion of dissolved gases in porous saturated media

Von der Fakultät für Georessourcen und Materialtechnik der Rheinisch-Westfälischen Technischen Hochschule Aachen und

Der Faculteit Wetenschappen, Katholieke Universiteit Leuven

zur Erlangung des akademischen Grades eines

Doktors der Naturwissenschaften (RWTH Aachen)

PhD in Sciences: Geology (KU Leuven)

genehmigte Dissertation

vorgelegt von **M.Sc.**

Elke Jacops

aus Zoersel, Belgien

Berichter: Univ-Prof. Dr. Ralf Littke
Univ-Prof. Dr. Rudy Swennen
Univ-Prof. Dr. Andreas Busch

Tag der mündlichen Prüfung: 02. Juli 2018

Diese Dissertation is auf den Internetseiten der Universitätsbibliothek online verfügbar

KU LEUVEN

ARENBERG DOCTORAL SCHOOL
FACULTY OF SCIENCE

RWTH AACHEN UNIVERSITY

Development and application of an innovative method for studying the diffusion of dissolved gases in porous saturated media

Elke Jacops

Supervisors:
Prof. Dr. Rudy Swennen
Prof. Dr. Ralf Littke
Dr. Bernhard Krooss
Dr. Alexandra Amann-Hildenbrand
Dr. Christophe Bruggeman

Dissertation presented in partial fulfilment of the requirements for the degree of Doctor of sciences

July 2nd, 2018

Uitgegeven in eigen beheer, Elke Jacops, Grobbendonk.

ABSTRACT

Many countries consider clay-based materials for the safe disposal of high- and intermediate level radioactive waste, either because of the choice of argillaceous formations to host the repository, or as a component in the engineered barrier system. The clays under consideration have a high capacity to retain radionuclides (strong fixation to clay), limited water flow by means of low permeability and high self-sealing properties by capillary sealing efficiency. In Belgium, Boom Clay is considered as a potential host rock. Within a geological repository, the production of gas is unavoidable whereby the dominant process is anaerobic corrosion of metals producing hydrogen. In a first stage, the generated gas will dissolve in the porewater and dissipate by diffusion. If the rate of gas generation is larger than the diffusive flux, a free gas phase will form which might have negative effects on the performance of the barriers. In order to obtain a reliable estimate about the balance between gas generation and gas dissipation, sound diffusion coefficients for dissolved gases are essential.

Our first goal was to develop a suitable technique to measure diffusion coefficients of dissolved gases. Besides diffusion coefficients for a variety of dissolved gases (He, Ne, Ar, CH_4, C_2H_6 and Xe), also diffusion coefficients for hydrogen are needed. It is well known that experiments with hydrogen often suffer from experimental problems such as microbial conversion of H_2 into CH_4. Therefore, it was necessessary to find a way to avoid/minimize this microbial activity during diffusion experiments.

It is known that diffusion coefficients in free water (D_0) depend on the size of the molecule. More specifically, the size dependency of D_0 can be described by an exponential function. In this study, it was observed that an exponential relationship was also found for the effective diffusion coefficient (D_{eff}) as a function of molecule size, which confirmed that molecule size also influences diffusion of molecules in porous materials. A third objective was to investigate whether similar exponential relationships could be found for other clayey materials, which finally could be used to estimate diffusion coefficients based on the size of the diffusing molecule.

As dissolved gases are considered to be conservative tracers, they are useful for the assessment of the transport properties and pore structure by means of their diffusion coefficients. Thus, these diffusion coefficients would also depend on the petrophysical properties of the material, characterising its pore structure. Hence, the last goal of this research study was to investigate the influence of different petrophysical properties on the diffusive behaviour of dissolved gases, thus, allowing coupling between measured petrophysical parameters, D_{eff} and molecule size.

In order to answer these questions, an innovative method was developed to measure the diffusion coefficient of dissolved gases using the double through-diffusion methodology. This allowed to measure the diffusion coefficients of two dissolved gases in a single experiment with a high precision. When using hydrogen, a complex sterilisation procedure combining heat sterilisation, gamma irradiation, gas filtration and the use of a microbial inhibitor was developed, which eliminated microbiological disturbances. By using this procedure, for the first time, reliable and accurate diffusion coefficients for dissolved hydrogen were obtained for three different samples of the Boom Clay. The obtained diffusion coefficients enable a more precise assessment of the problems related to H_2 production/dissipation in a repository environment.

To investigate the relationship between the molecule size and their diffusion coefficients in more detail, diffusion experiments with gases of different sizes and HTO were performed on different clay-rich / argillaceous samples (Boom Clay, Eigenbilzen Sands, Callovo-Oxfordian Clay, Opalinus Clay and bentonite). Similar to the relationship between D_0 and molecular size, for all samples under investigation, a reliable relationship between the molecular size and effective diffusion coefficient was

obtained which can be described by an exponential function. The difference in distance between the D_{eff} and D_0 curves relates to the geometrical factor ($G \sim D_0/D_{eff}$). This geometric factor provides information on how the porous network influences diffusing molecules and account for the tortuosity and constrictivity of the sample. For the samples of the Boom Clay and the Eigenbilzen Sands, the exponential coefficient is very similar to the D_0 relationship. Similar exponential coefficients indicate that the geometric factor will be quasi constant when the size of the diffusing molecule increases. This matches with the experimental results, where the difference in G between the smallest and the largest molecule is less than 3. However, for the other clayey samples (COX, OPA and bentonite), the exponential factors differ from the one of the D_0 relationship, hence G varies strongly with the size of the diffusing molecule, which is also experimentally observed.

In literature, diffusion coefficients are often estimated by using a constant value of G for a certain sample or formation (often derived from diffusion experiments with HTO). Based on the data presented in this work, one can conclude that this approach is not always correct and it can lead to a substantial overestimation of the diffusion coefficient. Therefore, we propose an alternative method to estimate diffusion coefficients of dissolved gases, based on the exponential relationship that has been observed on a large set of diversified samples. By measuring experimentally the effective diffusion coefficient of two unreactive, dissolved gases possessing a different size, one can determine the exponential function and as a consequence, one can derive the diffusion coefficients of other dissolved gases (with a size in between the two measured gases) based on their size. When using this approach for one of our samples, the predicted and measured diffusion coefficients differ by less than 30%, which is deemed satisfactory for predictive gas dissipation calculations.

In order to investigate how the transport properties of a dissolved gas molecule can be linked to the petrophyiscal and petrographical properties of a clay-rich sample, the main focus was on clay-dominated Boom Clay samples (Putte and Terhagen Member) and more sandy Eigenbilzen Sands. For these samples, a detailed petrophysical analysis has been performed. Diffusivity and hydraulic conductivity of the Boom Clay and Eigenbilzen Sands are very different. Petrophysical analysis showed large differences in mineralogy and grain size distribution: samples of the Boom Clay are rich in clay minerals and contain a large weight percent's (> 67%) clay fraction (< 2µm), while the samples of the Eigenbilzen Sands are rich in detrital quartz and contain a large (> 43%) sand fraction (> 62 µm). These differences in composition are also reflected by their micro-structure. The Boom Clay samples are characterised by a clay supported matrix with some homogeneously distributed quartz grains; pores are not visible by the techniques used (< 16 µm). Likely, the pores are mainly located in the clay matrix and are very small (< 250 nm). These observations are in line with previous studies. In contrast, samples of the Eigenbilzen Sands contain large amounts of quartz, a heterogeneous distribution of clay phases and interparticle porosity adjacent to the quartz grains. The pores are still partly located in the clay matrix, but there is also an important fraction of larger pores (> 250 nm) which allows enhanced transport of dissolved gases and water. Hence, a clear link was found between the transport properties and the petrophysical/petrographical properties of the samples.

SAMENVATTING

Vele landen beschouwen kleïge materialen als een geschikt materiaal voor de berging van hoog- en middel radioactief afval. Kleien worden gekozen als gastgesteente voor een bergingssite, of als onderdeel van het ontwikkelde barrière systeem. De beschouwde kleien hebben een hoge capaciteit om radionulciden tegen te houden (sterke fixatie op de klei), een beperkte waterstroming door een lage permeabiliteit en het vermogen om breuken terug te laten sluiten. In België wordt de Boomse Klei beschouwd als een potentieel gastgesteente. In een geologische berging zal de productie van gas onvermijdelijk zijn, waarbij vooral waterstof geproduceerd zal worden via anaërobe corrosie van metalen. In eerste instantie zal het gas oplossen in het poriewater en verwijderd worden door diffusie. Maar wanneer er meer gas wordt geproduceerd dan wat er wegdiffundeert zal er zich een vrije gasfase vormen welke negatieve effecten kan hebben op de performatie van de barrières. Om een betrouwbare schatting te verkrijgen van de balans tussen de productie van gas en de afvoer door diffusie, is het essentieel om over betrouwbare diffusiecoëfficiënten voor opgeloste gassen te beschikken.

Ons eerste doel was om een geschikte techniek te ontwikkelen waarmee diffusie coëfficiënten van diverse opgelosten gassen (He, Ne, Ar, CH_4, C_2H_6 and Xe) gemeten kunnen worden. Daarnaast is ook de diffusie coëfficiënt van waterstof nodig, maar het is algemeen geweten dat experimenten met waterstof onderhevig zijn aan experimentele problemen zoals de microbiële omzetting van H_2 in CH_4. Daarom was het noodzakelijk om een manier te vinden om deze microbiële activiteit te vermijden/minimalizeren tijdens de diffusie experimenten.

Het is gekend dat de diffusie coefficienten van gassen in water (D_0) afhankelijk zijn van de grootte van de molecule. Meer specifiek kan deze afhankelijkheid beschreven worden met een exponentiële functie. In deze studie werd waargenomen dat ook de relatie tussen de grootte van de molecule en de effectieve diffusie coëfficiënt kan beschreven worden met een exponentiële functie, wat bevestigt dat ook de grootte van de molecule het diffusie gedrag in poreuze materialen beïnvloedt. Een derde objectief was om na te gaan of gelijkaardige exponentiële relaties ook voor andere kleïge materialen gevonden kunnen worden, wat later gebruikt zou kunnen worden voor het berekenen van diffusie coëfficiënten op basis van de grootte van de molecule.

Diffusie coëfficiënten zouden ook afhangen van de petrofysische eigenschappen van het materiaal, die op hun beurt de porie structuur beïnvloeden. Daarom is het laatste doel van dit onderzoek om de invloed van verschillende petrofysische eigenschappen op het diffusief gedrag van opgeloste gassen na te gaan. Dit kan dan leiden tot een koppeling tussen de gemeten petrofysische eigenschappen, D_{eff} en de grootte van de molecule.

Om al deze vragen te kunnen beantwoorden, werd een innovatieve methode ontwikkeld om diffusie coëfficiënten van opgeloste te meten, gebruik makend van de dubbele door-diffusie methodologie. Hierdoor kunnen betrouwbare en preciese diffusie coëfficiënten van twee gassen in één experiment gemeten worden. Wanneer waterstof wordt gebruikt, is het volgen van de nieuw ontwikkelde en complexe procedure die hitte sterilisatie, gamma bestraling, gas filtratie en het gebruik van een microbiële inhibitor combineert belangrijk om microbiële activiteit te vermijden. Door gebruik te maken van deze procedure werden voor de eerste keer betrouwbare en accurate diffusie coëfficiënten voor opgeloste waterstof bekomen voor drie verschillende stalen Boomse Klei. De bekomen diffusie coëfficiënten laten toe om een preciezere benadering van de problemen rond H_2 productie en transport in een berging uit te voeren.

Om de relatie tussen de grootte van de molecules en hun diffusie coëfficiënten meer in detail te onderzoeken, werden diffusie experimenten met gassen van verschillende grootte en getritieerd water (HTO) uitgevoerd op verschillende klei rijke stalen (Boomse Klei, Zanden van Eigenbilzen, bentoniet, Callovo-Oxfordiaan en Opalinus klei). Overeenkomstig de relatie tussen D_0 en molecule grootte, kan de relatie tussen D_{eff} en grootte ook beschreven worden met een exponentiële functie, en dit voor alle stalen. Het verschil in afstand tussen de D_{eff} en D_0 curves is gelateerd aan de geometrische factor (G ~ D_0/D_{eff}). Deze geometrische factor bezorgt ons informatie over hoe het poreuze netwerk diffunderende moleculen beïnvloedt, en brengt de tortuositeit en de constrictiviteit in rekening. Voor de stalen Boomse Klei en Zanden van Eigenbilzen is de exponentiële coëfficiënt zeer gelijkaardig aan deze van de relatie met D_0. Gelijkaardige exponenten wijzen erop dat de geometrische factor quasi constant zal zijn wanneer de molecules groter worden. Dit komt overeen met de experimentele resultaten, waar het verschil in G tussen de grootste en kleinste molecule minder is dan een factor 3. Voor de andere materialen (COX, OPA, Bentoniet) wijkt de exponentiële factor af van deze van de D_0 fit, waardoor G sterk varieert met de molecule grootte, iets wat ook in de experimenten werd vastgeteld.

In de literatuur worden diffusie coëfficiënten vaak geschat door gebruik te maken van een constante waarde voor G voor een bepaald staal of formatie, en deze G werd meestal bekomen via diffusie experimenten met HTO. Maar gebaseerd op de gegevens die in dit werk getoond worden, kan men besluiten dat deze aanpak niet steeds correct is en kan leiden tot een substantiële overschatting van diffusie coëfficiënten. Daarom stellen we een alternatieve methode voor. Door experimenteel de diffusie coëfficiënten te meten van twee opgeloste gassen van verschillende grootte, kan men de exponentiële functie bepalen en vervolgens diffusie coëfficiënten van andere gassen (met een grootte tussen die van de twee gemeten gassen in) berekenen op basis van hun grootte. Wanneer deze benadering gebruikt wordt voor één van onze stalen, bedraagt het verschil tussen de geschatte en gemeten diffusie coëfficiënten minder dan 30%, wat voldoende precies wordt geacht voor berekeningen m.b.t. gas transport.

Om te onderzoeken hoe transport eigenschappen van opgeloste gassen gelinkt kunnen worden aan de petrofysische en petrografische eigenschappen van klei rijke stalen, wordt er voornamelijk gekeken naar de klei rijke stalen van de Boomse Klei (Putte en Terhagen Lid) en de meer zanderige stalen van de Zanden van Eigenbilzen. Voor deze stalen werd een gedetailleerde petrofysische en petrografische studie uitgevoerd. Er is een groot verschil in diffusiviteit en hydraulische geleidbaarheid tussen de Boomse Klei en de Zanden van Eigenbilzen. Petrofysische analyse toonde een groot verschil in mineralogie en korrelgrootte verdeling aan: stalen van de Boomse klei zijn rijk aan klei mineralen en bevatten een grote (> 37 massa %) fractie klei (< 2 µm), terwijl de stalen van de Zanden van Eigenbilzen rijk zijn aan erosie kwarts en een grote (> 43 massa %) fractie zand (> 62 µm) bevatten. Deze verschillen in samenstelling komen duidelijk naar voor in verschillen in de micro structuur van de betrokken stalen. De stalen van de Boomse Kei zijn gekarakteriseerd door een matrix van klei, met daarin homogeen verdeelde kwarts korrels en poriën zijn niet zichtbaar met de gebruikte technieken (< 16 µm). Poriën zijn voornamelijk terug te vinden in de klei matrix en zijn erg klein (< 250 nm). Deze observaties zijn in lijn met eerdere studies. De stalen van de Zanden van Eigenbilzen bevatten grote hoeveelheden kwarts, de klei fase is heterogeen verdeeld en er is porositeit zichtbaar tussen de kwartsdeeltjes. Poriën zijn nog steeds terug te vinden in de klei matrix, maar er is ook een belangrijke fractie grote poriën (> 250 nm) waarlangs versneld transport van water en opgeloste gassen kan plaats vinden. Bijgevolg werd er een duidelijk link gevonden tussen de transport eigenschappen van een staal, en de petrofysische/petrografische eigenschappen.

ZUSAMMENFASSUNG

In vielen Ländern werden Tongesteine im Konzept für die sichere Entsorgung von hoch- und mittelradioaktiven Abfällen in Betracht gezogen, entweder als potenzielle Wirtsgesteine für die Endlagerung, oder als Bestandteil des geotechnischen Barrieresystems. Potenzielle Tongesteine besitzen die Fähigkeit, Radionuklide zurückzuhalten (starke Fixierung an Ton) und weisen aufgrund der niedrigen Permeabilitäten und selbstabdichtenden Eigenschaften durch Kapillarkräfte eine geringe Wasserdurchlässigkeit auf. Innerhalb eines geologischen Endlagers ist die Produktion von Gas unvermeidlich. Vorwiegend wird Wasserstoff durch anaerobe Korrosion von Metallen produziert. In einer ersten Phase wird das erzeugte Gas im Porenwasser gelöst und durch Diffusion abgeführt. Wenn die Gaserzeugungsrate den Diffusionsfluss übersteigt, bildet sich eine freie Gasphase. Wird der kritische Gasdruck erreicht, kann es zur Leckage und Zerstörung des Barrieregesteins kommen. Für eine umfassende und zuverlässige Abschätzung des Gleichgewichts zwischen Gasentstehung und Gasdissipation sind zuverlässige Diffusionskoeffizienten der gelösten Gase unerläßlich.

Das erste Ziel dieser Arbeit war es, eine geeignete Technik zur Messung der Diffusionskoeffizienten von gelösten Gasen zu entwickeln. Im Laufe der Studie wurden Diffusionskoeffizienten für mehrere in Wasser gelöste Gase bestimmt (He, Ne, Ar, CH_4, C_2H_6 und Xe). Die Verwendung von Wasserstoff erwies sich als schwierig, da die Messungen mit diversen experimentellen Problemen verbunden waren, wie z.B. der mikrobiellen Umwandlung von H_2 in CH_4. Daher bestand das zweites Ziel darin, eine Methode zur Reduzierung/Minimerung der mikrobiellen Aktivitäten zu entwickeln.

Es ist bekannt, dass Diffusionskoeffizienten in Wasser (D_0) von der Molekülgröße abhängen. Dabei kann die Größenabhängigkeit von D_0 durch eine Exponentialfunktion beschrieben werden. Nach der Durchführung einer ersten Reihe von Messungen an einer Boom Clay Probe wurde eine ähnliche Beziehung für den effektiven Diffusionskoeffizienten (D_{eff}) gefunden. Dies deutete darauf hin, dass die Diffusion von Molekülen in Ton-Systemen auch durch die Größe des diffundierenden Moleküls beeinflusst wird. Das dritte Ziel war daher zu untersuchen, ob ähnliche exponentielle Beziehungen für weitere Tongesteine gefunden werden können. In diesem Fall könnten diese Exponentialfunktionen verwendet werden, um Diffusionskoeffizienten basierend auf der Molekülgröße abzuschätzen.

Gelöste Gase werden als konservative Tracer angesehen, die es ermöglichen, die Transporteigenschaften eines gegebenen Materials durch Messen der Diffusionsparameter gelöster Gase zu bestimmen. Die Diffusionskoeffizienten stehen wiederum im Zusammenhang mit anderen petrophysikalischen Eigenschaften des Materials, welche die Porenstruktur bestimmen. Das letzte Ziel war daher die Untersuchung petrophysikalischer Eigenschaften und die Bestimmung ihres Einflusses auf das Diffusionsverhalten gelöster Gase. Die gemessenen Diffusionsparameter, sowie die gewonnenen Beziehungen zwischen D_{eff} und der Molekülgröße können dann mit den petrophysikalischen Eigenschaften verglichen werden.

Um diese Ziele zu erreichen, wurde eine neue Methode zur Bestimmung von Diffusionskoeffizienten gelöster Gase entwickelt, sogenannte Doppel-Durchdiffusionsexperimente. Mit dieser neuen Methode können gleichzeitig die Diffusionskoeffizienten zweier gelöster Gase mit hoher Genauigkeit gemessen werden. Um zuverlässige Diffusionskoeffizienten für Wasserstoff zu erhalten, wurde ein komplexes Sterilisationsverfahren entwickelt, bei dem Hitzesterilisation, Gammastrahlung, Gasfiltration und die Verwendung eines mikrobiellen Inhibitors kombiniert wurden, wodurch mikrobiologische Störungen eliminiert werden konnten. Durch dieses Verfahren konnten zuverlässige, reproduzierbare und genaue Diffusionskoeffizienten für gelösten Wasserstoff für drei verschiedene Boom Clay Proben bestimmt werden. Die bestimmten Diffusionskoeffizienten ermöglichen eine bessere Beurteilungr der H_2-Verteilung in einem Endlagersystem.

Um den Zusammenhang zwischen Molekülgröße und deren Diffusionskoeffizienten näher zu untersuchen, wurden Diffusionsexperimente mit Gasen unterschiedlicher Größe und HTO an verschiedenen Tonproben (Boom Clay, Eigenbilzen Sande, Callovo-Oxfordian Clay, Opalinuston und Bentonit) durchgeführt. Die Differenz der Abstände zwischen den Kurven (D_{eff} und D_0) steht in Zusammenhang mit dem geometrischen Faktor ($G \sim D_0 / D_{eff}$). Für die Boom Clay- und die Eigenbilzen-Sand Proben ist der Exponential-Koeffizient der D_0-Beziehung sehr ähnlich. Ähnliche exponentielle Koeffizienten deuten darauf hin, daβ der geometrische Faktor nahezu konstant ist, wenn die Größe des diffundierenden Moleküls zunimmt. Dies spiegelt sich ebenfalls in den Versuchsergebnissen wieder. Der Unterschied von G zwischen dem kleinsten und dem größten Molekül ist um den Faktor 3 geringer. Bei den anderen tonhaltigen Proben (COX, OPA und Bentonit) unterscheiden sich die Exponentialfaktoren jedoch von denen der D_0-Beziehung; daher variiert G stark mit der Größe des diffundierenden Moleküls.

In der Literatur werden Diffusionskoeffizienten oft geschätzt, indem ein konstanter G-Wert für eine bestimmte Probe oder Formation verwendet wird (oft abgeleitet aus Diffusionsexperimenten mit HTO). Basierend auf den in dieser Arbeit präsentierten Daten kann man folgern, dass dieser Ansatz nicht immer korrekt ist und zu einer erheblichen Überschätzung des Diffusionskoeffizienten führen kann. Daher wird eine alternative Methode zur Schätzung der Diffusionskoeffizienten von gelösten Gasen vorgeschlagen, basierend auf der exponentiellen Beziehung, welche für alle untersuchten Proben beobachtet wurde. Durch die experimentelle Bestimmung des effektiven Diffusionskoeffizienten zweier unreaktiver gelöster Gase unterschiedlicher Größe können die Diffusionskoeffizienten anderer gelöster Gase (mit einer Größe zwischen den zwei gemessenen Gasen) basierend auf deren Molekülgröße hergeleitet werden. Basierend auf diesem Ansatzes wichen berechnete und gemessene Diffusionskoeffizienten weniger als 30% voneinander ab.

Letztes Ziel dieser Doktorarbeit war zu untersuchen, in welchem Zusammenhang die Transporteigenschaften eines gelösten Gases mit den petrophysikalischen und petrographischen Eigenschaften einer tonreichen Probe stehen. In diesem Teil der Dissertation lag der Fokus auf Boom Clay Proben (Putte und Terhagen Member) und Eigenbilzen Sanden. Für diese Proben wurde eine detaillierte petrophysikalische und petrographische Analyse durchgeführt. Große Unterschiede in der Diffusivität und der hydraulischen Leitfähigkeit wurden zwischen den beiden untersuchten Probentypen beobachtet wie auch hinsichtlich der Mineralogie und Korngrößenverteilung: Boom Clay Proben sind reich an Tonmineralien und enthalten eine große Tonfraktion (<2µm), während die Proben der Eigenbilzen Sande reich an Quarz sind und eine große Sandfraktion enthalten (> 62 µm). Diese Unterschiede in der Zusammensetzung spiegeln sich auch in Änderungen der Mikrostruktur wieder, die in der petrographischen Analyse beobachtet werden. Die Boom Clay Proben sind durch eine Tonmatrix gekennzeichnet, in der die Quarzkörner homogen verteilt und die Poren nicht sichtbar sind (< 16µm). Daher befinden sich die Poren hauptsächlich in der Tonmatrix und sind sehr klein (<250 nm). Im Gegensatz dazu zeigen die Proben der Eigenbilzen Sande große Mengen an Quarz, eine heterogene Verteilung der Tonphase und eine interpartikuläre Porosität um die Quarzkörner herum. Weiterhin befinden sich Poren teilweise in der Tonmatrix, aber es existiert auch ein wichtiger Anteil größerer Poren (> 250 nm), die einen erhöhten Transport von gelösten Gasen und Wasser ermöglichen. Somit wurde eine klare Verbindung zwischen den Transporteigenschaften und den petrophysikalischen / petrographischen Eigenschaften der Proben gefunden.

Acknowledgement

At last! The PhD thesis is finished, and the PhD project which started in 2013 now comes to an end! But in fact, the whole project started much earlier, with some very first ideas somewhere in 2007. At that time, I got the opportunity to start my own project on measuring diffusion coefficients of dissolved gases in Boom Clay, based on the idea of Geert Volckaert. Many months, and many failures later we managed to measure our first set of diffusion coefficients. And much more experiments would follow! I had a first poster on the Clay conference in Nantes, a first paper got published (which was quite a struggle) and we received some international attention. Also the results of our experments became the more and more interesting, especially when looking at the diffusive behaviour of gases with a different size. We were convinced that we could get out much more information than initially expected. But how to get it out … And this is how the idea of this PhD project originated! This project could only start with the support of SCK•CEN (hierarchy and the Academy) and both KU Leuven and RWTH Aachen. Thank you Rudy Swennen, Alexandra Amann, Bernd Krooss and Ralf Littke for believing in the project, and the support I got from the beginning till the very end! Most of the lab work was performed at SCK•CEN, with the technical support of the people from the mechanical workshop (Jef, Zjef, Jurgen, Koen) and colleagues in the lab (Marc, Frank, Tom, Dorien, Serge). Also the collaboration with, and help from the other PhD students (Lander and Timo) was highly appreciated! Having data is one point, interpreting them is a second point! Therefore thank you Mieke, Miro, Tri and Marc for having discussions and looking at the data in more detail! If you read through the manuscript, you will notice quite some mathematical formulas. Also finding the source of the kinetic diameter was quite a struggle! Luckily, Marc was always willing to help! Another thing which you might notice are the nice graphs, created in R. That would not have been possible without the support of Bart! Also special thanks to Christophe and Norbert who strongly supported the project, who were there to disucss results, change opinions, and give me some peptalk from time to time. Unfortunately, the road to a PhD is not always an easy one!

A part of the lab work was performed at KU Leuven. Thank you Steven and Nick to help me with the CT and µCT scans, data processing and data interpretation. Thank you Herman for preparing the nasty thin section of clayey samples, and thank you Ria for teaching me a lot on grain size analysis! I might have forgotten some people, hence thank you to all other PhD students and postdocs who helped me in one way or another!

I also would like to thank Pieter (and Timo) from RWHT Aachen, for performing a lot of BET measurements and for the interesting discussions we have had!

This project would not have been a succes without the support of my family! Thank you to the grandparents for picking up the kids at school when I could not make it in time, and for taking care of them when they got ill. Thank you to the kids for all funny moments, you made me realise that it was “only a job”! And thank you to my husband for supporting me during all these years!

Overview of commonly used transport parameters

Parameter	**Name/formula**
D_w or D_0 ($m^2 \cdot s^{-1}$)	Diffusion coefficient in free water
D_{pore} ($m^2 \cdot s^{-1}$)	Pore diffusion coefficient $D_p = D_{app}\, R = D_{eff}/\eta$
D_{eff} ($m^2 \cdot s^{-1}$)	Effective diffusion coefficient $D_{eff} = \eta \cdot D_{pore}$
D_{app} ($m^2 \cdot s^{-1}$)	Apparent diffusion coefficient $D_{app} = \frac{D_{pore}}{R} = \frac{D_{eff}}{\alpha}$
α	Capacity factor $\alpha = \eta \cdot R = \frac{D_{eff}}{D_{app}}$
δ	Constrictivity (measure for the widening and closing of pores) Frequently, it is assumed that $\delta = 1$
η (—)	Diffusion-accessible porosity
τ	Tortuosity (measure for the length of the diffusion path) Because the diffusion path is never shorter than the straight-line distance, $\tau \geq 1$
K (m/s)	hydraulic conductivity
R	Retardation factor If linear sorption is considered: $R = \frac{D_{pore}}{D_{app}}$

List of abbreviations and symbols

μ-CT: micro computer tomography
AF: anisotropy factor
ANDRA: Agence nationale pour la gestion des déchets radioactifs
BC: Boom Clay
BDT: below drilling table
BGR: Bundesanstalt für Geowissenschaften und Rohstoffe
BIB-SEM: broad ion beam scanning electron microscopy
Cl: clay
COX: Callovo-Oxfordian Clay
CT: computer tomography
D: diffusion coefficient
D_0: diffusion coefficient in free water
D_{app}: apparent diffusion coefficient
D_{eff}: effective diffusion coefficient
D_p: pore diffusion coefficient
EC-NF-PRO: European commission, Near field processes
EDZ: excavation disturbed and damaged zone
F: formation factor
F=C: filter = clay
FF: fixed filter
G: geometric factor or G-factor
GC: gas chromatograph
Gl: glauconite
HADES URL: High Activity Disposal Experimental Site underground research laboratory
HTO: tritiated water
ICP-MS: inductively coupled plasma mass spectroscopy
K: hydraulic conductivity
K_{calc} : calculated hydraulic conductivity
K_{exp}: experimentally measured hydraulic conductivity
L_{core}: length of a core
n: number of mole
N_2-BET: nitrogen adsorption with the Brunnauer-Emmett-Teller theory
NAGRA: Nationale Genossenschaft für die Lagerung radioaktiver Abfälle
ONDRAF/NIRAS: Organisme national des déchets radioactifs et des matières fissiles enrichies/
Nationale Instelling voor Radioactief Afval en verrijkte Splijtstoffen
OPA: Opalinus Clay
Po: pore
PRACLAY: Preliminary Demonstration Test for Clay Disposal
PVC: polyvinyl chloride
Py: pyrite
Q: quartz
Q_{core} : flow out of a cilindrical core with radius Rcore
r: distance between center of two molecules

R^2: (pearson correlation coefficient)²
R: retardation factor
R_{gas}: gas constant
$R_{pore,calc}$: calculated pore diameter
R_{pore}: pore diameter
SCK-CEN: Studiecentrum voor kernenergie/Centre d'étude de l'énergie nucleaire
SSA: specific surface area
TAW: Tweede algemene waterpassing (second general levelling)
TCD: thermal conductivity detector
$V_{LJ}(r)$: Lennard-Jones potential
XRD: X-ray diffraction
δ: constrictivity
Δp: pressure difference
ε: depth of the potential well
η: diffusion accessible porosity
ηR: Capacity factor
η_{tot}: total porosity
μ: viscosity
σ: kinetic diameter
τ: tortuosity

1. Contents

1. Introduction

1.1 Structure of the thesis

In the first two parts of this thesis, the relevance of diffusive transport of dissolved gases in the context of geological disposal in Boom Clay is described and analysed, and based on this analysis, the objectives of this work are formulated.

In a third part, the materials and methods are described: Information on the Boom Clay host formation is provided together with the details of the different types of samples used in this study. The methodologies to perform diffusion experiments with dissolved gases and tritiated water and to perform hydraulic conductivity measurements are described. This section contains also some theoretical aspects on diffusion and describes the modelling of the diffusion experiments.

In the fourth part, the obtained results are discussed. First, the mineralogical compositions and the grain size distributions are discussed, followed by the measured hydraulic conductivities and diffusion parameters. Next, the relation between diffusivity and the size of the diffusing gas molecule is described, which leads directly to an approach to estimate diffusion coefficients. Subsequently, we discuss how the petrophysical properties influence hydraulic conductivity and diffusivity, which leads us to the topic of the next section in which we investigate whether the relation between the petrophysical and transport properties can be used to estimate diffusion coefficients. The next section contains a petrographical description of some of the samples. Since now all necessary information is available, the next section will correlate the transport properties to the petrographical and petrophysical properties. Finally in the fifth part, the conclusions and an outlook are provided.

Several annexes are added to the manuscript. Annex 1 provides extra information on the selection of the kinetic diameters, annex 2 describes the used petrophysical characterization techniques. In annex 3, the paper which describes the diffusion experiments with hydrogen can be found as this topic is not discussed in detail in the thesis. Annex 4 provides a detailed petrographical description of the samples of the Boom Clay and Eigenbilzen Sands. Annex 5 provides extra information on the propagation of uncertainties.

1.2 Relevance of diffusive transport of dissolved gases in Boom Clay

Text modified from Jacops et al. (2016a).

The preferred option adopted by many countries for the long-term management of high- and intermediate level radioactive waste and/or spent fuel is final disposal in a geological repository. In Belgium, no formal decision has been taken yet but for R&D purposes, the Belgian radioactive waste management organization ONDRAF/NIRAS considers Boom Clay as a potential host formation for a geological disposal facility. Boom Clay has favourable properties such as a low hydraulic conductivity (Wemaere et al., 2008; Yu et al., 2013), a high sorption capacity for many radionuclides (Maes et al., 2004) and self-sealing properties due to its elasto-plastic behaviour (Van Geet et al., 2008).

When assessing the ability of sedimentary geological layers (such as Boom Clay) to act as a long term barrier (for instance for the disposal of nuclear waste), knowledge of their solute transport characteristics is important. Because of the low permeability and the low hydraulic gradient over this formation, solute transport in Boom Clay is dominated by diffusion.

The values of the diffusion parameters in clay are mostly determined from diffusion experiments with radiotracers. These can be performed in the lab or in-situ. Common methods are the closed-cell (also named back-to-back), the in-diffusion, the pulse injection and the through-diffusion method (Aertsens et al., 2008a; Bourg and Tournassat, 2015). In the through-diffusion method, the clay is placed between two water reservoirs. One of these reservoirs, the high-concentration reservoir or inlet, is initially doped with a tracer. The other reservoir, the low-concentration reservoir or outlet, is initially tracer-free. By measuring the time evolution of the tracer concentration in the low-concentration and/or the high-concentration reservoir and/or the tracer concentration in the clay at the end of the experiment, the diffusion parameters can be calculated using a mathematical model with the appropriate boundary conditions and formalisms.

The main advantage of using radiotracers in experiments is their low detection limit obtained via radioactivity counting (usual concentrations are far below the detection limit of more common techniques such as ICP-MS (inductively coupled plasma mass spectroscopy)). Disadvantages are that tracer experiments can only be performed in labs licensed to work with radiotracers and that - depending on the half-life - radioactive waste might be generated. The most common radiotracer used to study the transport of unretarded radionuclides (radionuclides not interacting with the negatively charged clay) in potential host sediments like Boom Clay is tritiated water (HTO).

For the safety assessment of a nuclear waste disposal site in Boom Clay, not only the diffusion of radionuclides is relevant, but also diffusion of dissolved gases. Within a repository, generation of gases is unavoidable (Capouet et al., 2015; Perko and Weetjens, 2011; Rodwell et al., 1999; Shaw, 2015; Volckaert et al., 1994; Yu and Weetjens, 2009). Gas is produced by different mechanisms: anaerobic corrosion of metals in waste and packaging, radiolysis of water and organic materials in the packages and microbial degradation of various organic waste streams. Corrosion and radiolysis yield mainly hydrogen while microbial degradation leads to methane and carbon dioxide (Rodwell et al., 1999; Yu and Weetjens, 2009). At the time of gas generation, the repository near field is considered to be saturated with pore water, and the water pressure is assumed to be almost recovered to the equilibrium hydrostatic pressure (Weetjens et al., 2009).

The gas (generated predominantly at steel or metal surfaces of waste and barriers and inside the waste packages) will dissolve in the pore water and will be transported away from the repository by diffusion as dissolved species. If the rate of gas generation is larger than the diffusive flux into Boom Clay, the porewater within the disposal gallery will become oversaturated and a free gas phase might form. It is assumed that desaturation will occur in materials with (relatively) low gas-entry pressure such as e.g. the cementitious backfill. For Boom Clay, tests indicate that the gas entry pressure exceeds the lithostatic pressure (Le et al., 2008 and Lima et al., 2012). If the gas pressure should reach this value, gas flow will probably happen through dilatant pathways (Harrington et al., 2012), corresponding to newly formed porosity. Whether Boom Clay will ever be subject to such high gas pressures depends on many factors: i.e. the gas generation source term, the (dissolved) gas diffusion coefficient, gas entry value of the concrete engineered barrier materials and total storage volume, characteristics of the seals, etc.

For safety and performance calculations, reliable diffusion coefficients for dissolved gases (mainly H_2, but also CH_4) are essential (Capouet et al., 2015; Jacops et al., 2015). However, in 2007 (at the time the gas diffusion project started), the only available gas diffusion parameters for hydrogen in Boom Clay

were obtained from the MEGAS project (Modelling and Experiments on Gas Migration in Repository Host Rocks) (Volckaert et al., 1994). During this project, 2 types of diffusion experiments with H_2 were performed: in-diffusion experiments and through-diffusion experiments. The in-diffusion experiments suffered from H_2 leakages, and the through-diffusion experiments were disturbed by CO_2-outgassing of the clay samples. These experimental problems lead to an uncertainty of up to 2 orders of magnitude (diffusion coefficient expressed as D_{app}) (4.2×10^{-12} m²/s < D_{app} < 1.6×10^{-10} m²/s). A more recent re-evaluation of the MEGAS experiments by Aertsens (2009) showed that the applied technique did indeed not allow a more precise determination of the diffusion coefficient. Due to different experimental problems like outgassing of the clay, occurrence of H_2 leaks and a too short duration of the experiment compared to the length of the samples, only the lumped parameter $\eta R \nu D$ (with η the diffusion accessible porosity, R the retardation factor and D the diffusion coefficient) could be fitted, from which only estimations of the apparent diffusion coefficient (D_{app}) could be made. This re-evaluation lead to a final estimated D_{app} between 5×10^{-12} m²/s and 4×10^{-10} m²/s (Aertsens, 2009).

Sensitivity calculations varying the diffusion coefficient for hydrogen (Weetjens and Sillen, 2006) showed that with this uncertainty range of the diffusion coefficient, combined with the uncertainty on the gas source term, the formation of a free gas phase could not be excluded for some waste types. Therefore, the unavailability of reliable diffusion coefficients for hydrogen in Boom Clay was considered as a knowledge gap.

Not only in Belgium, but also in Switzerland and France, argillaceous formations are being explored as potential host formations for disposal of nuclear waste. For these disposal concepts, the knowledge of diffusion coefficients of gases is again very relevant. Therefore, a literature review of available gas diffusion coefficients for these clayey materials was performed and an overview of measured diffusion coefficients is given in Table 1.

Table 1: Summary of diffusion coefficients for He in different clays. The diffusion coefficients (D_{app} or D_p) refer to those used in the mentioned publications. D_{app} is the apparent diffusion coefficients, D_p is the pore diffusion coefficient. When there is no retardation (as expected for these gases) $D_p = D_{app}$. More information can be found in § 3.8.

Formation	Reference	Type	Orientation with respect to bedding plane	Measured D (m^2/s)	η (%)	T (°C)
Opalinus Clay	Gómez-Hernández (2000)	D_{app}	//	$7.0 \cdot 10^{-10}$	30	
Opalinus Clay	Rubel et al., 2002	D_{app}	⊥	$3.5 (\pm 1.3) \cdot 10^{-11}$		Room temperature
COx	Bigler et al., 2005	D_p	sphere	$7.5\ 10^{-10} \pm 20\%$	16.3	20
COx	Bigler et al., 2005	D_p	⊥	$2.41 \cdot 10^{-10}$	15.4	20
COx	Rebour et al., 1997	D_{app}	⊥	$5 \pm 1 \cdot 10^{-11} \pm 20\%$	23	50

In general, 3 types of methods are used to determine gas diffusion coefficients: (I) outgassing of clay samples or boreholes, (II) calculating diffusion coefficients from natural tracer profiles and (III) in/through-diffusion experiments.

The first method consists of the outgassing of clay samples or boreholes: clay samples are stored in a vacuum container and the concentration of gas released by the sample is measured. For boreholes, the concentration of gas released by the formation into the borehole is measured. Based on these gas concentration measurements, the diffusion coefficient is determined. This method has been used by e.g. Bigler et al. (2005) and Gomez-Hernandez (2000).

Bigler et al. (2005) performed an ^4He outgassing experiment with a spherical sample of Callovo-Oxfordian Clay. With the best fit between the experimental results and the analytical solution, a pore diffusion coefficient (D_p) of 7.5 x 10^{-10} m^2/s was obtained with an uncertainty of 20%. The diffusion coefficient obtained for the spherical sample is actually a mixed diffusion coefficient with respect to bedding plane orientation. In addition, the sample was not a perfect sphere and might have been disturbed by cutting. Therefore it is reported that this value has to be considered as a maximum value, affected by experimental artefacts (Bigler et al., 2005). Bigler et al. (2005) also obtained an in situ pore diffusion coefficient based on the natural He profile in the Callovo-Oxfordian Clay: D_p = 2.41 x 10^{-10} m^2/s with a range of uncertainty from 0.8 x 10^{-10} to 7.2 x 10^{-10} m^2/s. This range of uncertainty is almost one order of magnitude, and the experimentally obtained value (from the spherical sample, D_p = 7.5 x 10^{-10} m^2/s) reported in the same study does not fall within this range. This discrepancy could be explained by the disturbed nature of the spherical sample, leading to an increased and mixed (with respect to bedding plane) diffusion coefficient. As mentioned above, the value D_p = 7.5 x 10^{-10} m^2/s has to be considered as a maximum value.

Gómez-Hernández (2000) performed an in situ in- and out-diffusion experiment with He parallel to the bedding plane in Opalinus Clay in the Mont Terri underground laboratory. The best fit for the apparent diffusion coefficient D_{app}(He) = 7.0 x 10^{-10} m²/s was obtained from an out-diffusion experiment but a porosity of 30% was used, which is twice the typical porosity value of 12 – 18 % reported for Opalinus Clay (Mazurek et al., 2011). This might be explained by the fact that during the drilling of the experimental borehole an excavation damage zone (EDZ) was created, leading to a higher permeability and increased porosity – as discussed by Gómez-Hernández (2000). If the higher porosity is indeed related to the creation of an EDZ, the measured diffusion coefficient might be not relevant for diffusion under undisturbed conditions. The other out- and in-diffusion experiments performed by Gomez-Hernandez (2000) could not confirm this value for D_{app} without adapting parameters like the circulation volume or the initial concentration of ^{4}He.

The main disadvantage of this method is the preservation of the cores: sample treatment after coring has to be done very carefully because cores will degas immediately after sampling, or they can take up gas from the atmosphere. Therefore, these experimental results always have to be interpreted with care.

The second method is calculating the diffusion coefficient based on the concentration profile as natural tracer. This profile is obtained by outgassing boreholes or samples. This method has been used by e.g. Rübel et al. (2002) and Bensenouci et al. (2011).

Rubel et al. (2002) fitted D_{app} for He (D_{app} = 3.5 x 10^{-11} m²/s) in Opalinus Clay based on the natural He concentration profile measured at Mont Terri, Switzerland. However, according to Mazurek et al. (2011) this D_{app} value is likely too low because of the use of an overly simplified model – in particular, of the unsubstantiated assumption of a steady-state situation in which out-diffusion of He is balanced by *in situ* production.

Bensenouci et al. (2011) obtained a He profile for samples collected from 2 vertical boreholes in the Toarcian/Domerian shale in Tournemire URL (France). The He content in the pore water was determined by outgassing in high-vacuum containers. Based on the obtained He profile, the pore diffusion coefficient (D_p) was calculated to be in a range between 2.4 and 12.7 × 10^{-11} m^2/s. But for 3 samples a discrepancy between the measured ^{4}He concentration and the model simulation was noticed.

Calculating diffusion coefficients for naturally present gases, based on their concentration profile is an interesting method, but it has two major disadvantages. The method is only applicable for gases which are naturally present in the clay and basically limited to He, Ar and CH_4. Therefore this method cannot be used to determine the diffusion coefficient for e.g. hydrogen.

The second disadvantage is that, similar to the method of the outgassing of cores, experimental results have to be interpreted with care. The uncertainty on the initial state of the sample and on the in situ boundary conditions increases the uncertainty of the obtained diffusion coefficient. Mazurek et al. (2011) stated that the core outgassing of noble gases requires sophisticated equipment and there is a possibility of gas leakage at several stages.

The third method to determine diffusion coefficients for gases is by performing lab experiments based on the in- or through-diffusion technique. This method has been used by Krooss and Schaefer (1987),

Rebour et al. (1997) and Volckaert et al. (1994). Krooss and Schaefer (1987) used a through-diffusion setup where the upstream reservoir was filled with a gas. The gas composition of the downstream reservoir was analysed on a regular base, and the diffusion coefficient was calculated by using the time-lag method. The described setup has some disadvantages: due to its design, gas pressure should be equal to atmospheric pressure and consequently sample thickness should be small (between 2 and 10 mm) in order to obtain the diffusion coefficient within a reasonable time period. Furthermore, due to the treatment of the sample during loading into the diffusion cell, the natural pore structure might have changed. The reported maximum error on the diffusion coefficient is 20%. Rebour et al. (1997) used a through-diffusion setup. Despite the fact that this setup could be used for different gases, only data for He diffusion on Callovo-Oxfordian Clay were reported (D_{app} = 5 ± 1 x 10^{-11} m²/s). Volckaert et al. (1994) used both in- and through-diffusion but as discussed above, experimental problems led to a large uncertainty on the obtained diffusion coefficients. We consider the in- and through-diffusion technique to be the most reliable, under the condition that the setup is well designed.

To conclude, for Boom Clay only diffusion coefficients for hydrogen were initially available, but the uncertainty on the reported value was very large. For other formations such as Callovo-Oxfordian Clay and Opalinus Clay, only data for He are available (Gómez-Hernández, 2000, Rebour et al., 1997, Rubel et al., 2002) but there is a large difference between the different reported values, and in our opinion some of the samples are not representative for the formation. Also, an inaccurate design of the setup or model can have a negative influence on the reliability of the results. So the lack of reliable diffusion coefficients for different gases and for different clay formations is clearly identified as a knowledge gap.

2. Objectives

As discussed above, up to 2007, no reliable diffusion coefficients for dissolved gases in Boom Clay were available. Therefore, SCK•CEN started (in collaboration with NIRAS/ONDRAF) a research project to develop a new method to measure diffusion coefficients of dissolved gases. The developed technique is based on double through-diffusion (Shackelford, 1991) and allows measuring simultaneously the diffusion coefficients of two dissolved gases with high precision. Besides some small modifications, the developed method can also be used to measure the diffusive transport of HTO.

Objective 1 was to develop a method which allows to measure diffusion coefficients of dissolved gases with high precision.

Objective 2 was to obtain diffusion coefficients for hydrogen. Experiments with hydrogen are known to be prone to leakage and microbial conversion of H_2 into CH_4. Several studies (Charlet et al., 2013; Didier et al., 2012; Truche et al., 2010; Truche et al., 2009; Truche et al., 2013) indicate an interaction between hydrogen and clay. Therefore, an extensive study was performed in order to investigate which interactions might influence the diffusion experiment and how microbial activity can be minimized/avoided.

Objective 3 was to investigate whether a relationship between the size of the diffusing molecules and their diffusion coefficients can be found for different clayey materials. After performing a first series of diffusion experiments with different gases, a relationship between the size of the diffusing molecule

(expressed as kinetic diameter, derived from the Lennard-Jones potential) and the measured diffusion coefficients was observed. Considering that for other clayey samples (e.g. Opalinus Clay, Callovo-Oxfordian Clay, bentonite) also such relationship is valid, the diffusion coefficients (for instance for hydrogen) could be estimated based on their size.

Objective 4 is to investigate which petrophysical properties influence the diffusive behaviour of dissolved gases. Given the fact that diffusion coefficients are influenced by the pore network/structure of the material, the obtained relationship should also be linked to petrophysical properties of the material.

3. Materials and methods

3.1 Boom Clay samples & sample preparation

Background on the Boom Clay

The Boom Clay is a marine sediment that was deposited in the early Oligocene (Rupelian), 29 to 32 million years ago in the North Sea Basin, at water depths between 50 and 100 m (Vandenberghe et al., 2014). Shortly after deposition, the accumulated sediment became reducing which is reflected in the common occurrence of framboidal pyrite. Boom Clay bulk mineralogy consists of inversely correlated quartz (20 – 60 %) and 2:1 clay minerals (22 – 56 %), plagioclase, potassium-feldspar and kaolinite (all between 10 and 15%), chlorite (1 – 4%), calcite (0 – 4%), pyrite (0 – 3 %), and some siderite and dolomite. The 2:1 clay minerals consist of illite (5 – 18% of bulk), smectite (7 – 24% of bulk), and randomly interstratified illite-smectite. The organic matter content varies between 1 and 5% (Vandenberghe et al., 2014).

The Boom Clay consists of different lithological sub-units. More specifically a rhythmic alteration of silty and more clay-rich layers has been observed, as well as the presence of organic-rich and carbonate-rich layers (Figure 1). This alteration is caused by a cyclic change in the sorting effect of a continuous supply of sediment particles (Figure 2). Vandenberghe et al. (2014) explains this alteration with a genetic model where climate is controlling the cyclically varying wave turbulence intensity at the bottom of the Boom Clay sea. In the model, a eustatically changing water depth is considered. It is also considered that the sorting of sediments by the waves becomes less effective when the sea level is rising. When the sea level is high at a certain location, turbulence intensity at the sea bottom is low and clay particles can sediment. When the sea level decreases at this location, turbulence intensity at the bottom increases and clay particles can no longer sediment and mainly silt particles are dominantly deposited. This hypothesis is supported by the provenance of the grains and by the position of the organic rich bands. Finally, the coastal land is flooded and plants are transported into the basin where they are deposited. When the water level is maximum, major part of the vegetation has been removed and the supply of phytoclasts stops so the peak of maximum continental organic matter has been passed. At the same moment, the lowest sorting degree is reached which is located in the middle of the clay layer. This explains why the black layers occur always just on top of the silty layers.

Figure 1: Boom Clay outcrop in Terhagen-Rumst. This picture shows clearly the alteration of clay and silty clay layers. The black layers contain land derived organic matter (picture from Vandenberghe et al. (2014)).

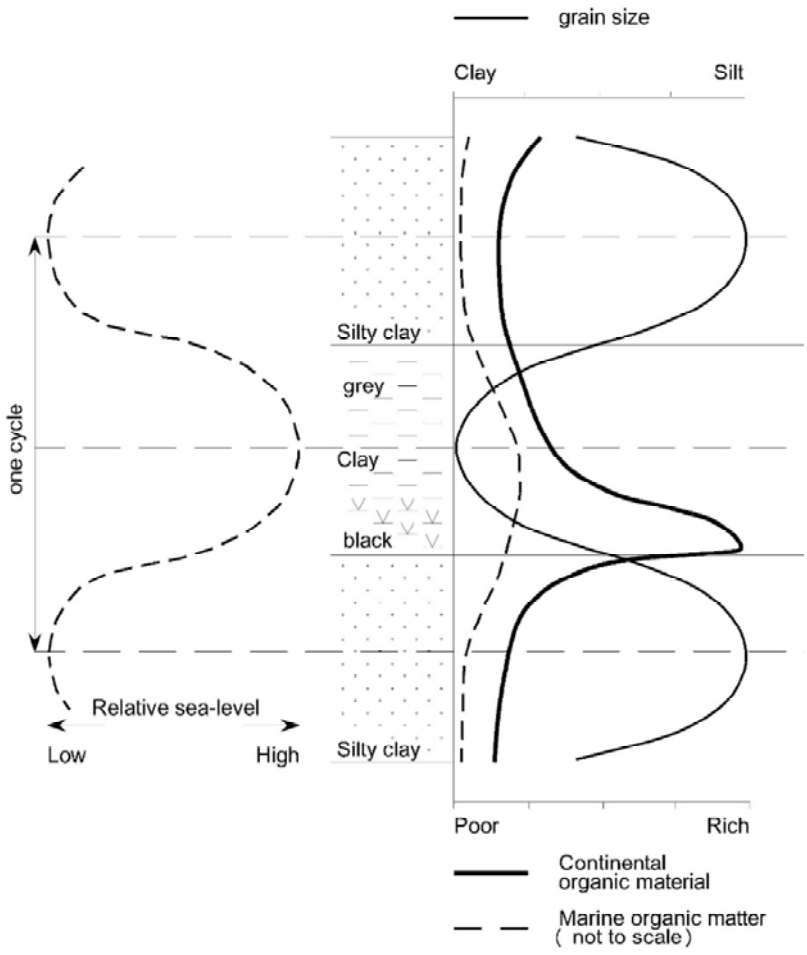

Figure 2: Schematic representation of the variations in grain size and organic matter content through a clay/silt couple. The left diagram shows the sequence stratigraphic interpretations of the clay/silt cycles. Modified from Vandenberghe et al. (2014).

Based on these lithological variations, the Boom Clay has been subdivided in four members: i.e. the Boeretang Member, the Putte Member, the Terhagen Member and the Belsele-Waas Member (Vandenberghe et al., 2014).

The sandy unit lying above the Boom Clay is named the Eigenbilzen Formation. This formation consists of dark green, glauconite rich, clayey, fine- to medium-grained sands, with bioturbations (National Commission for Stratigraphy Belgium). The amount of fine sand increases significantly but the silty and clayey intervals as observed in the Boom Clay remain (Vandenberghe et al., 2014).

In the Boom Clay, clay platelets sedimented as peloidal components (aggregated clay). Due to compaction, a preferential orientation (parallel to the bedding plane) of the clay platelets occurred. Due to this layered structure, diffusion coefficients are higher in the direction parallel (//) than perpendicular (⊥) to bedding (Figure 3) (Aertsens et al., 2009; Bruggeman et al., 2009; Van Loon et al., 2004; Wenk et al., 2008).

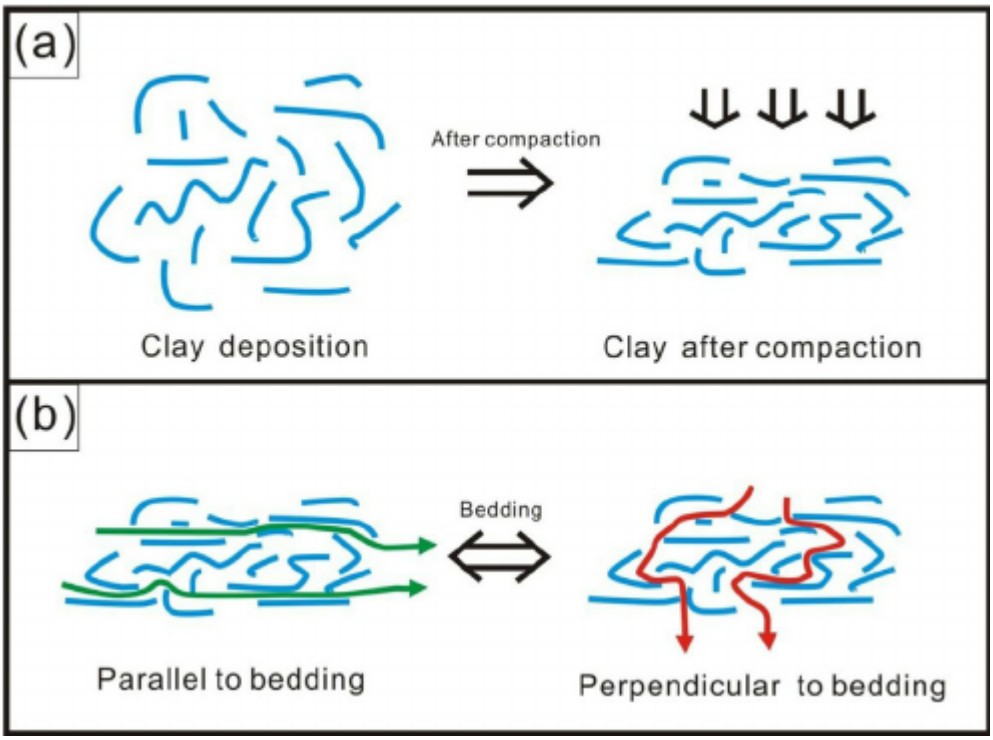

Figure 3: (a) Influence of compaction on the petrofabric; (b) impact on the tortuosity (taken from Wan et al. (2015)).

Boom Clay contains a certain amount of pyrite. Pyrite is formed in sediments during shallow burial, via the reaction of detrital iron minerals whereby the Fe is mobilised under reducing conditions and H_2S (Figure 4). H_2S is produced by the anaerobic reduction of sulphate by bacteria who use organic material as a reducing agent and energy source. The dissolved sulphide then reacts with mobilised iron and forms metastable greigite and mackinawite. Further reaction with elemental sulfur leads to the production of pyrite.

$$SO_4^{2-} + 2(CH_2O) \rightarrow 2HCO_3^- + \mathbf{H_2S}$$

The principal factors controlling pyrite precipitation are: anaerobic conditions and the availability of respectively dissolved sulphate, reactive iron and reactive organic matter in the sediment (Berner, 1984; De Craen, 1998).

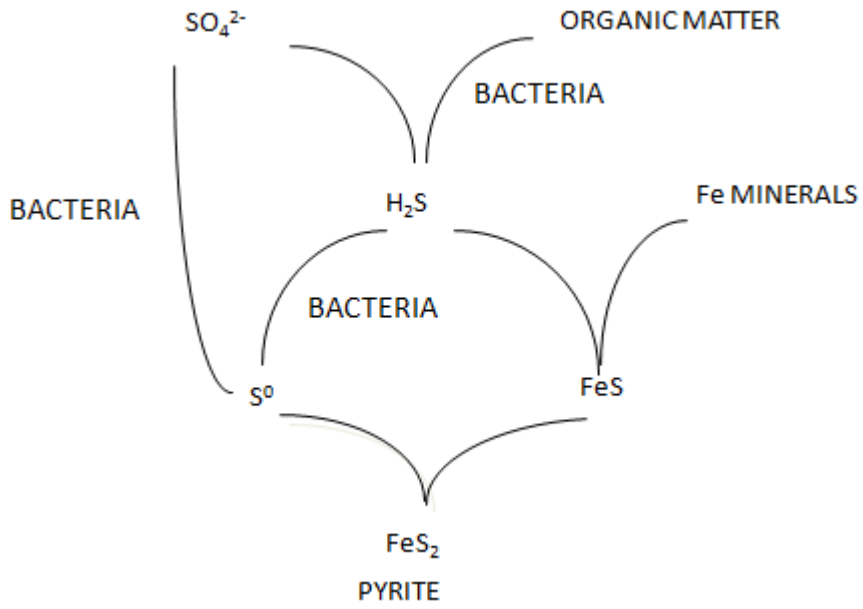

Figure 4: Schema of the formation of pyrite (after Berner (1984))

In the Boom Clay, different types of pyrite are observed, but pyrite is mainly present as framboids. Framboidal pyrite consits of discrete equigranular pyrite microcrystals which are packed into nearly spherical aggregates (see Figure 5). Also individual octahedral crystals occur frequently (see Figure 6). Framboidal and octahedral pyrite crystals are often grouped into clusters. Framboidal pyrite is concentrated in locations with a high organic matter content, e.g. in burrows or between faecal pellets. It can also be found in foraminifera, as interparticle filling.

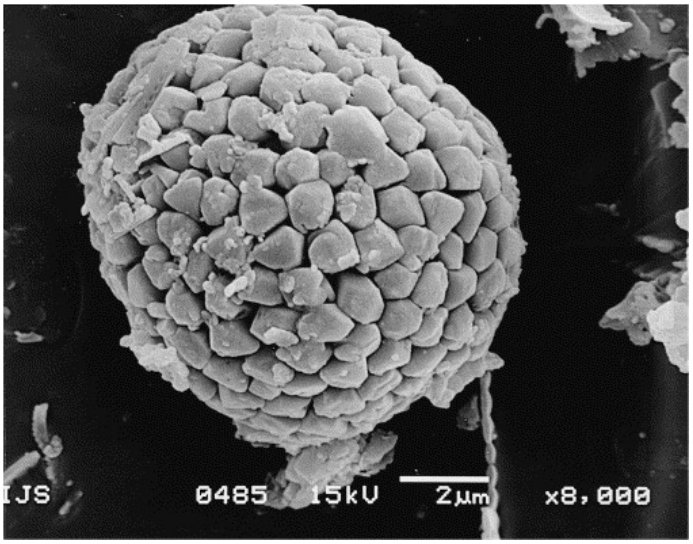

Figure 5: Example of framboidal pyrite: SEM micrograph of pyrite from a sediment layer, from Lojen et al. (1999)

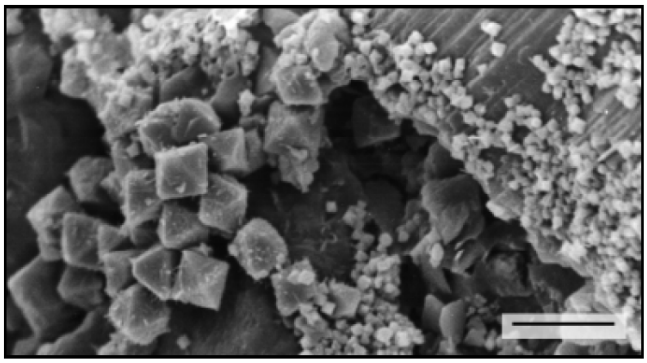

Figure 6: Octahedral pyrite crystals of different size. Scale bar = 10 µm. Picture taken from De Craen (1998).

Besides framboids and octahedral crystals, also hard and massive pyrite bodies are present. These are indicated by De Craen (1998) as concretionary pyrite bodies (Figure 7). Different subtypes of the concretionary bodies exist: pyritised worm tubes, pyrite nodules and semi-continuous to continuous layers.

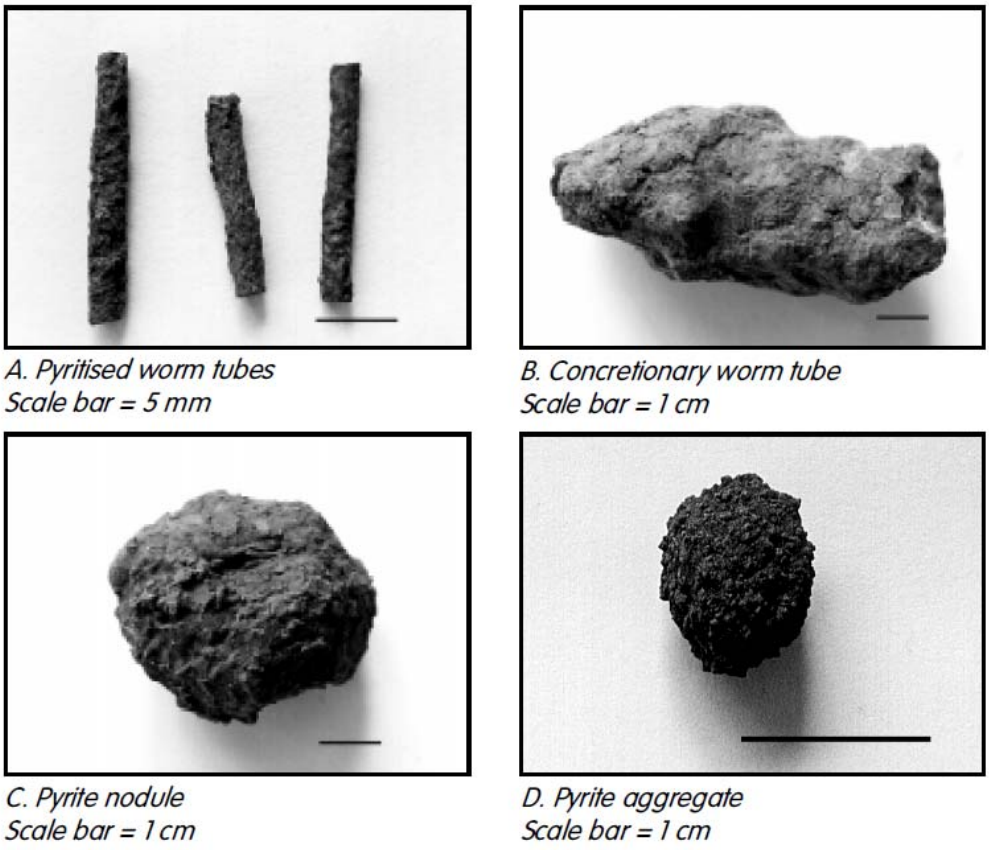

Figure 7: Different concretionary pyrite bodies, found in the Boom Clay (taken from De Craen (1998)).

Concretionary pyrite bodies are mostly composed of octahedral pyrite crystals or amorphous pyrite. Pyritised worm tubes have a diameter of 1 – 2 mm and contain pyrite framboids that are cemented by euhedral pyrite crystals. Concretionary worm tubes are elongated pyrite bodies with a nodular aspect and they can have a diameter up to 3 cm and a length up to 10 cm. They contain an inner tube of fine, crystalline pyrite octahedra and an outer tube of anhedral pyrite. Pyrite nodules have a more spherical

appearance, compared to worm tubes, but their characteristics are similar. Small pyrite aggregates contain octahedral pyrite and they are smaller than 2 cm. The main difference with the previously described bodies are the macroscopically visible pyrite crystals. Layered pyrite contains anhedral pyrite.

Samples and sample preparation (modified from Jacops et al., 2016a)

All Boom Clay samples used in this study are taken from the ON-Mol-1 borehole which was drilled in 1997, in the town of Mol, in the NE of Belgium (Lambert coordinates X (m) 200191.278 and Y (m) 211651.761). The samples are 100 mm in diameter and have a length of 100 or 200 mm. The depths at which the samples were taken and their orientation with respect to bedding are given in Table 2. Figure 8 shows the position of the samples in the lithostratigraphic column of the Boom Clay. The general mineralogical and physical properties of the Boom Clay have been described by Vandenberghe et al. (2014) and Zeelmaekers et al. (2015).

As we wanted to investigate which petrophysical properties influence the diffusive behaviour of dissolved gases, experiments have been performed on samples with a variable clay/silt/sand content. The samples have been selected based on their location in the lithostratigraphic column: clayey samples originate from the Putte Member, whereas the silty samples originate from the Boeretang Member and sandy samples from the Eigenbilzen Formation. Whether the samples are a representative selection or not is investigated by mineralogical analyses, grain size analyses and by measuring the hydraulic conductivity.

Table 2: Locations of all samples and orientation with respect to the bedding plane (see also Figure 8).

Core reference: ON-Mol-1 core #	SCK reference	Depth (m TAW*)	Depth (m BDT†)	Member	Clayey/silty/sandy	Orientation to bedding plane
84b	K2	203.29 - 203.39	233.02 – 133.12	Putte	clayey	⊥
127b	K4	245.89 - 245.99	275.62 – 275.72	Terhagen	silty	//
112a	K9	231.11 - 231.31	260.84 – 161.04	Putte	clayey	⊥
48a	K10	167.92 - 168.02	197.65 - 197.75	Boeretang	clayey	⊥
48a	K11	168.02 - 168.12	197.75 – 197.85	Boeretang	silty	⊥
36a	K14	155.99 – 156.19	185.72 – 185.92	Eigenbilzen Formation	sandy	//
37b	K15	156.89 – 156.99	182.62 – 186.72	Eigenbilzen Formation	sandy	//
35b	K16	154.91- 155.01	184.64- 184.74	Eigenbilzen Formation	sandy	⊥
39b	K17	158.89 – 158.99	188.62 – 188.72	Eigenbilzen Formation	sandy	⊥

* TAW: Tweede Algemene Waterpassing (second general levelling)

† BDT: Below drilling table. The drilling table was located at 29.73m TAW

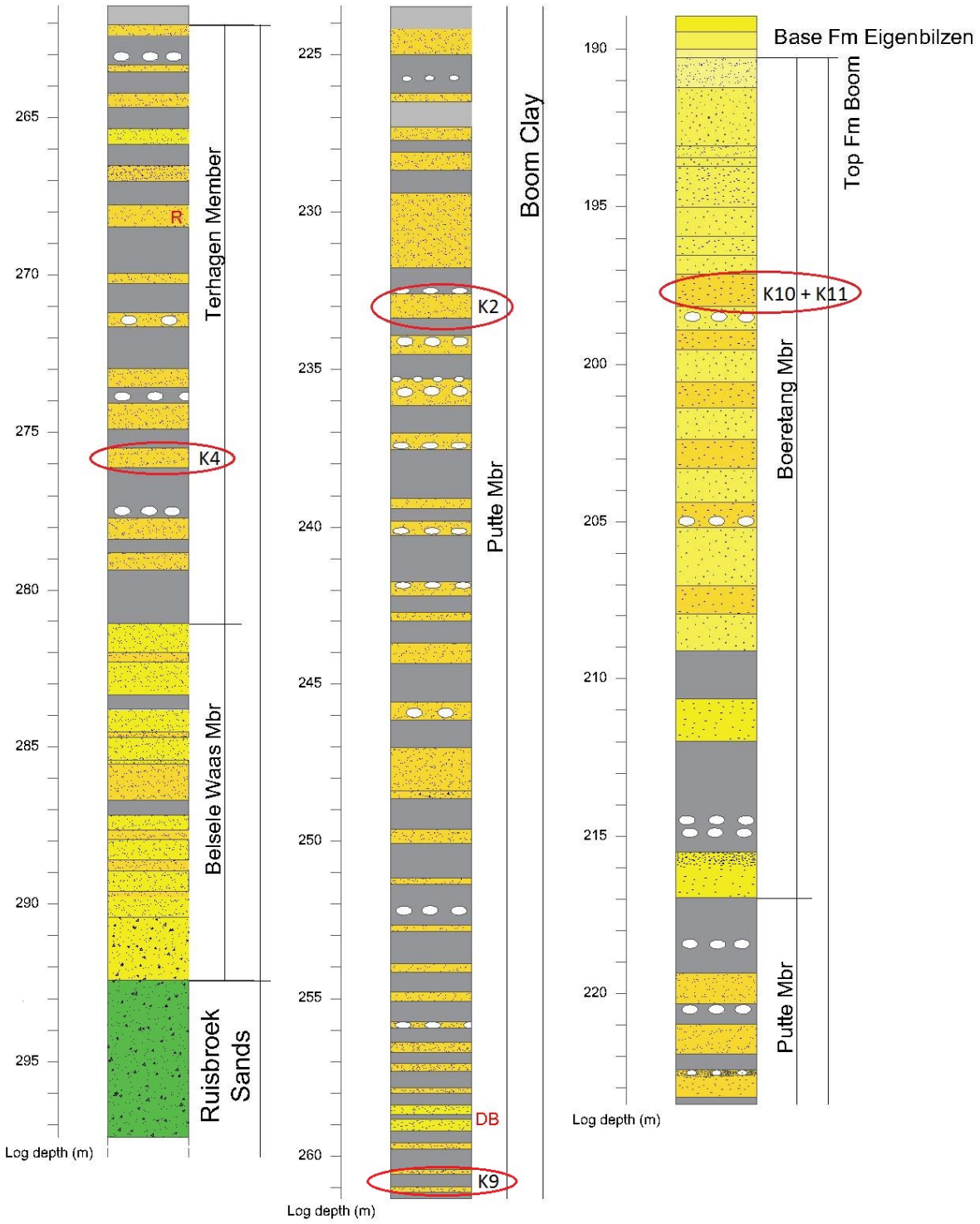

Figure 8: Litholog of the Boom Clay and indication of the position of the samples K2, K4, K9, K10, K11. Depths are expressed as log depth which is equal to meters Below Drilling Table (BDT). The drilling table was located at 29.73m TAW.

Since their retrieval in 1997, the cores have been stored under anoxic conditions at 4°C. More specifically, samples were sealed in PVC tubes and packed in alu-coated PE foil under vacuum. One of the main quality threats for sample alteration is oxidation. Oxidation of Boom Clay mainly leads to the oxidation of pyrite, which causes an increase in [SO_4^{2-}] in the pore water, ion exchange and mineral dissolution (De Craen et al., 2004a). As a first quality check, the sample package was carefully

inspected. If it was no longer vacuum, the sample might have been exposed to oxygen and could not be used for diffusion experiments. Next, after removing the sealed PVC tube, they were visually inspected for signs of oxidation. Other possible threats are, for instance, cracks and desaturation. When installing the samples in the diffusion cell, the outer rim (1 cm) and the top and bottom part (3.5 cm) of the clay, which might have dried out during storage and/or could have been prone to oxidation during handling of the cores, were removed. After loading the diffusion cell (see description below), the filter chambers at both sides of the clay core were filled with synthetic pore water (0.014 M $NaHCO_3$ to mimic the Boom Clay pore water (De Craen et al., 2004b) in order to resaturate the sample. Given the high sealing capacity of the Boom Clay (Van Geet et al., 2008), cracks possibly caused by the loading of the sample in the diffusion cell will seal within a few hours. Oxidation of the sample due to the loading in the cell is considered to be minimal because air in cracks is immediately replaced by (synthetic) pore water and these cracks are closed within a few hours. However, a small amount of oxidation due to sample handling cannot fully be excluded, but is considered to have no significant influence on the diffusion experiments.

3.2 Background information on other clayey materials and their sample preparation

Text modified from Jacops et al. (2017b)

As the third objectives is to investigate whether we can find a relation between the measured diffusion coefficients and the size of the diffusing molecules in different clayey materials, diffusion experiments with different gases have also been performed on Callovo-Oxfordian Clay, Opalinus Clay and bentonite (Volclay KWK, which is an MX80 type of bentonite) with a different dry density (1.4 and 1.6 g/cm³).

The Callovo-Oxfordian Clay (COX) is an indurated, Middle Jurassic mudstone from marine origin, which was deposited 150-160 million years ago. It has been intensively studied by the French National Agency for Radioactive Waste Management (ANDRA) on a 250 km² area in the Meuse-Haute Marne region (Bure, France). In this area, ANDRA has performed several drilling campaigns and constructed an Underground Research Laboratory (URL) at 490 m depth in the COX layer. The thickness of the COX formation is about 135 m at the URL. The COX consists mainly of clay minerals (illite, interstratified smectite/illite, and others), calcite, dolomite/ankerite, quartz, feldspars and minor amounts of accessory phases, such as pyrite (Gaucher et al., 2004). The used sample (EST 49109; depth - 478.52 m) was taken from the OHZ6560 borehole, which has been drilled from a technical gallery at the URL. The sample axis is oriented perpendicular to the bedding plane.

The Opalinus Clay is a fine-grained sedimentary rock, which was deposited 172 million years ago. It is proposed as a host rock for the disposal of nuclear waste in Switzerland by the National Cooperative for the Disposal of Radioactive Waste (NAGRA). The Opalinus Clay consists mainly of clay minerals (illite, illite/smectite, kaolinite and others), calcite, dolomite/ankerite, quartz, feldspars, pyrite and organic matter. Research on the Opalinus Clay is mainly performed in the Mont Terri Underground Research Lab, located in the canton Jura. The studied sample was, however, taken from the Schlattingen borehole (Northeast of Switzerland, canton Thurgau), at a depth of 860.32m below

surface. As the burial history for the Mont Terri site and Schlattingen is different, with deeper burial in Schlattingen (Mazurek et al., 2006), the physical properties of the Opalinus Clay are different at both locations. The sample axis is oriented perpendicular to the bedding plane.

The Volclay KWK (an MX 80 type bentonite) is a fine grained sodium bentonite with montmorillonite as the main component (Horseman et al., 1999). This type of bentonite was selected because it was characterized within the EC-NF-PRO project (Sneyers, 2008) and a batch was readily available at SCK•CEN. Besides, a similar type of bentonite was used as a sealing material within the PRACLAY heater experiment which is performed in the HADES URL (Van Marcke et al., 2014).

3.3 Through-diffusion method and experimental setup for diffusion of dissolved gases

Tekst modified from Jacops et al. (2013).

The principle idea with regard to our experiments consists of a double through-diffusion test (Shackelford, 1991 and Van Loon et al., 2003a) with two dissolved gases placed on opposite sides of a Boom Clay test core (Figure 9). In a classical through-diffusion test, the porous medium is placed in between 2 vessels, one containing a known concentration (high concentration compartment) of the diffusant while the other compartment is free of the diffusant (low concentration compartment). From the evolution of the diffusant concentration in both compartments, the diffusion characteristics of the diffusant can be obtained. In our setup 2 diffusants (2 dissolved gases) were used at the same time, each diffusant is initially present only at one side and both dissolved gases will diffuse simultaneously, but in opposite directions.

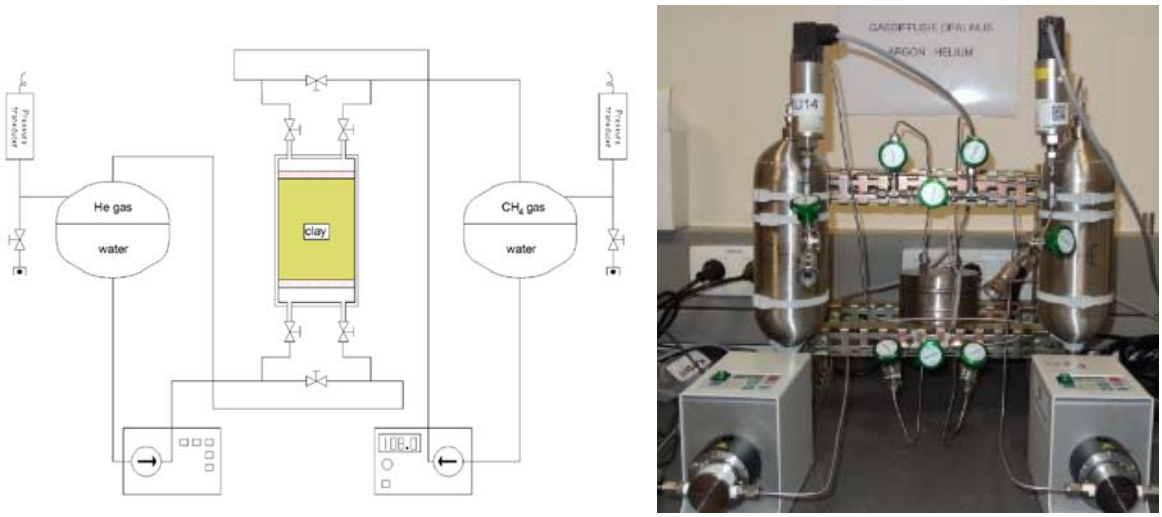

Figure 9: Schematic overview and a picture of the gas diffusion setup.

The clay samples are sealed in a stainless steel diffusion cell. Cores from the Boom Clay and the Eigenbilzen Sands (diameter 80 mm, height 30 mm) are pressed in the diffusion cell by using a hydraulic

press and confinement (constant volume) is achieved by sealing the diffusion cell. Due to the high plasticity (Van Geet et al., 2008), perfect sealing between clay and cell is achieved. As Callovo-Oxfordian Clay and Opalinus Clay contain lower proportions of swelling clay minerals, their swelling capacity/plasticity is therefore much lower compared to the Boom Clay. Therefore, the samples had to be embedded in a resin (Sikadur 52 Injection Normal) in order to seal the interface clay sample-cell. The embedded samples (80 mm diameter and 25 mm height for Opalinus Clay and 70 mm diameter and 30 mm height for the Callovo-Oxfordian Clay) were placed between an upper and lower flange, and subsequently the flanges were welded to the diffusion cell (confinement with constant volume). As the flanges were provided with a circulation loop, good contact between the water containing the dissolved gas and the clay sample was ensured.

The Volclay KWK was compacted to two different dry densities: i.e. 1.4 and 1.6 g/cm³. Prior to the compaction, the water content of the batch was measured by drying at 105°C for at least 24 hours. The correct amount of bentonite was compacted into a cylinder of 20 by 20 mm. Next, the compacted samples were saturated with a synthetic pore water of 0.05M $NaClO_4$.

All clay samples are connected via stainless steel filter plates (thickness 2 mm, porosity 40%) at both sides to water vessels that are pressurized with 2 different gases at the same pressure (Figure 9). In this way no advective flux can occur and the clay sample remains fully water saturated. According to Henry's law, equilibrium is obtained between the free gas in the gas phase and the dissolved gas in the water. The water at both sides is then circulated over the filters, which are in contact with the clay core, allowing the dissolved gases to diffuse through the clay core, towards the reservoir on the opposing side. The change in gas composition in both reservoirs is measured as a function of time by gas chromatography.

One of the most important aspects of this type of test is the gas tightness of the entire setup. Especially the gas tightness for H_2 and He might be a problem because both gases diffuse easily through many polymers that are often used as seals. To avoid gas leakage, all components are selected based on their gas tightness: polymers are avoided in valves, sensors and couplings and welding or metal-metal contacts are preferred. The sample cell is closed either by welding, either by using screws, bolts and a soft copper ring. Also the connections for the water in- and outlet are welded. Both vessels are equipped with a pressure sensor to follow the pressure evolution. The selected pressure sensor PTX 600 (DRUCK, New Fairfield, USA) measures the absolute gas pressure, contains a Hastelloy diaphragm which is welded to the body of the pressure sensor and is therefore considered to be gastight.

The water with the dissolved gas is circulated over the filters with a pump. For the selection of these pumps, there are 2 main requirements: gas tightness and low flow (approximately 10 ml/minute). A magnetically coupled gear pump REGLO-Z (ISMATEC, Glattbrugg, Switzerland) is selected because this type of pump has no direct coupling between the pump drive and the pump head (Micropump, Vancouver, Canada) which reduces the risk of leakage. Because of the synthetic seal between the magnetic cup and the pump body, diffusive He and H_2 leaks cannot be excluded, so the magnetic cup and the mounting plate are replaced by a new part which is welded onto the pump body. Also the connections for in- and outlet are welded. The pumps are calibrated for a flow rate of 5 to 10 ml/min.

All other construction parts (SWAGELOK, Ohio, USA) have metal-metal contacts and are considered to be gastight.

3.4 Test procedure for the diffusion of dissolved gases

Prior to the start of the diffusion experiment, the entire setup is checked for its leak tightness by pressurising the setup with 10 bar He during a few days. If the pressure remains constant during this time period, the setup is considered to be gastight.

Next, the diffusion cell is mounted into the setup. A solution of oxygen-free artificial porewater (composition is given in Table 3) is prepared in an anaerobic glovebox. After the transfer of 500 ml of the solution into each vessel of the setup, a gas buffer is put into the headspace (ca. 500 ml at 1 MPa pressure). Prior to the start of the diffusion process, a sample is taken to determine the initial gas composition of both vessels.

Sampling of the gas phase is performed on a regular basis (generally once per week) until 10 data points are obtained in the regime of approximately constant outlet flux of the diffusion process. The gas composition is analysed with a CP4900 micro GC (equipped with a Molsieve 5A and a Pora Plot U column and TCD detectors, Agilent, USA) or a CG4 Compact GC (equipped with a RT-Qbond column, a Molsieve 5A column and TCD detectors, Interscience, The Netherlands). Both GC's are operated with the EZChrom CDS software.

All experiments are performed in a temperature-controlled room (21 ± 2 °C).

The diffusion experiments with several gases on the same sample are performed consecutively: the content of the inlet and outlet vessel is replaced each time while the sample remains in the same position.

3.5 Through-diffusion for tritiated water (HTO)

To avoid a possible bias due to differences in the measuring technique, diffusion experiments with HTO are performed with a setup similar to the one used to measure through-diffusion of dissolved gases. Both vessels are filled with 250 ml artificial pore water (see Table 3) and 250 ml of gas (argon) at 1 MPa. A HTO spiking solution of approximately 50 kBq is added in the high concentration compartment. Both the decrease in activity in the high concentration compartment and the increase in the low concentration compartment are measured by taking at each side two samples of 1 ml. The water in both compartments is not replaced during the experiment. Sampling occurs regularly (once or twice per week) until 10 data points are obtained in the regime of approximately constant outlet flux. Samples are analysed for their radioactivity with a Packard TRI-CARB 2100TR liquid scintillation counter.

Table 3: Composition of the artificial pore waters

Chemical Component (mg/l)	Boom Clay (*)	Callovo-Oxfordian Clay (†)	Opalinus Clay (‡)	MX80
$NaHCO_3$	1176	216	50	
NaCl		1059	6132	
Na_2SO_4		2216	1632	
$CaCl_2.2H_2O$		947	1020	
$MgCl_2.6H_2O$		911	1004	
$SrCl_2.6H_2O$			84	
KCl		78	60	
$NaClO_4$				6122

* De Craen et al. (2004b)
† Savoye et al. (2010)
‡ Pearson et al. (2002)

3.6 Hydraulic conductivity

In general, the hydraulic conductivity (K) of a clay core is measured prior to the gas diffusion experiment. To measure the hydraulic conductivity, demineralised water or artificial pore water (composition listed in Table 3) is injected under pressure, and the water flowing out of the diffusion cell is collected in a flask that is placed on a precision balance. Both water inflow and water outflow are measured. The measurement is continued until the K-value is stable for 5 successive measurement intervals. A detailed description of the technique to measure the hydraulic conductivity can be found in Wemaere et al. (2008).

The hydraulic conductivity of the bentonite samples is measured according to the method of Phung et al. (2013) who apply a constant water flow instead of a pressure gradient.

3.7 Test procedure for experiments with H_2

Experiments with hydrogen often suffer from experimental problems such as leakage and microbial activity. In order to obtain reliable diffusion coefficients for hydrogen in Boom Clay, a dedicated protocol which combines different sterilisation techniques such as heat sterilisation, gamma irradiation, gas filtration and the use of a specific inhibitor has been designed by Jacops et al. (2015). This paper, containing a full description of the protocol, can be found in annex 3.

3.8 Interaction between gases and clay

The interaction between gases and clay is very often a topic of discussion within the field of geological disposal. During recent years, three major interaction mechanisms have been studied: biotic reactivity, abiotic reactivity and sorption, and most of these studies have been performed with hydrogen. When looking at other gases, mainly data for CO_2 and CH_4 (and some other hydrocarbons) can be retrieved from studies related to CO_2 sequestration, shale gas mining etc. However, for all these studies the boundary conditions (pressure, temperature, …) under which experiments have been performed play a very important role.

Abiotic reactivity is the occurrence of redox reactions in which gas (especially hydrogen) is consumed. In these reactions, hydrogen serves as an electron donor. Some possible reactions are the reduction of nitrate, sulfate, structural Fe(III) in clay minerals and pyrite (FeS_2) by hydrogen gas. The reduction of nitrate and sulphate by hydrogen is described by Truche et al. (2013) but it is important to consider that both reactions require high temperature (> 90°C) and high H_2 partial pressure (> 30 bar). Truche et al. (2010) observed also abiotic reduction of pyrite (FeS_2) to pyrrhotite in the temperature range of 90 – 180°C. Another possible redox reaction that can take place in an argillaceous environment is the reaction of Fe(III) with H_2. This Fe (III) can be present as structural Fe(III) in the clay fraction and in contact with H_2, Fe(III) can be reduced to Fe(II) (Didier et al., 2012). However, this reaction has not been demonstrated yet to occur at temperatures lower than 90°C. When comparing the boundary conditions of our experiments (fully saturated samples, gas partial pressure of 0.5 bar for H_2, room temperature) to the conditions under which abiotic reactivity was measured, we concluded that no significant interaction of H_2 with the clay will occur in our experiments. Moreover, no interaction ($R \neq 1$) was observed during the different diffusion experiments.

A major issue when performing experiments with H_2 is the biotic reactivity. Hydrogen is considered as one of the most energetic substrates for microbial life (Libert et al., 2011). Microbial organisms can use H_2 for different redox processes, and under anoxic conditions, the most common reactions are the reduction of NO_3^- to N_2 by denitrifying micro-organisms, the reduction of Fe(III) to Fe(II) by iron-reducing micro-organisms, the reduction of SO_4^{2-} to S^{2-} by sulphate reducing micro-organisms, the reduction of CO_2 to CH_4 by methanogenic micro-organisms (CO_2 (aq) + $4H_2 \leftrightarrow CH_4 + 2H_2O$) and the reduction of CO_2 to acetic acid by acetogenic micro-organisms (Libert et al., 2011). Most of the micro-organisms which are able to metabolize H_2 belong to the Archaea and can survive in extreme conditions (Madigan et al., 2000) so they might occupy certain higher-porosity niches in the repository or host formation (but presumably limited to the disturbed zone). The biotic reactivity has been described in the past by Ortiz et al. (2002) and Volckaert et al. (1994). Volckaert et al. (1994) performed batch experiments with Boom Clay slurries and hydrogen, and experimental results indicated the conversion of H_2 to CH_4 by methanogenic micro-organisms. Equal observations were reported by Ortiz et al. (2002): in experiments with Boom Clay slurries and iron/stainless steel powder: the hydrogen produced by metal corrosion was converted to methane by methanogenic micro-organisms. Microbial-driven gas conversion is thus a known phenomenon in experiments with hydrogen on Boom Clay samples and has also frequently been observed in diffusion experiments described in this work. More details can be found in Jacops et al. (2015). Similar observations have been made by Vinsot et al. (2014) when they performed an in-situ hydrogen injection experiment in the Mont Terri Underground Research Laboratory. Results showed that hydrogen disappeared much faster than He which was injected simultaneously. Analyses of the water gave indications that hydrogen could be consumed in

reactions where also sulphate and iron were reduced. As abiotic reactions do not occur under the experimental conditions, micro-organisms should be involved but hydrogenotrophs have not been identified yet (Vinsot et al., 2014). For the reported diffusion coefficients of hydrogen, the experiments were performed under sterile conditions and no biotic activity was monitored.

Besides the abiotic and biotic reactivity of hydrogen, hydrogen can also be sorbed to clay minerals. Most of the research on gas sorption focused on the sorption of CO_2 and CH_4 within the framework of CO_2 storage and shale gas research (Gasparik et al., 2013; Gensterblum et al., 2013; Ghanizadeh et al., 2013). Hence, sorption data are available, but the experimental conditions do not match with the conditions of a geological repository. For pure clay minerals, sorption data for CO_2 and/or CH_4 are available for dry illite, kaolinite and montmorillonte (Liu et al., 2013; Zhang et al., 2016). Also here, the experimental conditions are not comparable to those of a geological repository. Recently, data on the sorption of hydrogen on dried samples of Callovo-Oxfordian Clay have been published by Bardelli et al. (2014) and results indicate H_2 sorption up to 0.12% wt. for raw, dried COx and 0.3% wt. for purified COx. However, from other studies (Gensterblum et al., 2013; Ryan, 2006) it is known that the presence of water (moisture) also influences the sorption capacity of gases. The effect of moisture content on the sorption capacity was investigated in experiments on Opalinus Clay by conditioning the clay powders at different relative humidity levels but no relationship could be found between the degree of saturation and the sorption of H_2.

Let's now have a look again at our initial question: will gases (noble gases, light hydrocarbons and hydrogen) interact with clay in our diffusion experiments, or in a geological disposal? Based on what has been discussed above, and under conditions relevant for a geological repository, we expect no significant abiotic activity or sorption. On the other hand, a minor, insignificant interaction cannot be excluded. In order to confirm these hypotheses, a dedicated research programme, focussing on potential interactions between gases and clay, under a range of conditions relevant for a geological repository is advisable and currently under consideration by the different waste management organisations.

3.9 Diffusion theory

Text modified from Jacops et al. (2017a and 2017b).

Some theoretical aspects of the diffusion theory which are relevant for this PhD are summarized here. A summary of the diffusion parameters defined and used in this work is given in Table 4.

Table 4: Overview of used diffusion and other parameters (additional parameters are explained in the text).

Parameter	Name	unit	Formula
D_0	Diffusion coefficient in free water	m^2/s	
D_{app}	Apparent diffusion coefficient	m^2/s	$D_{app} = D_{eff}/\eta R$

D_{eff}	Effective diffusion coefficient	m²/s	$D_{eff} = \eta R\ D_{app}$
D_p	Pore diffusion coefficient	m²/s	$D_p = D_{app}\ R = D_{eff}/\eta$
ηR	Capacity factor	-	$\eta R = C_b/C$
G	Geometric factor or G-factor	-	$G = \eta\ D_0/D_{eff} = \tau/\delta$
F	Formation factor	-	$F = \frac{G}{\eta} = \frac{D_0}{D_{eff}}$
τ	tortuosity	-	
δ	constrictivity	-	
η	accessible porosity	-	
η_{tot}	total porosity	-	
AF	Anisotropy factor	-	$AF = D_{eff,//} / D_{eff,\perp}$
$V_{LJ}(r)$	Lennard-Jones potential	J or cm^{-1}	
σ	kinetic diameter	m	
r	distance between center of two molecules	m	
ε	depth of the potential well	J	
R_{gas}	gas constant	J mol^{-1} K^{-1}	8.314 J mol^{-1} K^{-1}
n	number of mole	mol	
K	Hydraulic conductivity	m/s	

In general, two transport parameters can be obtained from diffusion experiments: the apparent diffusion coefficient D_{app} (m^2/s) and the capacity factor ηR, being the product of the accessible porosity η (dimensionless) and the retardation factor R (dimensionless). The capacity factor is the ratio of the tracer concentration C_b in the bulk sample and the corresponding concentration C in the pore fluid (solution): $\eta R = C_b/C$.

From these two basic parameters, one can calculate the effective diffusion coefficient D_{eff} (m^2/s)

$$D_{eff} = \eta R\ D_{app} \quad (1)$$

and, assuming the accessible porosity equals the total porosity η_{tot}, the pore diffusion coefficient D_p (m^2/s)

$$D_p = R\, D_{app} \quad (2)$$

For unretarded species without ion exclusion (e.g. HTO), the retardation factor is generally put equal to one (R = 1), leading to $D_{app} = D_p$ and a capacity factor equal to the total porosity η_{tot}, which is measured independently. In the vicinity of clay surfaces, water diffuses slower than in bulk water (Bourg and Tournassat (2015) and references therein) making $R \neq 1$ possible. Still, pulse injection experiments in Boom Clay lead to an average HTO capacity factor ηR = 0.37 (Aertsens et al., 1999; Aertsens et al., 2004; Aertsens et al., 2005). The Boom Clay water content of 19 - 24 % (average 21.5 %) and dry bulk density ρ_{db} = 1.7 kg/l (De Craen et al., 2004b; Maes et al., 2011) lead to an average η_{tot} = 0.365, in agreement with ηR = 0.37. Also for Ypresian Clay at Doel, the HTO capacity factor and the water content are similar (Aertsens et al., 2003). Apart from H_2, it looks evident that for the dissolved gases studied in our experiments the retardation factor is one (R = 1). Considering no significant interaction between H_2 and the clay, we set R = 1 for H_2 as well. For the justification we refer to Jacops et al. (2015) and to §3.8.

The geometric factor relates the diffusion coefficient in a porous medium to the corresponding diffusion coefficient D_0 (m^2/s) in water and is defined by

$$G = \frac{D_0}{D_p} = \frac{D_0}{R\, D_{app}} = \frac{\eta D_0}{D_{eff}} \quad (3)$$

Due to the anisotropy of the apparent diffusion coefficient ($D_{app,//} > D_{app,\perp}$), the geometric factor is anisotropic as well, with $G_{app,\perp} > G_{app,//} > 1$.

Although the geometric factor is a black box factor, it is often split in two factors: tortuosity τ and constrictivity δ:

$$G = \frac{\tau}{\delta} \quad (4)$$

In this expression, used in this study and in (Grathwohl, 1998), tortuosity is defined as the square of the ratio of the effective path length (along the path) of a diffusing component to the shortest distance (end to end distance) of that path. It is more common (Amann-Hildenbrand et al., 2015; Epstein, 1989) to write $G = \tau^2/\delta$ with tortuosity the ratio of effective path length to its shortest distance. Constrictivity takes into account the reduction of the effective diffusion coefficient due to a drag by the pore wall, and depends on the ratio of the solute diameter to the pore size distribution. In case of large pores, the constrictivity factor δ is one. Constrictivity becomes important (much smaller than one) if the solute diameter has the same order of magnitude as the pore diameter.

Analogous to the electrical conductivity of water-saturated rocks, the diffusion coefficient in free water and the effective diffusion coefficient can be used to define a "formation factor" F (unit: dimensionless), defined by

$$F = \frac{G}{\eta} = \frac{D_0}{D_{eff}} \quad (5)$$

Generally, geometric factors and formation factors can be derived in four different ways: from diffusion experiments (mostly with HTO) (Fourre et al., 2011; OECD, 2008), by calculating them while using different models (e.g. Archie (1942); Boudreau (1996); Chou et al. (2012) and Saripalli et al. (2002)) or by calculating them from diffusion simulations on reconstructed clay structures (Keller et al., 2015; Robinet et al., 2012) or by using empirical expressions (Grathwohl, 1998).
A well-known empirical relation which relates the formation factor (or tortuosity) to porosity is Archie's law (Archie, 1942).

$$F = A\,\eta^{-m} \quad (6)$$

with the exponent *m* corresponding to the cementation factor and the dimensionless factor *A* often taken equal to one.

Meanwhile, many variatons on Archie's law have been proposed, e.g. by Weissberg (1963) and Boudreau (1996) and they allow to calculate the geometric factor based on different properties of the material. For instance, Saripalli et al. (2002) described a method to calculate tortuosity and constrictivity (the two factors which make up the geometric factor) from the specific surface which can be determined from e.g. N_2 adsorption measurements while Chou et al. (2012) discussed different models which can be used to calculate tortuosity for variously saturated soil samples, based on their water content. Expression (6) can also be used to describe D_{eff}: Substituting (6) in (5) with *A* = 1 leads to

$$D_{eff} = \eta^m D_0 \quad (7)$$

Although empirically, expression (7) is able to describe in an approximate way the effective (and thus also the apparent) diffusion coefficient as a function of the accessible porosity in a porous medium. This expression is used for instance by Van Loon and Mibus (2015) who - in case of anisotropic media - only considered diffusion vertical to the bedding. A possible way to interpret expression (7) is that on average a lower accessible porosity means less or smaller pores and correspondingly a lower diffusion coefficient.

Both Robinet et al. (2012) and Keller et al. (2015) calculated geometric factors from diffusion simulations on reconstructed mesostructures of respectively the Callovo Oxfordian and the Opalinus Clay. This technique allowed the determination of "*G*" as a function of mineralogy.
All described methods calculate the geometric factor of a specific material, without taking into account the possible effect of the size of the diffusing molecule.

Constrictivity is described by Grathwohl (1998) by some empirical expressions and some take into account the effect of the size of the diffusing molecule, e.g.

$$\delta = exp\left(-4.6\,\frac{\sigma}{R_{pore}}\right) \quad (8)$$

with σ the size (diameter) (m) of the diffusing molecule and R_{pore} the pore width (diameter) (m). Substituting (8) in (4) leads to

$$G = \tau \, exp\left(4.6 \, \frac{\sigma}{R_{pore}}\right) \quad (9)$$

Evidently, reducing the pore size distribution of clay to a single pore size R_{pore} is an enormous simplification as clays have in reality a wide pore size distribution. In expression (9), like in reality, the influence of the size of the diffusing molecule σ depends on the ratio of molecular size to pore width. Although empirical (and certainly not valid over the entire σ/R_{pore} range), expression (9) also takes into account that sufficiently large molecules ($\sigma \rightarrow \infty$) can no longer diffuse through the clay anymore ($G \rightarrow \infty$ corresponding to a zero effective/apparent/pore diffusion coefficient). This has been observed e.g. for the transport of colloids (natural organic matter) in Boom Clay (Durce et al., 2017), where small sized diffusing molecules can move through the clay while larger ones cannot. This is related to a percolation transition (Stauffer and Aharony, 1992). If the size of the diffusing molecule rises, fewer pores are available for the transport (diffusion) of that molecule. In a first stage, this will lead to longer travel paths ('tortuosity') since only pores with a pore size larger than the size of the diffusing molecule are available. When still increasing the molecular size, there is no longer a connected path (of pores available for transport) between the larger pores and the diffusion coefficient becomes zero. In the remainder of this thesis, expression (9) is used as a simple empirical expression, trying to capture the evolution of the *G*-factor as a function of size of the diffusing molecule (but clearly wrong when $\sigma/R_{pore} >> 1$), which does not imply the approval of expression (4) and the corresponding definition of tortuosity and constrictivity.

3.10 Single pore size hydraulic conductivity model

Text modified from Jacops et al. (2017b).

Due to the single pore size approximation in the *G*-factor, also a single pore size model is presented for advective flow. The flow Q_{core} (m^3/s) out of a cylindrical clay core with radius R_{core} (m) and length L_{core} (m) is provided by Darcy's law,

$$Q_{core} = \pi R_{core}^2 \, \frac{\Delta p}{L_{core}} \, K \quad (10)$$

with Δ*p* the pressure difference (in meter water column) over the core.
Poiseuille's law gives the flow Q_{pore} (m^3/s) through a cylindrical pore with radius R_{pore} (m)

$$Q_{pore} = \frac{1}{\mu} \, \frac{\pi R_{pore}^4}{8} \, \frac{\Delta p}{L_{core}} \quad (11)$$

with μ the viscosity (kg/(m s)) (a value μ = 0.7978 mPa s = 8.135 x 10^{-8} m s was used (Edge Engineers)). If C_{pore} is the number of pores per unit surface (m^{-2}), the flow Q_{core} also equals

$$Q_{core} = \pi R_{core}^2 \, C_{pore} \, Q_{pore} \quad (12)$$

and the core porosity η_{tot} is given by

$$\eta_{tot} = \pi R_{pore}^2 \, C_{pore} \quad (13)$$

Combining expressions (13) leads to the next expression for the hydraulic conductivity

$$K = \frac{1}{8\mu} R_{pore}^2 \, \eta_{tot} = \frac{\pi}{8\mu} R_{pore}^4 \, C_{pore} \quad (14)$$

showing that for two clays with the same porosity, the hydraulic conductivity is highest for the clay with the largest pore size. It is also clear that in case of a pore size distribution, a major contribution to the hydraulic conductivity comes from the largest pores.

3.11 Diffusion as a function of the size of the diffusing molecule

Text modified from Jacops et al. (2017b).

Molecular size can be characterized in several ways. The most widely used measure for the size of a (small) gas molecule is the kinetic diameter (σ) (Yampolskii et al., 2006). Therefore, the interaction potential between two (gas) molecules is assumed a Lennard-Jones $V_{LJ}(r)$ (with r distance between the center of two molecules) (Hirschfelder et al., 1964)

$$V_{LJ}(r) = 4\varepsilon \left(\left(\frac{\sigma}{r}\right)^{12} - \left(\frac{\sigma}{r}\right)^{6} \right) \quad (15)$$

The potential $V_{LJ}(r)$ is zero at $r = \sigma$ and minimal at $r = 2^{1/6}\,\sigma$, where the potential energy is $-\varepsilon$. The distance σ, called the kinetic diameter, is considered representative for the size of the gas molecule.

The values of the parameters σ and ε can be fitted from p (pressure) V (Volume) isotherms over a range of temperatures (T) by the virial expansion (Hirschfelder et al., 1964)

$$\frac{pV}{nR_{gas}T} = 1 + B(T)\frac{n}{V} + C(T)\left(\frac{n}{V}\right)^2 + \cdots \quad (16)$$

with n the number of moles, R_{gas} the gas constant (8.31 J/(K mol)) and $B(T)$, $C(T)$, … the virial coefficients which (assuming a Lennard-Jones interaction) are a function of σ and ε (Beattie et al., 1951; Hirschfelder et al., 1964). Gas viscosity is a function of σ and ε as well, allowing to estimate also these parameters from viscosity measurements at different temperatures. The data determined by both

methods often show differences in the values of the Lennard Jones parameters (Yampolskii et al., 2006). According to (Hirschfelder et al., 1964) kinetic diameters obtained via second virial coefficients should be used for thermodynamic properties and calculations of the equation of state, whereas kinetic diameters obtained from viscosity measurements should be used for transport property calculations. Therefore, kinetic diameters from viscosity measurements are selected for use in this study (Table 5). However, the selected kinetic diameters are representative for dilute gas mixtures and are thus only an approximation for gases dissolved in water. Besides, a Lennard Jones potential does not take into account molecular shape anisotropy, nor does it look appropriate for a polar molecule like H_2O. Still, the kinetic diameter is able to describe rather well the decreases of the diffusion coefficient of gases in polymers as a function of size (Yampolskii et al., 2006). More detailed information on the selection of these kinetic diameters can be found in annex 2.

Table 5: Size of the used gases and HTO (values from Hirschfelder et al. (1964), and their diffusion coefficients in free water (D_0 – values from Boudreau (1997))

	σ (Å)	**D_0 x 10^{-9} (m^2/s)**
He	2.58	7.3
HTO	*2.75*	*2.2*
Ne	2.79	4.0
H_2	2.97	5.1
Ar	3.42	2.4
CH_4	3.82	1.8
Xe	4.06	1.5
C_2H_6	4.42	1.4

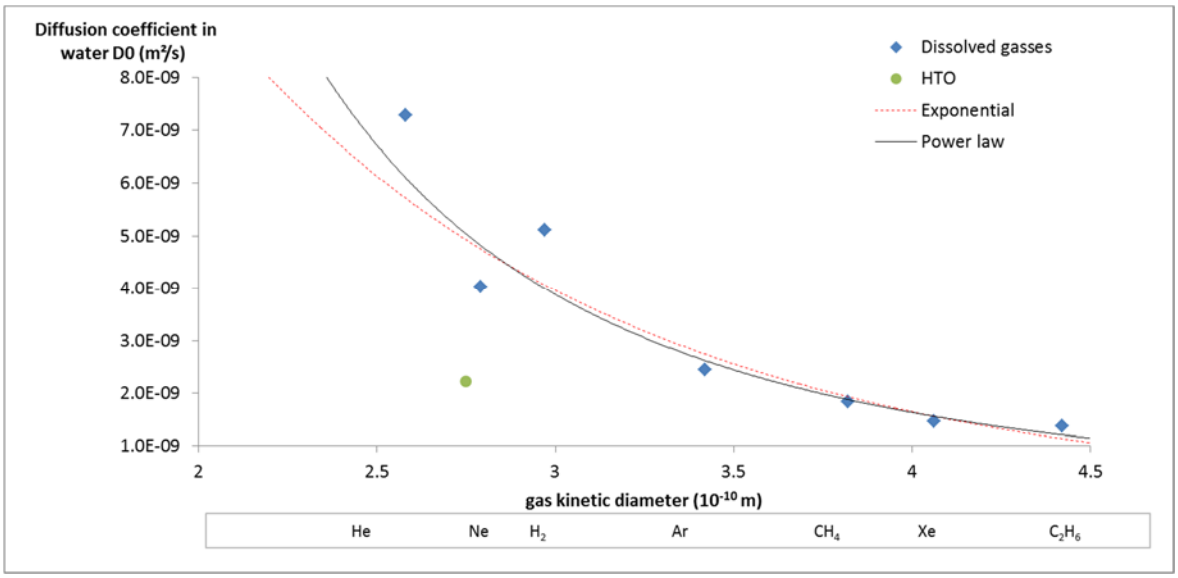

Figure 10: The relation between the diffusion coefficient D_0 in free water and the kinetic diameter for dissolved gases fitted with an exponential fit and a power law fit. The HTO value is not included in the fit and given only for comparison with dissolved gases.

Plotting in Figure 10 the gas diffusion coefficients D_0 in water (values taken from Boudreau (1997), Table 5) versus the kinetic diameter (values taken from Hirschfelder et al. (1964)) also shows that generally D_0 decreases as a function of the kinetic diameter σ. Empirically, this can be fitted by e.g. an exponential equation,

$$D_0 = D_{0,exp}\exp(-n_{0,exp}\sigma) \qquad (17)$$

leading to $D_{0,exp}$ = (5.5 ± 2.3) x 10^{-8} m^2/s and $n_{0,exp}$ = (8.8 ± 1.2) x 10^9 m^{-1} (see Figure 10). Notice that a better fit was obtained by a power law (Figure 10).

$$D_0 = D_{0,pow}\,\sigma^{-n_{0,pow}} \qquad (18)$$

where the kinetic diameter is expressed in 10^{-10} m, $D_{0,pow}$ = (1.1 ± 0.45) x 10^{-7} m^2/s and $n_{0,pow}$ = 3.0 ± 0.4. A power law is also used to describe (*i*) the decrease of the diffusion coefficient D_0 of organic molecules with increasing volume in aqueous solutions (the latter however should not be used for small molecules like H_2 or H_2O, see (Grathwohl (1998) and references therein) and (*ii*) the diffusion coefficient of gases in polymers (Yampolskii et al., 2006). The fits in Figure 10 are of a similar quality as e.g. Figure 1.3 in Yampolskii et al. (2006), describing the dependence of the diffusion coefficient in polymers as a function of the kinetic diameter. Because expressions (17) and (18) do not take into account details like anisotropy in the molecular shape or polarity of a molecule, they can only be expected to describe a global evolution without predicting correctly every single point (similarly like e.g. Archie's law). Clearly, both fits represent rather well the D_0 values for the larger molecules (Ar to C_2H_6), but not for the smaller ones (in particular HTO).

Due to its polar nature, water (HTO) might interact with the aqueous solution in a different way than noble gases and light hydrocarbons. Therefore, it is not included in the fits of (17) and (18). To allow a

comparison with gases, it is included in Figure 10. The water kinetic diameter is 2.75 x 10^{-10} m (Franks, 1975). Water and HTO have similar self-diffusion coefficients: 2.30 x 10^{-9} m²/s for water (Holz et al., 2000) and 2.22 x 10^{-9} m^2/s for HTO (Boudreau, 1997).

3.12 Modelling of diffusion experiments

Text modified from Jacops et al. (2016a).

The diffusion experiments are modelled by fitting the solutions of the diffusion equation with the appropriate boundary and initial conditions. For both gas and HTO diffusion experiments, the diffusion equation is solved by COMSOL coupled with MATLAB for optimization. An example is shown in Figure 11. Before fitting, for HTO, the measured concentrations are recalculated to zero time (thus taking into account radioactive decay).

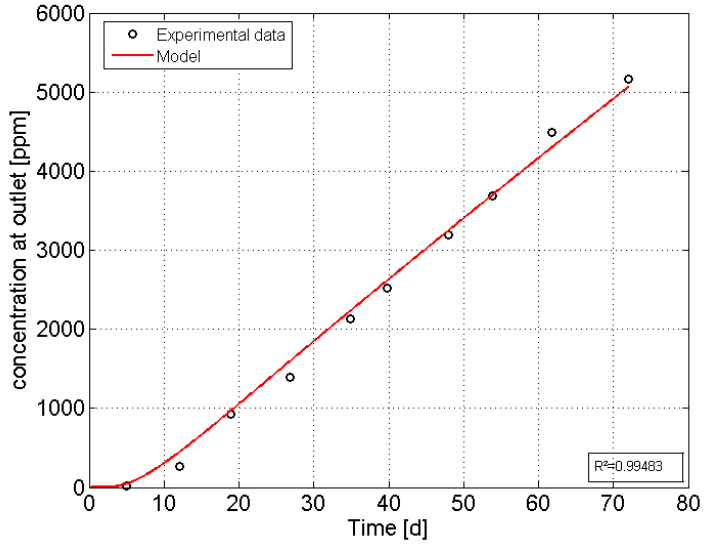

Figure 11: Example of fitting a diffusion experiment (diffusion of CH_4 in sample K2)

For HTO diffusion, because neither the inlet, nor the outlet is replaced, basically the VC-VC (Variable Concentration at inlet and outlet) case (Takeda et al., 2008) is solved. In addition, the numerical solution takes into account diffusion through the confining filters. Also the loss of tracer and the loss of water volume in the inlet and outlet vessels due to sampling are taken into account. Two parameters need to be determined: the apparent diffusion coefficient D_{app} (unit: m^2/s) and the capacity factor ηR (unit: dimensionless). Minimizing the same χ^2 function as in Aertsens et al. (2011) allows simultaneous fitting of the tracer evolution in the inlet compartment as well as in the outlet compartment.

A through-diffusion experiment allows fitting both the apparent diffusion coefficient D_{app} and the capacity factor ηR, which are in general both unknown. Besides, also the initial concentration, which is known but prone to measurement errors, is fitted. For HTO and (inert) gases, an alternative fit strategy is possible: assuming $R = 1$, only D_{app} is fitted and ηR is a constant equal to η_{tot} (either measured

on that sample or an average value from literature which has been measured on other Boom Clay cores previously such as in Bruggeman et al. (2009)). For HTO, both the one and three parameter fit strategy are used, making it possible to compare the optimal parameter values for the transport parameters in both cases. In some gas through-diffusion experiments where the (quasi) stationary state is reached very fast, a nearly total correlation is observed between the capacity factor, the apparent diffusion coefficient and the initial concentration. So only the effective diffusion coefficient can be determined and a one parameter fit is the only option. For allowing an optimal comparison of all gas transport parameters, all values have to be obtained in the same way. Therefore, all gas diffusion coefficients are obtained from a one parameter fit. The water content of a core which is necessary to calculate porosity is measured at the end of the diffusion experiments.

The gas diffusion model (Jacops et al., (2013 and 2015)) takes into account the pressure reduction in both vessels due to sampling.

As discussed above, confining filters are used in the diffusion experiments. As discussed by Aertsens et al. (2011), Birgersson and Karnland (2009) and Glaus et al. (2008) the filters might have an influence on the results as they contribute to the diffusive resistance of the experiment. Therefore, two fitting strategies are possible: one assuming the same transport parameter values for clay core and filter (case 'Filter=Clay' – 'F=C') and once with fixed (= the measured but not very accurate values) filter parameter values (case 'Fixed Filter'- 'FF'). However, the only element for which the values of the transport parameters in the filters are measured is HTO (Aertsens et al., 2011). For Boom Clay oriented perpendicular to the bedding plane, the values of the transport parameters are roughly similar to those of the filter so it can be a good approximation to assume the same transport parameters for the filter as for the clay core (case “F= C”). However, also Boom Clay cores oriented parallel to the bedding plane and other types of cores are investigated and in these cases, the diffusion coefficient of the filter differs considerably from the HTO diffusion coefficient in the samples. Therefore, the most correct approach is to use in the model the known HTO filter diffusion coefficient (case Fixed Filter - “FF”).

Diffusion coefficients of dissolved gases in the filters are not available and therefore only the value of HTO could be used as an approximation. Taking into account the uncertainty on this filter diffusion coefficient for HTO (around 50%, Aertsens et al. (2011)), using the latter would also introduce a large uncertainty into the model. Given also the large length of the samples (35 mm) compared to the length of the filters (2 x 2 mm), the effect of the filter on diffusion is not taken into account in the experiments with dissolved gases.

3.13 Sample characterisation

The different techniques which are used for the petrophysical description of the samples are described in detail in annex 2.

3.14 selection of kinetic diameters

Within this manuscript, the size of the different molecules is described by their kinetic diameter. In order to justify the use of the kinetic diameter as a measure for the size of dissolved gases, a detailed discussion can be found in annex 3.

4. Results

4.1 Mineralogy, grain size distribution and specific surface area

The mineralogical composition of each sample is shown in Table 6 while the grain size distribution is shown in Table 7 and Figure 12. Please note that the values shown in this manuscript do not always correspond to the values shown in Jacops et al. (2017a). Initially, the samples were analysed with a Sedigraph (Micromeritis, USA), at KU Leuven, but the apparatus broke down during this study and could not be repaired. Therefore, all samples have been (re)measured with a similar Sedigraph at the Federal Institute for Geosciences and Natural Resources (BGR) in Hannover. Due to some instrumental and operational differences (mainly related to the use of an ultrasonic probe to disperse the sample), there was a serious discrepancy between the results obtained in Leuven and in Hannover. After internal discussion (in the framework of the PhD of L. Frederickx), the results obtained in Hannover were considered to be more reliable and only these data are shown here.

Both the Boom Clay and the Eigenbilzen Sands are mainly composed of quartz and 2:1 clay minerals. As shown in Table 6 the main differences between the samples of the Boom Clay and the Eigenbilzen Sands are logically related to the main components quartz and 2:1 clay minerals. Given the high quartz content and the lower content of 2:1 clay minerals, the samples of the Eigenbilzen Sands can be considered as “sandy”. When looking at the grain size distribution of the different samples (Figure 12 and Table 7), there is a very clear difference between the samples of the Boom Clay and the Eigenbilzen Sands. The latter contain less clayey and silty particles, but much more sandy particles. Therefore, these samples are located in and near the “clayey sand” region of Figure 12 and are named “clayey sand” in this manuscript. All Boom Clay samples contain silty particles (27 ± 3 %), and therefore these samples are mainly located in the “silty clay” region. The correlation between the mineralogical composition and the grain size distribution is discussed later on.

Samples K10 and K11 are located in the Boeretang Member and are expected to be more silty compared to the samples of the Putte and Terhagen Member (K2, K4, K9). However, this is not clear from the mineralogical composition: the composition of samples K10 and K11 is very similar to the one of K2 so there seems to be no significant difference between these samples. When looking at the grain size distributions, the conclusion is similar: we observe no significant difference between both types of samples. From this point of view, the samples of the Boeretang Member cannot be considered as respresentatives of “silty” samples.

The composition of the Callovo-Oxfordian Clay (COX) sample corresponds well with the reference values presented in ANDRA (2005). The composition of the Opalinus Clay (OPA) samples corresponds well to results obtained for samples located nearby our analysed sample (Wersin et al., 2012).

The specific surface are is shown in Table 6. Measurements were performed at RWTH Aachen with liquid nitrogen in a TriStar 3020 (Micromeritics), using the Brunauer-Emmett-Teller theory. From a subset of these data (pressure range P/P_0 0 – 0.15), and by using the Dubinin-Ashtakov theory, the volume of micro pores was calculated (Dubinin and Astakhov, 1971; Thommes et al., 2015). The correlations between the SSA, micro pore volume and mineralogy/grain size distribution will be discussed later on.

Table 6: Mineralogical composition, specific surface area and volume of micro pores of all samples. Bent = bentonite, COX = Callovo-Oxfordian Clay and OPA = Opalinus Clay

	Boom Clay					Eigenbilzen Sands				Bent	COX	OPA
	K2	**K4**	**K9**	**K10**	**K11**	**K14**	**K15**	**K16**	**K17**			
Quartz (%)	31	28	26	32	33	59	58	60	54	3	24	28
K-feldspar (%)	8	5	5	10	6	8	9	10	8	BD	5	3
Plagioclase (%)	3	1	0.7	2	3	6	6	5	5	3	3	BD
Calcite (%)	0.2	2	BD	0.8	0.4	BD	BD	BD	BD	BD	21	8
Ankerite/ Dolomite (%)	BD	BD	BD	0.6	0.5	BD	BD	BD	BD	BD	4	BD
Pyrite (%)	2	2	2	1	1	0.6	0.5	1	0.5	BD	1	0.6
Gypsum* (%)	0.6	0.5	0.3	BD	BD	1	1	BD	BD	BD	BD	BD
Anatase (%)	0.6	0.7	0.7	0.6	0.7	BD	BD	BD	BD	BD	BD	BD
Kaolinite (%)	8	9	9	7	5	2	4	2	3	BD	0	BD
2:1 Al Clay (%)	34	41	46	32	39	20	18	21	27	93	39	59[†]
Muscovite (%)	9	8	8	11	9	BD	BD	BD	BD	BD	BD	BD
Chlorite (%)	2	2	2	3	2	3	3.5	BD	2.5	BD	3	BD

Opal A (%)	2	1	1	BD	BD	BD	BD	BD	BD	BD	BD	BD
Specific surface area (m^2/g)	38	45	46	44	41	14	12	8	20	[+]	28	21
volume of micro pores (mm^3/g)	18	20	22	20	18	7	5	4	9	[+]	[+]	[+]

***** gypsum is a secondary phase, it is an oxidation product of pyrite after exposure of the sample to air.

[†] this value contains all clay minerals (counted together)

[+] not measured

Table 7: Grain size distribution of the different samples: results and averages ± standard deviation per origin

Sample name	Sample origin	clay	silt	sand
		< 2 µm	2 to 62 µm	> 62 µm
K17	Eigenbilzen Sands	35	22	43
K16	Eigenbilzen Sands	30	13	58
K15	Eigenbilzen Sands	33	22	45
K14	Eigenbilzen Sands	36	16	49
K11	Boeretang Member	67	31	3
K10	Boeretang Member	73	24	2
K9	Putte & Terhagen Member	76	23	0
K4	Putte & Terhagen Member	69	29	2
K2	Putte & Terhagen Member	70	25	5
Opalinus Clay		59	38	2
Callovo-Oxfordian Clay		67	31	2
avg Eigenbilzen Sands		33 ± 3	18 ± 5	49 ± 7
avg Boeretang Member		70 ± 5	28 ± 4	2 ± 0.3
avg Putte & Terhagen Member		72 ± 4	26 ± 3	3 ± 3
avg Boom Clay		71 ± 4	27 ± 3	2 ± 2

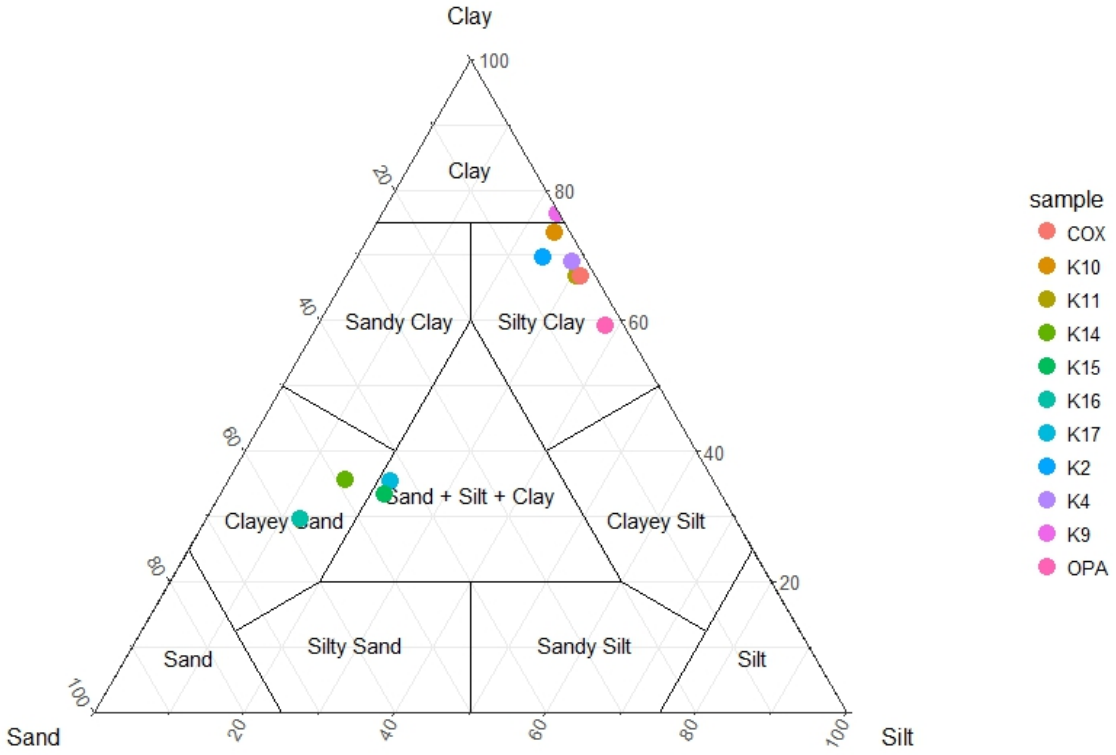

Figure 12: Grain size distribution of the different samples. COX = Callovo-Oxfordian Clay, OPA = Opalinus Clay

4.2 Hydraulic conductivity

As hydraulic conductivity is a very important transport parameter which is known to vary over the entire Formation, a measurement was performed on each sample. Measured hydraulic conductivities and reference values of the analysed samples are shown in Table 8.

Table 8: Overview of measured hydraulic conductivities and the reference values

Material	code	orien-tation	K (m/s)	Reference K (m/s)
Boom Clay (Putte Member)	Core 84b (K2)	⊥	$3.3 \pm 0.05 \times 10^{-12}$	1.7×10^{-12}
Boom Clay (Terhaegen Member)	Core 127b (K4)	//	$3.4 \pm 0.04 \times 10^{-12}$	4.4×10^{-12}
Boom Clay (Putte Member)	Core 112a (K9)	⊥	$2.4 \pm 0.05 \times 10^{-12}$	1.7×10^{-12}
Boom Clay (Boeretang Member)	Core 48a (K10)	⊥	$15 \pm 0.6 \times 10^{-12}$	2.8×10^{-12}
Boom Clay (Boeretang Member)	Core 48a (K11)	⊥	$10 \pm 0.2 \times 10^{-12}$	2.8×10^{-12}
Eigenbilzen Sands	Core 36a(K14)	//	$4.4 \pm 0.05 \times 10^{-10}$	3.1×10^{-10}
Eigenbilzen Sands	Core 37b (K15)	//	$1.1 \pm 0.3 \times 10^{-10}$	3.1×10^{-10}
Eigenbilzen Sands	Core 35b (K16)	⊥	$1.2 \pm 0.1 \times 10^{-8}$	3.1×10^{-10}
Eigenbilzen Sands	Core 39b (K17)	⊥	$4.2 \pm 0.2 \times 10^{-10}$	3.1×10^{-10}
Bentonite, 1.4 g/cm³	Bent 1.4		$1.5 \pm 0.002 \times 10^{-13}$	
Bentonite, 1.6 g/cm³	Bent 1.6		$5.8 \pm 0.007 \times 10^{-14}$	
Callovo-Oxfordian Clay	COX	⊥	$3.4 \pm 0.09 \times 10^{-13}$	$5 \times 10^{-14} – 5 \times 10^{-13}$
Opalinus Clay	OPA	⊥	$1.2 \pm 0.1 \times 10^{-13}$	$6 \times 10^{-15} – 3 \times 10^{-14}$

For the Boom Clay samples from the Putte and Terhaegen Member (ON-Mol-1 core 84b, 127b and 112a), the measured hydraulic conductivities correspond well to the reference values of Yu et al. (2013). The measured values for the samples from the Boeretang Member (formerly called 'Transition Zone') differ considerably from the reference values. When looking at previously measured values for samples of the Boeretang Member, a variation of one order of magnitude can be observed: *K* varies from ≈ 1×10^{-12} to 1.1×10^{-11} m/s (Aertsens et al., (2004, 2005 and 2008b)). The values measured for samples ON-Mol-1 core 48a1/2 (K10 + K11) are slightly larger, but given the large variability in the Boeretang Member we consider these values as reliable measurements.

The largest K values were measured for the samples of the Eigenbilzen Sands and these are in line with the reported average value of 3.1 x 10^{-10} m/s from Aertsens et al. (2005), except for sample K16 (core 35b). This sample has a very high hydraulic conductivity. A possible explanation could be that the sample was damaged when a too large pressure gradient was applied at the start of the hydraulic conductivity measurement.

As described by Wemaere et al. (2002), samples with an increased silt/sand content are expected to have higher hydraulic conductivities compared to clayey samples. Our measurements confirm indeed that the two samples from the Boeretang Member (ON-Mol-1 core 48a1/2 K10 + 11) which were initially expected to be more silty have a higher hydraulic conductivity than the clayey samples (selected from Putte/Terhaegen Member) (Table 8). But when looking back at the mineralogical composition and the grain size distribution of all these samples, the previous section already discussed the large similarities between both sample types and their positioning in the “silty clay” and “clay” region. So the difference in hydraulic conductivity between both types cannot be explained by their composition. Clearly, other factors are at play and this will be discussed later on. Also Ren and Santamarina (2018) discuss the dependency of the hydraulic conductivity on different petrophysical parameters such as grain size, specific surface area, clay content, porosity and pore geometry. An equation which takes into account different factors (specific surface area, density, fluid viscosity and void ratio) is the Kozeny-Carman relation which considers the porous network as a bundle of tubes. Though, Ren and Santamarina (2018) conclude that the Kozeny-Carman relation is still only an approximation and that other important information such as pore size distribution, pore geometry, tortuosity, … is missing. The latter matches with the observations in this work: hydraulic conductivity is not only linked to the composition or porosity. This is discussed later on in paragraphs § 4.6 to 4.8.

For both bentonite samples, the hydraulic conductivity is low and evidently, the 1.6 g/cm³ bentonite has a lower hydraulic conductivity than the 1.4 g/cm³ bentonite. Both samples have been measured with the method described by Phung et al. (2013), which allows for reliable measurements < 10^{-12} m/s. For Callovo-Oxfordian clay the measured hydraulic conductivity corresponds well to the reference values. For Opalinus Clay, the measured value is larger than the reference value. However, one should take into account that for Opalinus Clay, the measuring time for the sample was only 18 days. Based on our experience with this kind of measurements, we must acknowledge that this is too short for samples with a low (< 10^{-12} m²/s) hydraulic conductivity. Due to the short duration, the obtained result K_v = 1.2 x 10^{-13} m/s is probably biased by artefacts and not fully representative for the sample. However, at that time the main goal of the measurement was to verify whether good sealing was obtained between the clay, resin and the cell. As the measured hydraulic fluxes were low enough, the interface clay/resin/cell was considered to be thight.

4.3 Diffusion coefficients and geometric factors

This section provides all measured diffusion coefficients with the 95% uncertainty on the fit and the calculated geometric factors. The measured values are compared with each other, and with data from the literature.

Table 9: Overview of all measured diffusion coefficients. COX= Callovo-Oxfordian Clay, OPA = Opalinus Clay

					He			HTO			Ne			H_2			Ar			CH_4			Xe			C_2H_6		
Kinetic diameter σ (x 10^{-10} m)					2.58			2.75			2.79			2.97			3.42			3.82			4.06			4.42		
D_0 (x 10^{-9} m^2/s)					7.28			2.20			4.03			5.11			2.44			1.84			1.47			1.38		
Core	Code		K	η_{tot}	D_{eff}			D_{eff}			D_{eff}			D_{eff}			D_{eff}			D_{eff}			D_{eff}			D_{eff}		
			(m/s)	(-)	(x 10^{-11} m^2/s)			(x 10^{-11} m^2/s)			(x 10^{-11} m^2/s)			(x 10^{-11} m^2/s)			(x 10^{-11} m^2/s)			(x 10^{-11} m^2/s)			(x 10^{-11} m^2/s)			(x 10^{-11} m^2/s)		
BC 84b	K2	⊥	3.3 x 10^{-12}	0.4	46.8	±	1.7	18.7	±	0.6	17.5	±	0.3	NM			6.9	±	0.2	9.7	±	0.3	6.1	±	0.2	4.6	±	0.2
BC 127b	K4	//	3.4 x 10^{-12}	0.38	74.7	±	2.0	27.8	±	0.9	22.9	±	1.0	51.2	±	1.1	14.5	±	0.2	15.5	±	0.5	6.6	±	0.9	5.9	±	0.1
BC 112a	K9	⊥	2.4 x 10^{-12}	0.42	45.0	±	1.0	16.0	±	0.5	NM			NM			NM			8.8		0.3	NM			NM		
BC 48a	K10	⊥	1.5 x 10^{-11}	0.39	50.0	±	0.6	20.6	±	0.6	NM			NM			NM			11.0		0.1	NM			NM		
BC 48a	K11	⊥	1.0 x 10^{-11}	0.34	51.0	±	2.0	17.6	±	0.9	NM			NM			NM			8.4		0.2	NM			NM		
BC 36a	K14	//	4.4 x 10^{-10}	0.37	67.9	±	0.7	32.1	±	3.0	33.6	±	1.1	NM			NM			23.1	±	0.6	NM			14.3	±	0.1
BC 37b	K15	//	1.1 x 10^{-10}	0.40	82.3	±	2.1	43.9	±	2.3	40.0	±	2.1	NM			NM			27.8	±	0.5	NM			15.2	±	0.2
BC 35b	K16	⊥	1.2 x 10^{-8}	0.41	74.5	±	2.1	33.1	±	1.8	35.4	±	1.3	NM			NM			37.2		0.5	NM			13.7	±	0.4
BC 39b	K17	⊥	4.2 x 10^{-10}	0.40	58.2	±	1.1	29.9	±	2.7	30.6	±	0.6	NM			NM			24.4	±	0.5	NM			8.9	±	0.3
Bent 1.4	Bent 1.4		1.5 x 10^{-13}	0.47	17.7	±	1.1	15.6	±	1.2	10.3	±	0.4	NM			NM			2.8	±	0.1	NM			1.1	±	0.02
Bent 1.6	Bent 1.6		5.8 x 10^{-14}	0.4	27.0	±	0.9	8.07	±	0.5	8.7	±	0.7	NM			NM			0.9	±	0.1	NM			0.3	±	0.04
COX 1	COX 1	⊥	3.4 x 10^{-13}	0.18	8.1	±	0.2	NM			2.1	±	0.1	NM			0.7	±	0.02	NM			NM			0.2	±	0.01
OPA 1	OPA 1	⊥	1.2 x 10^{-13}	0.096	6.8	±	0.3	1.2	±	0.04	0.6	±	0.03	NM			0.4	±	0.1	F			F			F		

Table 10: Overview of calculated geometric factors (according to eq. (3)) BC = Boom Clay, EZ = Eigenbilzen Sands.

				He	HTO	Ne	H_2	Ar	CH_4	Xe	C_2H_6
Sample Code	**Material**		η_{tot} (-)	***G*** **(-)**	***G*** **(-)**	***G*** **(-)**	***G*** **(-)**	***G*** **(-)**	***G*** **(-)**	***G*** **(-)**	***G*** **(-)**
K2	BC	⊥	0.4	6.2 ± 0.2	4.7 ± 0.2	9.2 ± 0.1		14.1 ± 0.4	7.6 ± 0.2	9.6 ± 0.3	11.9 ± 0.5
K4	BC	//	0.38	3.7 ± 0.1	3.0 ± 0.4	6.7 ± 0.3	3.8 ± 0.1	6.4 ± 0.1	4.5 ± 0.2	8.4 ± 1.1	8.9 ± 0.1
K9	BC	⊥	0.42	6.8 ± 0.2	5.8 ± 0.2				8.8 ± 0.3		
K10	BC	⊥	0.39	5.7 ± 0.0	4.1 ± 0.2				6.5 ± 0.7		
K11	BC	⊥	0.34	4.9 ± 0.1	4.2 ± 0.9				7.4 ± 0.2		
K14	EZ	//	0.37	4.0 ± 0.0	2.5 ± 0.1	4.4 ± 0.2			2.9 ± 0.1		3.6 ± 0.0
K15	EZ	//	0.4	3.5 ± 0.1	2.0 ± 0.4	4.0 ± 0.0			2.6 ± 0.1		3.6 ± 0.1
K16	EZ	⊥	0.41	4.0 ± 0.1	2.7 ± 0.2	4.7 ± 0.1			2.0 ± 0.1		4.1 ± 0.2
K17	EZ	⊥	0.4	5.0 ± 0.1	2.9 ± 0.3	5.3 ± 0.1			3.0 ± 0.1		6.2 ± 0.3
Bent 1.4	MX80		0.47	19.3 ± 1.2	6.6 ± 0.6	18.4 ± 0.7			30.7 ± 1.3		60.3 ± 1.2
Bent 1.6	MX80		0.4	10.8 ± 0.4	10.9 ± 0.8	18.5 ± 1.6			79.9 ± 4.6		161.7 ± 17.7
COX 1	COX	⊥	0.16	16.1 ± 0.3		34.6 ± 1.9		60.2 ± 1.5			131.1 ± 3.6
OPA 1	OPA	⊥	0.096	10.2 ± 0.5	17.5 ± 0.7	62.1 ± 1.5		54.0 ± 3.6			

4.3.1 Diffusion coefficients and geometric factors measured for HTO

As discussed in § 3.12, the calculation of the transport properties from the diffusion profiles can be performed by different fitting strategies: a one parameter fit (only D_{app}, R = 1 and $\eta = \eta_{tot}$), a two parameter fit (D_{app} and ηR) and a three parameter fit (D_{app}, ηR and the inlet concentration). A comparison between the results for the one and the three parameter fit was made in Jacops et al. (2017a), and a difference of about 20% was noticed between both fitting strategies.

The results for HTO, shown in Table 9, have been obtained with the three parameter fit. All HTO diffusion coefficients reported in Jacops et al. (2017b) have been calculated using fixed filter values, while the D_{eff} values for K9, K10 and K11 have been calculated assuming that diffusion in the filter is equal to diffusion in the clay. Given the fact that, indeed, the diffusion coefficient for HTO in the filters is very similar to the diffusion coefficient of HTO in Boom Clay samples oriented perpendicular to bedding plane, this approach is also correct (Aertsens, 2017, personal communication) and for traceability the values from Jacops et al. (2017a) are kept. Data can also be fitted by ignoring the filters, which leads for K14 to a difference of 10% compared to the use of fixed filter values.

The measured diffusion coefficients for the clayey and silty clay samples correspond to previously measured diffusion coefficients, as reported by Aertsens et al. (2017). However, the latter author also indicated that the calculated diffusion coefficient strongly depends on the type of experiment and this is currently the subject of a new study.

For our sample of Callovo-Oxfordian Clay, the HTO diffusion coefficient has not yet been measured. For Opalinus Clay, the obtained value of 1.2×10^{-11} m²/s corresponds well to the value of 1.1×10^{-11} m²/s which has been reported by Van Loon (2015) for a sample of the same borehole (depth 857.96m).

For the compacted bentonite samples, the diffusion coefficient depends on the degree of compaction. When increasing the compaction from 1.4 to 1.6 g/cm³, D_{eff} decreases from 15.6×10^{-11} m²/s to 8.07×10^{-11} m²/s. Similar results have been obtained by Glaus et al (2017) who obtained for Volclay samples with dry densities of 1.3 and 1.6 g/cm³ D_{eff} values of respectively 1.4×10^{-10} and 8.2×10^{-11} m²/s. In these experiments, a synthetic bentonite pore water was used which composition can be found in Van Loon and Glaus (2008).

4.3.2 Diffusion coefficients and geometric factors measured for dissolved gases

All measured diffusion coefficients for dissolved gases have been obtained with a one-parameter fit and the results are shown in Table 9. For Boom Clay, the only gas for which data can be found in the literature is H_2 but the results suffered from experimental problems, leading to large uncertainties. Aertsens (2009) and Volckaert et al. (1994) obtained for D_{app} a range of 5×10^{-12} m²/s to 4×10^{-10} m²/s, but when looking at the diffusion coefficients obtained by Jacops et al. (2015), all measured values are larger than the proposed range.

For Callovo-Oxfordian Clay and Opalinus Clay, more data can be found in the literature (Bigler et al., 2005; Gómez-Hernández, 2000; Rebour et al., 1997; Rubel et al., 2002). An extensive review of the available data and a comparison with our data can be found in Jacops et al. (2016b), and also in §1.2.

For all samples, we observe a decrease in diffusivity when the size of the diffusing molecule increases. For the geometric factor, there are two different observations: for some samples, *G* increases with the size of the diffusing molecule, while for other samples *G* is rather constant (Table 10). This observation is discussed in more detail in §4.4.

When comparing the measured diffusion coefficients in the Boom Clay samples and the samples from the Eigenbilzen Sands, one can observe that despite a comparable porosity, the diffusion coefficients in the Eigenbilzen Sands are slightly higher than in Boom Clay. On the other hand, there is no significant difference in diffusivity between the clayey samples and the silty clay samples from Boeretang Member. All this agrees with previous results from pulse injection experiments (Aertsens et al., 2005), showing on average higher HTO dispersion coefficients in the Eigenbilzen Sands than in Boom Clay. The effect of variations in the clay/silt content on diffusivity is discussed more in detail in §4.6.

Despite its higher porosity compared to the Boom Clay and the Eigenbilzen Sands, the diffusion coefficients in bentonite 1.4 are smaller (as was also the case for the hydraulic conductivity). For helium, we observed that the diffusion coefficient for bentonite 1.4 is considerably lower than for bentonite 1.6. In fact, one would expect the opposite and we cannot explain this observation (only 1 replicate was done). The other three gases show the expected behaviour: lower diffusion coefficients in bentonite 1.6 compared to bentonite 1.4. The lowest diffusion coefficients were observed for the clays with the lowest porosity: Callovo-Oxfordian Clay and Opalinus Clay.

As shown in Table 9, some of the experiments on the Opalinus Clay failed: no diffusion coefficient could be obtained for gases larger than argon (CH_4, Xe and C_2H_6).

- For CH_4 the measurements were scattered and all below 100 ppm. As 100 ppm is the lower limit for reliable CH_4 peak detection and measurement, all measurements contain a significant portion of noise and are therefore considered non-significant.
- For Xe, no breakthrough was measured after 200 days, which could also be related to the detection limit of 100 ppm.
- For C_2H_6, where the detection limit is only 5 ppm, a clear breakthrough curve was detected, but could not be fitted by a simple diffusion model (see Figure 13): a quasi-stationary state is reached very soon, but after about 150-200 days, the outlet concentration starts to increase much faster. Because the system is probably very close to the percolation threshold, a possible explanation might be diffusion over another percolating, but much longer pathway.

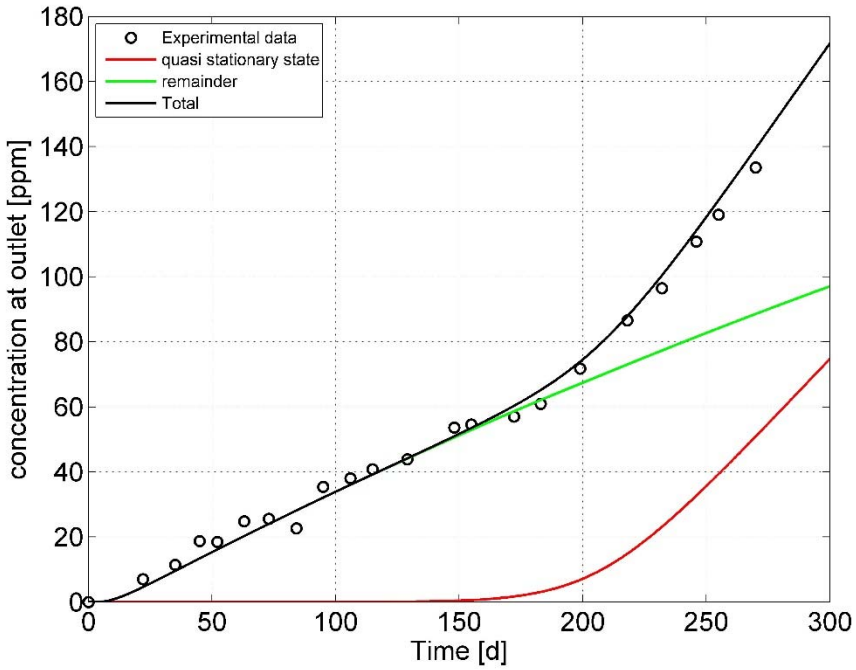

Figure 13: Evolution of the outlet concentration vs. time in the C_2H_6 diffusion experiment in Opalinus Clay. A clear breakthrough after a couple of days, leading to a quasi-stationary state is followed by an sudden unexplained increase after more than 150 days.

To explain this strange behaviour, our initial hypotheses were degassing of the sample or interaction of the gases with the clay. However, further investigation revealed that only very small amounts of trapped ethane could come out of the sample (Wersin et al., 2012), and that under the given conditions (pressure, temperature, saturation) gas sorption is not likely.

With a porosity of only 9.6%, Opalinus Clay has the lowest porosity of all the samples discussed in this thesis, and probably it has also the smallest pores. Therefore, it might be possible that from a certain gas size on, only very few connected pores are left for diffusive transport through the sample. As discussed in §3.9, this is also described as "percolation transition problem". Percolation transition occurs when the pores become so small (compared to the size of the diffusing molecule), that the number of connected paths diminishes drastically, and finally there is no longer a connected path of pores available for transport. Based on the currently available information, we believed that this phenomenon occurred in the Opalinus Clay for all gases larger than argon. Percolation transition in Opalinus Clay has been discussed by Keller et al. (2013), based on the analyses of the connected pore space, derived from FIB-SEM images. Though, the effect of the size of the diffusing molecule has not been considered.

Note that for the samples from the Eigenbilzen Sands and Boom Clay, the diffusion coefficients for HTO and Ne (two molecules with a nearly equal kinetic diameter) are about the same. However, due the very different values for the HTO and Ne aqueous diffusion coefficients (D_0), the corresponding geometric factors differ considerably.

Anisotropy

Diffusion in Boom Clay is known to be anisotropical (Aertsens et al., 2009; Bruggeman et al., 2010) with for HTO an average anisotropy factor of 2 – 3 (Aertsens et al., 2009). Evidently, the present results confirm that diffusion coefficients in our samples are higher for cores parallel to bedding compared to cores perpendicular to bedding.

In order to have an idea on the anisotropy, we should make sure that we do not compare apples to oranges. Therefore, we calculated the average diffusion coefficients for two samples of the Boom Clay (K2 and K4) and 4 samples of the Eigenbilzen Sands (K14, 15, 16 and 17), with orientation parallel and perpendicular to the bedding plane. For all these samples, we took into account the diffusion coefficients of He, Ne, CH_4 and C_2H_6. Hence, in each average value, the same gases are represented. A similar approach was followed for HTO.

From Table 11, we observe that the average anisotropy factor for HTO for the Boom Clay samples (K2, K4) is 1.5, while for the Eigenbilzen Sands samples (K14, K15, K16 and K17) it is 1.3. This is much lower compared to the range of Aertsens et al. (2009), but one should take into account that the latter has been obtained from pulse injection experiments. This means that the anisotropy factor is estimated as a ratio of dispersion coefficients instead of diffusion coefficients, which could be a reason for the observed difference.

Table 11: Average diffusion coefficients for dissolved gases (He, Ne, CH_4 and C_2H_6) and for HTO, measured in Boom Clay (K2, K4) and Eigenbilzen Sands samples (K14, K15, K16, K17) and the corresponding anisotropy factors. K9 was not taken into account as Ne and C_2H_6 were not measured for this sample.

	Boom Clay (K2, K4)	**Eigenbilzen Sands (K14, K15, K16, K17)**
Avg D_{eff} // (He, Ne, CH_4, C_2H_6)	3.0×10^{-10}	3.8×10^{-10}
Avg D_{eff} ⊥ (He, Ne, CH_4, C_2H_6)	2.0×10^{-10}	3.4×10^{-10}
Anisotropy factor	1.5	1.1
Avg D_{eff} // (HTO)	2.8×10^{-10}	3.8×10^{-10}
Avg D_{eff} ⊥ (HTO)	1.9×10^{-10}	3.0×10^{-10}
Anisotropy factor	1.5	1.3

For the diffusion experiments with dissolved gases, the average anisotropy factor for the Boom Clay samples is 1.5 while it is 1.1 for the Eigenbilzen Sands samples. Please note that in the calculations, only the data for the commonly measured gases (He, Ne, CH_4 and C_2H_6) were taken into account.

The anisotropy factors for dissolved gases and HTO are very similar, but all lower than the value of 2 - 3 reported by Aertsens et al. (2009). For both dissolved gases and HTO, the anisotropy factor is lower for the clayey sand samples compared to the clayey samples. As anisotropy is mainly caused by the

typical layering of clay platelets, it is expected to decrease when the clay content decreases (and hence the silt/sand content increases). This is clearly observed for the samples of the Eigenbilzen Sands. Likely, the decrease starts only at a certain treshold value which is currently unknown.

4.4 Relation between the measured diffusion coefficients and the size of the diffusing molecules

Text modified from Jacops et al. (2017b).

As discussed in §3.11, the relation between the size of a diffusing molecule and its diffusion coefficient in free water can be described by an exponential or a power law function. This section will discuss whether similar relation ships can be found between the size and D_{eff} , for different clayey materials. Also the evolution of the geometric factor with size is investigated, and also some empirical relations to estimate the pore radius (R_{pore}) are proposed.

As mentioned earlier, for all samples, D_{eff} decreases with the size of the diffusing molecule (Figure 14). This means that despite some deviations, a larger molecule exhibits a smaller effective diffusion coefficient. As for the diffusion coefficient D_0 in free water, we inferred trend lines for the dependence of the effective diffusion coefficient on the size of the diffusing molecule σ (kinetic diameter) by assuming similar expressions as (17) and (18) ((Jacops et al., 2017a)):

$$D_{\mathrm{eff}} = D_{eff,exp}\exp(-n_{exp}\sigma) \quad (19)$$

and

$$D_{eff} = D_{eff,pow}\,\sigma^{-n_{pow}} \quad (20)$$

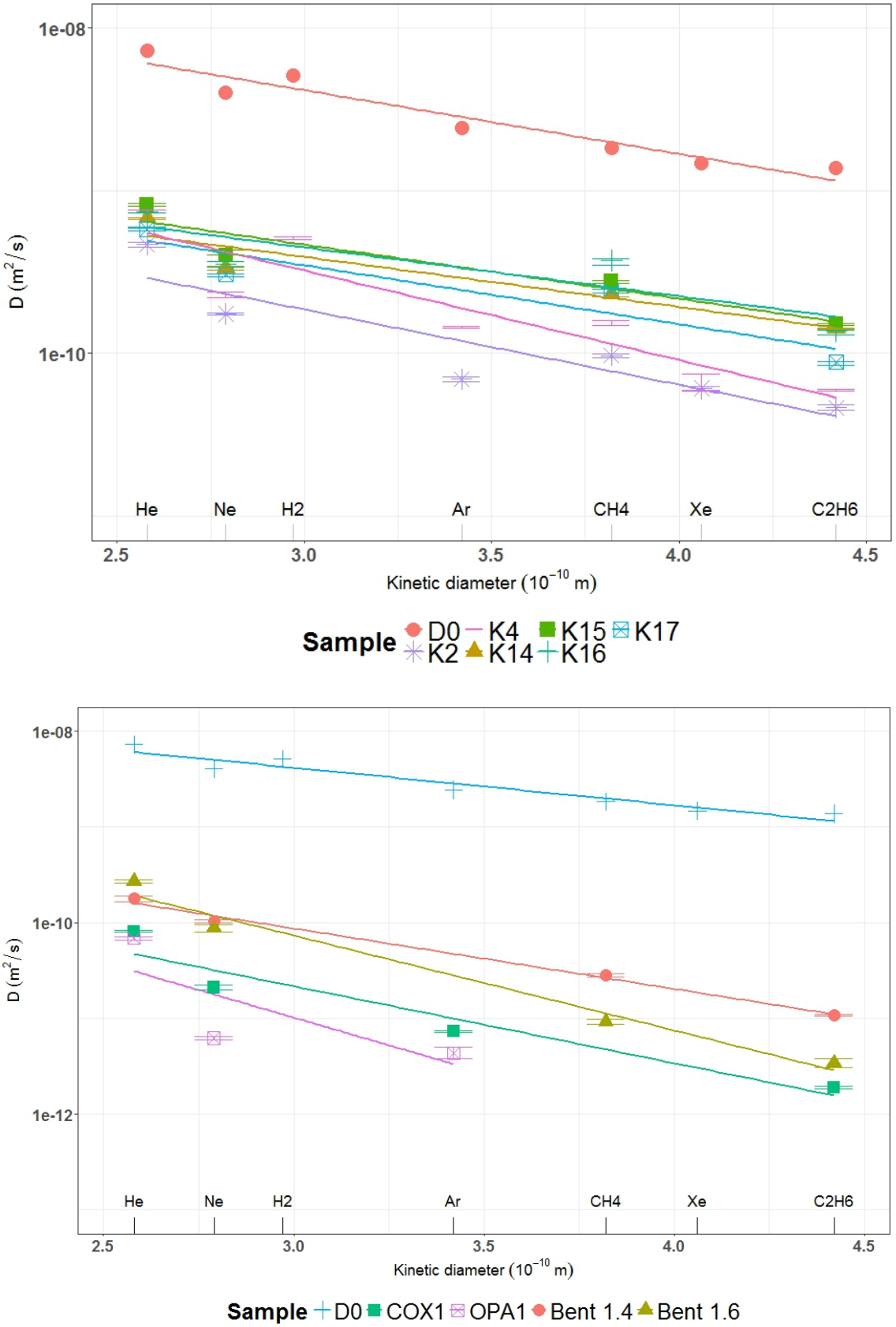

Figure 14: Effective diffusion coefficients for dissolved gases in Boom Clay (top) and other clayey materials (bottom), fitted with expression (19). The diffusion coefficient D is either the diffusion coefficient D_0 in pure water or the effective diffusion coefficient D_{eff} in a porous medium.

Table 12: Parameter values obtained by fitting the effective diffusion coefficient vs. molecular size by the exponential expression (19). The numbers in the top line are taken from Jacops et al. (2017a). R_{pore} is calculated from expression (24) and $R_{pore,K}$ is calculated from expression (14). From the fitted R_{pore} value, the hydraulic conductivity is calculated (K_{calc}) and compared to the experimental value K_{exp}

			$D_{0,exp}$ (m^2/s)			$n_{0,exp}$ (m^{-1})							
Water			5.5E-08	±	2.3E-08	8.8E+09	±	1.2E+09					
Code		η_{tot}(-)	$D_{eff,exp}$ (m^2/s)			n_{exp} (m^{-1})			τ (-)	R_{pore}	$R_{pore,K}$	K_{calc} (m/s)	K_{exp} (m/s)
K2	⊥	0.4	2.0E-09	±	2.1E-09	8.7E+09	±	3.0E+09	11.1	-1.5E-07	2.3E-09	1.4E-08	3.3E-12
K4	//	0.38	5.7E-09	±	5.4E-09	1.1E+10	±	2.7E+09	3.7	2.5E-09	2.4E-09	3.7E-12	3.4E-12
K14	//	0.37	2.4E-09	±	1.6E-09	6.4E+09	±	1.9E+09	8.4	-1.9E-09	2.8E-08	2.1E-12	4.4E-10
K15	//	0.4	3.4E-09	±	2.4E-09	6.9E+09	±	2.0E+09	6.4	-2.5E-09	1.3E-08	3.9E-12	1.1E-10
K16	//	0.41	2.8E-09	±	2.7E-09	6.6E+09	±	2.7E+09	8.0	-2.1E-09	1.4E-07	2.7E-12	1.2E-08
K17	⊥	0.4	3.7E-09	±	2.9E-09	8.2E+09	±	2.2E+09	5.9	-8.2E-09	2.6E-08	6.5E-11	4.2E-10
Bent 1.4		0.47	6.4E-09	±	2.0E-09	1.4E+10	±	8.7E+08	4.0	8.2E-10	4.6E-10	4.8E-13	1.5E-13
Bent 1.6		0.4	4.5E-08	±	4.4E-08	2.2E+10	±	2.8E+09	0.5	3.5E-10	3.1E-10	7.7E-14	5.8E-14
COX 1	⊥	0.18	2.3E-09	±	3.0E-09	1.6E+10	±	3.8E+09	4.5	6.2E-10	1.2E-9	1.1E-13	3.4E-13
OPA 1	⊥	0.096	9.6E-11	±	5.7E-10	9.3E+09	±	1.9E+10	55.0	9.2E-09	9.0E-10	1.2E-11	1.2E-13

Table 12 shows the fitted values according to expression (19) from the measured effective gas diffusion coefficients. The corresponding graphs are shown in Figure 14. Although HTO is included in Table 9, it is not included in the fits shown in Table 12 as we only describe the data for dissolved gases.

Most of the fits of Table 12 are fair, but the OPA fit is not reliable: for both fit parameters, the error is larger than 100 %.

When looking at Figure 14, we observe that some of the gases are always below (Ne, Ar) or above (He) the curve, for both D_0 and $D_{eff.}$ Hence there is a systematic deviation from the fitted curve. Up to now, we have no explanation for this observation.

For all Boom Clay and Eigenbilzen Sands samples, the exponential factor n_{exp} is on average (7.9 ± 2.0) x 10^9 which is similar to the exponential factor $n_{0,exp}$ of the fit of D_0 ((8.8 ± 1.2) x 10^9). For the other clayey samples, the factor n_{exp} is always substantially larger than $n_{0,exp}$.

As discussed earlier, for gases, the geometric factor G can be calculated from diffusion experiments. Similar to the evolution of D_{eff} with size, also the evolution of G with size can be described with an exponential or a power law function.

Substituting (17) and (19) in (3) (for unretarded tracers and no ion exclusion the retardation factor R = 1) provides an expression for the geometric factor

$$G = \eta \frac{D_{0,exp}}{D_{eff,exp}} exp\left(\left(n_{exp} - n_{0,exp}\right)\sigma\right) \qquad (21)$$

An exponential function is one of the empirical forms for constrictivity listed in Grathwohl (1998) with the property δ(σ= 0)=1. Comparing (21) with (4), it is also consistent considering exp(-(n_{exp} - $n_{0,exp}$)σ) as (part of) the constrictivity δ.

A similar combination as (21) can be made with expressions (18) and (20) leading to (and assuming $n_{pow} >= n_{0,pow}$)

$$G = \eta \frac{D_{0,pow}}{D_{eff,pow}} \sigma^{(n_{pow} - n_{0,\mathrm{pow}})} \qquad (22)$$

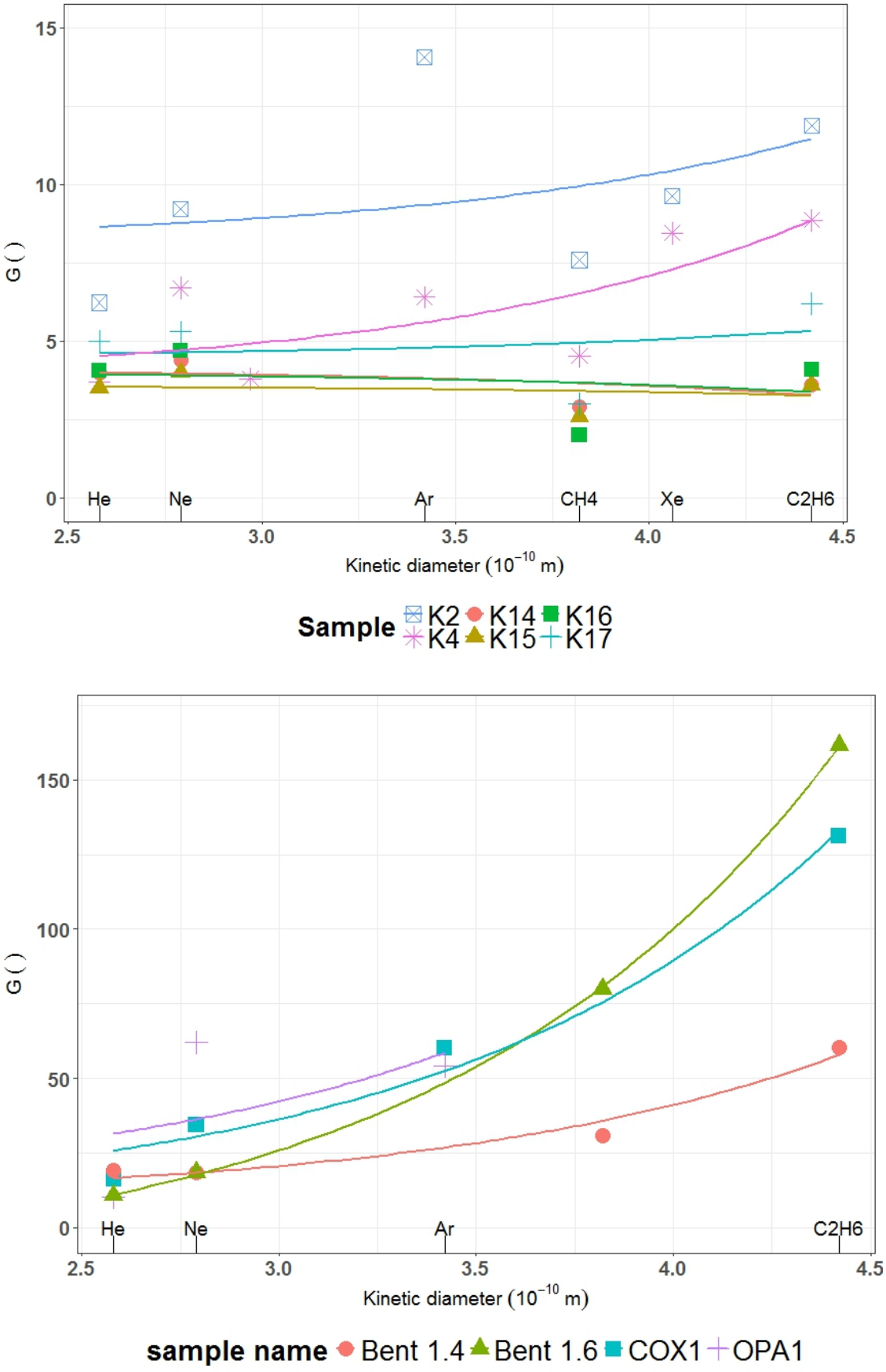

Figure 15: Geometric factors for dissolved gases in Boom Clay (top) and other clayey materials (bottom)

From Table 10 and Figure 15, one can observe that for the Boom Clay sample 127b (K4) the geometric factor tends to increase with the kinetic diameter, but the difference in *G* between the smallest (He) and largest (C_2H_6) molecule is smaller than a factor 3.

For the Eigenbilzen Sands samples, the geometric factor is rather a constant value. This can also be deduced from the exponential factors of the fit of D_{eff} (Table 12): if $n_{0,exp}$ and n_{exp} are similar ($n_{exp-} - n_{0,exp} \approx 0$), according to expression (21), the variation of *G* with molecular size is small, in agreement with the experimental results (see Table 10).

For the other clayey samples, the geometric factor clearly increases significantly with the kinetic diameter: the *G* ratio between smallest and largest molecule ranges from a factor 3 (bentonite 1.4) up to a factor 16 (Bentonite 1.6). This is also reflected in the exponential factors n_{exp} which differ much more from the $n_{0,exp}$ factor compared to the Boom Clay and Eigenbilzen Sands samples (Table 12).

When combining Expression (21) with the Gratwohl (1998) expression (9), two new formulas can be derived

$$\tau = \eta \frac{D_{0,exp}}{D_{eff,exp}} \quad (23)$$

$$R_{pore} = \frac{4.6}{n_{exp} - n_{0,exp}} \quad (24)$$

where a positive pore size R_{pore} requires that $n_{exp} > n_{0,exp}$.

An expression similar to (23) can be defined for the power law (22), but no characteristic distance similar to R_{pore} exists. Also note that with the power law, $G(\sigma=0) = 0$ (assuming $n_{pow} >= n_{0,pow}$), instead of $G(\sigma=0) = \tau$ for the exponential relation (21).

From the fits in Table 12, the tortuosity factors τ and R_{pore} (expressions (23) and (24) respectively) can be calculated. The calculated tortuosity factors are, apart from the unreliable OPA value and the small Bentonite 1.6 value, quite similar. But the calculated R_{pore} values are sometimes negative which is physically impossible (Boom Clay sample K2 and the four samples of the Eigenbilzen Formation). For these samples, the values of $n_{0,exp}$ and n_{exp} are within each other's error interval which means in some cases that $n_{0,exp} > n_{exp}$, which leads according to expression (24) to negative R_{pore} values. For these samples, the difference in D_{eff} between the largest and smallest molecule is about one order of magnitude. So a slight change in one of the D_{eff} values can strongly influence n_{exp}. This points to a limitation of this approach: it can only be used when n_{exp} differs significantly from $n_{0,exp}$. From the measured K values, $R_{pore,K}$ can be calculated according to expression (14) and these results are also shown in Table 12. When comparing both calculated R_{pore} values, is it clear that when a reliable exponential fit is obtained, and when n_{exp} differs significantly from $n_{0,exp}$ (so no negative R_{pore} values) both calculated R_{pore} values are relatively similar.

According to expression (9) which relates the geometric factor to the size of the diffusing molecule and the pore size, the geometrical factor always increases as a function of the size of the diffusing molecule. For a sufficiently small molecular size σ (with respect to the pore size R_{pore}) the exponential factor $\exp(\sigma/ R_{pore})$ can be approximated by one, so that the geometrical factor is approximately constant.

This means that, according to expression (9), the geometric factor for a very small diffusing molecule (kinetic diameter $\sigma \rightarrow 0$) is roughly similar in all these clays and the pore size R_{pore} is not relevant. This applies most to the smallest molecule, helium, for which indeed the variability of G over the different samples is small. From expression (9), one can also conclude that if for the same sample, all diffusing molecules are sufficiently small compared to the pore size, the geometric factor is also approximately constant. This is the case for the samples of the Eigenbilzen Sands: as $R_{pore,K}$ (calculated from expression (14)) is in average 5.4×10^{-8} m, the pores are much larger than the diffusing molecules.

When the diffusing molecules are not small compared to the pore size, the pore size becomes more important. To be more correct, it will be the pore throats which will determine whether a gas can easily pass through the pore network or not. When in this case, the size of the diffusing molecule increases, the geometric factors in the different clays diverge, and the geometric factor for different gases in a single sample is not constant. For both bentonites and COX, both fitted R_{pore} values are small (see Table 12) (similar to the size of the diffusing molecules) and the geometric factor clearly rises with increasing molecular size (see Figure 15). For Boom Clay, sample K4 which is expected to have larger pores compared to COX and the bentonites, the geometric factor also increases with the size of the diffusing molecule - although less steeply.

Despite the enormously simplifying assumption to replace a whole pore (size) distribution by just one pore size in both the hydraulic conductivity model and the effective diffusion coefficient vs. diffusing molecule size model, both models lead to similar values for the typical pore size. Using the fitted R_{pore} values to predict the hydraulic conductivity with expression (14) gives quite a good agreement between the calculated hydraulic conductivity K_{calc}, and the experimental value K_{exp} for both bentonites, COX and Boom Clay sample K2 (see Table 12). It is straightforward that for negative R_{pore} values (sample K2 and the Eigenbilzen Sands), this prediction cannot be good, and it has already been mentioned that the OPA fits are not reliable.

The effective diffusion coefficients can also be fitted as a function of size by using the power law expression (20), leading to the optimal values summarized in Table 13

Apart from the fact that for the power law no typical pore size like R_{pore} exists, the conclusions are similar as for the exponential fit: a bad fit for OPA, a steep increase of the geometric factor as a function of molecular size for both bentonites and COX, a slower increase for both Boom Clay samples and a hard to explain (apart from measurement errors) decrease for the Eigenbilzen Sands.

Table 13: Parameter values obtained by fitting the effective diffusion coefficient vs. size of the diffusing molecule by the power law expression (20). The numbers in the top line are taken from (Jacops et al., 2017a). 'Tortuosity' τ is defined similarly as expression (23).

			$D_{0,pow}$ (m^2/s)			$n_{0,pow}$ (-)				
Water			1.1E-07	±	4.6E-08	3.0	±	0.4		
Sample		η_{tot} (-)	$D_{eff,pow}$ (m^2/s)			n_{pow} (-)			τ (-)	n_{pow}-$n_{0,pow}$ ( )
K2	⊥	0.4	5.0E-09	±	5.8E-09	3.2	±	0.9	8.4	0.2
K4	//	0.38	1.3E-08	±	1.4E-08	3.7	±	0.9	3.1	0.7
K14	//	0.37	4.0E-09	±	3.1E-09	2.2	±	0.6	10.0	-0.8
K15	//	0.4	5.9E-09	±	4.8E-09	2.4	±	0.7	6.6	-0.6
K16	⊥	0.41	4.8E-09	±	5.5E-09	2.3	±	0.9	8.3	-0.7
K17	⊥	0.4	7.0E-09	±	6.8E-09	2.9	±	0.8	5.5	-0.2
Bent 1.4		0.47	1.8E-08	±	7.2E-09	5.0	±	0.3	2.8	1.9
Bent 1.6		0.4	2.3E-07	±	1.9E-07	7.5	±	0.7	0.2	4.5
COX 1	⊥	0.18	1.0E-08	±	1.3E-08	5.8	±	1.1	1.9	2.8
OPA 1	⊥	0.096	1.1E-10	±	7.1E-10	2.7	±	5.9	94.2	-0.4

4.5 A method to estimate gas diffusion coefficients as a function of the size of the diffusing molecule

Text modified from Jacops et al. (2017b).

Based on the results presented in this work and in Jacops et al. (2017a and 2017b), one can state that the approach of using one geometric factor for estimating D_{eff} of species with a different molecular size is not always correct and the validity depends on the type of sample and the size of the diffusing

molecule. For instance, for the Eigenbilzen Sand samples, the geometric factor from HTO could be used to calculate the D_{eff} for e.g. C_2H_6. On the contrary, for COX or bentonite, using the geometric factor of HTO to calculate D_{eff} for C_2H_6 would lead to a serious overestimation. In order to illustrate this, we use for COX a geometric factor of 17 for HTO, as suggested by Jacops et al. (2016b). If this value would be used to predict D_{eff} for C_2H_6, a value of 1.5 x 10^{-11} m²/s would be obtained while the measured value is only 0.2 x 10^{-11} m²/s, leading to an overestimation of a factor 7.5.

A more correct way to estimate diffusion coefficients would be by using the exponential or power law relation between D_{eff} and the molecular size (expressions (19) and (20)). Each expression has two parameters, meaning that the effective diffusion coefficient needs to be determined experimentally for two gases. Evidently, it is best to do this for a large molecule (e.g. C_2H_6) and a small one. Helium is the smallest of all molecules considered here, but its diffusion coefficients are always higher than expected (located above the fitted curve in Figure 14). This leads to the observation that the measured D_{eff} is 1.7 times larger than the calculated D_{eff} (see). For the second smallest molecule (neon), the calculated D_{eff} is similar to the measured D_{eff}, hence Ne is recommended to be used in this approach. An example of such a prediction with the exponential expression (19) is shown in Table 15. Evidently, because Ne and C_2H_6 are used to determine the fit parameters, for both these gases the predicted value corresponds exactly to the experimental value. For the other gases, the prediction can be improved by multiplying the predicted diffusion coefficient with the averages of the ratio of the experimental to fitted value for all measured clays (see Table 14). This manipulation allows correcting for the specific bias of this ratio, which is different for each gas. After this correction, for sample K2 (one of the experiments for which most measurements were carried out) the predicted and measured effective diffusion coefficients differ less than 30 % (see Table 15).

By using this approach, the diffusion coefficient of for instance H_2 (which is difficult to measure due to microbial activity (Jacops et al., 2015)) can be estimated based on its molecular size.

Table 14: Ratios between the experimentally determined D_{eff} (values see Table 9) and the fittted D_{eff} (using the fits given in Table 12), as well as the averages for each gas molecule. Due to the deviating value of He for sample OPA1, the corresponding D_{eff} is not included in the average.

	He	Ne	H_2	Ar	CH_4	Xe	C_2H_6
Sample	**Ratio experimental/fitted (-)**						
K2	2.3	1.0		0.7	1.4	1.1	1.1
K4	2.0	0.8	2.1	1.0	1.6	0.9	1.1
K14	1.4	0.8			1.1		1.0
K15	1.4	0.8			1.2		1.0
K16	1.4	0.8			1.6		0.9
K17	1.3	0.8			1.5		0.9
Bent 1.4	1.1	0.9			1.1		1.0
Bent 1.6	1.7	0.8			0.8		1.2
COX 1	2.4	0.9		0.9			1.2
OPA 1	7.8	0.9		1.1			
Average	1.7	0.8	2.1	0.9	1.3	1.0	1.0
Standard deviation	0.4	0.1		0.2	0.3	0.2	0.1

Table 15: Predicting the gas effective diffusion coefficients of sample K2 after measuring the Ne and C_2H_6 effective diffusion coefficients. In a first phase, the prediction is based only on expression (19). Subsequently, this prediction is improved by multiplication with a 'correction factor' which takes into account the gas specific deviation between the experimental and the predicted value.

		He	Ne	H_2	Ar	CH_4	Xe	C_2H_6
Kinetic diameter σ	(x 10^{-10} m)	2.58	2.79	2.97	3.42	3.82	4.06	4.42
D_{eff} (experiment)	(x 10^{-11} m^2/s)	74.7	22.9	51.2	14.5	15.5	6.6	5.9
D_{eff} (prediction)	(x 10^{-11} m^2/s)	27.2	22.9	19.7	13.6	9.7	8.0	5.9
Ratio D_{eff}(exp)/D_{eff} (pred)	( )	2.7	1.0	2.6	1.1	1.6	0.8	1.0
Correction factor	( )	1.7	0.8	2.1	0.9	1.3	1.0	1.0
D_{eff}(pred) * Corr factor	(x 10^{-11} m^2/s)	45.8		41.2	12.2	12.4	7.7	
Ratio D_{eff}(exp)/(D_{eff} (pred)*Corr factor)	( )	1.6		1.2	1.2	1.2	0.9	

4.6 Influence of the petrophysical properties on diffusivity and hydraulic conductivity

In the previous sections (§4.1, 4.2, 4.3), we discussed the petrophyiscal and the transport properties of our samples. Now we can start to discuss objective 4 of this PhD: how do all these properties influence each other. Therefore, the next section will describe the correlations between the transport and the petropyisical properties.

4.6.1 Variability of the different transport and petrophysical parameters

By performing transport experiments complemented by a full petrophysical characterisation, an extended dataset is obtained. In order to find relations between all measured parameters, a correlation analysis is performed with R, a software package for statistical computing and graphics and the correlation coefficients for different parameters are calculated. Correlation coefficients can be calculated in different ways, but the most usual measure is the Pearson correlation coefficient. It is a measure for the linear correlation between two variables, and defined as the covariance of the two variables divided by the product of their variance. It is scaled between 1 (for a perfect positive correlation) to -1 (for a perfect negative correlation) and 0 would be complete randomness. In graphs, the linear correlation is mostly indicated with R^2, hence R^2 is shown in Figure 16 and a scale for the strength of correlation (from Napitupulu, (2018)) is given in Table 16.

Table 16: Interpretation of the Pearson correlation coefficients R and R^2

R	R^2	strength of correlation
< 0.2	< 0.04	Very weak relationship
0.2 - 0.4	0.04 – 0.16	Weak relationship
0.4 - 0.6	0.16 – 0.36	Moderate relationship
0.6 - 0.8	0.36 – 0.64	Strong relationship
> 0.8	> 0.64	Very strong relationship

When calculating Pearson correlation coefficients, the test statistic is based on Pearson's product moment correlation coefficient and follows a t-distribution with length (x)-2 degrees of freedom if the samples follow independent normal distributions. If there are at least 4 complete pairs of observation, an asymptotic confidence interval is given based on Fisher's Z transform (Hollander; 2013) .

In a next step, the p-value (also known as probability value) is calculated. The p-value is the probability that the null hypothesis (which is no linear correlation in our case) is true. A small p-value (≤ 0.05) rejects the null hypothesis, while a large p-value (> 0.05) means that the null hypothesis cannot be rejected. By setting the significance level at 0.05, the risk of concluding a correlation when no correlation exists is 5%.

With respect to the interpretation, one should also keep in mind that as discussed earlier, the relation of D_{eff} and G with the size of the diffusion molecule is best described with an exponential or a power law function. Also other relations may be better described by a non-linear function, and therefore the logarithmic values of K, D_{eff} and G (logK, logD_{eff} and logG) are equally taken up into the correlation analysis.

When performing correlation analyses, the minimum sample size (in this case referring to the minimum number of data points) is often a point of discussion. In theory, a correlation analyses can be performed from 2 data points on, but it is of course more correct when the data set is larger. In the literature, there is not at all a consensus on what this minimum sample size should be. The data set, discussed in this work is at first sight rather limited: 5 samples of the Boom Clay, 4 of the Eigenbilzen Sands, one Callovo-Oxfordian Clay, one Opalinus Clay and two bentonite samples, making 13 samples in total. But when looking for similar data sets in the field of geological disposal, this data set turns to be large and unique as it contains diffusion data for different gases and HTO, measured for different samples, complemented with a full petrophysical analysis. One of the objectives of this PhD is to investigate which petrophysical parameters influence the transport properties of clayey samples, and correlations should be interpreted from this point of view. At this stage, it is not yet our aim to predict diffusion coefficients based on their petrophysical properties or to propose empirical laws. Though, at the end of this section we point to potential applications of the correlations described in this section.

The correlation analysis is performed for the entire dataset (samples of Boom Clay, Eigenbilzen Sands, Callovo-Oxfordian Clay, Opalinus Clay and bentonite) (Figure 16, top), and also for the samples of the Boom Clay and Eigenbilzen Sands (Figure 16, bottom).

Within the next sections, we will focus on

- The correlation between the mineralogical composition (mainly quartz, the 2:1 clay minerals (denoted as Clay21) and the sum of all the clay minerals (denoted as allclay), the grain size fractions (clay, silt and sand fraction) and the specific surface area (SSA) and micro pore volume;
- The correlation between the hydraulic conductivity (K and log K) at one side and the mineralogy, grain size fraction, specific surface area and micro pore volume at the other side;
- The correlation between the diffusion parameters (D_{eff}, logD_{eff}, G and log G) at one side, and the mineralogy, grain size fraction, specific surface area and micro pore volume at the other side;
- The correlation between diffusivity (D_{eff} and logD_{eff}) and hydraulic conductivity (K and log K)).

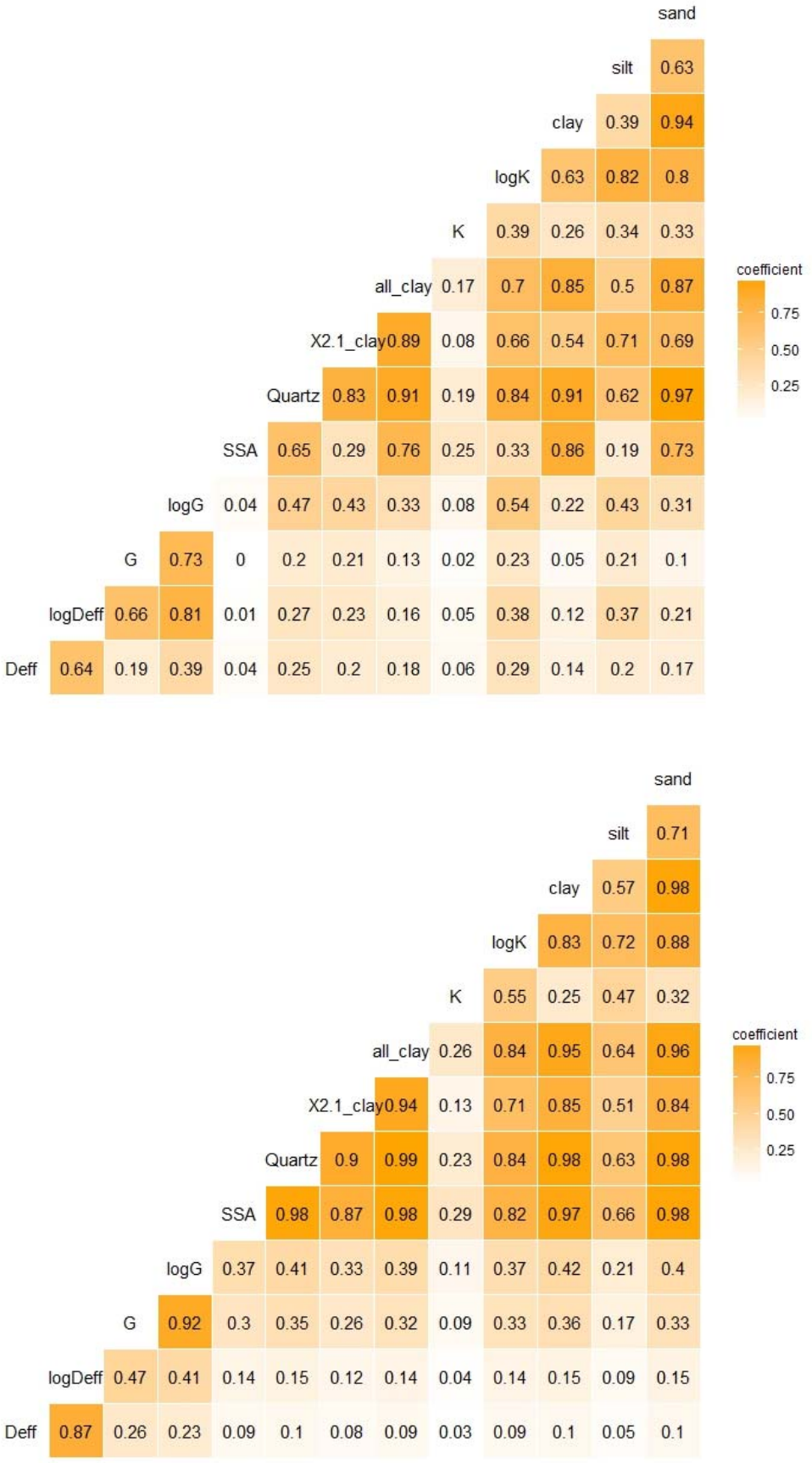

Figure 16: Correlation (R^2) of transport parameters en petrophysical parameters for all clay samples (top) and Boom Clay and Eigenbilzen Sand samples (bottom)

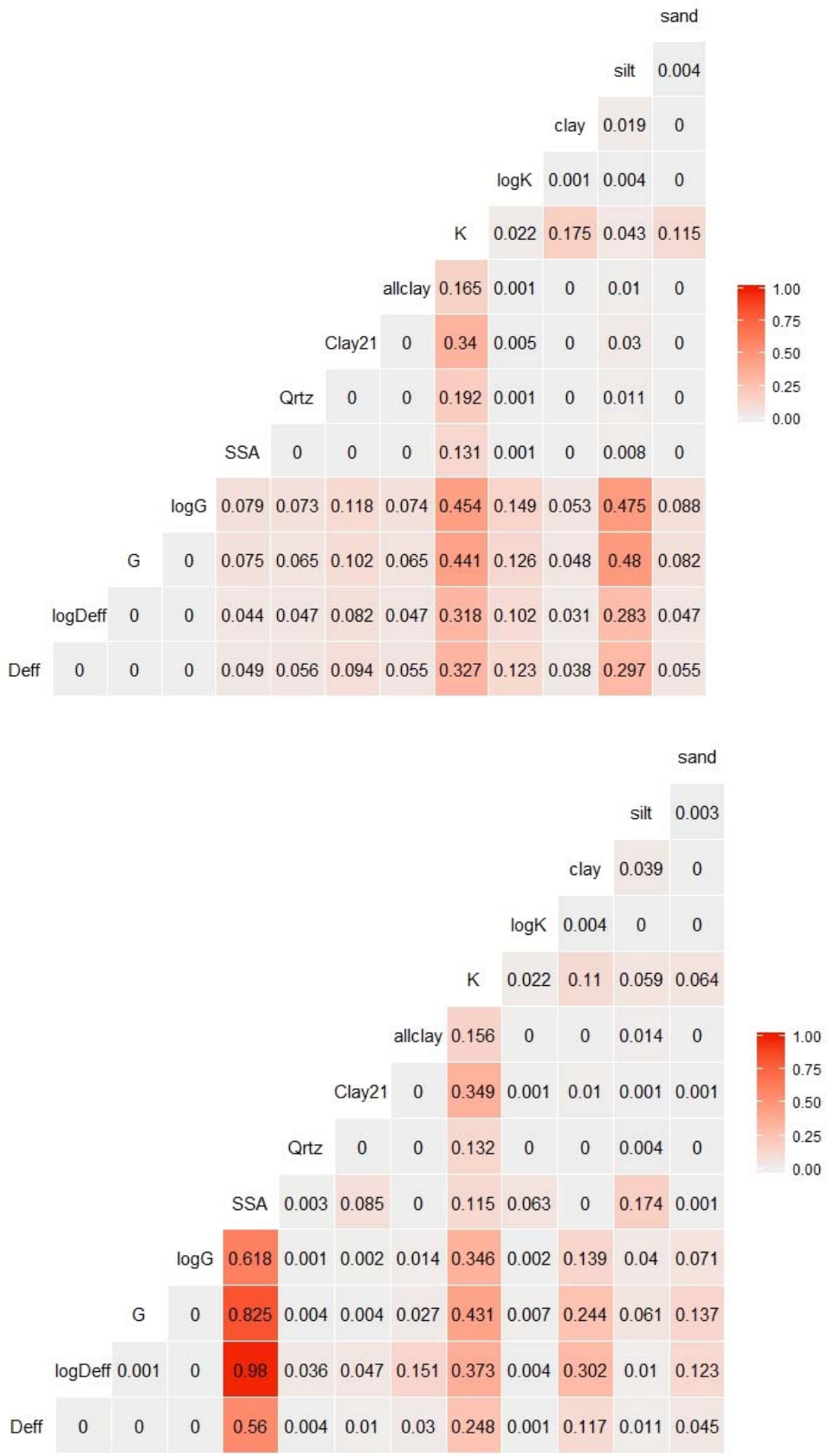

Figure 17: probability values (p-values), indicating the probability that the null hypothesis (being no linear correlation) is true. $p \leq 0.05$ and $p > 0.05$ indicate respecively strong and weak evidence against the null hypothesis. P-values are given for all clay samples (top) and Boom Clay and Eigenbilzen Sand samples (bottom)

4.6.2 Correlation between mineralogy and grain size distribution

For the Boom Clay and Eigenbilzen Sands, the grain size distribution is strongly correlated with the mineralogical composition, as shown in Figure 18. As one could expect and as visible on Figure 18, the sand fraction is positively correlated with the quartz content, and negatively correlated with the content of the clay minerals (both all clay minerals and 2:1 clay minerals). For the clay fraction, it is the other way around. For the silt fraction, the datapoints are more spread, hence leading to lower correlation coefficients, but the same trend as for the clay fraction can be observed. Similar observations are made in Adriaens et al. (2016), where quartz and feldspars are associated to the coarser size fractions and clay minerals preferentially occur in the finer fractions.

Due to the origin of the samples, the datapoints are split into two groups and therefore the proposed correlation could be a point of discussion. When studying a much larger data set, e.g. the one from Frederickx (2018), similar observations are made (Figure 19). Therefore, the correlations proposed in this work are considered to be valid. Futher work, integration the data of Frederickx (2018) and data of this work is advised.

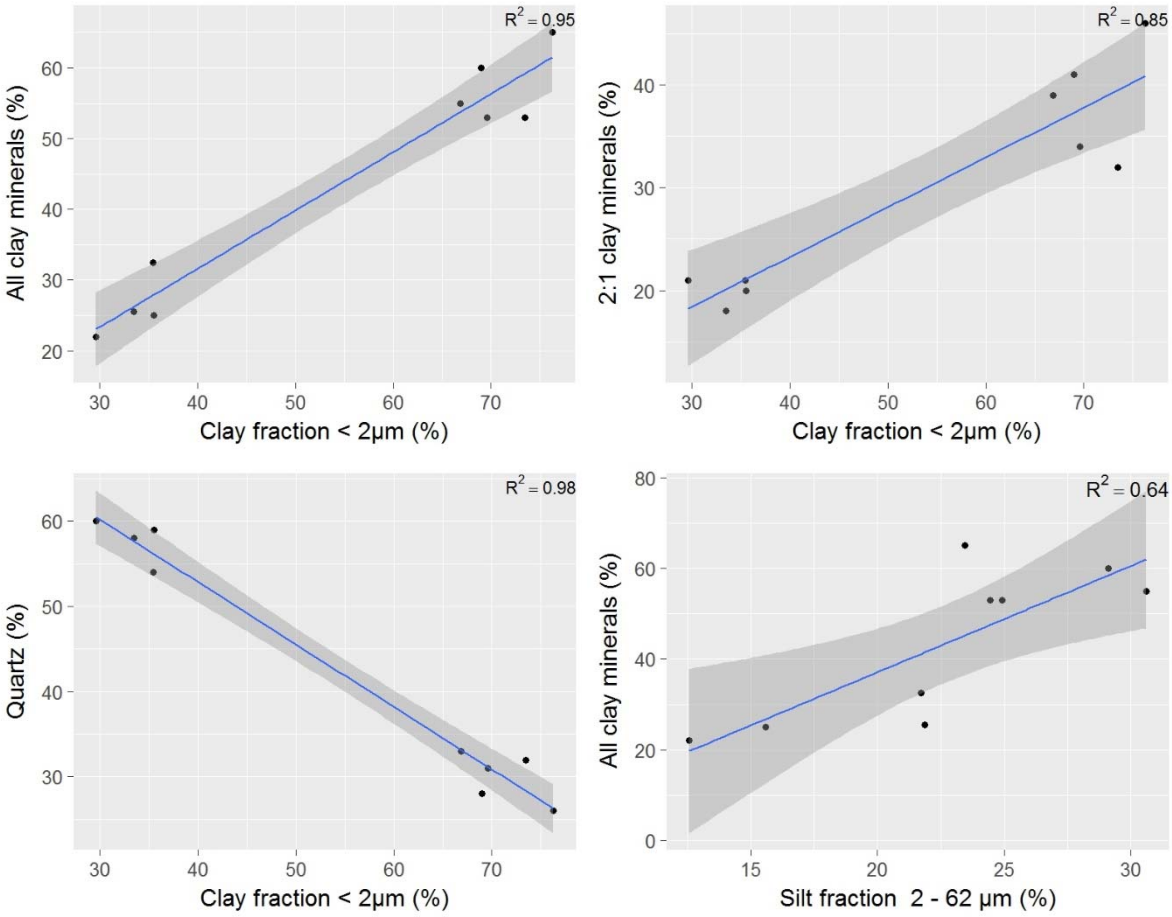

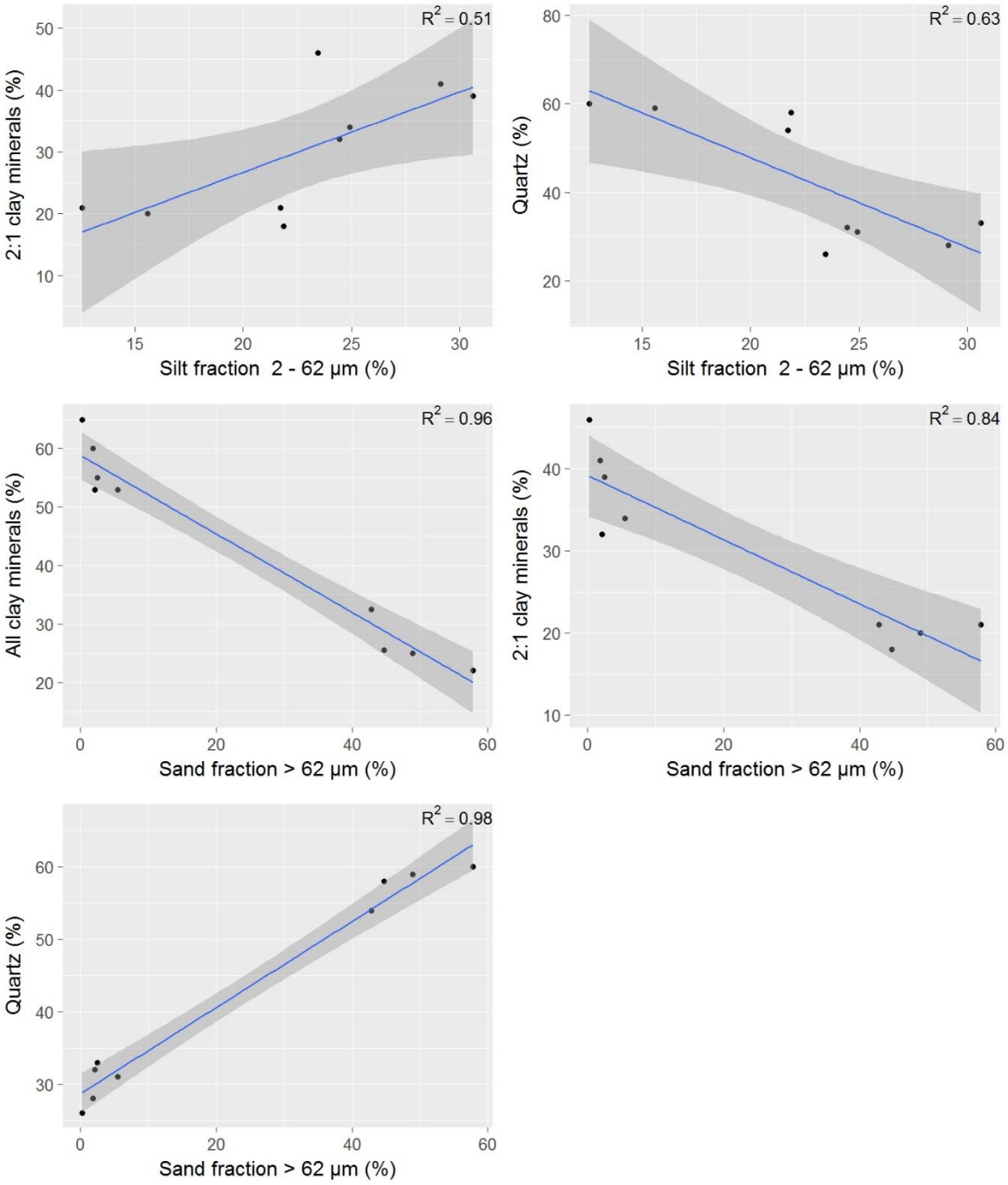

Figure 18: Relationship between the mineralogy of the Boom Clay and Eigenbilzen Sands samples (% of all clay minerals, 2:1 clay minerals and quartz) and their grain size distribution (sand, silt and clay fraction)

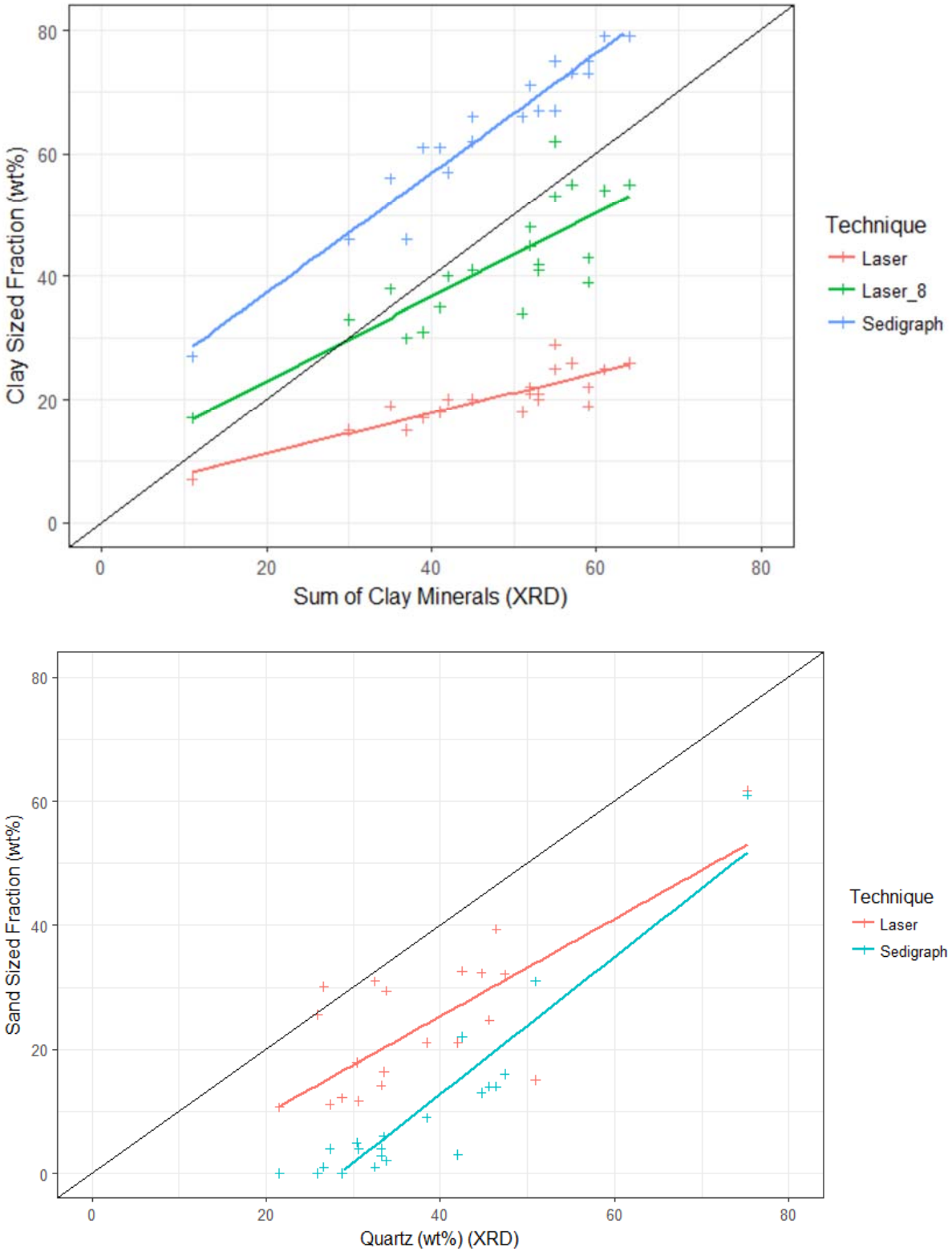

Figure 19: Scatter plot indicating the correlation of the clay size fraction to the sum of the clay minerals (top) and the correlation of the sand size fraction to the quartz content (bottom). Figures taken from Frederickx (2018).

We also investigated the correlation between mineralogy and grain size distribution for the complete dataset. In general, the correlations are less good and often the data points of COX and OPA plot outside the confidence interval. An example is given in Figure 20. Given the dominance of the datapoints of the Boom Clay and Eigenbilzen Sands in the complete dataset (9 samples out of 13), it is difficult to generalize these correlations. The p-values (Figure 17) for all the mineralogy and grain size distribution values are very low (all < 0.05), hence the linear correlation is considered to be significant.

Given the strong correlation of the grain size distribution and the mineralogical composition, both petrophysical parameters will often be discussed together in the next sections.

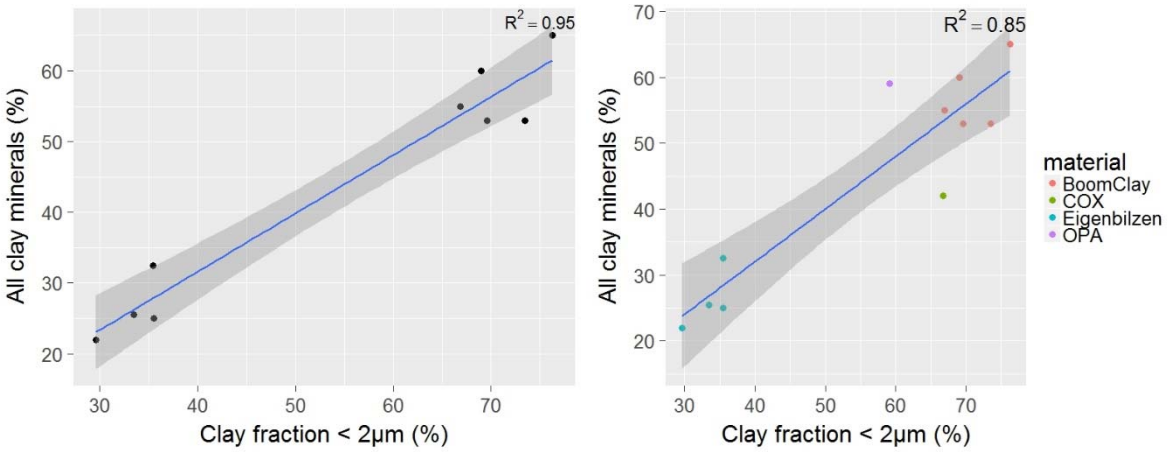

Figure 20: Comparison for the correlation between the clay fraction and the amount of all clay minerals for the Boom Clay and Eigenbilzen Sands (left) and the extended dataset, including also Callovo-Oxfordian Clay (COX) and Opalinus Clay (OPA). For bentonite, no grain size data are available. The correlation is good in both figures, but the datapoints of COX and OPA fall outside the confidence interval

4.6.3 Correlation between mineralogy/grain size distribution and specific surface area

The specific surface area of each sample is shown in Table 6, together with the mineralogical composition. As described by Frederickx (2017), for Boom Clay, a very strong correlation can be observed between the total clay content or the content 2:1 clay minerals and the specific surface area. This observation was also made in this study: both the 2:1 clay minerals and the sum of all clay minerals are positively correlated with the specific surface area, while the quartz content is negatively correlated with the specific surface area (Figure 21). All p-values are zero, which confirms the linear correlation.

When all data points are taken into account, the correlation between the mineralogy and the SSA is less good. For the sum of the clay minerals and quartz the correlation is still good (respectively 0.76 and 0.65) and the p-values are below 0.05, but for the 2:1 clay minerals it is only 0.29 (Figure 22) and the p-value is above 0.05. The latter could be explained by the fact that COX and OPA contain a larger fraction of illite compared to the Boom Clay, and illite is known to have a lower SSA compared to smectite (Macht et al., 2010). Similar to the observations for grain size and mineralogy in § 4.6.2, the data points for COX and OPA are located outside the confidence interval.

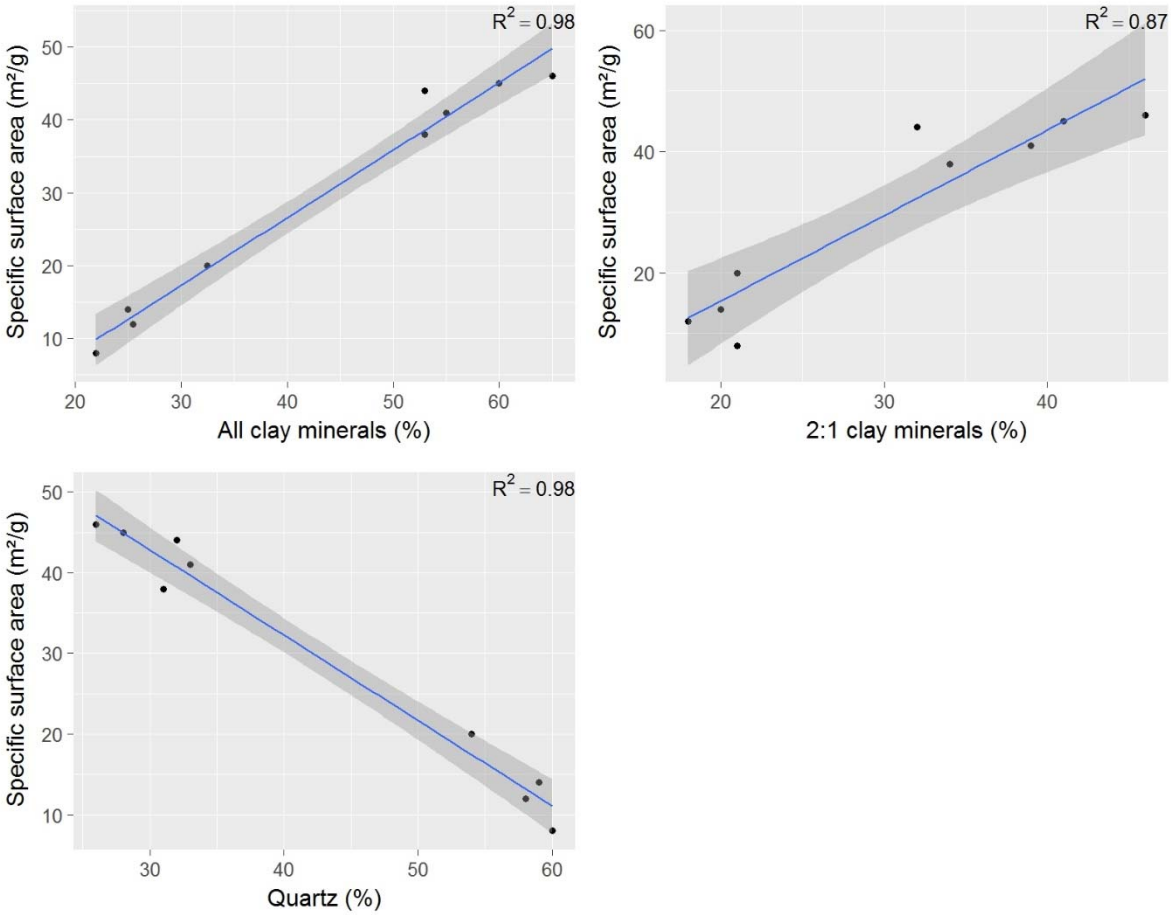

Figure 21: Relationship between mineralogy of the samples and the specific surface area for the Boom Clay and Eigenbilzen Sands samples

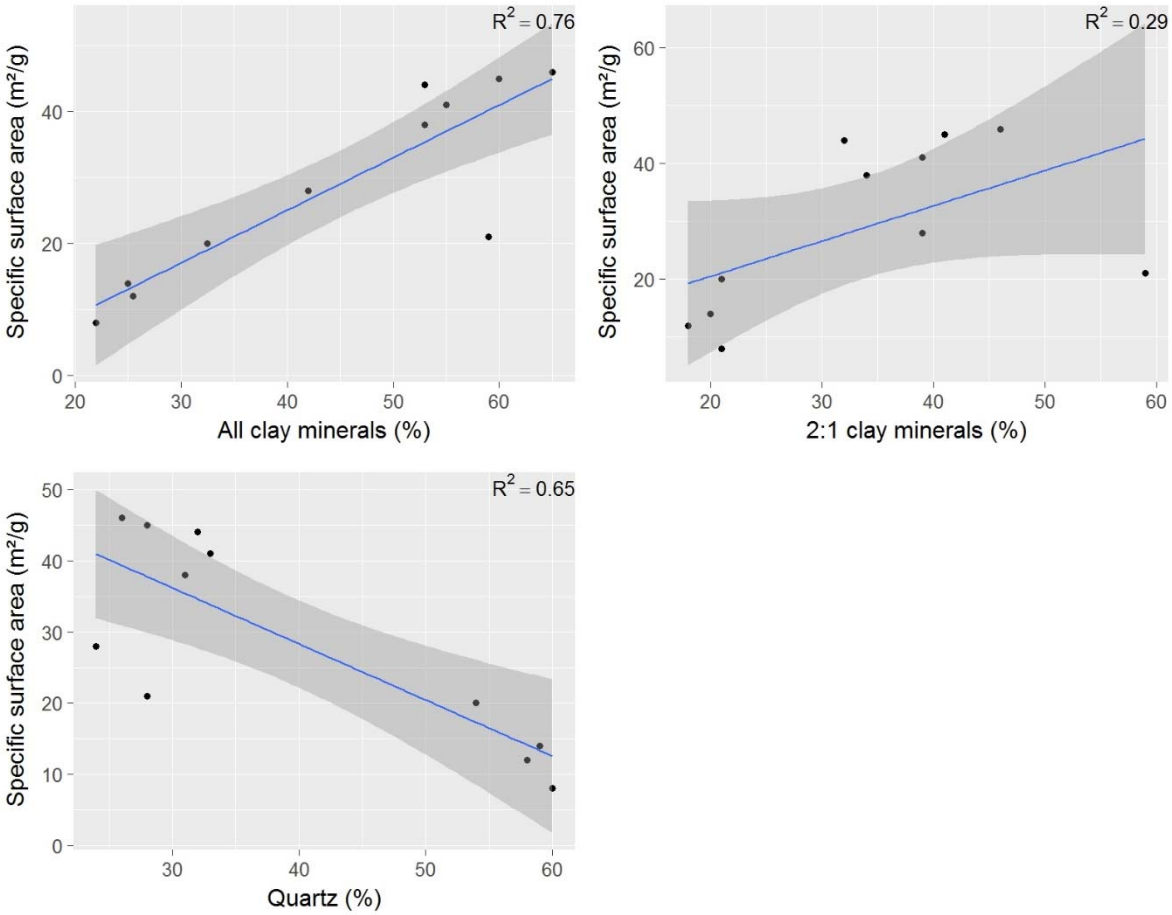

Figure 22: Relationship between the mineralogical composition and the specific surface area for Boom Clay, Eigenbilzen Sands, Callovo-Oxfordian Clay and Opalinus Clay

As we know that the mineralogical composition is closely correlated to the grain size distribution, one would expect also a correlation of grain size distribution with the specific surface area (Figure 23). A positive correlation is observed between the fractions of clay and silt and the SSA, while we observe a negative correlation between the sand fraction and the SSA. When all data points are taken into account, again the correlations are less good and for the silt fraction R^2 decreases from 0.66 to 0.19 (Figure 24) and the p-value is above 0.05.

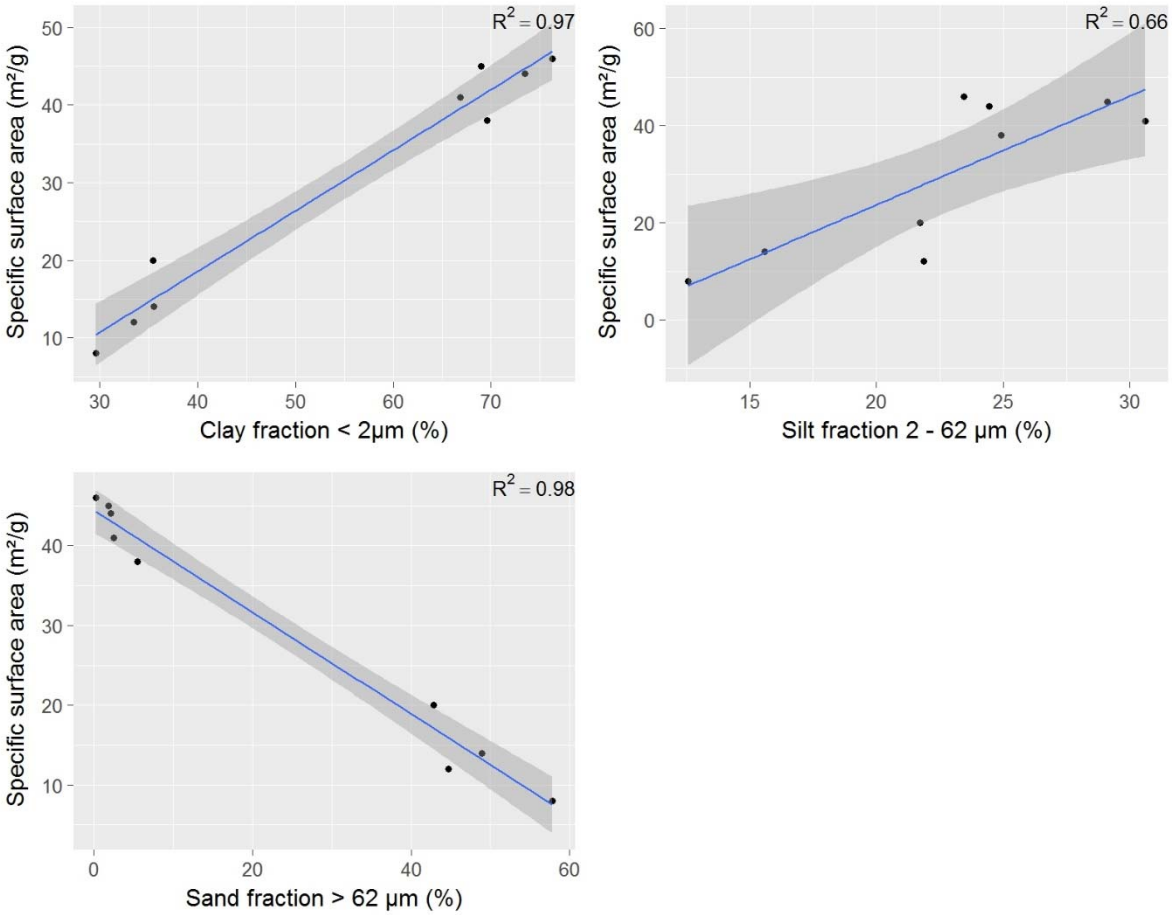

Figure 23: Correlation between grain size distribution and the SSA, measured for the samples of Boom Clay and Eigenbilzen Sands

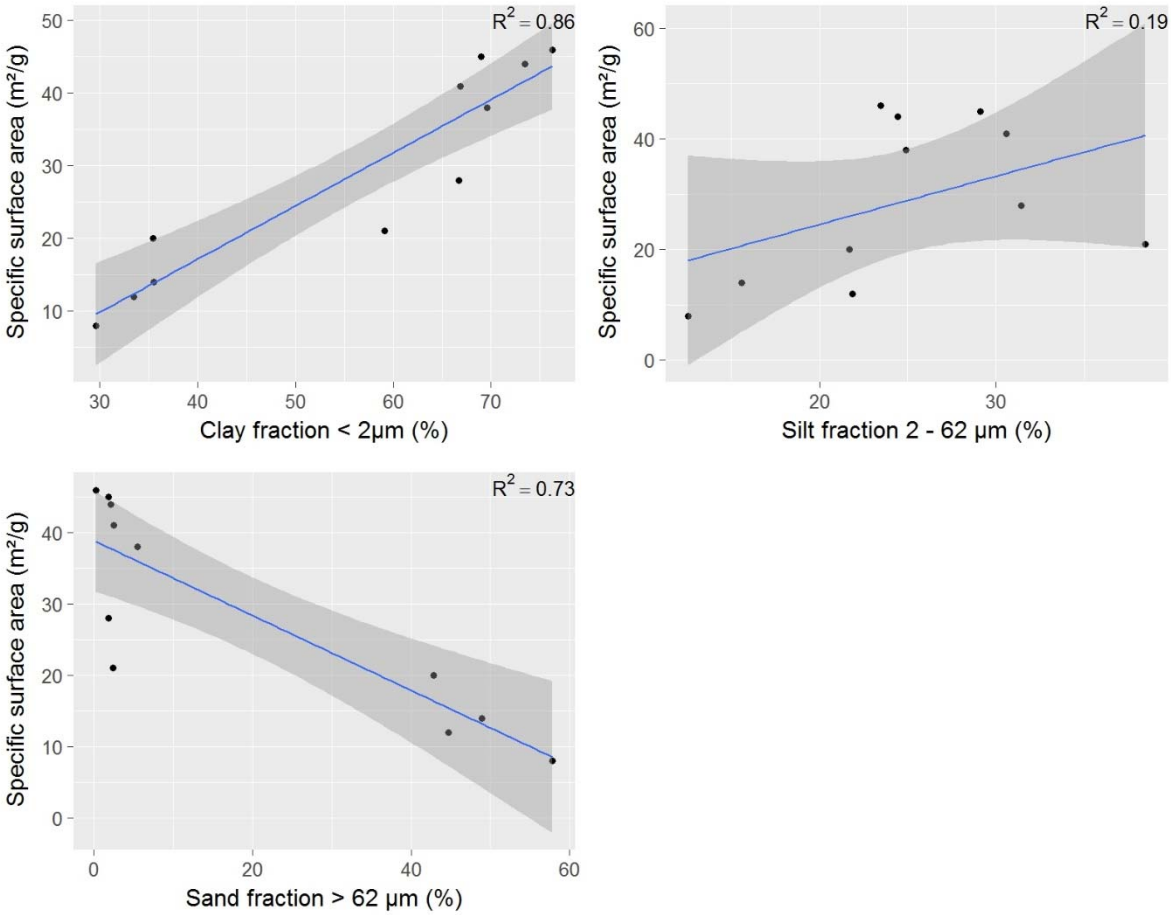

Figure 24 Correlation between grain size distribution and the SSA, measured for the samples of Boom Clay, Eigenbilzen Sands, Opalinus Clay and Callovo-Oxfordian Clay.

Similar to the correlation of SSA with mineralogy and grain size distribution, also correlations with the volume of micro pores can be found (Figure 25 and Figure 26). As the volume of micro pores is derived from the SSA, the correlations are very similar. The more clay minerals, 2:1 clay minerals, clay fraction or silt fraction, the larger the volume of micro pores, which is in fact obvious.

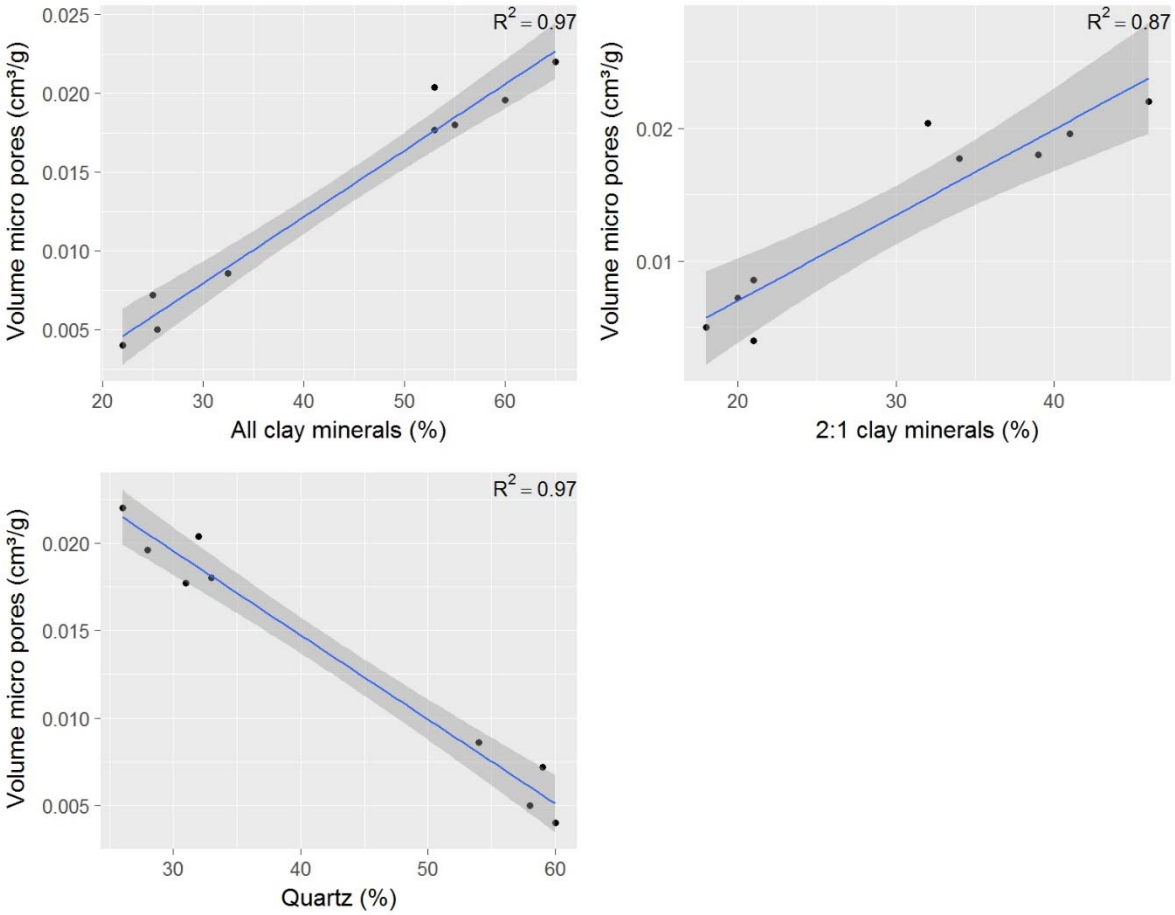

Figure 25: Relationship between mineralogy of the samples and the volume of micro pores for the Boom Clay and Eigenbilzen Sands samples

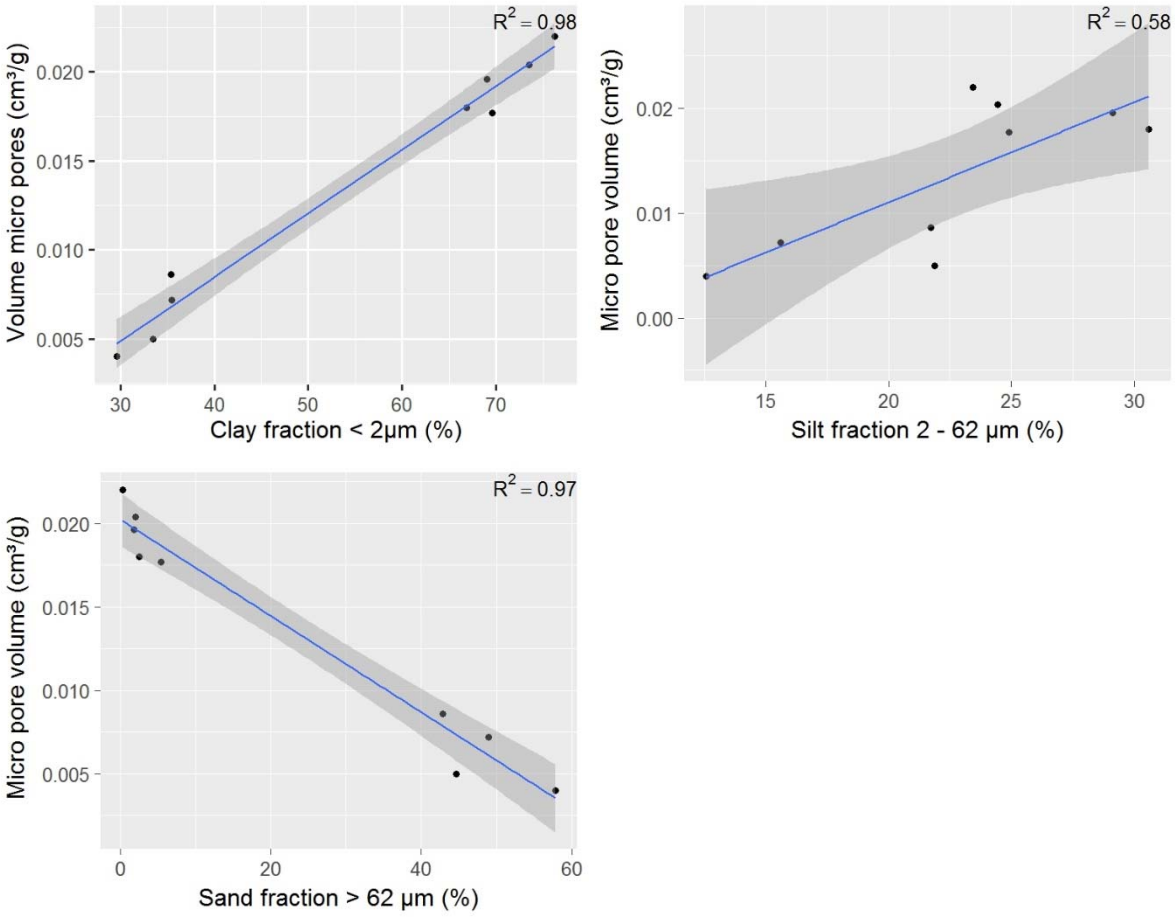

Figure 26: Relationship between grain size distribution of the samples and the volume of micro pores for the Boom Clay and Eigenbilzen Sands samples

4.6.4 Correlation between hydraulic conductivity, mineralogy & specific surface area

Figure 16 shows that the correlation between the hydraulic conductivity and mineralogical composition over all the clay samples is weak (< 0.20, p-values > 0.05), while the correlation between K and the grain size distribution is slightly better (~0.30) but still has p-values > 0.05. The correlation with log K is much better (from 0.6 – 0.8, all p-values < 0.05), which indicates that the relationship between K and mineralogy/grain size distribution is not well fitted with a linear relationship, but better with an exponential function. Hence, in the following graphs, logK is plotted and the reported R^2 is related to the correlation with log K. As the uncertainty on logK is very small for all samples (Table 8), the error bars are smaller than the datapoints and smaller than the confidence interval of the fitted correlation, hence the error bars are not shown (see also annex 5).

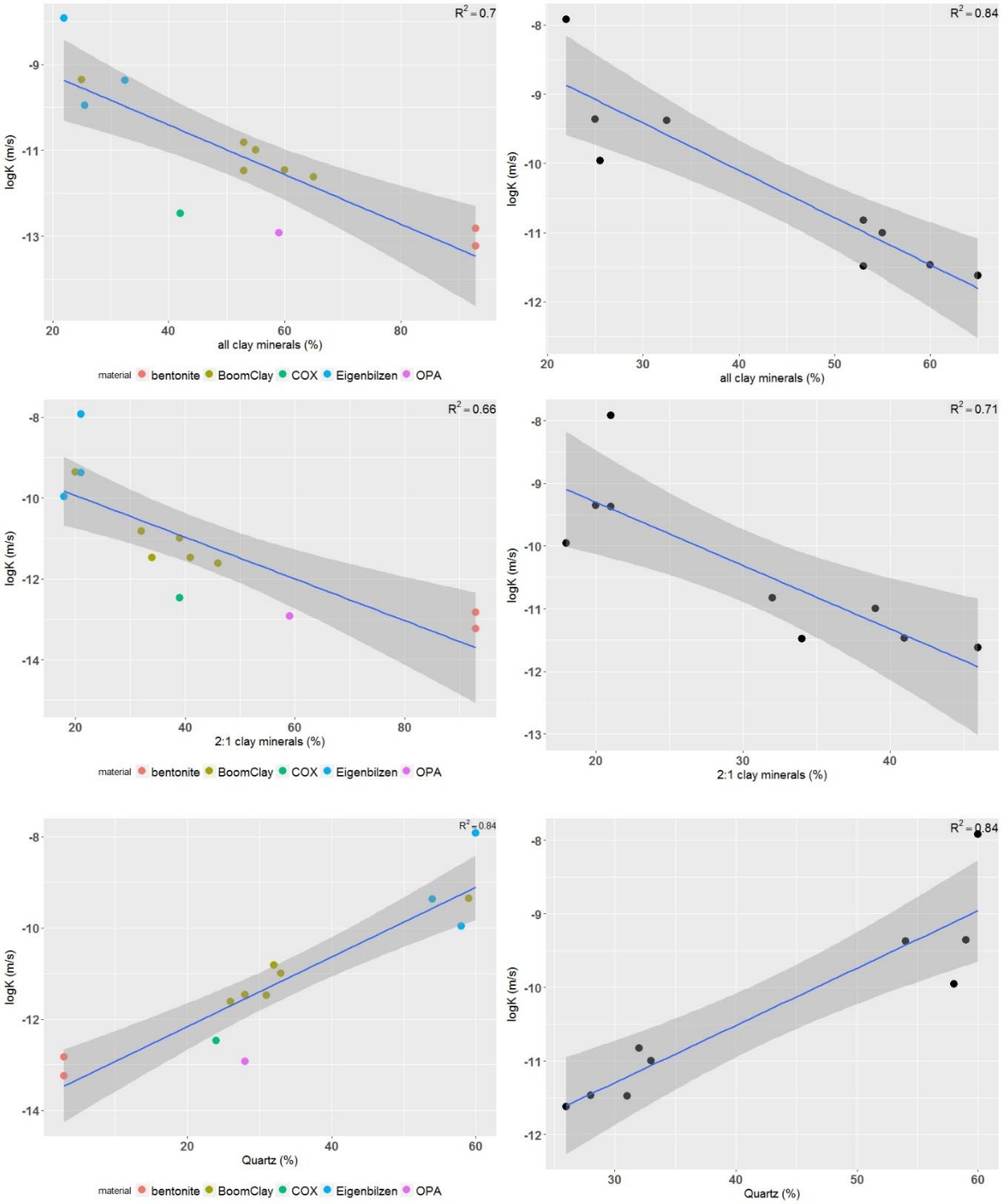

Figure 27: A negative correlation between the clay minerals (all clay minerals (top) and the 2:1 clay minerals (middle)) and log K; a positive correlation between and between quartz and log K (bottom) for all available samples (left) and for the samples of the Boom Clay and the Eigenbilzen Sands (right)

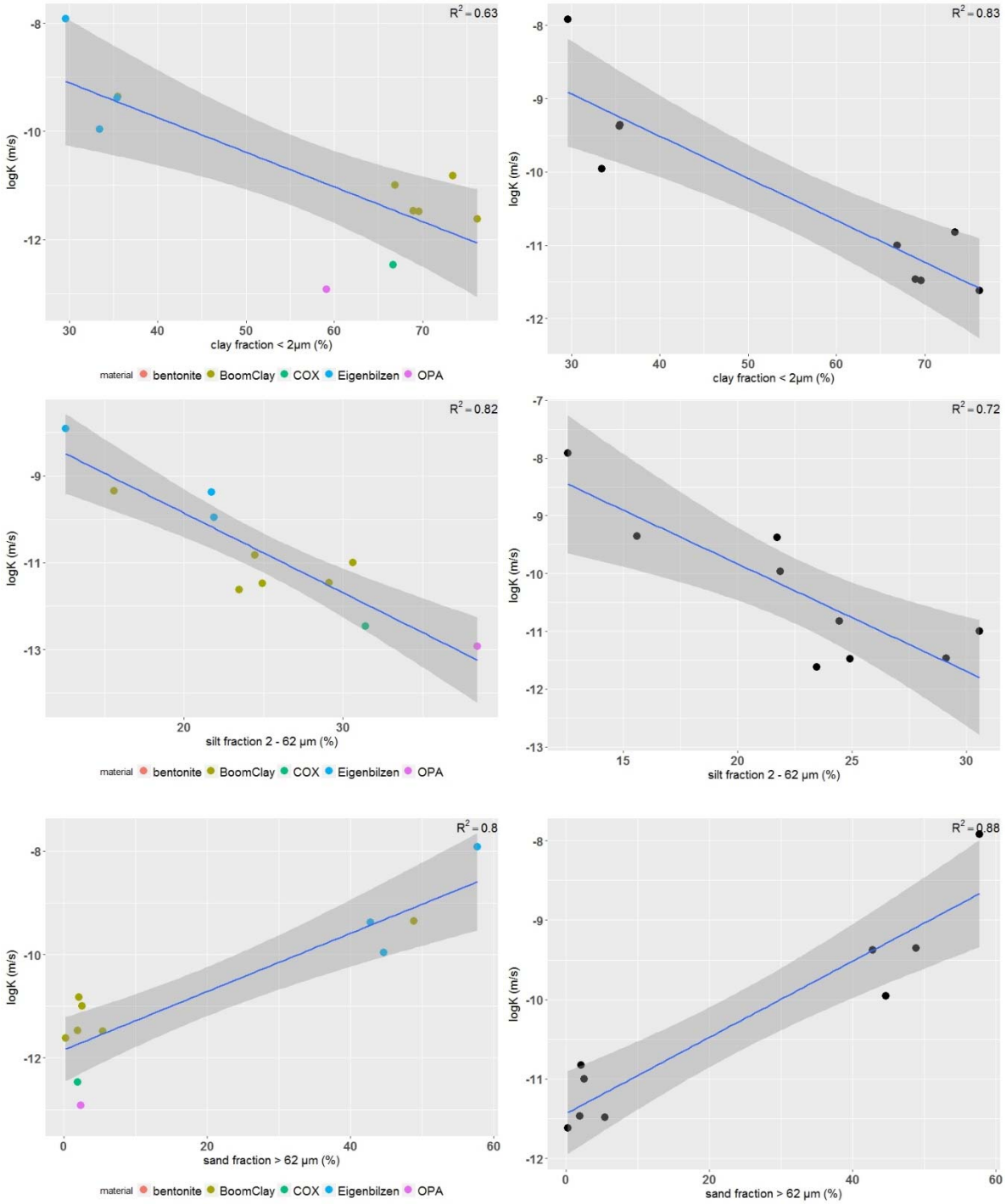

Figure 28: A negative correlation between the clay and the silt fraction and log K (top and middle); a positive correlation between and between the sand content and log K (bottom) for all samples of the data set (left) and the samples of the Boom Clay and the Eigenbilzen Sands (right)

A clear trend is observed in Figure 27 and Figure 28. As expected, log K is positively correlated with the quartz content and the sand fraction and negatively correlated with the clay content, the clay fraction and the silt fraction. When focusing only on the data for samples of the Boom Clay and the Eigenbilzen Sands, the correlation of log K with mineralogy and grain size distribution is in general slightly better. When interpreting the correlations, one should take into account the limited variability in the mineralogical composition and grain size distribution. The proposed correlations can only be confirmed when samples with intermediate clay and sand content, providing data points in the middle part of

each curve, would also have been tested. Currently, it is unclear whether e.g. a variance in quartz content leads automatically to a variance in logK, or variance is only observed when a certain treshold value is passed. Using the current data set, the existence of such a treshold value cannot be confirmed, nor denied. Further research regarding the existence of a treshold value is recommended.

For the Boom Clay and the Eigenbilzen Sands, we also observe a clear correlation (R^2 = 0.82) of the specific surface area with log K and the p-value is < 0.05, while this correlation is weak (R^2 = 0.33) with p-value > 0.05 for the complete data set (including also Opalinus Clay and Callovo-Oxfordian Clay) (Figure 29). The correlation of hydraulic conductivity with the specific surface area is also described by Ren and Santamarina (2018). As expected, we also observe a very good correlation between the volume of micro pores and logK for the samples of the Boom Clay and Eigenbilzen Sands (Figure 30). For these samples, the total pore volume is similar. When a sample has less micro pores, it will have more meso and macro pores and these will enhance the advective transport of water. Obviously, samples with a large clay content have more micropores, and hence K (and logK) is lower.

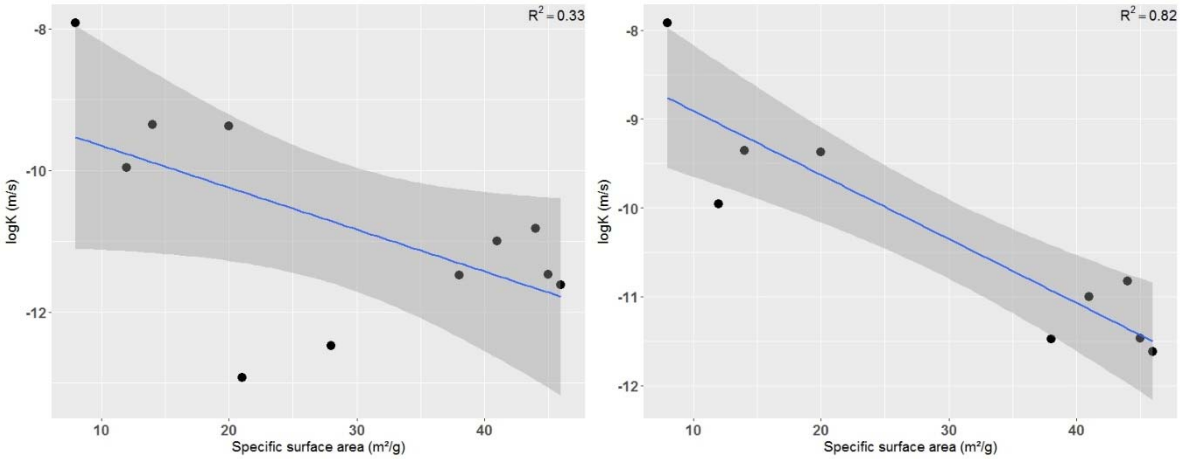

Figure 29: correlation between the SSA and log K for all the samples (left) and the samples of the Boom Clay and Eigenbilzen Sands (right)

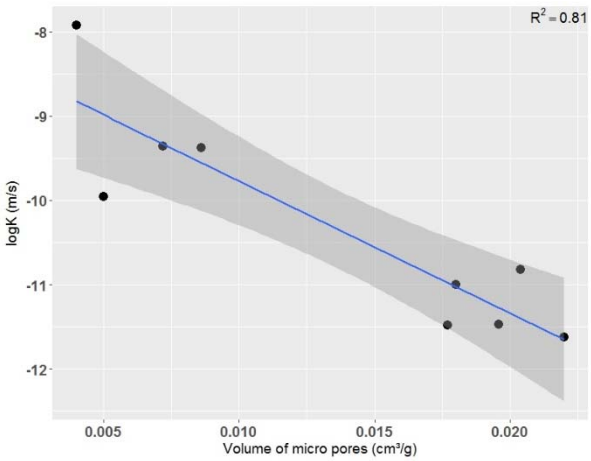

Figure 30: correlation between the volume of micro pores and log K for the samples of the Boom Clay and Eigenbilzen Sands

4.6.5 Correlation between diffusivity and mineralogy/grain size distribution

The correlation between diffusivity (both D_{eff} and $logD_{eff}$) and the main mineral components/grain size distribution is weak to moderate (0.12 to 0.38) (Figure 16). Similar to the relation with (log)K, better correlation coefficients are obtained for $logD_{eff}$ and therefore only graphs with $logD_{eff}$ are shown.

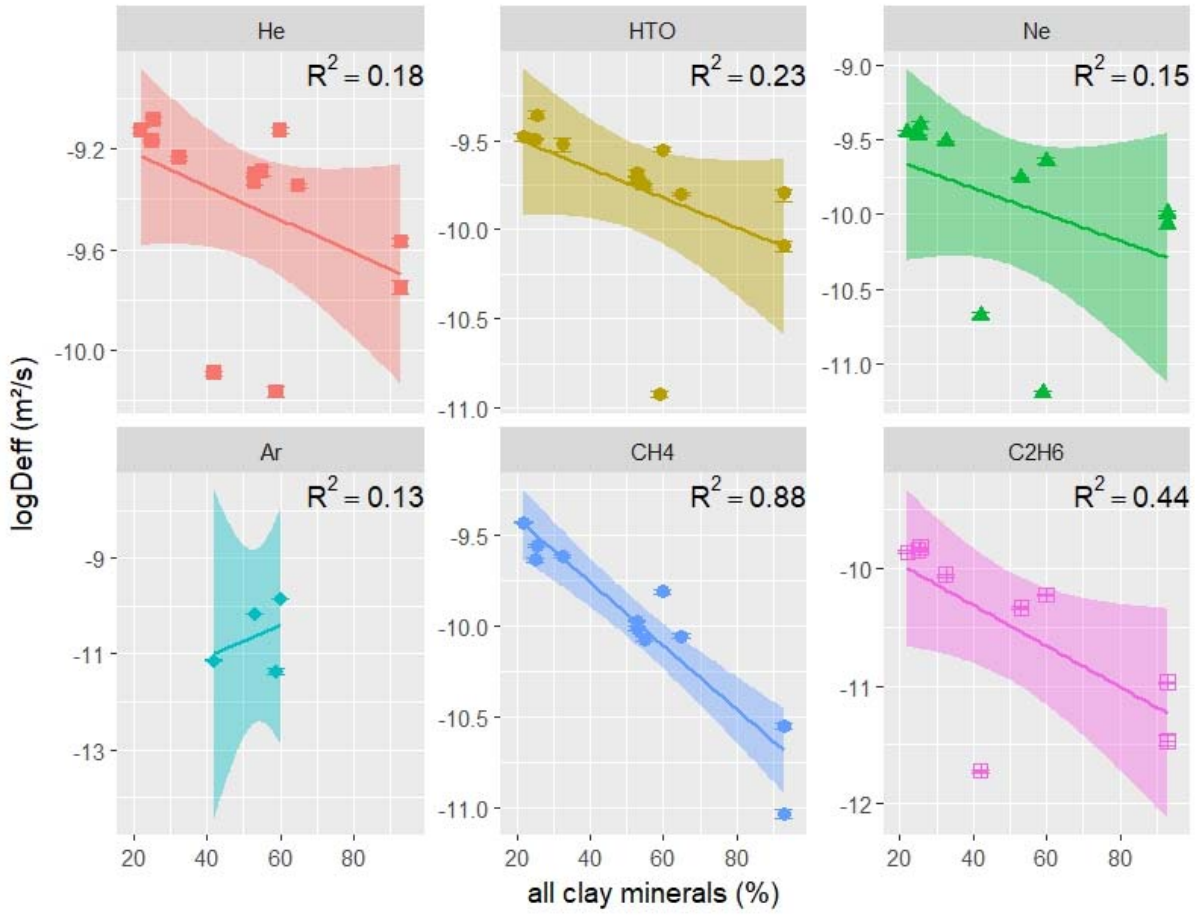

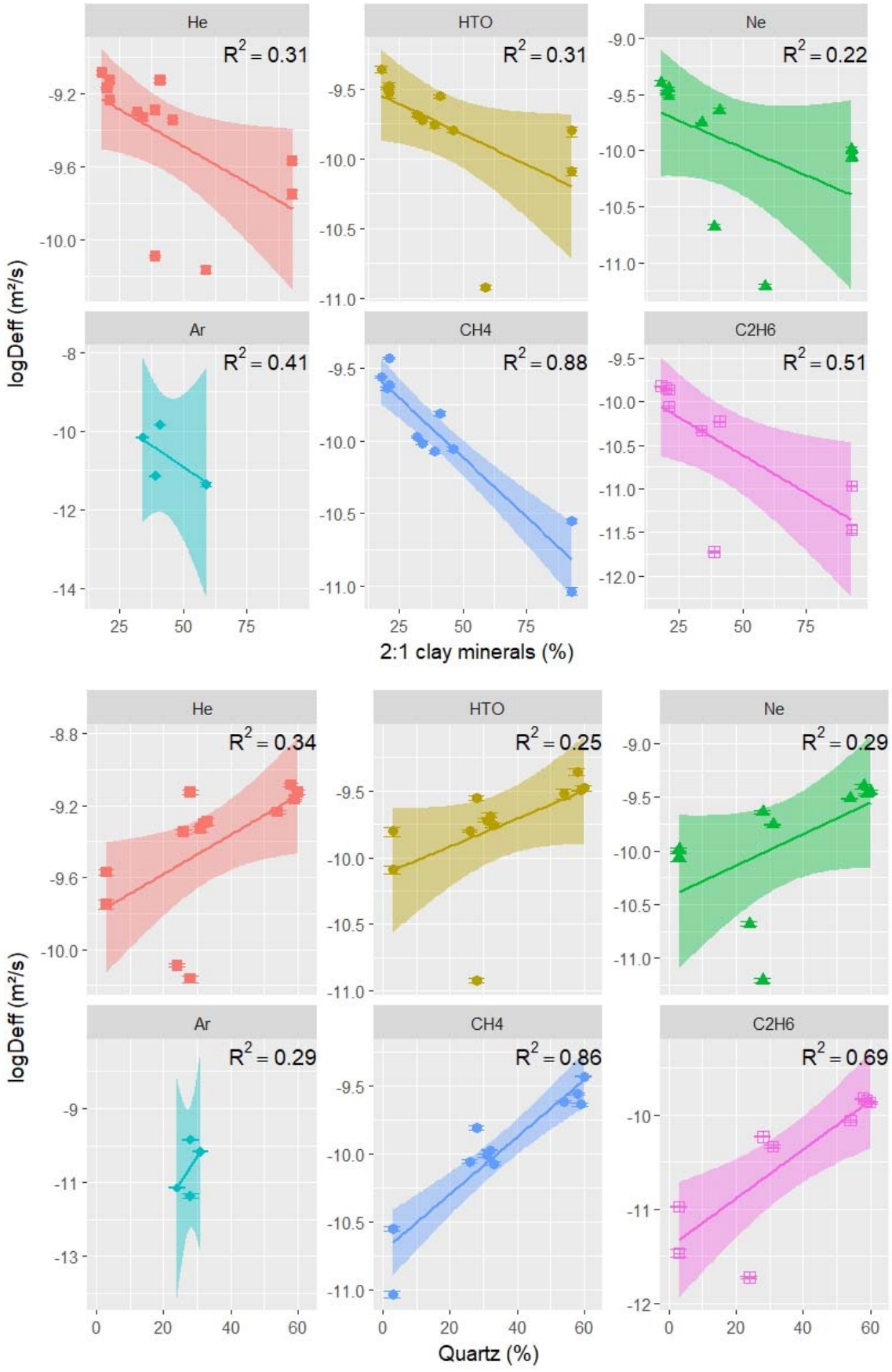

Figure 31: Relationship between the $logD_{eff}$ and the mineralogy of all the samples with content of all clay minerals (top), content of 2:1 clay minerals (middle) and the quartz content (bottom). Note that the shown fit and R^2 are related to $logD_{eff}$.

Figure 31 shows for the different gases the correlation between diffusivity ($logD_{eff}$) and mineralogy. In general, for most of the gases diffusivity tends to increase when the quartz content increases, while it tends to decrease when the amount of clay minerals (both the 2:1 clay and all clay minerals) increases. Figure 32 shows a similar evolution, but for the grain size distribution: diffusivity increases when the sand content increases, while it decreases when the silt and clay content increases.

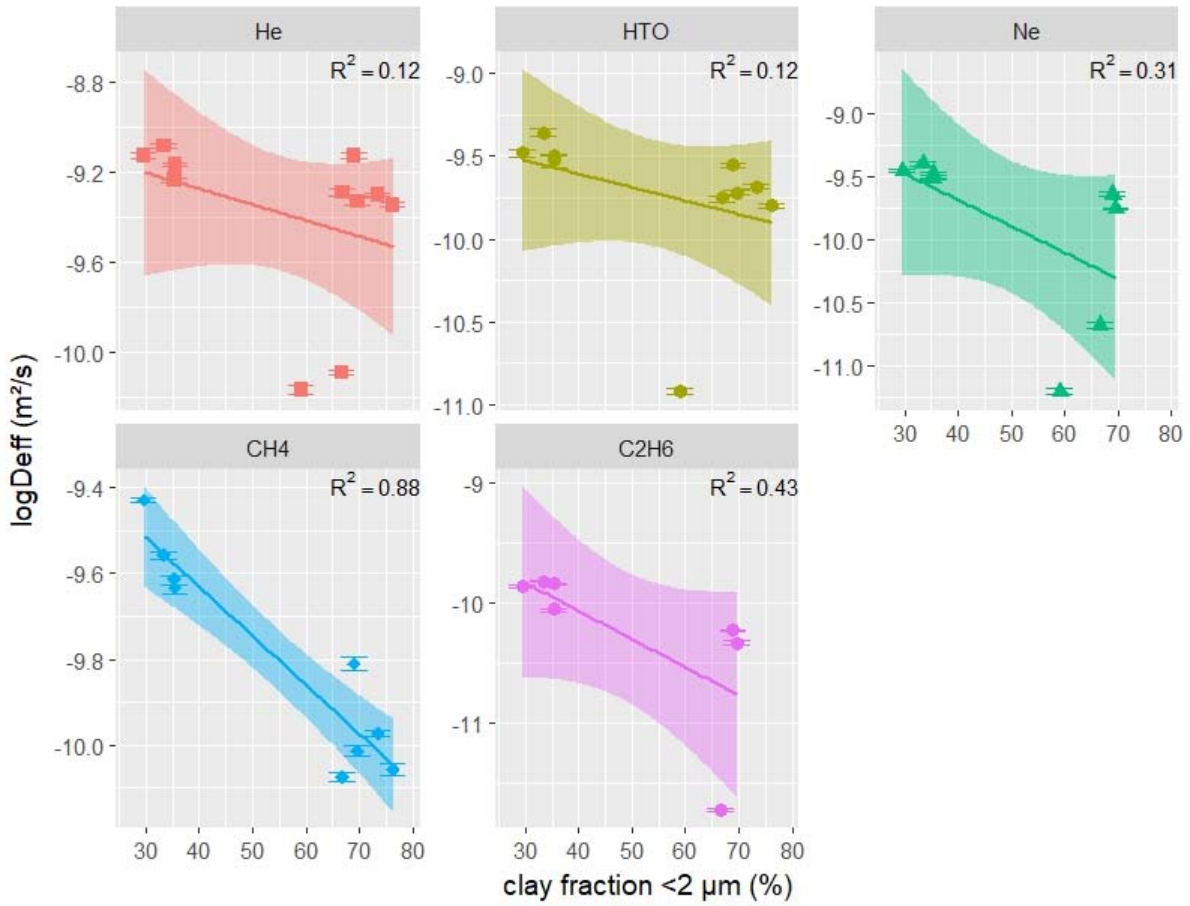

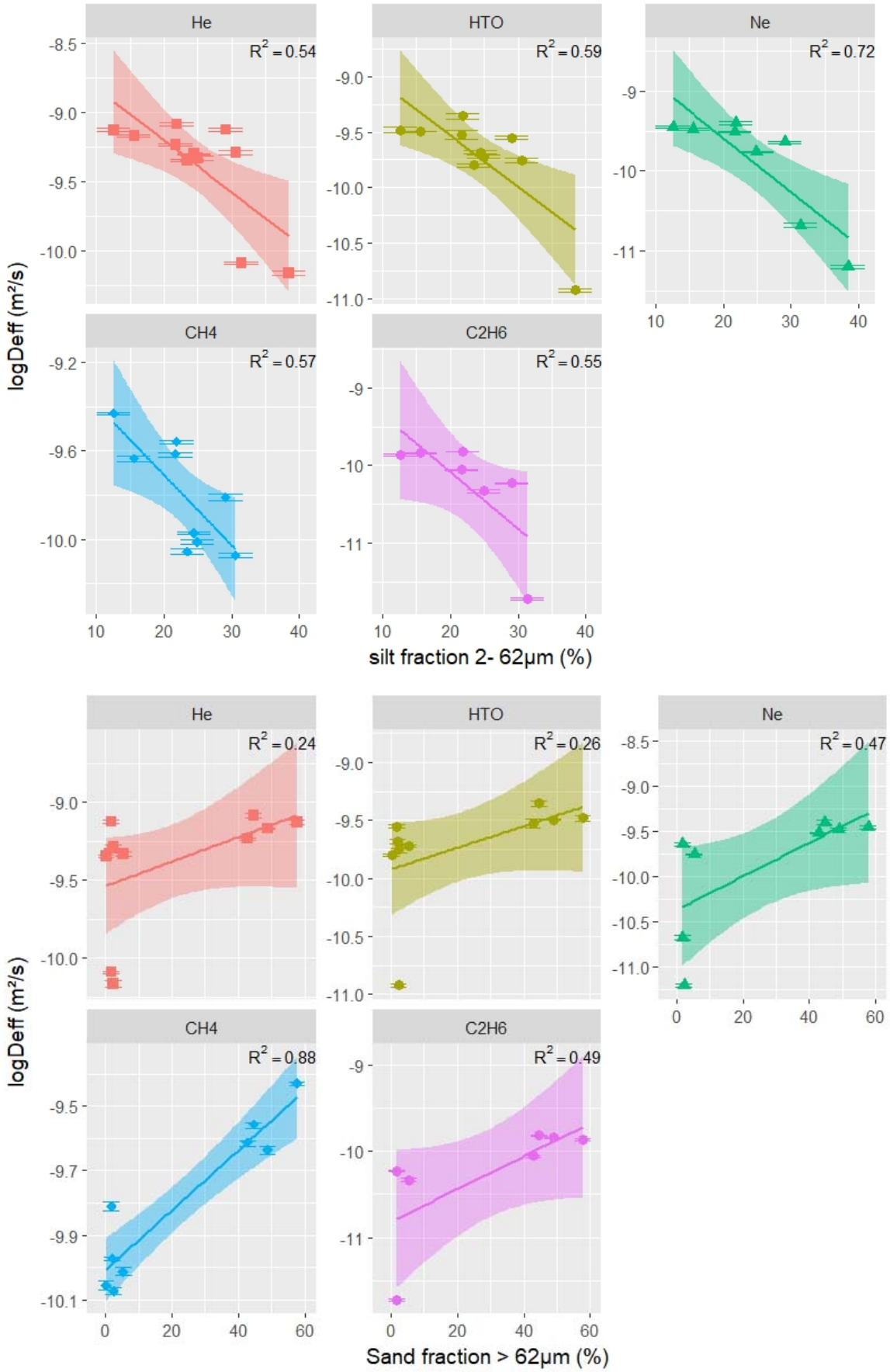

Figure 32: Relationship between $logD_{eff}$ and the grain size distribution (clay – top, silt – middle, sand – bottom)

However, Figure 31, Figure 32 and Table 17 show that the correlation depends on the gas: the best correlation is obtained for respectively CH_4 and C_2H_6, while the correlations for the other gases and HTO are considerably lower and their relative standard deviation is larger.

Table 17: Overview of correlation coefficients of log D_{eff} and the mineralogy and grain size distribution for the entire dataset with average and standard deviation. BC = Boom Clay, EZ = Eigenbilzen Sands

	He	HTO	Ne	Ar	CH_4	C_2H_6
size of the gas (in Å)	2.58	2.75	2.79	3.42	3.82	4.42
ALL SAMPLES						
all clay minerals	0.18	0.23	0.15	0.13	0.88	0.44
2:1 clay minerals	0.31	0.31	0.22	0.41	0.88	0.51
Quartz	0.34	0.25	0.29	0.29	0.86	0.69
Clay fraction	0.12	0.12	0.31		0.89	0.43
Silt fraction	0.54	0.59	0.72		0.53	0.55
Sand fraction	0.24	0.26	0.47		0.88	0.49
average	0.29	0.29	0.36	0.28	0.82	0.52
stdev	0.15	0.16	0.21	0.14	0.14	0.10
%stdev	51	54	57	51	17	18
ONLY BC+EZ						
	He	**HTO**	**Ne**	**Ar**	**CH_4**	**C_2H_6**
all clay minerals	0.45	0.7	0.79		0.82	0.87
2:1 clay minerals	0.37	0.69	0.72		0.73	0.76
Quartz	0.45	0.7	0.84		0.83	0.88
Clay fraction	0.51	0.74	0.87		0.88	0.85

Silt fraction	0.16	0.29	0.2		0.57	0.58
Sand fraction	0.45	0.68	0.8		0.88	0.84
average	0.40	0.63	0.70		0.79	0.80
stdev	0.12	0.17	0.25		0.12	0.11
%stdev	31	27	36		15	14

When studying only the samples of the Boom Clay and Eigenbilzen Sands, the same trends as for the full dataset can be observed (Figure 33 and Figure 34), but the correlation is much better (Table 17). The average correlation coefficients have increased significantly and the relative error is much smaller. Again, the best correlation is observed for C_2H_6 and CH_4, but the difference with the other gases and HTO has become smaller. For both datasets, one can consider that both the mineralogical composition and the grain size distribution are equally well correlated with $logD_{eff}$.

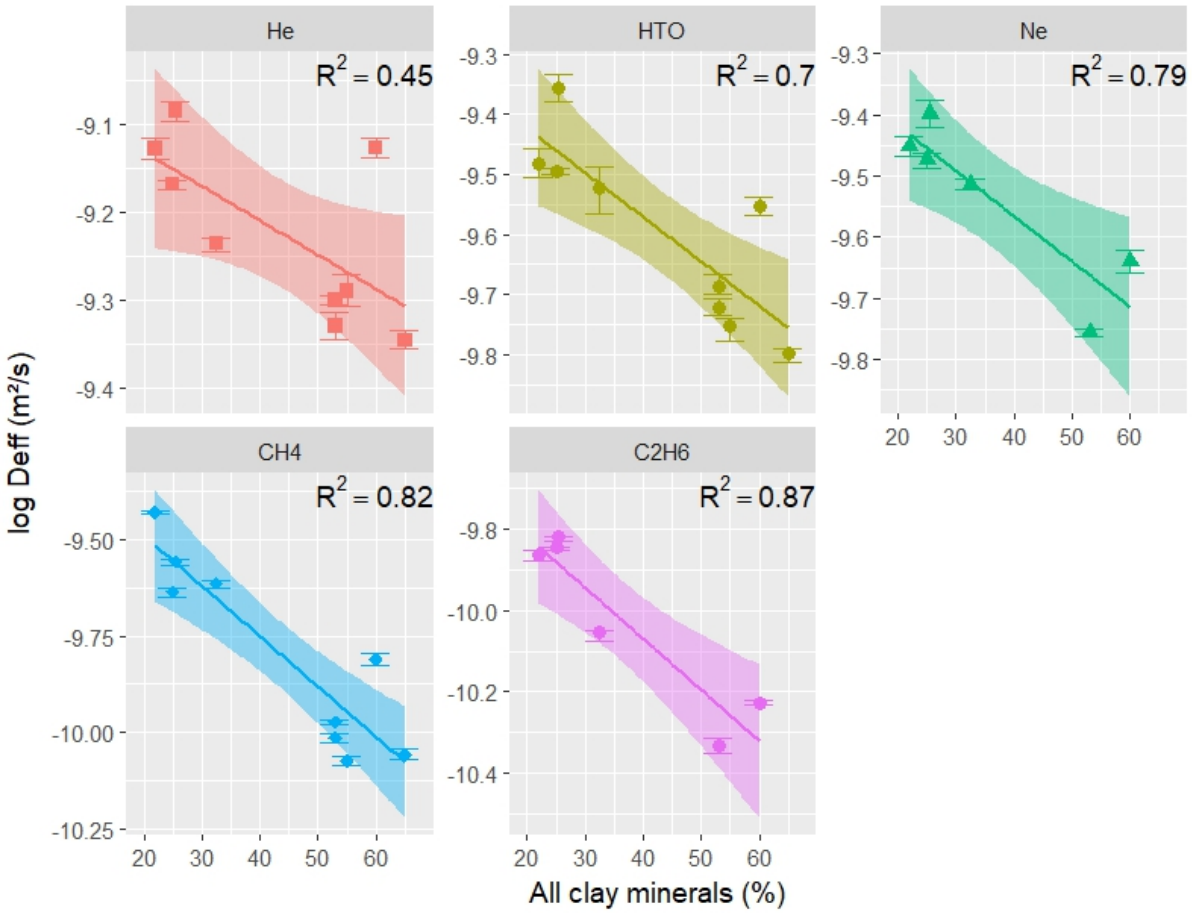

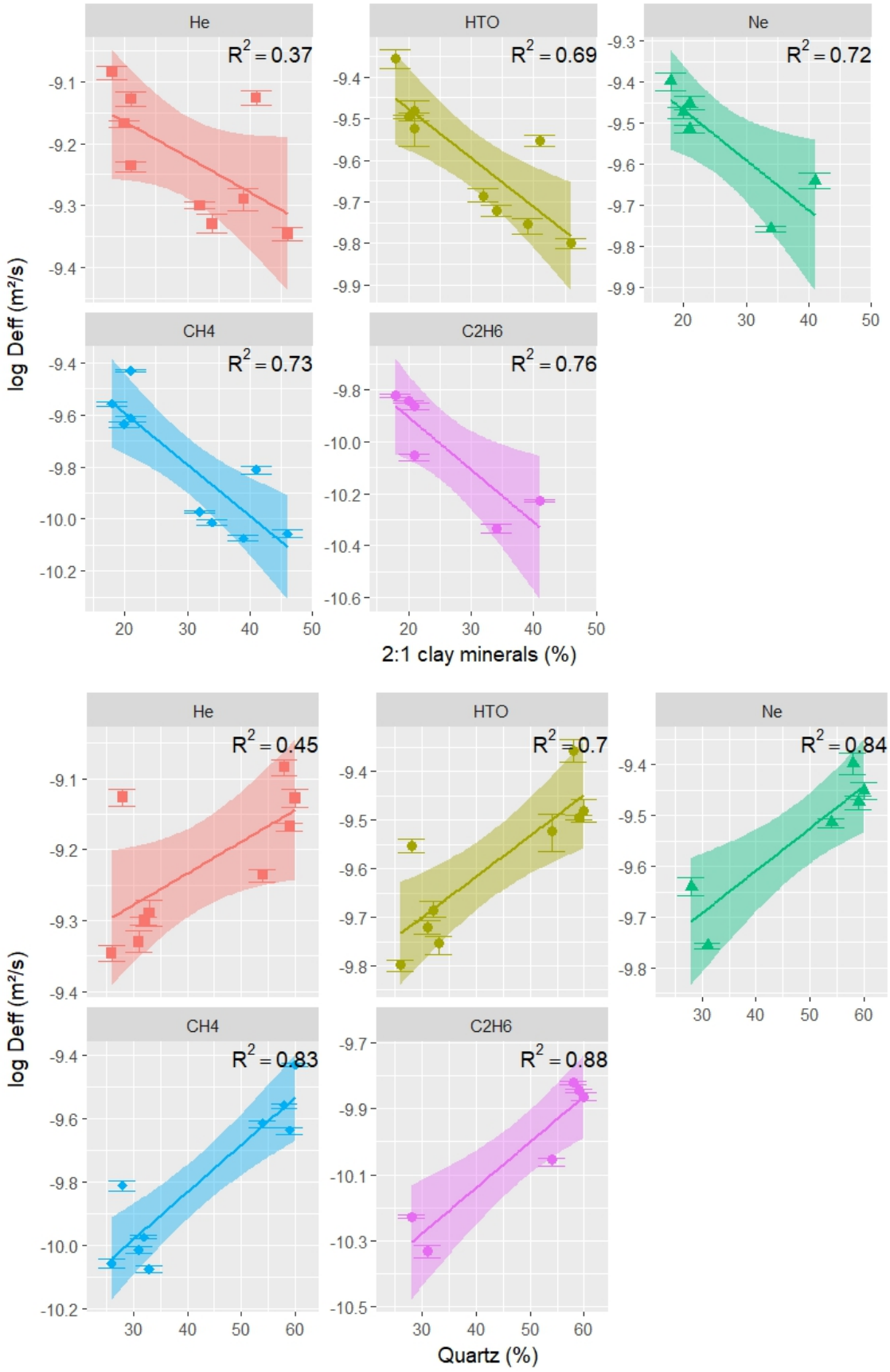

Figure 33: Relationship between the logD_{eff} and the mineralogy of the Boom Clay and Eigenbilzen Sands samples with the content of 2:1 clay minerals (top), content of all clay minerals (middle) and quartz content (bottom)

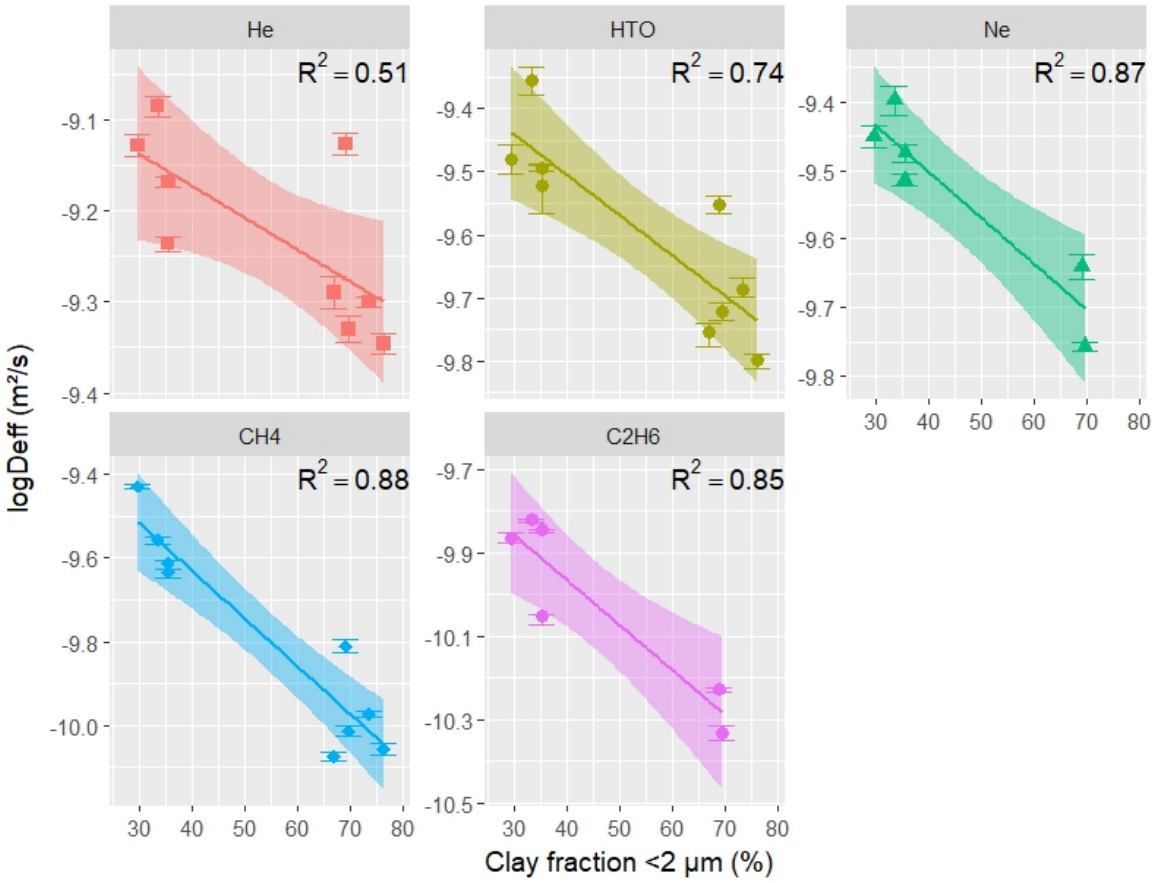
He
$R^2 = 0.51$
HTO
$R^2 = 0.74$
Ne
$R^2 = 0.87$
CH4
$R^2 = 0.88$
C2H6
$R^2 = 0.85$
logDeff (m²/s)
Clay fraction <2 µm (%)

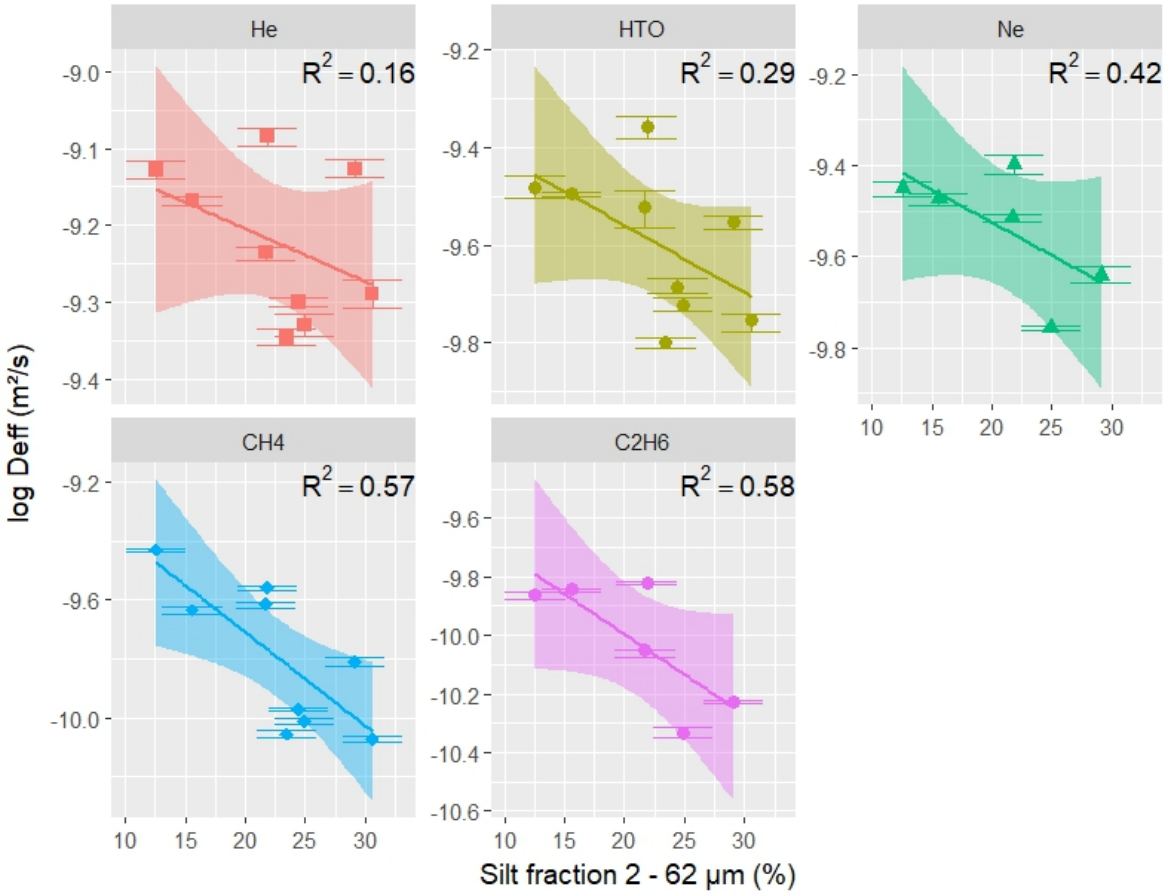
He
$R^2 = 0.16$
HTO
$R^2 = 0.29$
Ne
$R^2 = 0.42$
CH4
$R^2 = 0.57$
C2H6
$R^2 = 0.58$
log Deff (m²/s)
Silt fraction 2 - 62 µm (%)

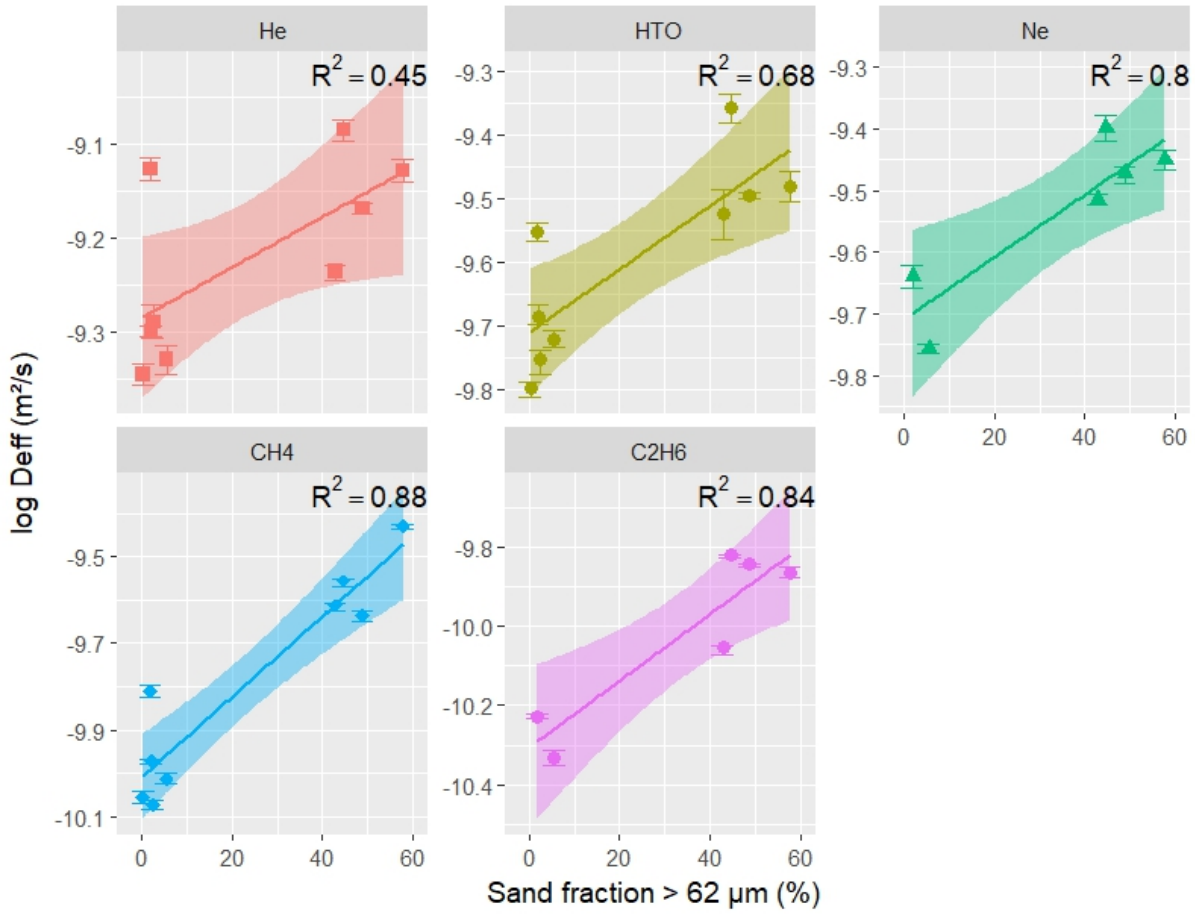

Figure 34: Relationship between the $logD_{eff}$ and the grain size distribution of the Boom Clay and Eigenbilzen Sands samples with the clay (top), silt (middle) and sand (botttom) fraction

When studying the relation between the volume of micro pores and $logD_{eff}$ for the different gases, we observe a strong to very strong relationship for the different gases, and the correlation improves when the size of the diffusing molecule increases (Figure 35). This indicates that larger gases are stronger influenced by a change in the volume of micro pores.

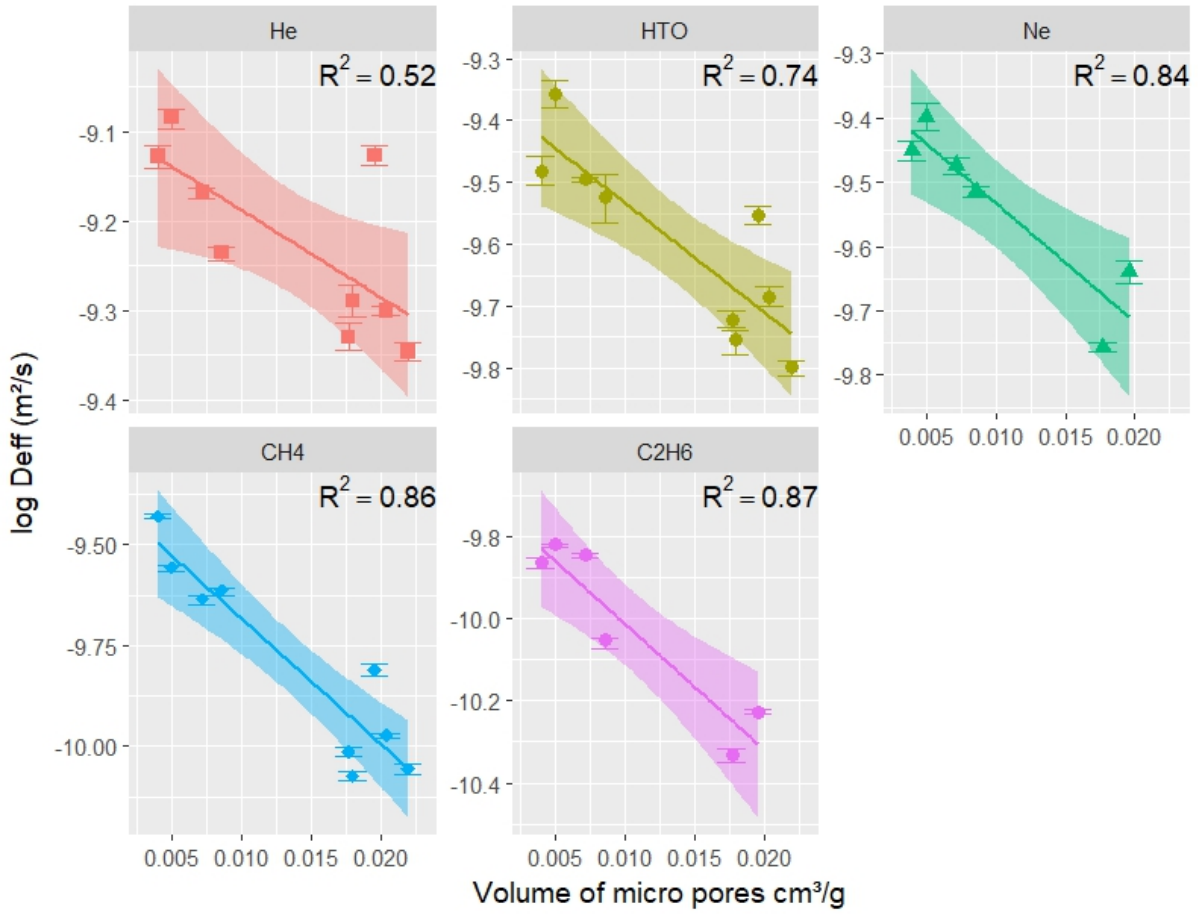

Figure 35: Relationship between the volume of micro pores and logD_{eff} for the samples of the Boom Clay and Eigenbilzen Sands

As discussed in Jacops et al. (2017a), the relation between G and the size of a diffusing molecule is best described with an exponential function. Hence, also logG was taken up in the correlation matrix of Figure 16, and similar to the relations with K/logK and D_{eff}/logD_{eff}, the correlation is in general better for logG than for G (especially for the full dataset which includes all samples, which is refleced in lower p-values for logG). Therefore, the next section discusses the correlation of logG with the mineralogy and grain size distribution.

A weak to moderate (< 0.2 for the full dataset, < 0.36 for the samples Boom Clay and Eigenbilzen Sands) correlation is also found between the geometric factor and the mineralogy/grain size distribution, while the correlation is moderate to strong (between 0.2 and 0.47) for log*G*. As expected from previous observations, the geometric factor increases with an increase in clay minerals (2:1 and all), clay and silt fraction, while it decreases with an increase in quartz content and sand fraction (Figure 36, Figure 37, Figure 38, Figure 39). P-values are considerably lower for mineralogy than for grain size.

For the full dataset, the average correlation is very strong for CH_4, but moderate or strong for the other gases and HTO and in general the standard deviation is large (Table 18). When looking at the data for the samples Boom Clay and Eigenbilzen Sands only, the correlation is very strong for C_2H_6 and CH_4 (> 0.7), and moderate or strong for the other gases and HTO.

Table 18: Overview of correlation coefficients of log*G* and the mineralogy and grain size distribution for the entire dataset with average and standard deviation

	He	HTO	Ne	Ar	CH_4	C_2H_6
size of the gas (Å)	2.58	2.75	2.79	3.42	3.82	4.42
ALL SAMPLES						
all clay minerals	0.44	0.53	0.33	0.29	0.89	0.58
2:1 clay minerals	0.59	0.59	0.41	0.22	0.91	0.65
Quartz	0.62	0.55	0.5	0.32	0.87	0.79
Clay fraction	0.23	0.27	0.38	0.48	0.9	0.48
Silt fraction	0.39	0.57	0.74	0.44	0.53	0.58
Sand fraction	0.32	0.41	0.54	0.06	0.88	0.54
average	0.43	0.49	0.48	0.30	0.83	0.60
stdev	0.15	0.12	0.15	0.15	0.15	0.11
%stdev	35	25	31	51	18	18
ONLY BC+EZ						
all clay minerals	0.39	0.69	0.75		0.84	0.84
2:1 clay minerals	0.31	0.67	0.67		0.75	0.73
Quartz	0.39	0.69	0.8		0.85	0.86
Clay fraction	0.43	0.72	0.81		0.9	0.82
Silt fraction	0.08	0.22	0.39		0.53	0.56

Sand fraction	0.36	0.64	0.75		0.88	0.81
average	0.33	0.61	0.70		0.79	0.77
stdev	0.13	0.19	0.16		0.14	0.11
%stdev	39	31	23		17	15

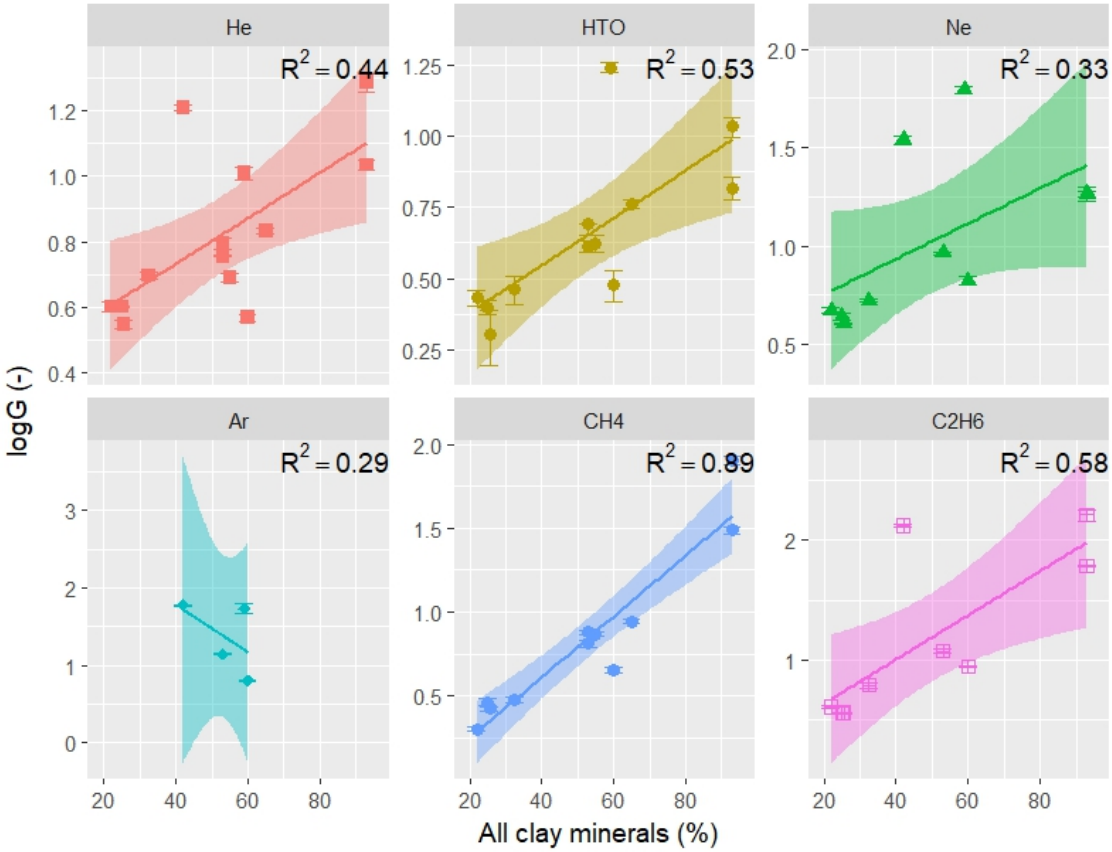

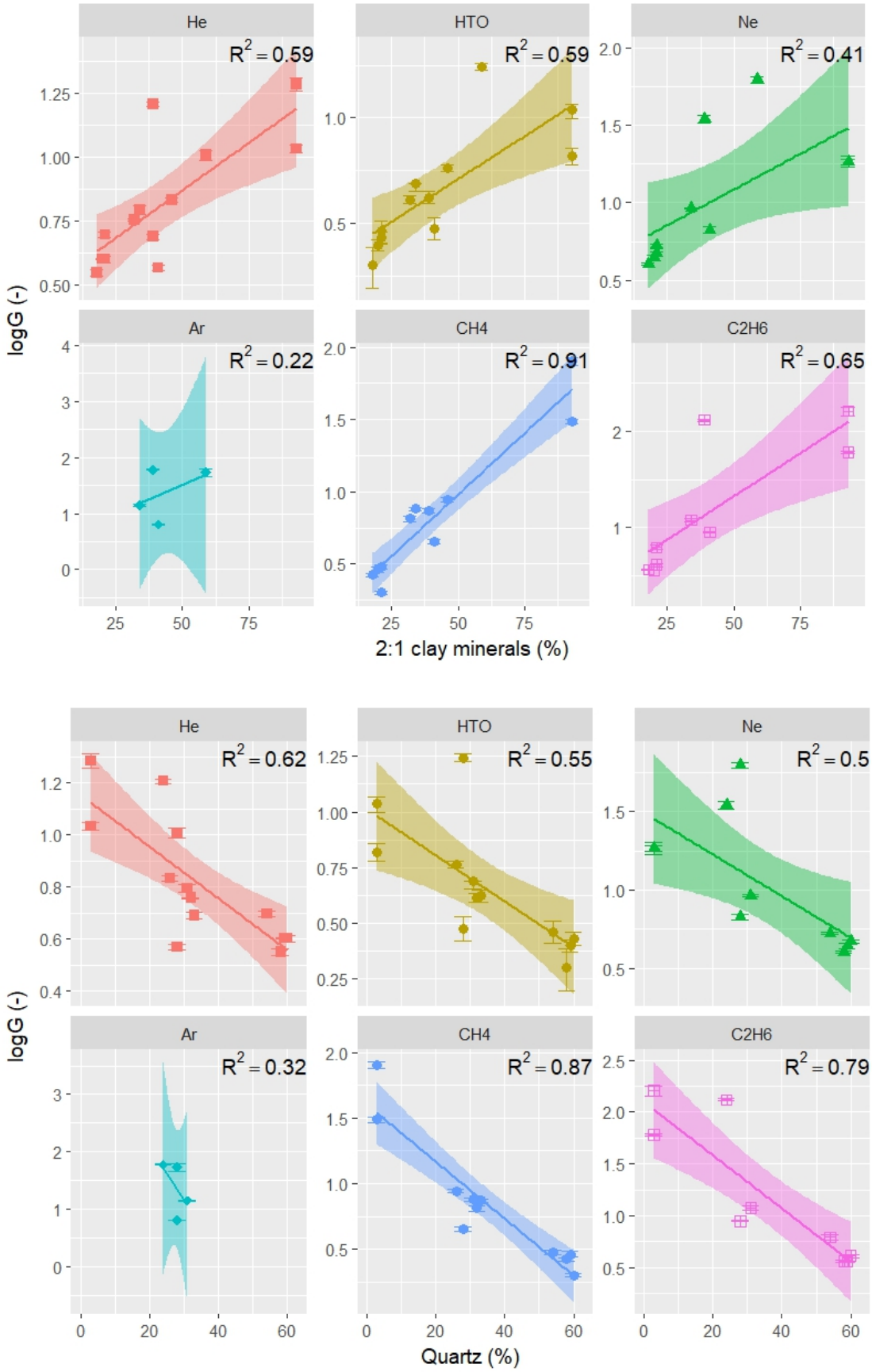

Figure 36: Relationship between the geometric factor (logG) and the mineralogy of all the samples with the content of all the clay (top) and the 2:1 (middle) clay minerals, and the quartz content (bottom)

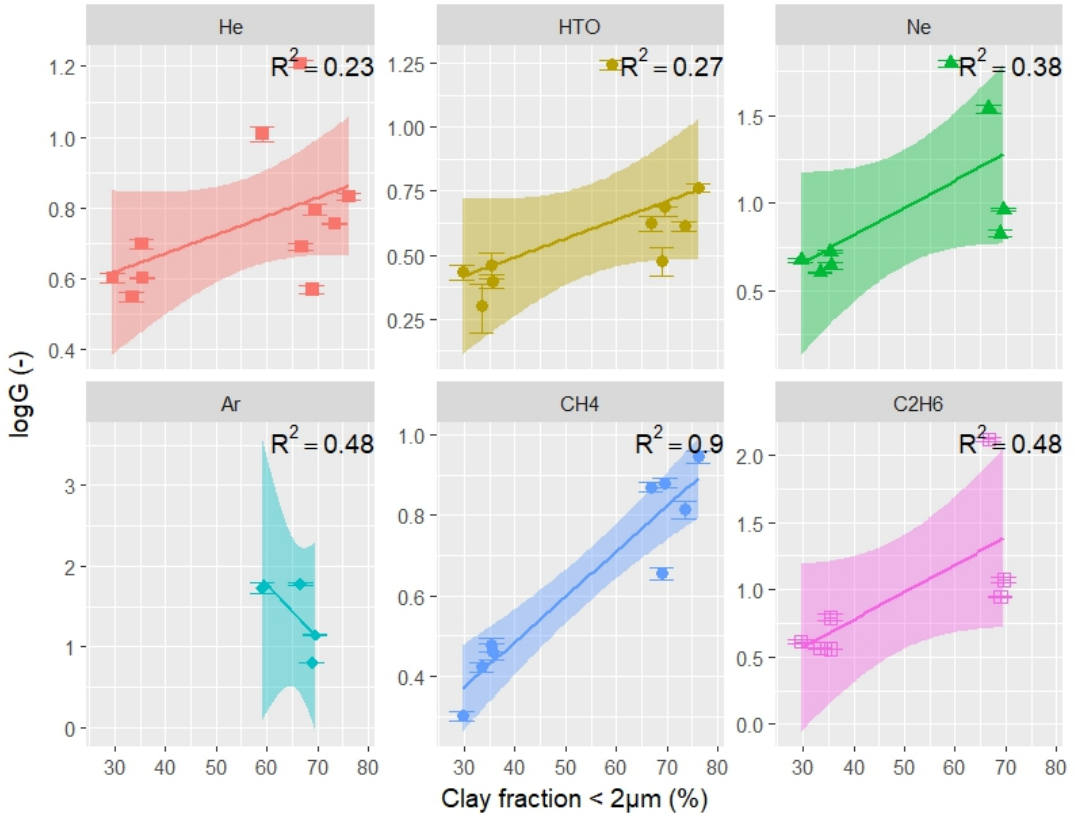
He
HTO
Ne
Ar
CH4
C2H6
R2 = 0.23
R2 = 0.27
R2 = 0.38
R2 = 0.48
R2 = 0.9
R2 = 0.48
logG (-)
Clay fraction < 2µm (%)

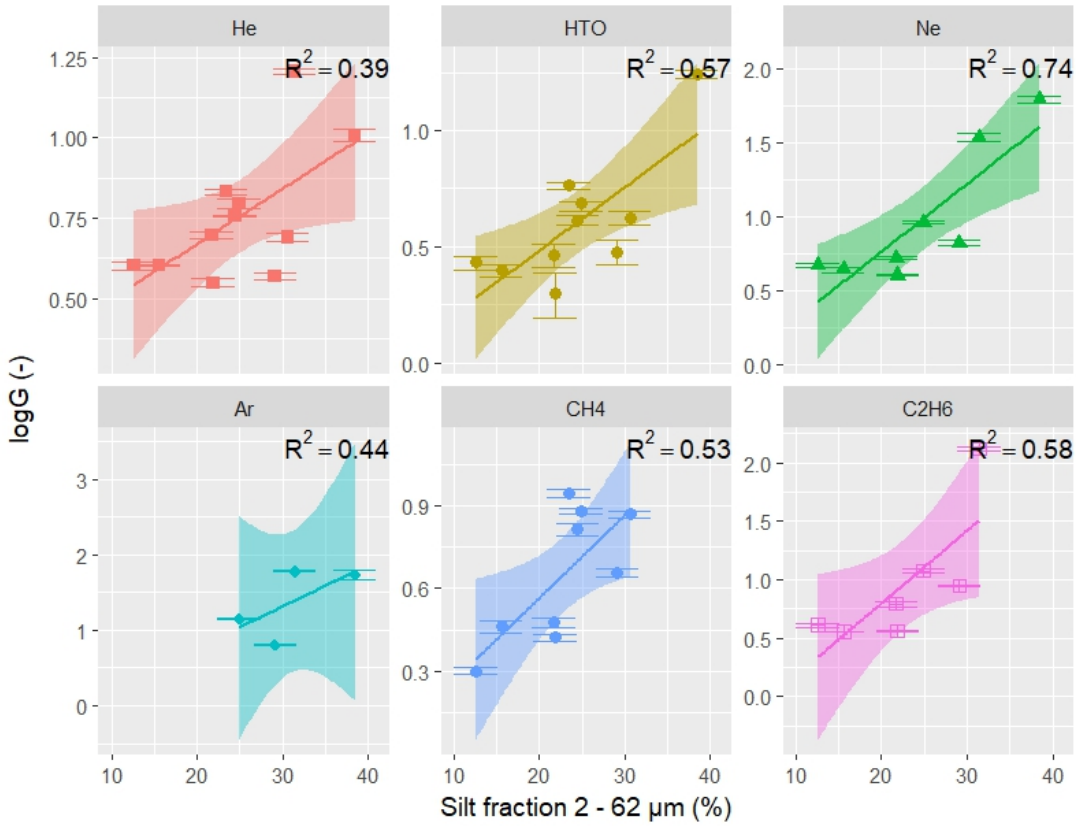
He
HTO
Ne
Ar
CH4
C2H6
R2 = 0.39
R2 = 0.57
R2 = 0.74
R2 = 0.44
R2 = 0.53
R2 = 0.58
logG (-)
Silt fraction 2 - 62 µm (%)

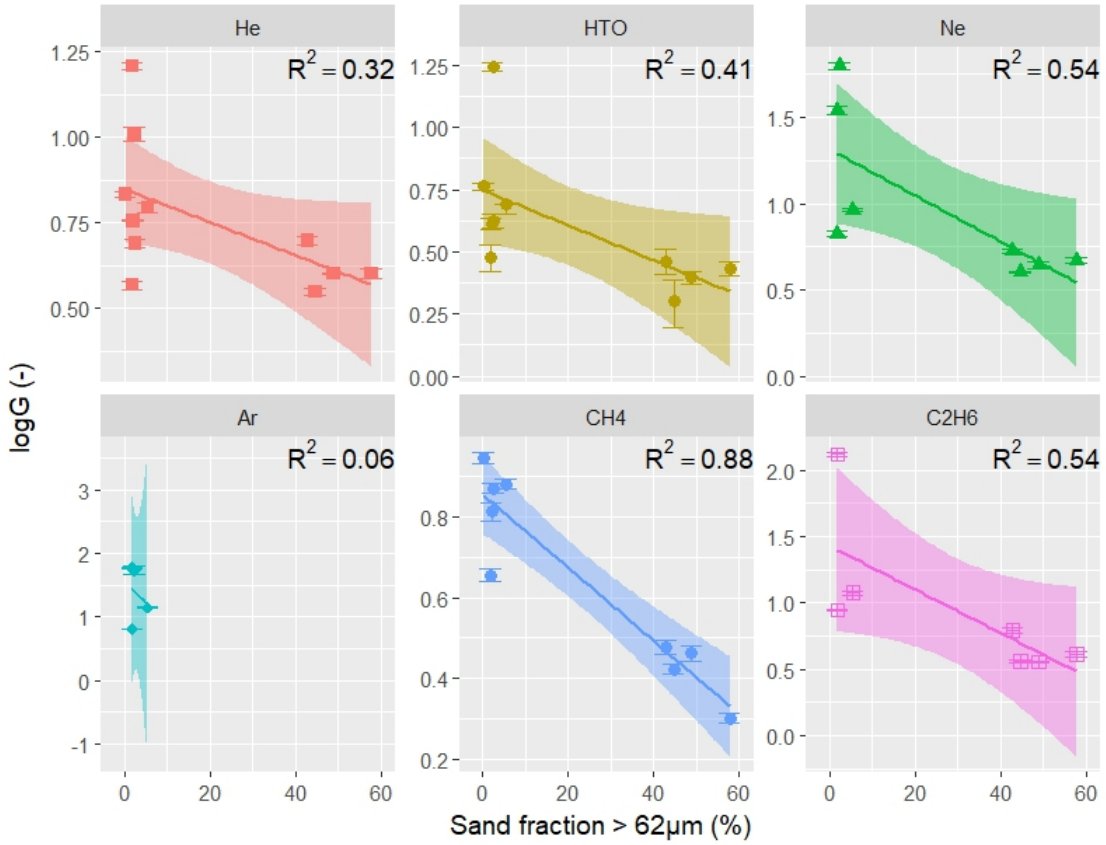

Figure 37: Relationship between the geometric factor (logG) and the grain size distribution (clay – top, silt – middle, sand – bottom) for all samples

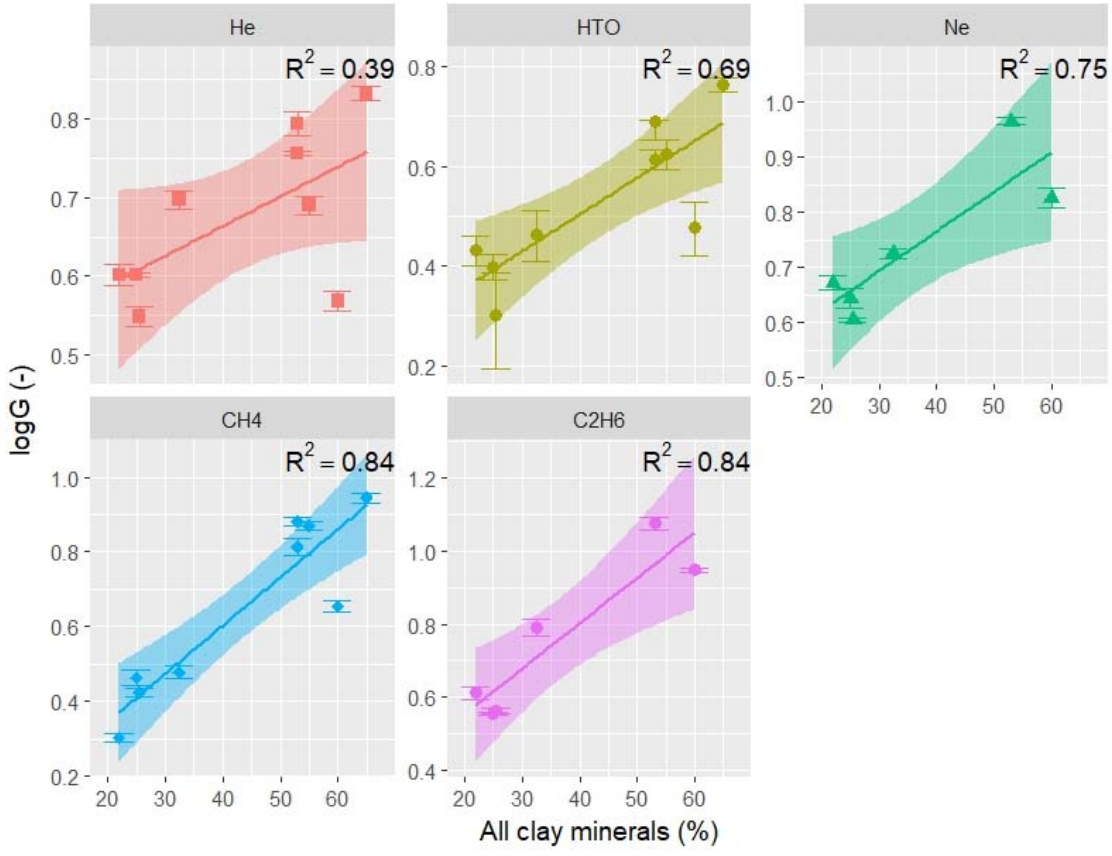

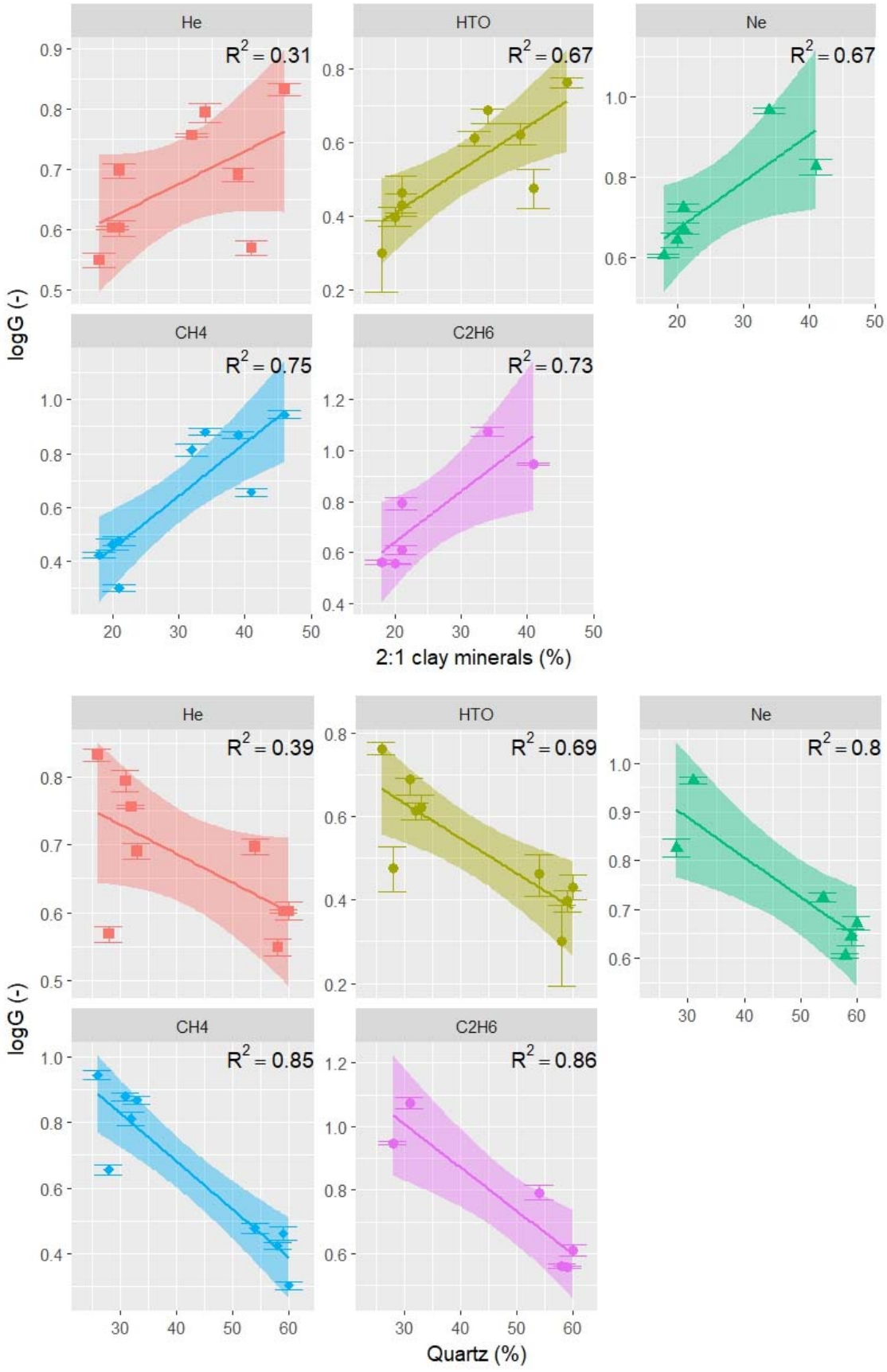

Figure 38: Relationship between the geometric factor (logG) and the mineralogy of the Boom Clay and Eigenbilzen Sands samples with the content of all clay minerals (top), the content of 2:1 clay minerals (middle) quartz content (bottom)

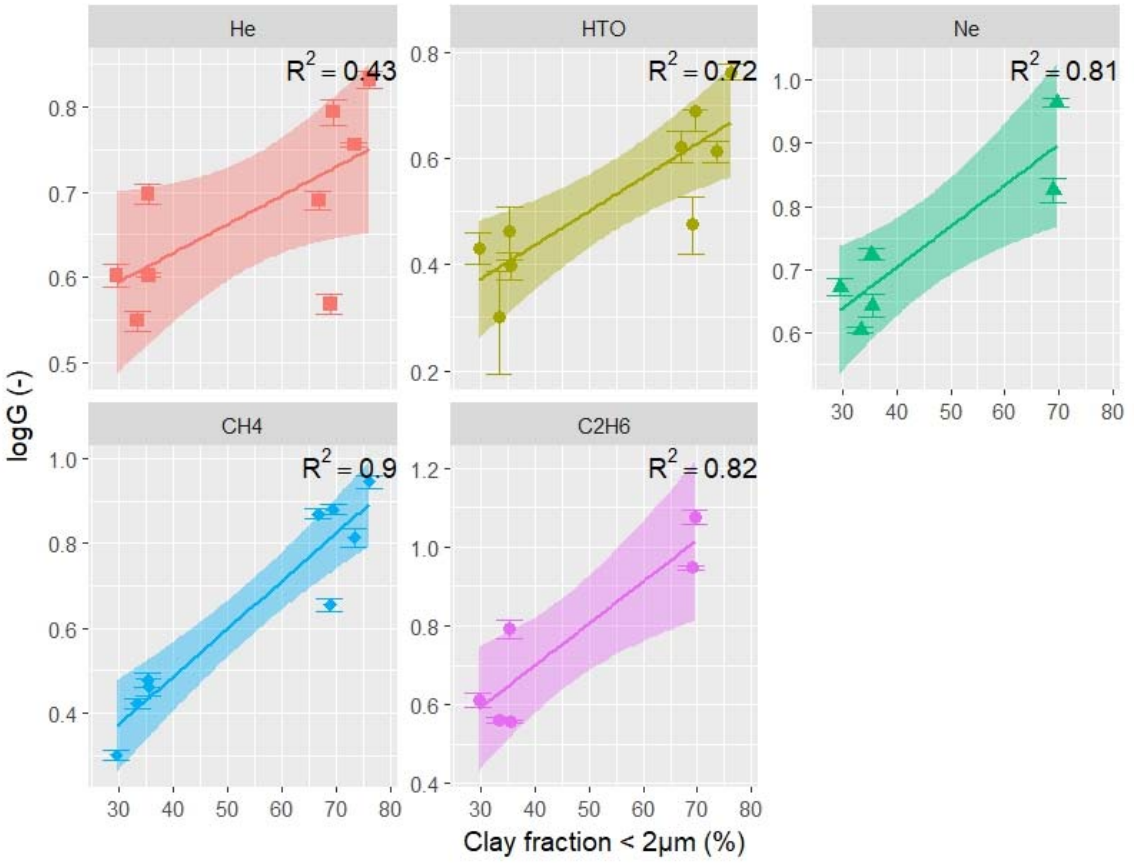
He
$R^2 = 0.43$
HTO
$R^2 = 0.72$
Ne
$R^2 = 0.81$
CH4
$R^2 = 0.9$
C2H6
$R^2 = 0.82$
logG (-)
Clay fraction < 2µm (%)

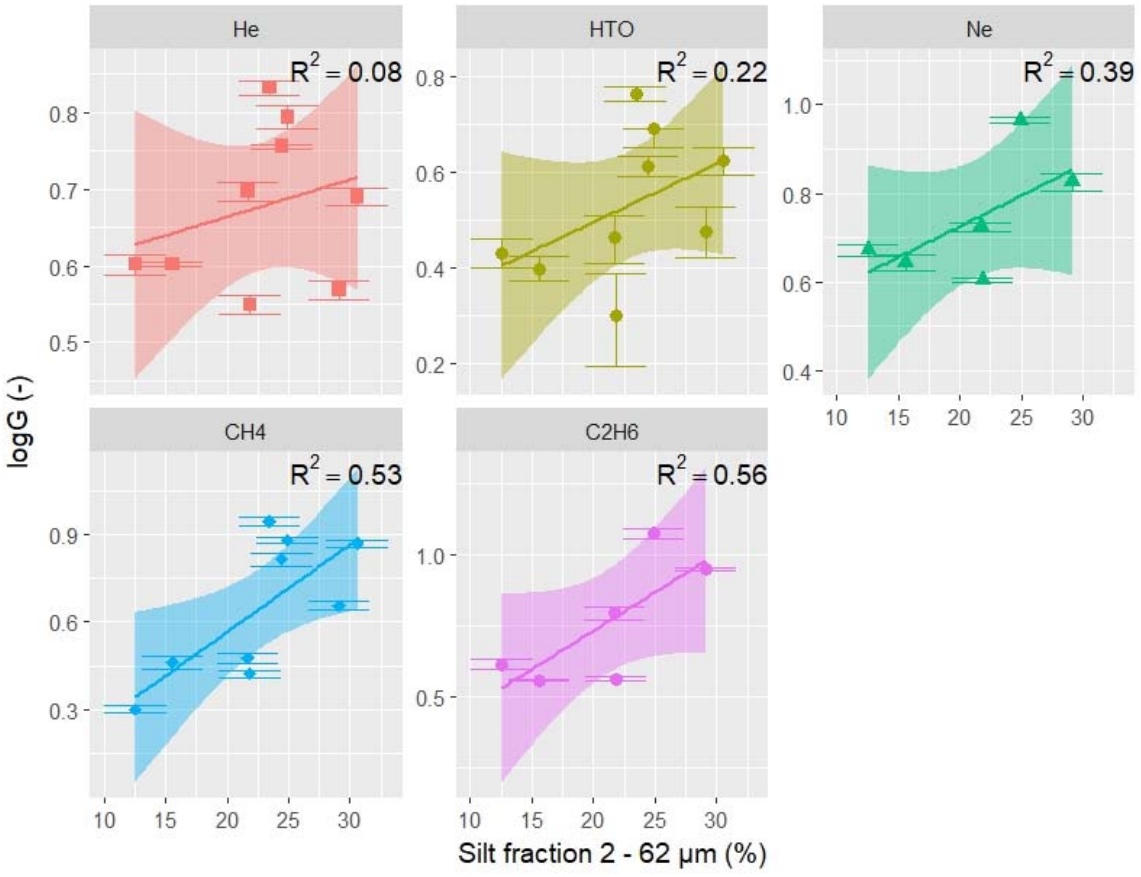
He
$R^2 = 0.08$
HTO
$R^2 = 0.22$
Ne
$R^2 = 0.39$
CH4
$R^2 = 0.53$
C2H6
$R^2 = 0.56$
logG (-)
Silt fraction 2 - 62 µm (%)

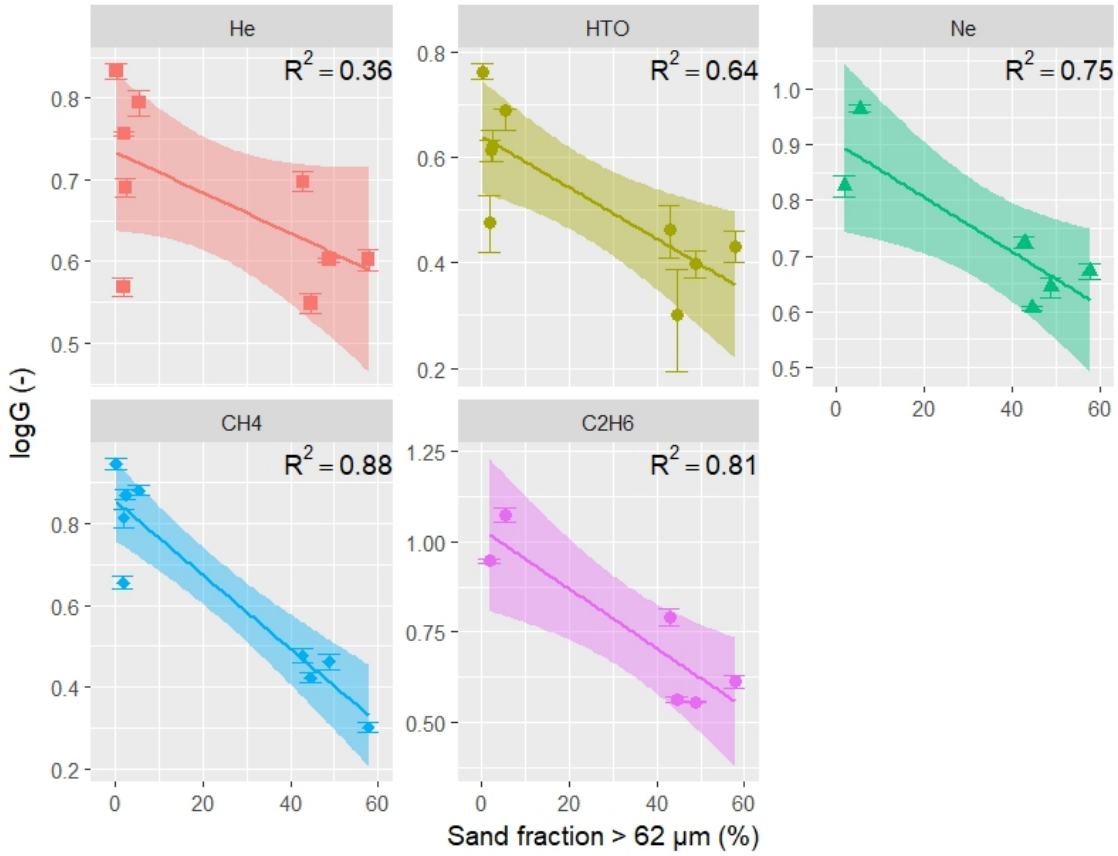

Figure 39: Relationship between the geometric factor (logG) and the grain size distribution (clay fraction – top, silt fraction – middle, sand fraction – bottom)

As the mineralogy is very strongly correlated with the specific surface area, the geometric factor is also correlated with the specific surface area: *G* increases with an increasing specific surface area (Figure 40). Similar observations are made for the volume of micro pores: the more micro pores, the more a gas is hindered in its transport, and the larger G (Figure 41). This is especially clear for the larger gases (CH_4 and C_2H_6) as these are most hindered in the micro pores, while the smaller gases are hindered less.

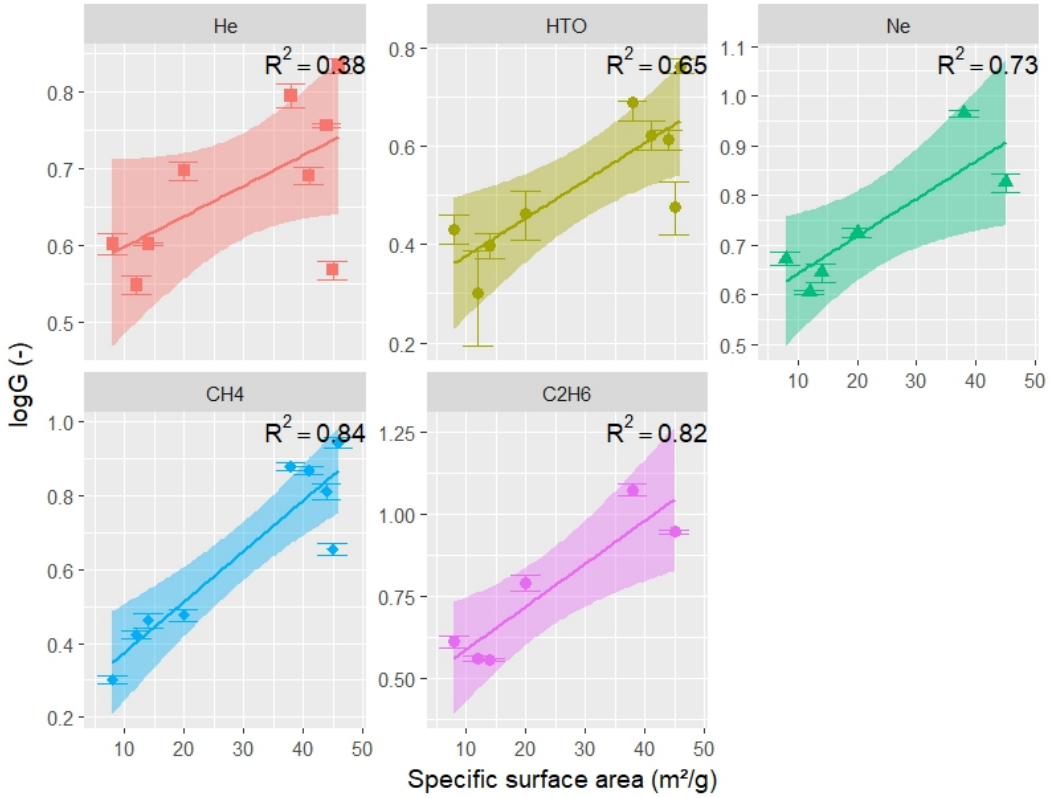

Figure 40: Specific surface area vs log*G* for samples of the Boom Clay and Eigenbilzen Sands

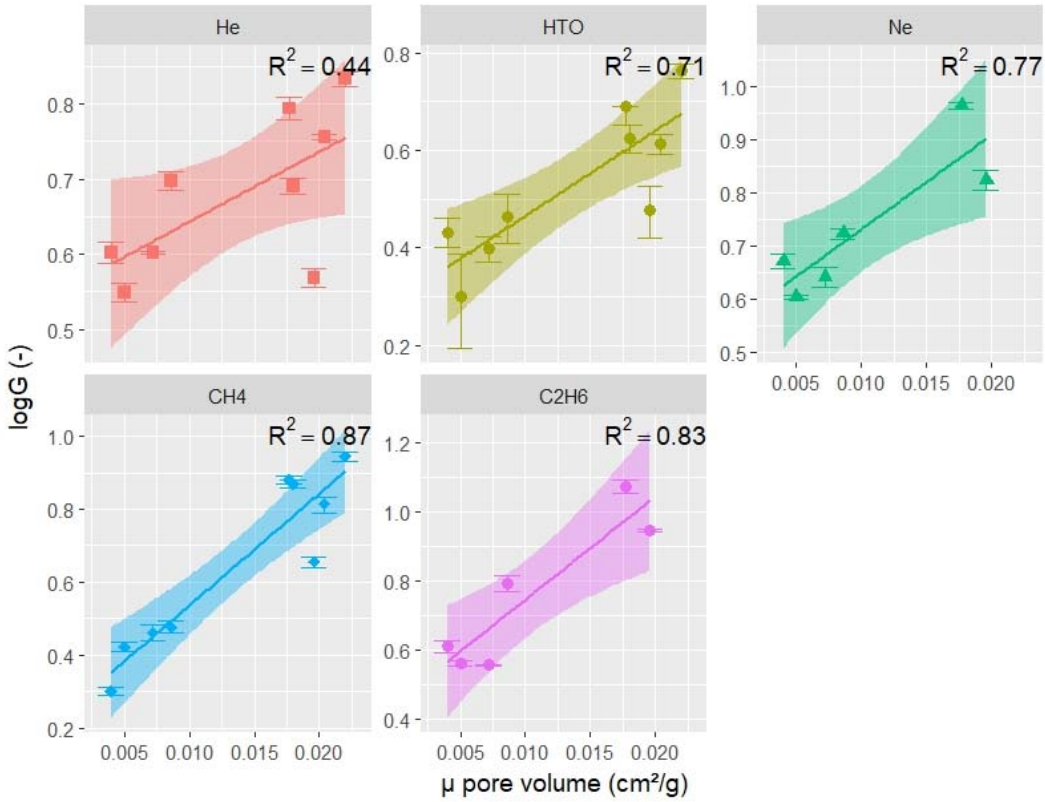

Figure 41: Volume of micro pores vs log*G* for samples of the Boom Clay and Eigenbilzen Sands

4.6.6 Correlation between diffusivity and hydraulic conductivity

Hydraulic conductivity and diffusivity are two important transport parameters, and we expect them to be related to each other (Boving and Grathwohl, 2001). As shown in previous paragraphs, both parameters are also related to the composition of the samples. In case of the Boom Clay, hydraulic conductivity is related to the content of quartz and clay minerals (see earlier).

However, in previous work (Aertsens et al., 2004 and 2005; Jacops et al., 2017a) this relationship was not clear: variations in hydraulic conductivity were observed (about one order of magnitude) between different samples of the ON-Mol-1 drilling, but they appeared to have no effect on diffusivity. Nevertheless, this statement needs to be taken with care since Aertsens et al. (2005) measured dispersion coefficients (using an advective component in the experiment) instead of diffusion coefficients. So, for Boom Clay, the effect of variations of the clay and silt content on diffusivity remained unclear.

When looking at the evolution of diffusivity (D_{eff}) as a function of hydraulic conductivity, in general, we observe a weak correlation (~0.06) and high p-values between K and D_{eff} and a moderate correlation (~0.38, from Figure 16) with low p-value (< 0.05) between logK and logD_{eff}: when the hydraulic conductivity increases, also diffusivity increases (Figure 42). This is even more clear when looking at each individual diffusing molecule: for all molecules we observe a general increasing trend and the correlation is strong to very strong.

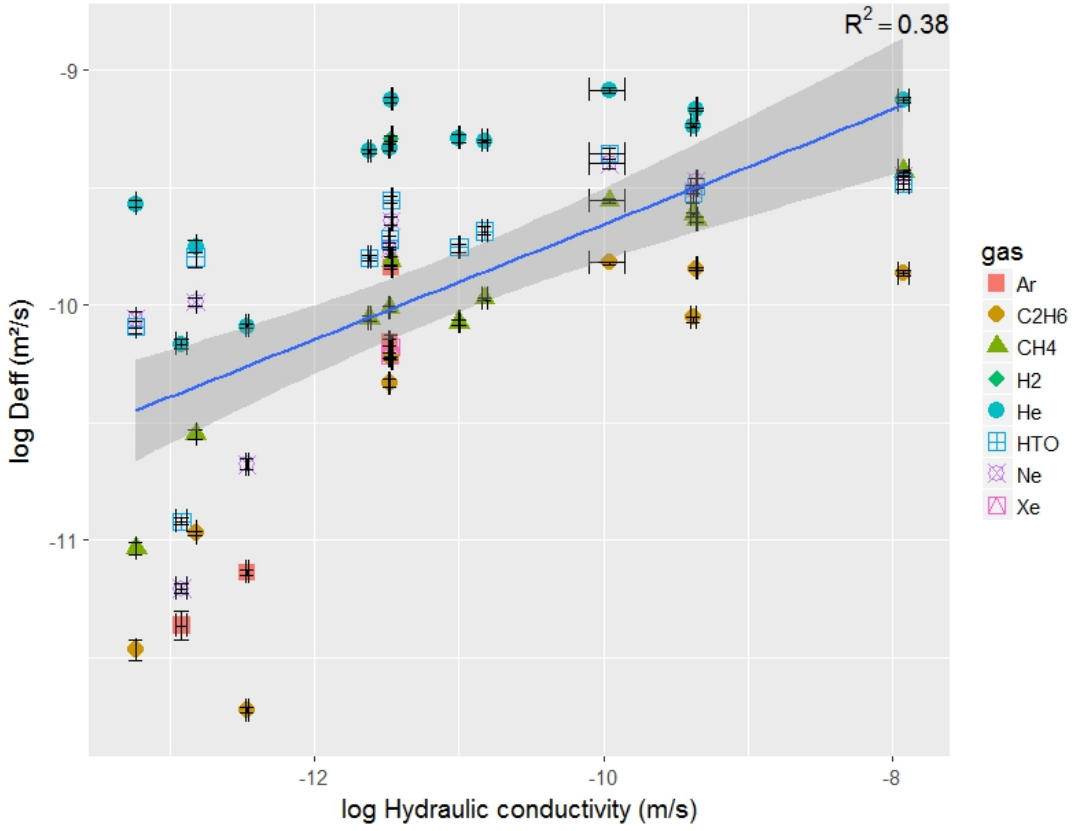

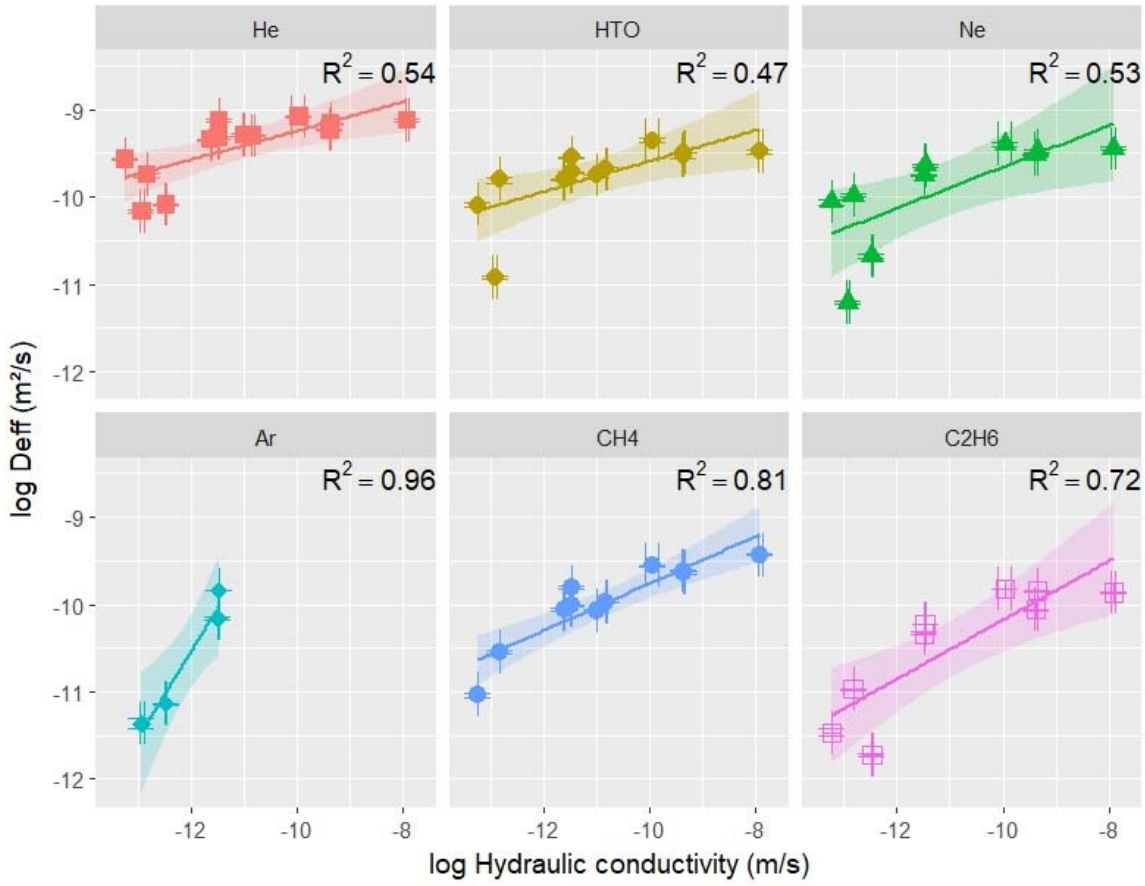

Figure 42: Relationship between diffusivity and hydraulic conductivity in all clayey samples, with the data points (logK vs $logD_{eff}$) plotted all together (top) and for each individual diffusing molecule (bottom).

Similar observations on clayey materials are scarce in literature. Some data are available for other materials such as sandstone, limestone rock and concrete. Boving and Grathwohl (2001) measured diffusivity and hydraulic conductivity for several limestone and sandstone samples with a variable porosity in which they proposed a relation between porosity and diffusivity which is based on Archie's law. Besides, an increase in K leads to an increase in diffusivity (observed for iodide) but the relation is very scattered. According to their explanation, such a poor relationship has to be expected since hydraulic conductivity depends mainly on the pore sizes, whereas diffusion (according to their results) depends on the total porosity of a rock. Based on our data, this statement needs to be revised. For almost all samples of the Boom Clay and the Eigenbilzen Sands, the porosity is very similar (around 38%). Also both bentonite samples have a similar porosity (around 40%), but the diffusion coefficient of C_2H_6 in bentonite (1.6 g/cm³) is two orders of magnitude smaller compared to Boom Clay samples. So probably also for diffusivity, the pore size distribution is a key factor determining the diffusivity of the sample. This will be further discussed in §4.7 and 4.8.

When zooming in to the Boom Clay and Eigenbilzen Sand samples (Figure 43), we also observe the increase of diffusivity with increasing hydraulic conductivity and again the correlation is strong to very strong. We also observe that despite a variability of K over 3 orders of magnitude, D_{eff} varies much less, e.g. only with a factor 4 for CH_4. This difference can be explained by the fact that the difference between the hydraulic conductivity of sand and compacted clay is about ten orders of magnitude, while the difference between e.g. the self-diffusion coefficient of tritiated water (diffusion in free

water, 2.22 x 10^{-9} m^2/s; (Boudreau, 1997)) and the HTO diffusion coefficient in Boom Clay is only about one order of magnitude.

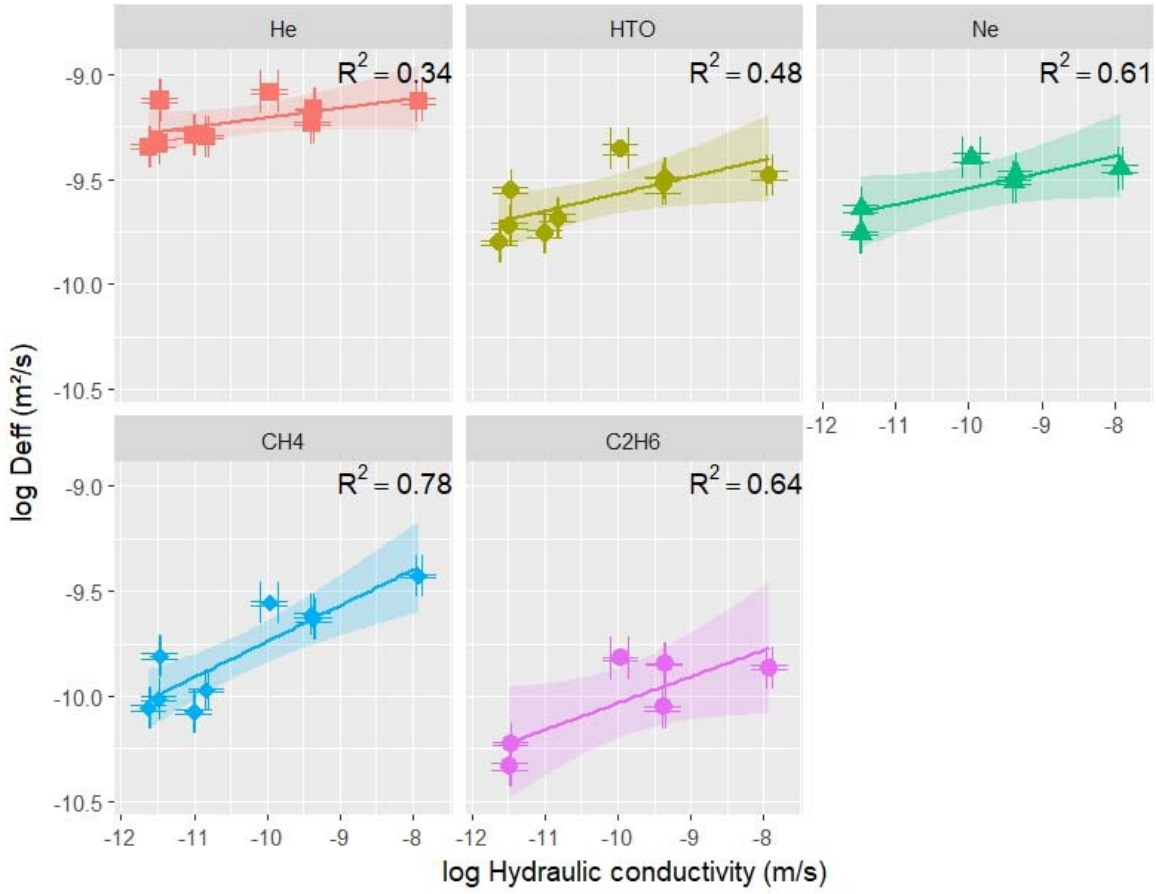

Figure 43: Evolution of diffusivity with hydraulic conductivty for different gases and HTO in the Boom Clay and Eigenbilzen Sands

4.6.7 Can the correlation between the petropysical and the transport properties be used to estimate transport properties?

The previous sections have shown that some of the petrophysical properties of clay-containing samples show a good correlation with some of the transport properties of these samples. A good example is the correlation between logK and both the mineralogy and grain size distribution. Figure 44 shows the correlation coefficients (value for R, not R^2!) between the different variables, plots of the datapoints (graphs with black dots) and the Kernel density estimation (lines). This Kernel density estimation estimates the probability density function of a variable: e.g. if the density of data points is high, the curve shows a peak. More information can be found in Parzen (1962).

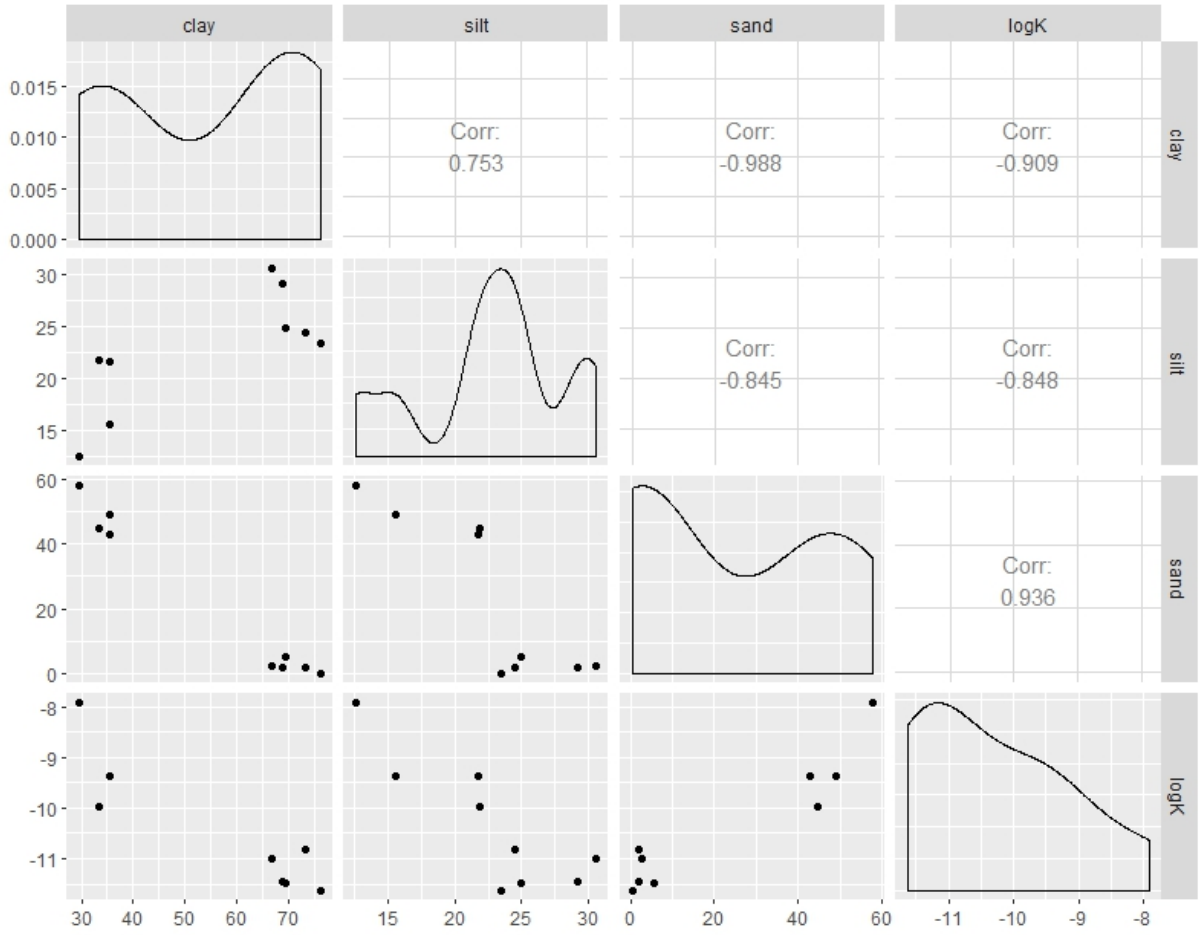

Figure 44: correlation between logK and the grain size distribution for the samples of the Boom Clay and the Eigenbilzen Sands

Given the good correlation and the low (< 0.05) p-values, logK (and thus K) can be estimated based on these petrophysical parameters. This was tested for the samples of the Boom Clay and the Eigenbilzen Sands. Different fits were performed, a first one for the dataset containing all the samples of the Boom Clay and Eigenbilzen Sands, which provides an equation which can be used to estimate K of other samples. Next, also fits were performed with all data, except K2 in fit 2 and K14 in fit 3 (Table 19). These fits were used to estimate logK (hence K) for K2 (fit 2) and K14 (fit 3) by using the grain size data as input and the results are shown in Table 20. For both samples, the measured and estimated K values differ by a factor 3. Similar approaches were performed for the same samples, using the mineralogical composition as input, and a combination of mineralogy and grain size distribution, but the results were less good (up to a factor 11 difference between the measured and estimated data). Hence, these results have not been taken up.

Table 19: fits for logK and the grain size distribution, performed for all data from the Boom Clay and Eigenbilzen Sands, and when leaving one sample at a time aside (first K2, next K14). x_1 is the % of clay, x_2 the % of sand

all samples BC +EZ	**logK = -14.6 + 0.043 x_1 + 0.083 x_2**
all samples BC +EZ, no K2	logK = -15.1 + 0.051 x_1 + 0.087 x_2
all samples BC +EZ, no K14	logK= -15.6 + 0.057 x1 + 0.096 x_2

Table 20: comparison between the estimated and measured K for 2 samples

	K2	K14
measured value K (m/s)	3.3E-12	4.4E-10
estimated value (m/s)	9.3E-12	1.4E-09
ratio	3	3

Probably also the geometric factor and the effective diffusion coefficient can be estimated based on the petrophysical properties of the samples. But as shown previously, the correlation strongly depends on the type of gas. Hence the analysis is not that straightforward, and has not been taken up in this thesis.

When looking at all the different data points and all results shown in section 4.6, it is clear that many parameters have an influence on K and D_{eff}. However, most of the petrophysical parameters are also correlated with each other, and also the two transport parameters are correlated. In order to investigate which parameters are the most important ones, a principal component analysis was performed (Figure 45). A principal component analysis is a multivariate analysis method, used to describe a large data set by a smaller number of variables, which are named the principal components. So it makes a distinction between the more and the less important variables. More detailed information can be found in Pearson (1901). Figure 45 shows the principal component analysis of our data set. On the arrows to the left, we find logK, quartz and sand. As their length is similar, they are of the same importance and positively correlated with each other. In the opposite direction, we see clay fraction, silt fraction, all clay minerals, 2:1 clay minerals and SSA. As also these arrows have a similar length, they are of the same importance. As they are in the opposite direction of the group of "quartz", the variables in both groups are negatively correlated (e.g. quartz is negatively correlated with all clay minerals). The correlation of both groups with D_{eff}, $\log D_{eff}$, G and logG is less good, which is due to use of different gases. If both groups would be perpendicular, there would be no correlation. As this is not the case, we can observe lower correlation between D_{eff} (and $\log D_{eff}$) and the "quartz" group and between G and logG and the "clay" group. One can also observe that, as disucced above, the correlation is better for logK than for K (shorter arrow, not in line with the others).

In general, it is still unclear with variables are moest important, and it confirms earlier statements: most of the petrophysical parameters are correlated (arrows in similar or opposite direction) with each other and with K, but the correlation with D_{eff}/$\log D_{eff}$/G/logG is less good. Hence a more in depth analysis is needed.

In theory, we should be able to estimate the transport properties based on some of the petrophysical properties. Given the complexity of this analysis, the existing correlations and the lack of knowledge, this topic is not studied in more detail in this thesis.

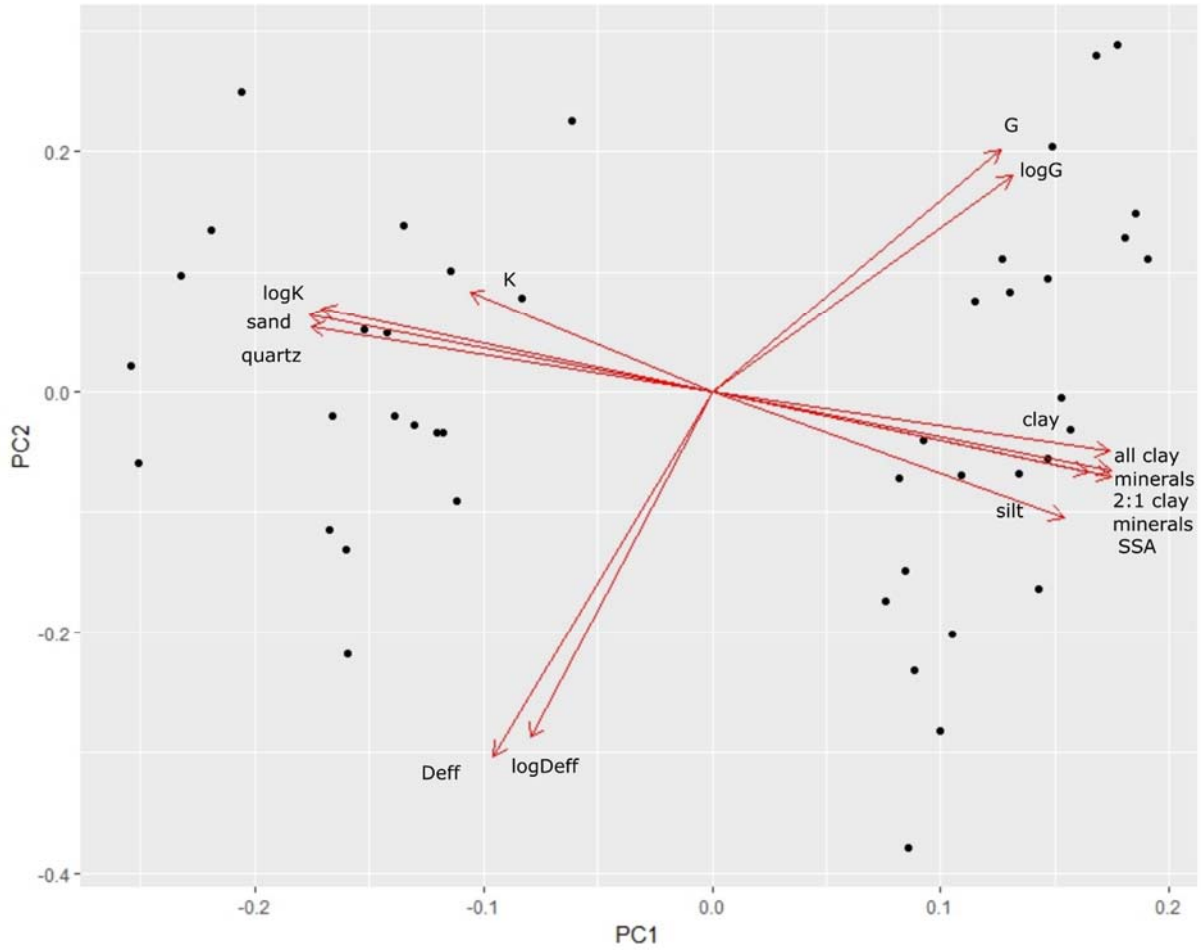

Figure 45: principal component analysis of the full dataset

4.7 Description and comparison of some of the petrographical properties of the different samples of the Boom Clay and Eigenbilzen Sands

In the next section, the petrographical and petrophysical properties will be discussed for the three different sample groups (Putte & Terhagen Member, Boeretang Member and Eigenbilzen Sands).

A very detailed description of some of the petrophysical and petrographical properties of the different samples of the Boom Clay and Eigenbilzen Sands can be found in annex 4, and a detailed description of the used techniques is given in annex 2. A summary of the properties is given in Table 21. The different techniques which have been used are considered to be complementary. The composition of the samples (mineralogy with quartz and the 2:1 clay minerals as main mineral phases, and the grain size distribution) was derived from XRD analyses and grain size distribution measurements. By performing nitrogen adsorption experiments, the specific surface area was obtained, but also information on the pore size distribution (1.5 - 250 nm) and the volume of micro pores could be derived. In order to obtain more information on the micro structure of the samples, CT and µCT scanning was performed and thin sections were studied. In general, the resolution of the CT is too high to obtain detailed information on the micro structure. More detailed information was acquired from the µCT scans, where (depending on their size) pores and zones with increased porosity and their connectivity could be visualised. Studying thin sections allowed us to visualise the distribution of the different mineral phases. In order to get a clear view on the structure of our samples, all petrophysical and petrographical data have to be combined.

Table 21: Overview of the petrophysical and petropgraphical properties of the different samples

	K2	K4	K9	K10	K11	K14	K15	K16	K17
Quartz (%)	31	28	26	32	33	59	58	60	54
2:1 clay minerals (%)	34	41	46	32	39	20	18	21	27
Clay fraction (%)	70	69	76	73	67	36	33	30	35
Silt fraction (%)	25	29	23	24	31	16	22	13	22
Sand fraction (%)	5	2	0	2	3	49	45	58	43
SSA (m^2/g)	38	45	46	44	41	14	12	8	20
Visual observation		Pyrite nodule		Pyrite nodule Silty texture	Silty texture	Less consistent	Less consistent	Less consistent	Bit more consistent
CT	Pyrite filaments	Pyrite filaments and a nodule	Thick pyrite wire and some filaments	Pyrite filaments	Pyrite filaments	Less pyrite, local spots. Very large nodule	Less pyrite, local spots	Less pyrite, local spots. Black spots: pores	Less pyrite, local spots

µ-CT	Many pyrite filaments and nodules	Many pyrite filaments and nodules	Many pyrite filaments and nodules	Many pyrite filaments and nodules. Darker zones: increased porosity around quartz grains	Many pyrite filaments and nodules. Darker zones: increased porosity around quartz grains	Less pyrite: framboids. Many quartz grains. Darker grey patches: clayey zones with micropores. Black spots: pores	Less pyrite: framboids. Quartz grains. Darker grey patches: clayey zones with micropores. Black spots: pores. More than in other samples, and running over full length	Less pyrite: framboids. Quartz grains. Darker grey patches: clayey zones with micropores – more than in the other samples. Black spots: pores	Less pyrite: framboids. Many quartz grains. Darker grey patches: clayey zones with micropores. Black spots: pores
µ-CT 3D "pores"	Local spots, not connected	Local spots, not connected	Local spots, not connected	Interconnected zones, looking like wormholes	Interconnected zones, looking like wormholes	In clayey patches (bit) and around quartz grains (mainly). Visible pores not connected	In clayey patches and around quartz grains (mixed). Visible pores connected	In clayey patches (mainly) and around quartz grains. Visible pores not connected	In clayey patches (mainly) and around quartz grains. Visible pores connected

Thin sections (LM)	Homogeneous clay matrix, quartz grains regularly distributed	Homogeneous clay matrix, quartz grains regularly distributed	Homogeneous clay matrix, quartz grains regularly distributed	Clusters of quartz, linked to wormholes. Interparticle porosity	Clusters of quartz, linked to wormholes. Interparticle porosity.	Large quartz grains, large pores. Least clayey	Large quartz grains, large pores. Many clayey zones, a lot of bioturbations	Large quartz grains, large pores. Strongly bioturbated	Large quartz grains, large pores. Strongly bioturbated. Most clayey
Thin sections scan	Very clayey, some more quartz grains	Still clayey and more quartz grains	Most clayey, some quartz grains	Less clayey than K11, but more and larger quartz clusters	More clayey than K10, less and smaller quartz clusters	Mainly quartz, little clay	Some clay bands	Some clay bands. Framboidal pyrite	Most clayey. More pyrite
Pore size distribution	Less pores than K4+9	Many pores	Many pores	More pores than K11	Less pores than K10	Middle pores of this group	Middle pores of this group	Least pores of this group	Most pores of this group

Samples of the Putte and Terhagen Member

The main mineral phases are the 2:1 clay minerals (> 34%) and quartz (< 31%), while the grain size distribution is dominated by the clay (> 69%) and the silt fraction (< 29%). Given the large amount of (swelling) clay minerals, the specific surface area is also high (> 38 m^2/g). On the CT and µ-CT images, only pyrite (filaments and nodules) is visible, and no distinction can be made between the main mineral phases quartz and clay (Figure 46). They are clearly below the resolution of the applied technique (16 µm for µCT). When the darker zones (less dense material, so potential increased porosity) are filtered out of the µ-CT images and reconstructed in 3D, only local spots with increased porosity become visible (Figure 47).

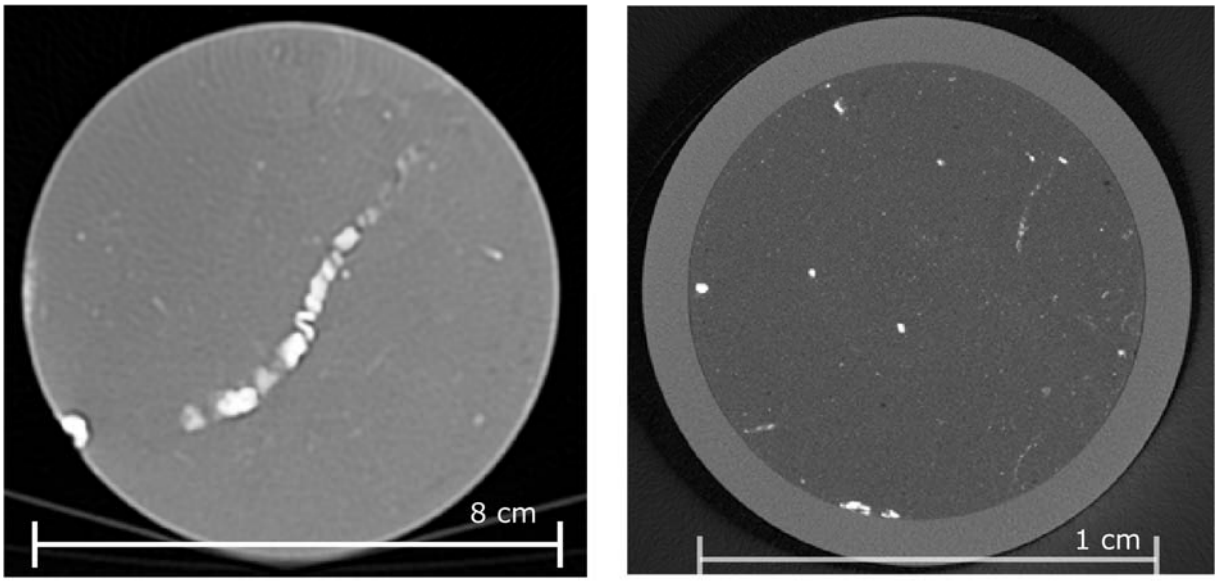

Figure 46: CT and µCT image of sample K9, showing mainly pyrite. The main mineral phases(clay and quartz) cannot be distinguished

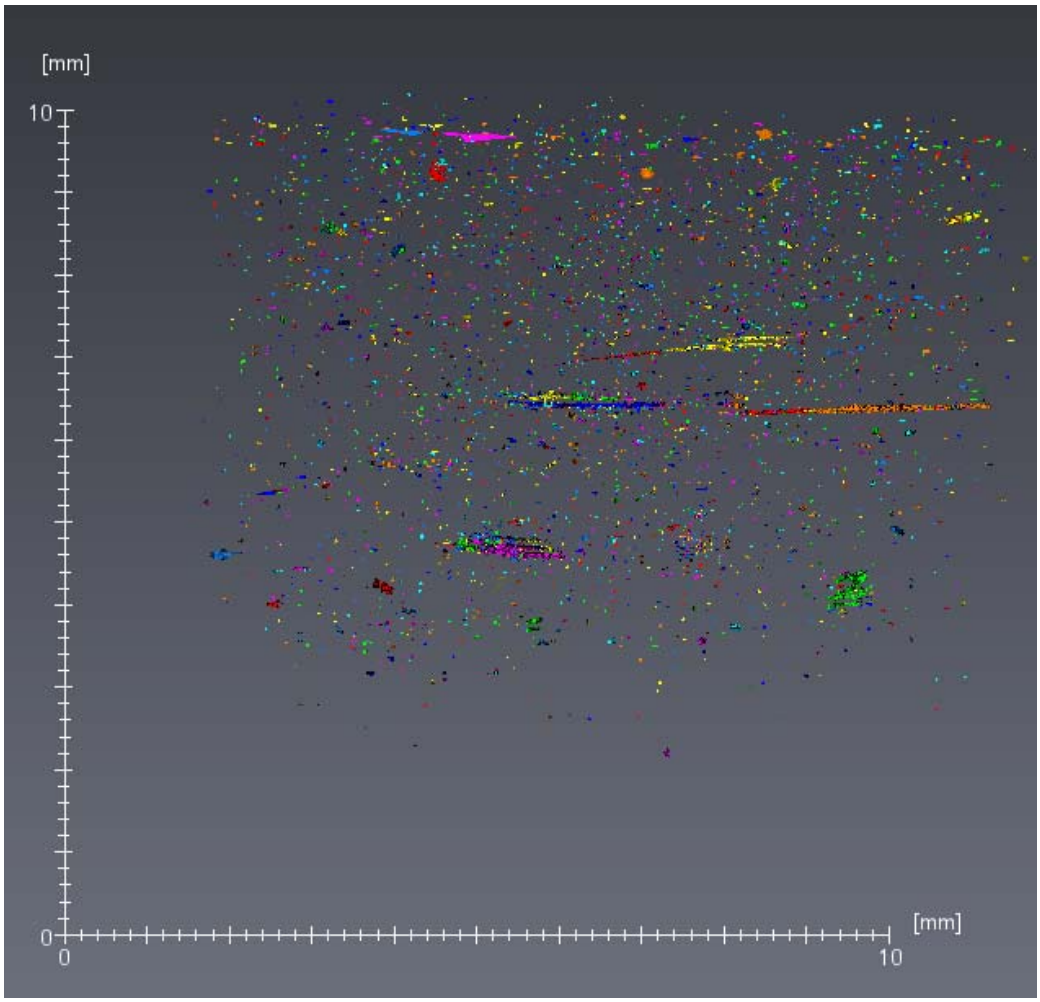

Figure 47: Reconstructed µCT image of sample K9, with zones with higher grey value (hence higher porosity) indicated in color.

Visual inspection of the thin sections (Figure 48) shows that sample K9 is the most clayey. This sample also possesses the largest amount of 2:1 clay minerals and the largest clay fraction. Sample K4 looks the least clayey, though this sample has not the lowest amount of clay minerals or the smallest clay fraction, but it has the largest silt fraction. When studying the thin sections under the microscope (Figure 49), the previous observations are confirmed: sample K9 is the most clayey sample, while especially sample K4 contains more quartz grains. Though, the latter is not confirmed by the mineralogical composition. The general appearance of the thin sections of these clayey samples matches well with the observations for similar samples in Adriaens et al. (2016). When looking at the pore volume distribution (volume of micro pores, range 1.5 -250 nm, Table 6), samples K4 and K9 have the largest pore volume while sample K2 has a smaller pore volume. This observation corresponds to a difference in mineralogy as K2 contains less 2:1 clay minerals, which can be explained by the fact that pores in the range 1.5 to 250 nm are mainly located in the clay phases, hence less clay minerals will lead to smaller pore volumes in this range.

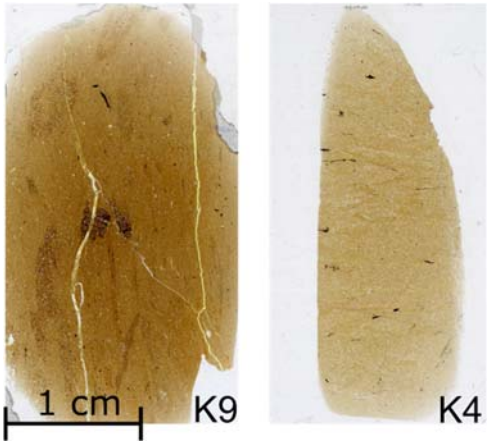

Figure 48: Scanned thin sections of samples K9 (left) and K4 (right)

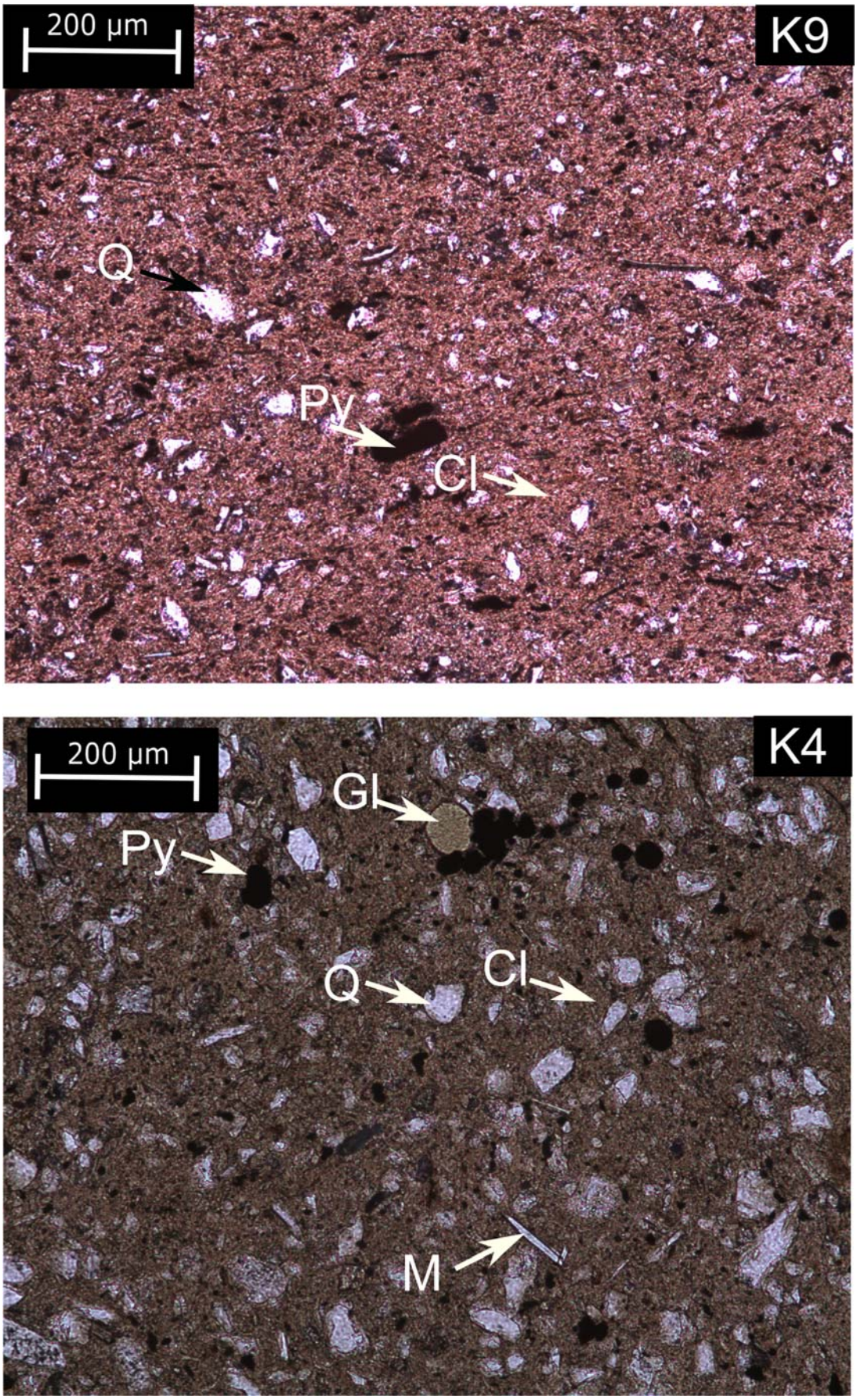

Figure 49: Thin sections of sample K9 (top) and K4 (bottom) with transparent quartz grains (Q) floating in a clay matrix (Cl), with local mica platelets (M) and glauconite grains (Gl). Black spots corresponds to framboidal pyrite (Py)

Samples of the Boeretang Member

The mineralogical composition and grain size distribution of the samples of the Boeretang Member is very similar to the samples of the Putte and Terhagen Members. From that point of view and despite our initial assumptions, the samples of Boeretang Member cannot be considered to be more silty than the samples of the Putte and Terhagen Member. CT images are very similar to those shown in Figure 46 and are not shown here. Some differences can be observed within the µ-CT images: within the clay matrix, darker zones can be observed (e.g. zones enriched in silt/sand). When these zones (expected to have a higher porosity) are filtered out and reconstructed in 3D, they are highly connected, spread all over the sample and have the appearance of former wormholes (Figure 50).

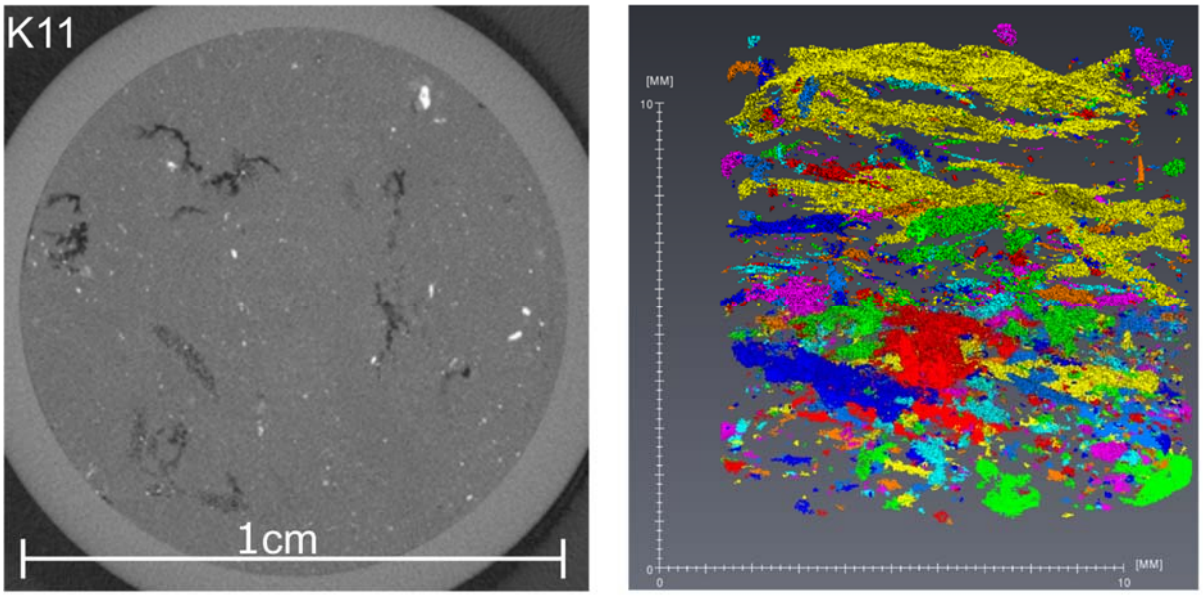

Figure 50: µCT image (left) and reconstructed 3D-µCT image of sample K11. In the reconstructed image, zones with a higher porosity are indicated in different colours and connected pixels received a similar colour

Visual inspection of the thin sections and comparison with the samples of the Putte and Terhagen Member (Figure 48) shows an increased quartz content, with quartz grains grouped into clusters (Figure 51). Compared to sample K10, sample K11 has the most clayey appearance (and less quartz), which matches with the mineralogical composition but not with the grain size distribution of both samples. Moreover, sample K10 seems to be more heterogeneous. When studying the thin sections under the microscope (Figure 52), the observations are very similar: the quartz and clay minerals are heterogeneously spread over the sample, and the quartz grains are grouped into clusters. In some of these clusters, interparticle porosity can be observed. As the quartz clusters are often associated with pyrite, this is another indication that the quartz clusters are linked to former wormholes. Indeed the pyrite framboids preferentially accumulate at former places where organic matter existed and in wormholes, organic slime was sticking to the wall to keep the holes temporary open. Hence, the µCT images and the thin sections are complementary.

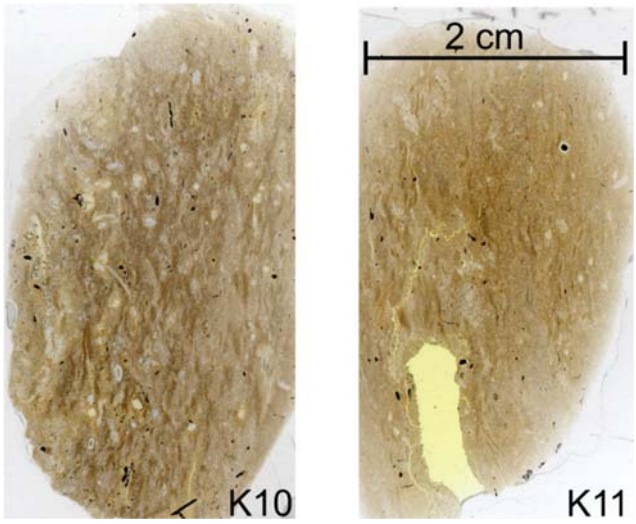

Figure 51: Scanned thin sections of samples K10 (left) and K11 (right). Sample K11 has a more clayey appearance, while in sample K10 the quartz grains seem to be more abundant and grouped into clusters. Hence, sample K10 has a more heterogeneous appearance.

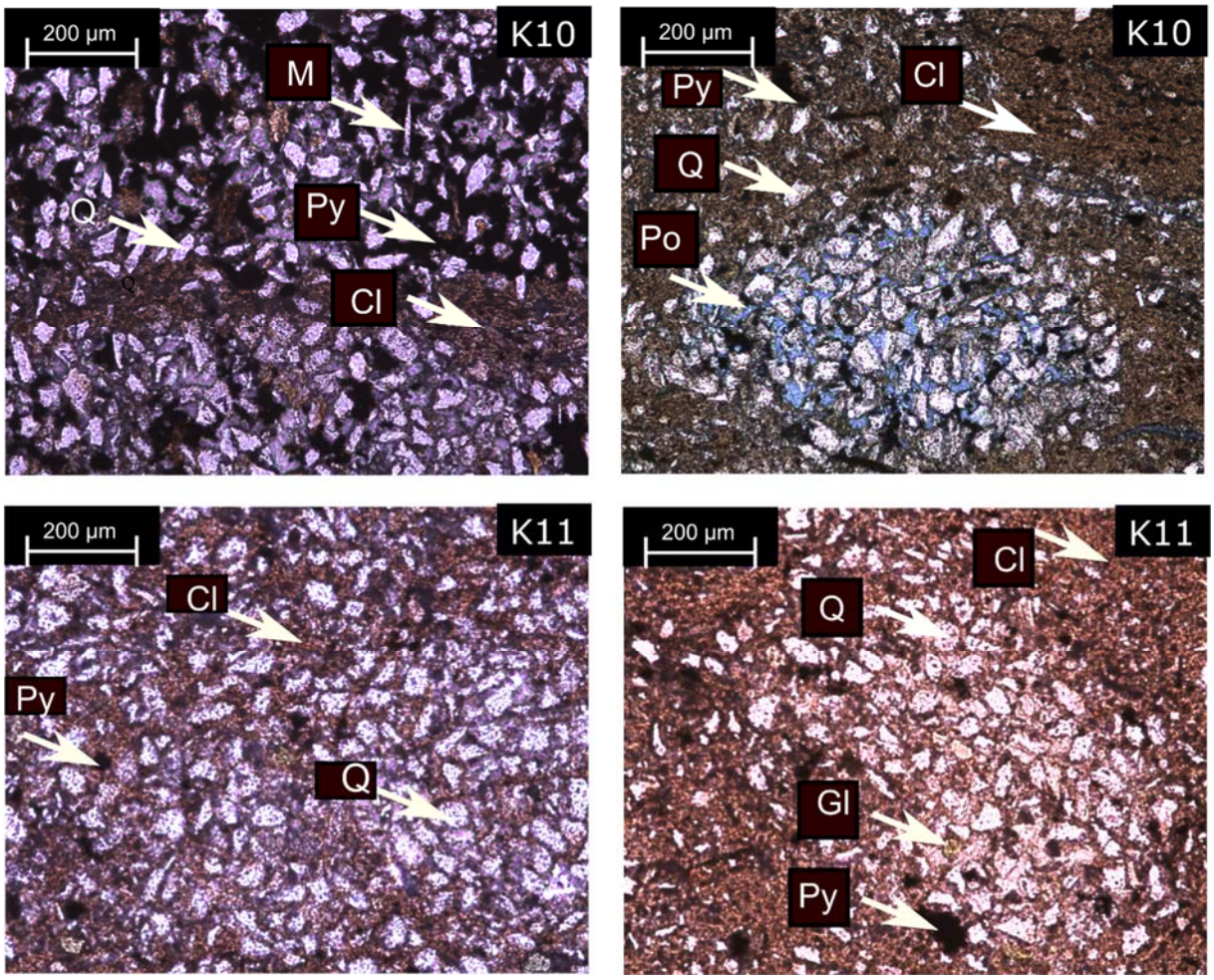

Figure 52: Transmitted light microscopy images of thin sections of samples K10 (top) and K11 (bottom). All images show the grouping of quartz grains, and often these quartz clusters are accentuated by the presence of pyrite. In the upper right image the blue epoxy between the quartz grain indicates intergranular porosity.

Similar observations for thin sections of samples of the Boeretang Member can be found in Adriaens et al. (2016). The pore volume distribution (Table 6) shows that K10 has a larger pore volume in the

range of 1.5 – 250 nm compared to K11, which is opposite to what one would expect from the mineralogy. This observation could partly be explained by a lower porosity of K11 (34% vs. 39 % for K10). Both samples have a lower pore volume compared to the more clayey samples of the Putte & Terhagen Member (K4 and K9) and this can not only be explained by small differences in mineralogy. Probably, because of the heterogeneous distribution of the quartz grains and the presence of interparticle porosity, there is a larger proportion of macro-pores, hence a smaller fraction of micro- and meso-pores.

Another section of core ON-Mol-1 48 (the c-section, whereas we used the a-section) has been studied in detail by Hemes et al. (2013), using BIB-SEM (broad ion beam scanning electron microscopy) and the results were compared with those of more clayey samples. The observations, described by Hemes et al. (2013) are very similar to this work. For the clayey samples, they describe a dominance of the clay matrix, containing mainly small pores, whereas the coarser samples such as core 48a (in Hemes et al. (2013) referred to as sample EZE52) are dominated by larger non-clay minerals (mainly quartz), a larger amount of inter-aggregate pores (which we named interparticle pores) and much less clay in between the clasts (Figure 53). Hemes et al. (2013) also suggest that for clay-rich samples, the overall porosity is mainly located in the clay matrix (small pores) whereas for the more silty samples, the larger (inter particle) pores contribute more to the total visible porosity. This is confirmed by pore counting: the obtained results indicate that many of the pores are located within the clay matrix, but their proportion depends on the sample type. For instance, for the clayey samples 85-88 % of the BIB-SEM visible porosity was found in the clay matrix, while this was only 33-40 % for sample EZE52 (core 48). To the contrary, interparticle pores account for 60 % of the porosity in sample EZE52 (core 48), but for only 11 – 14 % of the pores in the clayey samples.

All the observations described in Hemes et al. (2013) correspond very well to the petrographical descriptions in this work. Therefore, all techniques (CT, μ-CT, N2-BET and BIB-SEM) are complementary and provide essential pieces of information.

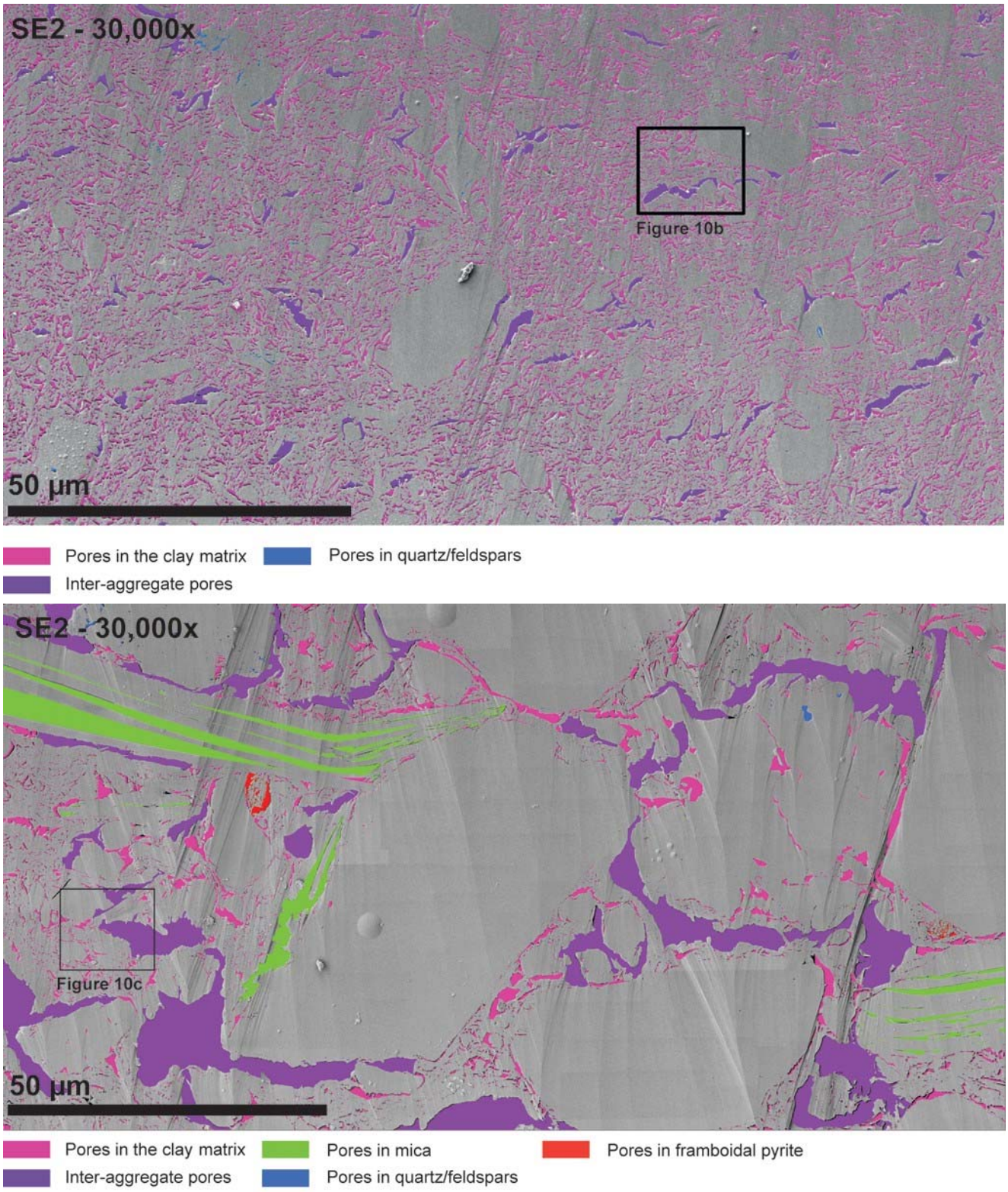

Figure 53: Microstructural overview of sample EZE55 (top, clayey) and EZE52 (bottom, more silty). Sample EZE52 is taken from core 48 from which K10 and K11 were also taken. The images are obtained with a scanning electron microscope using the conventional SE (secondary electron) dectector. Figures taken from Hemes et al. (2013).

Samples of the Eigenbilzen Sands

The samples of the Eigenbilzen Sands have a different composition compared to those of the Boom Clay. They contain mainly quartz (> 54%) and less 2:1 clay minerals (< 27%). When looking at the grain

size distribution, the sand fraction is dominant (> 43%) and the clay fraction is reduced to less than 36%. When looking at the CT images, one observes in general less pyrite (only few filaments and nodules), but sample K14 shows a very large pyrite nodule which is about 2 cm in diameter (Figure 54). All samples show some darker patches, which are likely zones with a higher porosity and sample K16 even shows pores (in black) which are spread all over the sample. Due to the smaller clay content, most samples have been deformed during the unloading and scanning process. Sample K17 shows no deformation, which might be related to the composition of the sample (largest clay content, lowest quartz content).

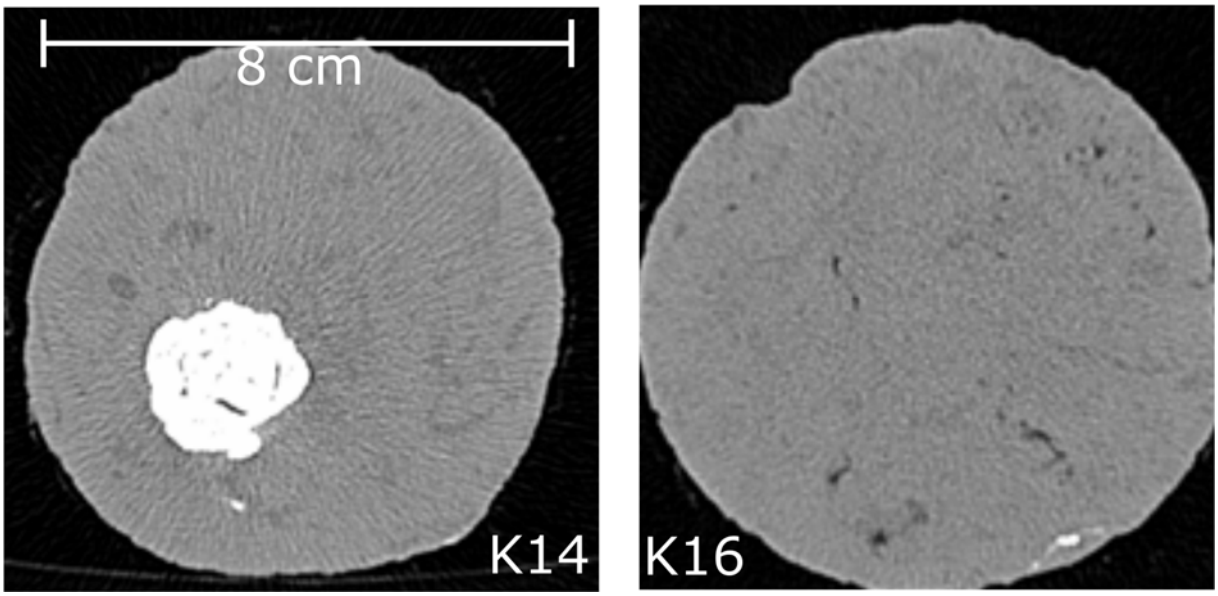

Figure 54: CT images of samples K14 (left) and K 16 (right). K14 shows a large pyrite nodule (white spot), and in both samples darker patches can be observed (zones with larger porosity). In sample K16, pores (in black) are observed all over the sample.

On the µ-CT images, the quartz grains can be clearly observed, and similar to the CT images also darker patches (increased porosity – probably micro pores in the clayey patches) and pores can be detected (Figure 55).

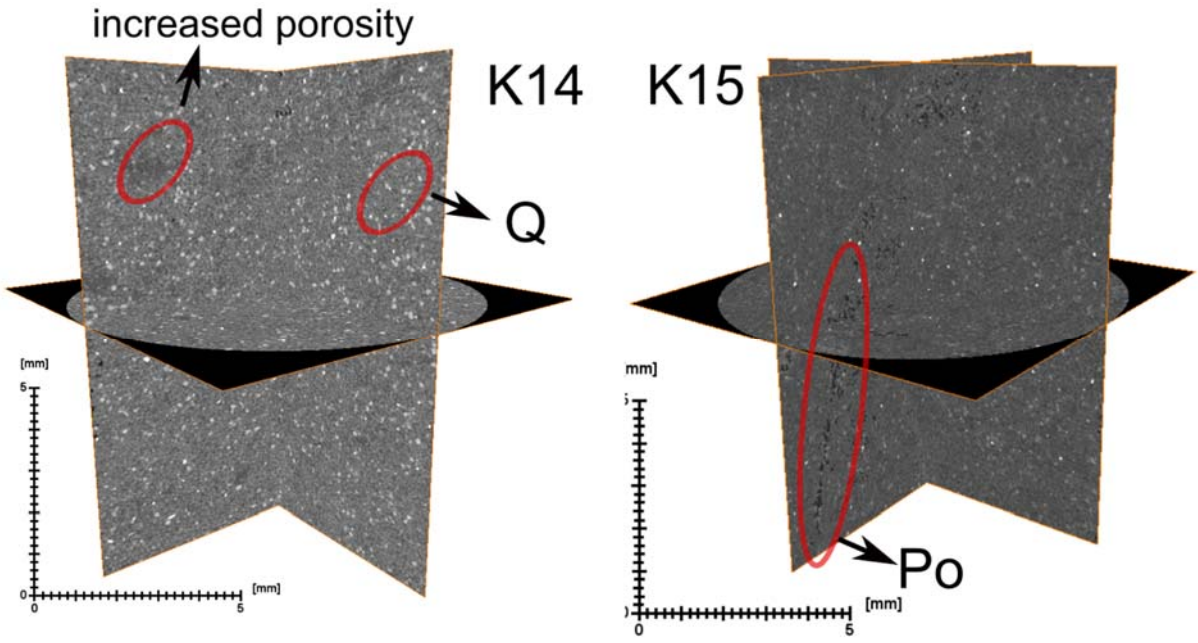

Figure 55: Orthogonal projection of µCT images of sample K14 (left) and K15 (right). Both samples show clearly the presence of quartz grains(white, Q), as well as darker patches with increased porosity and sample K 15 shows pores (in black, Po)

When filtering out the zones with increase porosity, one can observe that the porosity is mainly located around the quartz grains and/or in the clayey zones (micro pores). Figure 56 shows the zones with increased porosity in blue and the difference between both samples is clear: for sample K14, the porosity is mainly located around the quartz grains while for sample K17 it can be found in the clayey zones. Notice that similar observations can be made for the 3D reconstructed images (not shown here, but in annex 4). These observations match with the mineralogical composition and grain size distribution: sample K14 is more sandy (more quartz, less clay minerals, larger sand fraction) while sample K17 is more rich in clay and silt.

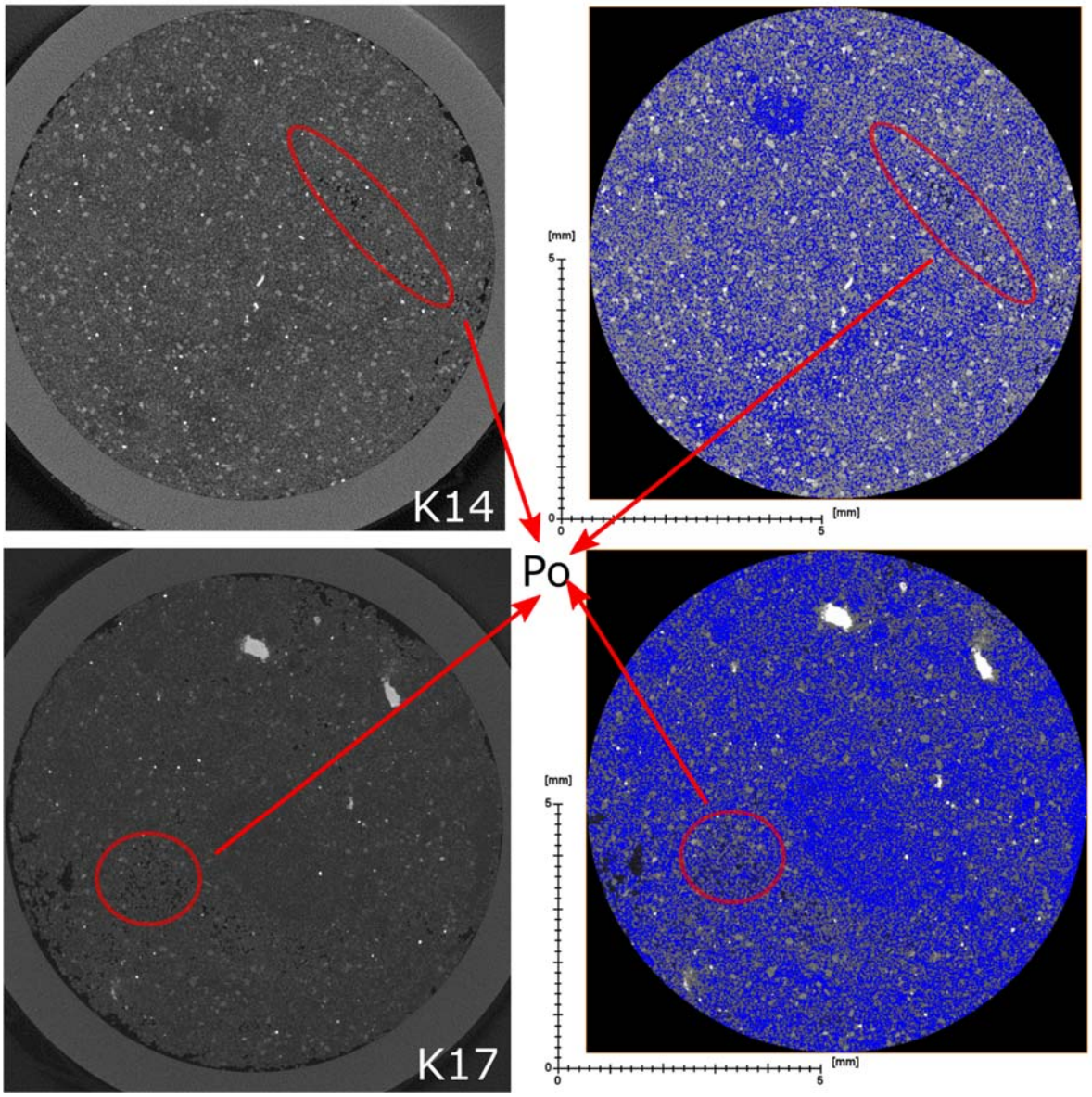

Figure 56: Comparison between an unprocessed image, and an image where the darker zones (increased porosity) are indicated in blue. Top: sample K14, slice 347 and bottom: sample K17, slice 1414. Localised pores (in black, Po) are not taken into account in the processed image.

Figure 57 shows the scanned thin sections of samples K14 and K17. Sample K17 is the most clayey sample as it contains a lot of brown zones which are rich in clay, while sample K14 is the most sandy sample (only very small, hardly visible brown zones). The differences between both samples are also observed within the mineralogy, grain size distribution and µCT images.

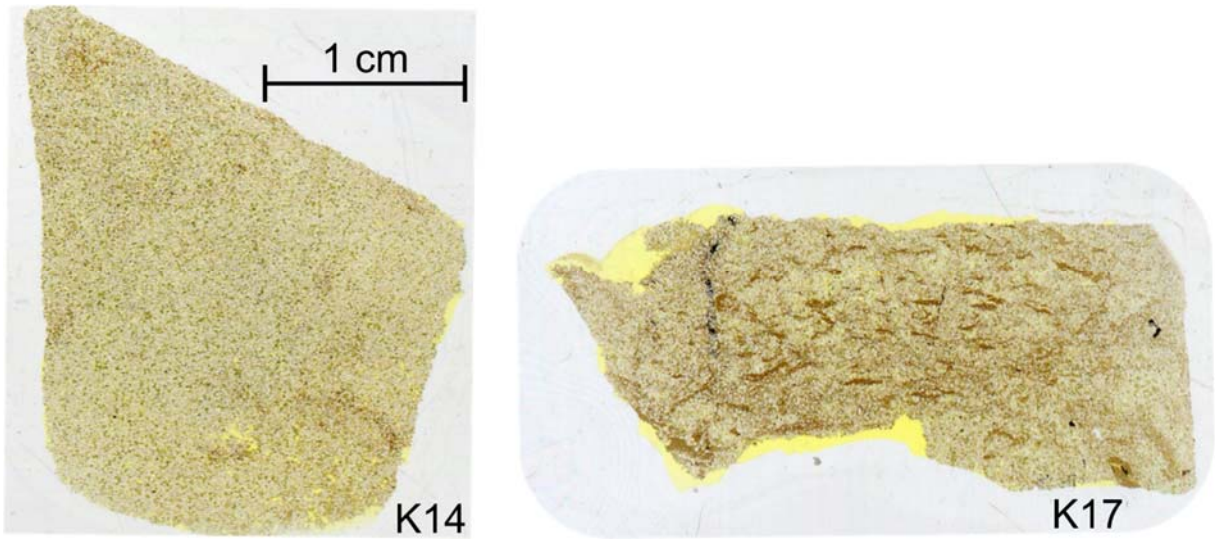

Figure 57: Sanned thin sections of samples K14 (left) and K17 (right). K17 is the most clayey sample as it contains several brown, clayey patches while sample K14 is more sandy as we observe mainly quartz grains and clayey patches are hardly visible

These observatons are also confirmed by the transmitted light microscopy image of Figure 58. Sample K14 shows images which are dominated by quartz grains, while clay can generally be found locally between the quartz grains. To the contrary, sample K17 shows large strings of clay which are disturbed by quartz grains (due to bioturbations). Both samples show also glauconite (green), biotite (white plates), muscovite (brown plates) and framboidal pyrite (black dots). The latter is clearly present in sample K17. Note also that similar to the samples of the Boeretang Member, interparticle porosity can be observed between the quartz grains (in yellow, due to the impregnation of the sample with a fluorescent resin) but it is more abundant in sample K14 than in sample K17.

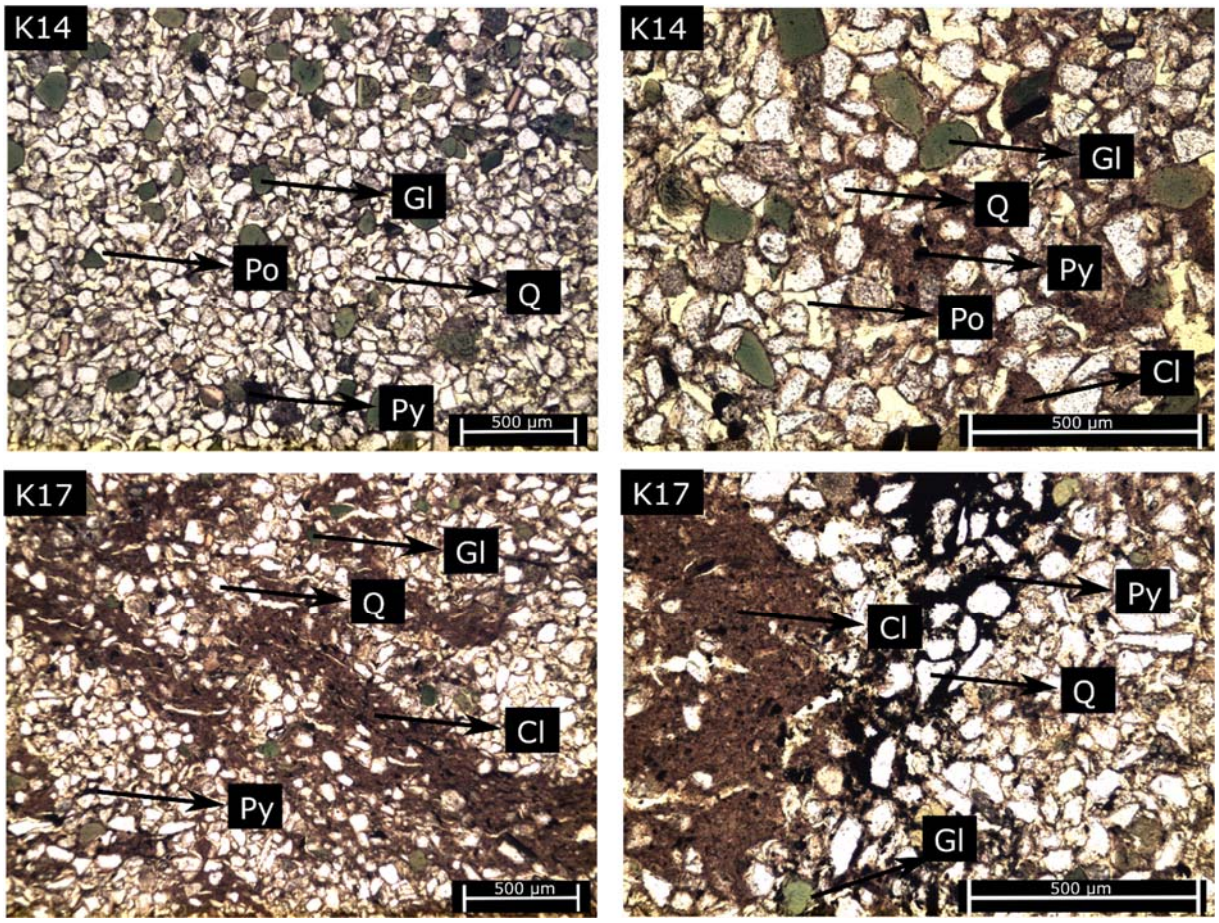

Figure 58: Transmitted light microscopy images of the thin sections of samples K14 (top), and K17 (bottom). For both samples, quartz grains (Q) are abundant, but sample K17 contains considerable more clay (Cl) and framboidal pyrite (Py) than sample K14, while sample K14 contains more interparticle porosity (Po). Glauconite grains (Gl) are omnipresent.

When studying the pore volume distribution of both samples (K14 + K17, Table 6), sample K17 shows clearly more pores in the range 1.5 – 250 nm, compared to sample K14. This matches also with the observations discussed above. As this sample contains more clay, it has also a larger amount of micro and meso pores. Sample K14 contains more quartz and hence interparticle porosity, so it will have a larger proportion of pores > 250 nm.

4.8 How the transport properties are linked to the petrophysical and petrographical properties of the samples of the Boom Clay and the Eigenbilzen Sands

In this section, we will investigate for the Boom Clay and Eigenbilzen Sands how the transport properties are linked to the petrophysical and petrographical properties which were discussed in the previous section (§4.7). First we will focus on the differences between the two groups, later we discuss the minor differences within each sample group.

Major differences between the samples of the Boom Clay and the Eigenbilzen Sands

For both diffusivity and hydraulic conductivity, a significant difference can be observed between the samples of the Boom Clay and those of the Eigenbilzen Sands. More specifically, the hydraulic conductivity is about two orders of magnitude larger and diffusivity (D_{eff}) is a factor 1.7 larger in the Eigenbilzen Sands. For most of the petrophysical and petrographical properties which have been investigated, large differences between both sample groups can be observed. When looking at the mineralogy and grain size distribution, the samples of the Eigenbilzen Sands are enriched in quartz and contain less 2:1 clay minerals. Hence the clay fraction has decreased and the sand fraction increased. This change in composition is reflected in differences in the micro-structure. Samples of the Boom Clay are characterised by a very clayey matrix, with a homogeneous distribution of quartz grains and only localised increased porosity for samples of the Putte and Terhagen Member; the samples of the Boeretang Member showed a heterogeneous distribution of the quartz grains and interparticle pores in the thin sections and zones with increased porosity in the 3D µ-CT reconstructed images. By contrast, samples of the Eigenbilzen Sands all showed large amounts of quartz, with a heterogeneous distribution of the clay matrix and an increased porosity around the quartz grains. The way the different mineral phases are distributed leads to changes in the pore size distribution, and this pore distribution heavily influences transport. From the results of nitrogen adsorption experiments, we observe that the samples of the Boom Clay contain a larger fraction of pores in the range 1.5 – 250 nm, compared to the samples of the Eigenbilzen Sands. Hence the latter contain more pores in the range > 250 nm. As water and solutes are hindered less in their transport when using larger pores, the transport parameters in the Eigenbilzen Sands are larger compared to those of the Boom Clay.

Minor differences between the samples of the Boom Clay (Putte & Terhagen Member vs. Boeretang Member)

From the Boom Clay, two different sample types were investigated: the “clayey” samples from the Putte & Terhagen Member, and “silty” samples from the Boeretang Member. Due to the large similarities in the mineralogical composition and in the grain size distribution, the “silty” samples cannot be classified as such. However, when looking at the transport parameters of the samples of the Boeretang Member, we observe an increase in hydraulic conductivity (around factor 5-10), while the diffusivity is similar. This increased hydraulic conductivity can be explained by a change in the micro-structure. Indeed, as discussed in previous sections, the micro-structure of the samples of the Boeretang Member differs considerably from the one of the Putte & Terhagen Member. Quartz grains are often grouped into clusters, and interparticle porosity can be observed. On reconstructed 3D µ-CT images one can observe that some of these clusters are connected and they can be found all over the sample. This leads to the conclusion that the quartz clusters are mostly remainders of wormholes which have been filled during the sedimentation process. As the interparticle pores are larger compared to the pores of the clay matrix, a small decrease in the pore fraction 1.5 – 250 nm, and hence an increase in the fraction of the larger pores has been observed. Though, the difference between both sample types is not very large. Probably, only the advective transport of water under a pressure gradient benefits from the locally increased pores sizes (being a preferential path), while the diffusive transport is still dominated by the micro-pores located in the clay matrix.

Minor differences between the samples of the Eigenbilzen Sands

For the Eigenbilzen Sands, four samples have been studied: two oriented parallel and two perpendicular to bedding plane. Of course, transport parameters can only be compared between samples with the same orientation.

When looking at the samples oriented parallel to bedding plane (K 14 + K15), K15 shows larger diffusivities, but a lower hydraulic conductivity. Based on their mineralogical composition and grain size distribution, both samples are very similar. When looking at the micro-structure, K14 shows mainly quartz grains, associated with interparticle porosity, and a small amount of clay, while K15 has a similar appearance, but with some more zones with clay. The pore size distribution for the range 1.5 – 250 nm is very similar, so probably the amount of pores in the clay matrix is similar as well. When looking at the water accessible porosity, K15 is more porous than K14 (40 vs. 37 %) so K15 could in that case contain more pores > 250 nm which could be responsible for the enhanced transport. This is somehow observed in Figure 78, where sample K15 shows numerous larger, connected pores. But it remains unclear why only diffusivity is enhanced, and not the hydraulic conductivity.

When looking at the samples oriented perpendicular to the bedding plane, there is a very clear difference between K16 and K17: both diffusivity and hydraulic conductivity are enhanced in K16. The mineralogical composition and the grain size distribution already indicate that both samples are very different: K16 contains more quartz and less clay minerals, and hence has a larger sand and smaller clay fraction. This is also clearly visible in the micro-structure: sample K16 contains more quartz, and the increased porosity is located around the quartz grains and in the clayey zones, while sample K17 is more enriched in clay and shows mainly an increased porosity in the clayey zones. As expected, K17 has more pores in the range 1.5 -250 nm as they are mainly located in the clay zones. As the porosity of both samples is similar, K16 will contain more pores > 250 nm (which is for instance visible in Figure 82), and most likely these larger pores are responsible for the enhanced transport.

5. Conclusions and outlook

In a geological disposal of radioactive waste, understanding the transport behaviour of gases is important, next to that of radionuclides. Therefore, a new and innovative technique to measure diffusion coefficients of dissolved gases by using a cross-diffusion technique was developed. By using this technique, diffusion coefficients of a range of dissolved gases (noble gases, light hydrocarbons and hydrogen) have been obtained for samples of the Boom Clay, Eigenbilzen Sands, Callovo-Oxfordian Clay, Opalinus Clay and bentonite, the latter at different dry densities.

Measuring the diffusion coefficient of hydrogen (the most important and safety relevant gas in a geological repository) turned out to be a real struggle due to microbial activity interference: microbes converted hydrogen into methane, leading to many failed experiments. Only after following a strict sterilisation procedure, diffusion coefficients were obtained. The obtained value now enables a better assessment of the problems related to H_2 production/evacuation in a repository environment which was considered as an important knowledge gap in past assessments. Because of the experimental problems related to the use of H_2, He is in many cases used as a proxy. As shown in this work, the diffusion coefficients of He were sometimes much larger than expected based on their size, and up to

now no clear explanation for this strange behaviour can be given. Therefore, we suggest to consider the use of Ne as a better proxy to estimate the H_2 diffusion behaviour.

After measuring diffusion coefficients of a suite of gases, we observed for all samples an exponential relationship between the size of the diffusing molecule (expressed as "kinetic diameter") and the effective diffusion coefficient. A similar relation exists for the size and the diffusion coefficients of the gases in free water (D_0). For the samples of the Boom Clay and the Eigenbilzen Sands, the exponential coefficient is very similar to one of the D_0-fit. As the geometric factor is related to the ratio D_0/D_{eff}, (and hence to the distance between the D_0 and the D_{eff} fitted curve) similar exponential coefficients indicate that the geometric factor will be quasi constant when the size of the diffusing molecule increases. This matches with the experiments results: the difference in G between the smallest and the largest molecule is smaller than a factor 3. However, for the other clayey samples (COX, OPA and bentonite), the exponential factors differ from the one of the D_0 relationship, hence G varies strong with the size of the diffusing molecule: for bentonite with a dry density of 1.6 g/cm³ the difference in G between the smallest and the largest molecule is a factor 16.

In the literature, diffusion coefficients are often estimated, based on their D_0 value and a fixed geometric factor which is mostly obtained from a diffusion experiment with HTO. As discussed above, the geometric factor can be highly variable, depending on the sample. Hence, using a constant value is not always a correct approach. Therefore, we propose an alternative method, using the exponential relation between the size of the dissolved gas and its effective diffusion coefficient. By measuring experimentally the effective diffusion coeffient of two unreactive dissolved gases with a different size, the diffusion coefficient of other dissolved gases (with a size in between the two measured gases) can be estimated by using the fitted exponential relationship. When using this approach for one of our samples, the predicted/interpolated and measured diffusion coefficients differ up to less than 30%.

The evolution of the geometric factor can also be described with an exponential function, using the ratio between the size of the diffusing molecule and a characteristic pore size. When applying this to our samples, the high variability of G with the size of the diffusing molecule which is observed for some of the samples could be explained by a small characteristic pore size (close to the size of the dissolved gases). At a certain point, there will be no longer a connected path through which the gas molecules can diffuse, which leads to a percolation treshold and which has been observed in the sample Opalinus Clay for gases larger than argon. Also for the hydraulic conductivity, different formulas relating different petrophysical properties exist (mineralogy, grain size distribution, pore size distribution, specific surface area, …) and this topic is currently investigated by other colleagues who make use of the data in this manuscript.

As diffusion coefficients are linked to the microstructural characteristics (lumped into the G-factor), another objective of this PhD was to investigate how the transport properties are linked to the petrophyiscal and petrographical properties. Herefore, we focussed on the data obtained for the samples of the Boom Clay and Eigenbilzen Sands. Large differences in diffusivity and hydraulic conductivity have been observed between the samples of the Boom Clay on the one hand and the samples of the Eigenbilzen Sands on the other hand. Petrophysical analysis showed also large differences in mineralogy and grain size distribution: samples of the Boom Clay are rich in clay minerals and contain a large clay fraction (< 2µm), while the samples of the Eigenbilzen Sands are rich in quartz and contain a large sand fraction (> 62 µm). These differences in composition are also reflected in

changes in the micro structure, which is observed in the petrographical analysis. The samples of the Boom Clay (those of the Putte and Terhagen Member) are characterised by a clay matrix where the quartz grains are homogeneously spread and pores are not visible. Hence, the pores are mainly located in the clay matrix and they are very small (< 250 nm). To the contrary, samples of the Eigenbilzen Sands showed large amounts of quartz, a hetergeneous distribution of the clay phase and interparticle porosity around the quartz grains. The pores are still partly located in the clay matrix, but there is also an important fraction of larger pores (> 250 nm) which allow enhanced transport of dissolved gases and water. The samples of the Boom Clay (Boeretang Member) are somehow in between. The hydraulic conductivity is cleary enhanced, but diffusivity is similar to the other samples of the Boom Clay. These samples still contain a large clay matrix, but the quartz grains are grouped into clusters (probably remainders of bioturbations by worms) where interparticle porosity can be observed. For these samples, the pore size distribution is still dominated by small pores, though also a fraction of larger pores (interparticle pores) has to be accounted for. However, for these samples only the advective transport of water benefits from the locally increased pore size as K is increased, while the diffusive transport is still dominated by the micro pores located in the clay phase.

Within this research topic, pore network modelling would be a very interesting additional step. By reconstructing the pore network and performing virtual diffusion experiments, the effect of changes in composition and structure could be further investigated. This is currently under consideration for a new European project, which is prepared in the framework of the 'European Joint Programming'.

The initial reason to start the gas diffusion project was to have more reliable diffusion coefficients in order to improve the scoping calculations for the formation of a free gas phase. Yu and Weetjens (2012) used in their calculations the apparent diffusion coefficients, measured for He by Jacops et al. (2013) as an approximation for hydrogen. Later diffusion experiments with hydrogen showed that the value D_{app} = 1.1 x 10^{-9} m²/s is an overestimation as the value measured for another sample oriented perpendicular to bedding plane was D_{app} = 0.7 x 10^{-9} m²/s . Based on the currently available information, and especially the strange behaviour of He in some of the samples for which we have no clear explanation, we propose to use the diffusion coefficient of Ne as a better approximation. For diffusion parallel to bedding plane, the value used by Yu and Weetjens (2012) is a good approximation. Hence, after internal discussion we decided that the currenlty available scoping calculations are still reliable and that there is no need to redo them with other values.

To summarize, this PhD provides an extended dataset of diffusion coefficients, measured for different gases and on different types of clayey samples, complemented with detailed microstructural analysis. Further analysis of these data led to new insights in the variability of diffusivity (both D_{eff} and the geometric factor) with the size of the diffusing molecule. After performing petrophysical and petrographical analyses, the transport properties could be linked to the microstructure of the samples, which led to new and improved insights in the diffusive transport processes.

6. Annexes

ANNEX 1: On the selection of the kinetic diameter

Within this PhD, the size of the diffusing gas molecue is often used for correlations with the transport parameters. This “size” can be expressed in different ways, e.g. by using the molecular mass (and deviations), the hydrated radius, the atomic number etc. (Dagnelie et al., 2014). None of these approaches lead to a significant relationship with the transport parameters. The most widely available and accepted measure is the “gas kinetic diameter”. However, different theoretical approaches for the calculation of this kinetic diameter exist. As this parameter is frequently used throughout this manuscript, some background information on the selection of the used values is given in this annex. In the first part, we explain how kinetic diameters can be calculated from viscosity measurements – assuming that the gas molecules are hard spheres. However, the hard sphere theory is only an approximation because molecules interact with each other. Therefore, in the second part, the calculation of kinetic diameters from an interaction potential (the Lennard-Jones potential) is explained. In the third part, it is addressed how kinetic diameters can be calculated from the Chapman-Enskog theory and the Stokes-Einstein equation. In the fourth part, a review and comparison of available values for kinetic diameters is given and the annex ends with a discussion and conclusion.

Table 22: overview of used constants, symbols and their units

σ_{cross}	collision cross section	m^2
σ_{LJ}	kinetic diameter	
η	viscosity	Pa•s
ε_{LJ}	depth of the potential well	J
$\Omega^{2,2}$	reduced collision integral	
a_{radius}	radius of a spherical particle	m
A	molar concentration	Mol·• m^{-3}
d	collision diameter	m
D_0	diffusion coefficient of a gas in water	m^2/s
k_B	Boltzmann constant	$1.38\ 10^{-23}$ J • K^{-1}
l	mean free path	m
m	mass of one molecule	kg
M	molar mass	kg • mol^{-1}
N_a	Avogadro's number	$6.022\ 10^{23}$ mol^{-1}
n	number of moles	mol

n_V	number of particles per volume unit	m^{-3}
p	pressure	Pa
R	gas constant	8.314 J • mol^{-1} • K^{-1}
r	distance between center of two molecules	m
T	temperature	K
v	velocity of molecule	m • s^{-1}
v_p	most probable velocity	m • s^{-1}
v_{RMS}	root mean square velocity	m • s^{-1}
v_{av}	average velocity	m • s^{-1}
V	volume	m^3

A1.1 Calculation of the kinetic diameter from viscosity data with the hard sphere model

The simplest version of the kinetic theory of gases describes gas molecules as hard spheres with diameter *d* (also called collision diameter) making binary collisions only (Haynes, 2012).

In a gas under thermodynamic equilibrium, the velocities of individual molecules cover a wide range and because of collisions in the gas, velocities are continually redistributed among the molecules. The velocity is described by the Maxwell-Boltzmann distribution (Atkins and de Paula, 2006)(Figure 59).

$$f(v) = 4\pi \left(\frac{M}{2\pi RT}\right)^{3/2} v^2 \, e^{\left(-\frac{Mv^2}{2RT}\right)} \quad (1)$$

With *R* the gas constant (8.314 J mol^{-1} K^{-1}), *T* the temperature in K, *v* the velocity of a molecule in m s^{-1}, *M* the molar mass of the molecules in kg • mol^{-1} and

$$M = m\,N_a \qquad (2)$$

with m the mass of one molecule in kg and N_a Avogadro's number which is 6.022 10^{23} mol^{-1}.

From the Maxwell-Boltzmann distribution, different average velocities can be derived (Figure 59)

The most probable velocity (v_p) is determined from the location of the maximum value of the distribution:

$$\frac{\partial f(v)}{\partial v} = 0 \;\rightarrow\; v_p = \sqrt{\frac{2RT}{M}} \qquad (3)$$

The Root Mean Square velocity (v_{RMS}) is the second-order moment of speed and described as

$$v_{RMS} = \sqrt{v^2} = \sqrt{\int_0^\infty v^2 f(v)dv} = \sqrt{\frac{3RT}{M}} \qquad (4)$$

and the average velocity (v_{av}) is described as

$$v_{av} = \int_0^\infty v\, f(v)dv = \sqrt{\frac{8RT}{\pi M}} \qquad (5)$$

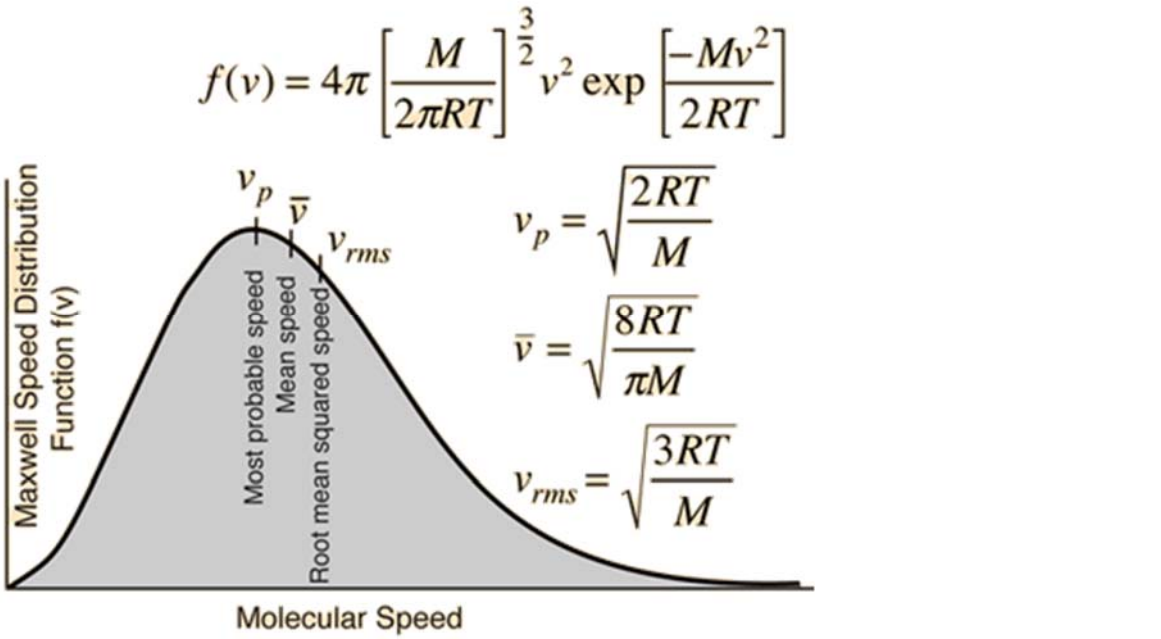

Figure 59: Maxwell-Boltzmann distribution of speeds with an indication of the most probable speed, the root mean square speed and the average speed (from http://hyperphysics.phy-astr.gsu.edu/hbase/Kinetic/kintem.html)

Within the hard sphere theory, the collisional cross section σ_{cross} (m²) is seen as the area around a particle, in which the center of another but similar particle must be in order to collide (IUPAC, 1997). As shown graphically in Figure 60, a collision will only occur for particles within a cross section with diameter *d* (m) (called the kinetic diameter or collision diameter). So for two similar particles, this collisional cross section is described as

$$\sigma_{cross} = \pi\, d^2 \qquad (6)$$

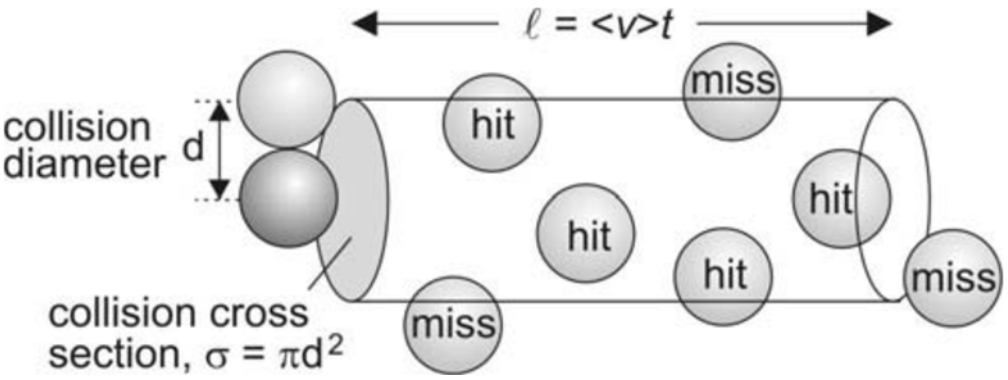

Figure 60: Schematic representation of the collision diameter and the collision cross section (from Vallance C., Properties of gases)

In the kinetic theory of gases, the mean free path *l* (m) of a gas molecule is seen as the average distance that a particle travels between collisions with other particles (Chapman and Cowling, 1990) and can be written as

$$l = \frac{1}{n_V\, \sigma_{cross}} \qquad (7)$$

with n_V the number of particles per volume unit (m^{-3}) and σ_{cross} the collisional cross section (m²). If the velocities of identical particles have a Maxwell distribution, than the mean free path *l* can be described according to Chapman and Cowling (1990) as

$$l = \frac{1}{n_V\, \sigma_{cross}\, \sqrt{2}} \qquad (8)$$

By using the ideal gas law and introducing the Boltzmann constant k_B (which is the ratio of the gas constant over Avogadro's number); n_V in eq. (7) can also be written as

$n_V = p / k_B T$ (9)

with p the pressure (Pa); k_B the Boltzmann constant (1.38 10^{-23} J K^{-1}).

When substituting eq. (6) and (9) in eq, (8) this leads to following equation for the mean free path:

$$l = \frac{k_B T}{p \pi d^2 \sqrt{2}} \quad (10)$$

In order to be able to calculate the kinetic diameter from the viscosity of the gas, the dynamic viscosity η (Pa s) is introduced and is described as Atkins and de Paula (2006)

$$\eta = \frac{1}{3} m l v_{AV} N_a A \quad (11)$$

with A the molar concentration (mol m^{-3})

Substituting eq. (6) and (8) into eq. (11) leads to

$$\eta = \frac{m v_{AV}}{3\sqrt{2} \pi d^2} \quad (12)$$

Combining equation (12) with equation (5)

$$\eta = \frac{2}{3 \pi d^2} \sqrt{\frac{m k_B T}{\pi}} \quad (13)$$

By equations (12) and (13) the kinetic diameter is linked to the viscosity of the free gas phase.

The kinetic diameter d can thus be calculated from eq. (13) as follows:

$$d = \sqrt{\frac{2}{3 \pi \eta} \sqrt{\frac{m k_B T}{\pi}}} \quad (14)$$

However, different versions of eq. (13) can be found in literature and some examples are given below.

$\eta = \frac{5}{16}\frac{1}{\sigma_{cross}^2}\sqrt{\frac{m\,k_B\,T}{\pi}}$	(Kaye and Laby, 2005)	(15)
$\eta = \frac{2}{3}\frac{1}{\sigma_{cross}}\sqrt{\frac{m\,k_B\,T}{\pi}}$	http://www.chem.hope.edu/~polik/Chem345-1997/gasviscosity/GasViscosity.html	(16)
$\eta = \frac{2}{3}\frac{1}{\sigma_{cross}^2}\sqrt{\frac{m\,k_B\,T}{\pi}}$	(Hildebrand, 1976)	(17)

All three equations are similar to eq. (13), except for the first constant which varies between 5/16 and 2/3. Both factors σ_{cross} and σ_{cross}^2 are used. As σ_{cross} is defined as the collisional cross section (eq. (6)) and is expressed in m^2, σ_{cross} should be used instead of σ_{cross}^2.

In Haynes (2012), the kinetic diameter is calculated from the viscosity (in this equation expressed as µPa s) and the molar mass (in this equation expressed in g/mol) by following equation:

$$\eta = \frac{2.67\ 10^{-20}\ (MT)^{\frac{1}{2}}}{d^2} \qquad (18)$$

$$\eta = \frac{2.67\ 10^{-20}\ (mN_aT)^{\frac{1}{2}}}{d^2}$$

A1.2 Calculation of the kinetic diameter assuming a Lennard-Jones interaction potential

The equations above assume that gas molecules behave as hard spheres. But this is only an approximation. It is well known that molecules will interact with each other (also when they do not collide): they attract one another on large distance, but repel one another when the intermolecular distance is quite small.

Different interaction potentials exist, but the one which is most frequently used is the Lennard-Jones potential (V_{LJ}) which is described by following equation (Hirschfelder et al., 1964):

$$V_{LJ}(r) = 4\varepsilon\left(\left(\frac{\sigma_{LJ}}{r}\right)^{12} - \left(\frac{\sigma_{LJ}}{r}\right)^{6}\right) \qquad (19)$$

with r the distance between the centers of two molecules and σ_{LJ} and ε constants which are characteristic of the chemical nature/form of the interacting molecules.

At the distance where $r = \sigma_{LJ}$, the potential is zero. Therefore, σ_{LJ} is the closest approach of two molecules which collide with zero initial kinetic energy. When looking at the equation and Figure 61, $V_{LJ}(r)$ is minimal (potential energy is –ε) at $r = 2^{1/6}\,\sigma_{LJ} = 1.12\,\sigma_{LJ}$.

This distance σ_{LJ} is called the 'kinetic diameter' and is considered to be representative for the size of the gas molecule.

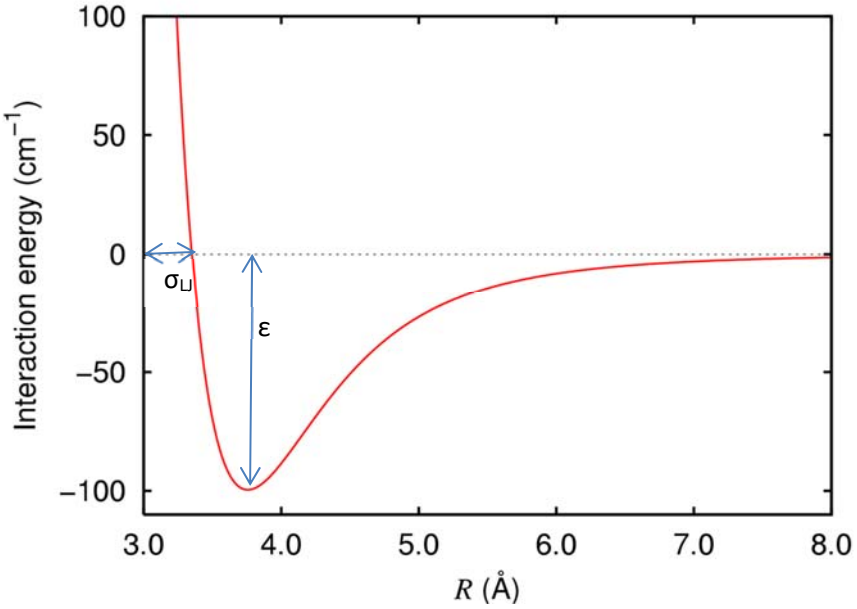

Figure 61: example of an interaction potential (from Aziz (1993))

The values of the parameters σ_{LJ} and ε_{LJ} can be fitted from p V (Volume) isotherms over a range of temperatures by the virial expansion

$$\frac{pV}{nRT} = 1 + B(T)\frac{n}{V} + C(T)\left(\frac{n}{V}\right)^2 + \cdots \qquad (20)$$

with n the number of moles and $B(T)$, $C(T)$, … the virial coefficients which, when assuming a Lennard – Jones interaction, are a function of σ_{LJ} and ε_{LJ} (Beattie et al., 1951; Hirschfelder et al., 1964).

In practice, p-V-T data are recorded for a certain gas (temperature is the most frequently varied parameter) and the second virial coefficient $B(T)$ is measured simultaneously. Values of kinetic diameters, calculated from second virial coefficients can be found in, for example, Hirschfelder et al. (1964)

The viscosity of a gas is function of σ_{LJ} and ε_{LJ} as well. Consequently, the kinetic diameter can also be calculated from viscosity measurements at different temperatures.

These viscosities are measured with an oscillating disc viscosity apparatus. Gases at different temperatures are sent through the apparatus and their viscosity at each temperature is calculated (Johnston and McCloskey, 1940). Values of kinetic diameters, calculated from viscosity data can also be found in Hirschfelder et al. (1964).

As shown in Table 23, both approaches lead to different values for σ_{LJ}.

A1.3 Calculating kinetic diameters from the Chapman-Enskog theory and the Stokes-Einstein equation

When dealing with gas mixtures, the dependency of the diffusion coefficient on temperature is expressed by the Chapman-Enskog theory. In order to calculate the diffusion coefficient of a gas mixture at a certain temperature, the average collision diameter (obtained from the hard sphere model) is needed. For these values wikipedia refers to Hirschfelder et al. (1964). In theory, this relation could be used to calculate the average collision diameter from the diffusion coefficient. But as we use the values later on to relate diffusion coefficients to the size of the diffusing molecules, this way of calculating points to circular reasoning.

Diffusion of spherical particles through a liquid with low Reynolds number is described by the Stokes-Einstein equation.

$$D = \frac{k_B\ T}{6\ \pi\ \eta\ a_{radius}} \qquad (21)$$

with η the viscosity (dynamic) of the fluid through which the gas diffuses and a_{radius} the radius of the spherical particle. Calculated values (T = 298K, η = 0.89 10^{-3} Pa s, D_0 from Boudreau (1997)) for a_{radius} of gases in water can be found in Table 23. Also here, a_{radius} is determined from diffusion coefficients and would later on be used to interpret other diffusion coefficients. Similar to the Chapman-Enskog theory, this points to circular reasoning.

A1.4 Review and comparison of available values for kinetic diameters

As discussed above, the calculation of kinetic diameters is based on different theories, leading to different values. An overview of values for kinetic diameters can be found in Table 23.

Within the hard sphere theory, the size of a gas molecule is described by the collision diameter *d* and can be calculated from viscosity measurements. When looking into the literature, all equations are similar, except for the pre-factor. In Table 23, kinetic diameters are calculated according to equations (18), (15) and (17) for a temperature of 298 K. Viscosity data (of a free gas phase) are taken from Haynes (2012). Despite the fact that similar equations and the same input parameters are used, differences are relatively large – up to a factor 1.9 - which is entirely attributed to the different prefactors.

When a Lennard-Jones interaction potential between molecules is considered, the size of a gas molecule is described by the kinetic diameter σ_{LJ} which can be calculated from second virial coefficients or from viscosity data. For this type of kinetic diameters, Hirschfelder et al (1964) was our primary

source of kinetic diameters and the values from this source can also be found in Table 23. With respect to these data, it is imported to notice that, according to Hirschfelder et al. (1964) kinetic diameters obtained via second virial coefficients should be used for thermodynamic properties and calculations of the equation of state, whereas kinetic diameters obtained from viscosity measurements should be used for transport property calculations. Therefore, kinetic diameters from viscosity measurements are considered to be most relevant in this study. However, the differences between both datasets are minor: the average difference is 0.9%, except for ethane where the difference is 11%.

When searching for kinetic diameters, also other sources can be found. Kinetic diameters can be found for instance in Yampolskii et al. (2006). They present a table with kinetic diameters for a set of gases, but all values are taken from other authors. The values for the kinetic diameter are taken from Breck (1984) and from Poling et al. (2000). When going more into detail in the work of Breck (1984), it turns out that many of these kinetic diameters (certainly Ne, Ar, Xe and CH_4) have been taken from Hirschfelder et al. (1964). When going more into detail in the work of Poling et al. (2000), it turns out that some of the values have been obtained from Svehla (1995). However, in the report of Svehla (1995), only numbers of σ_{LJ} for CH_4 and C_2H_6 can be found, and these do not correspond to the values in the book of Poling et al. (2000). For other gases, reference is made to Gordon et al. (1984) but also here, no values can be found. Reference is also made to Svehla (1962) and finally here some more information can be retrieved.

In the report of Svehla (1962), viscosities for different gases at different temperatures are calculated according to

$$\eta \, x \, 10^6 = \frac{26.693 \, (MT)^{\frac{1}{2}}}{\sigma_{LJ}^{\,2} \, \Omega^{2,2}} \qquad (22)$$

with η x 10^6 the viscosity in micropoises, T the absolute temperature, M the molecular weight, σ_{LJ} the collision diameter in angstrom and $\Omega^{(2,2)}$ the reduced collision integral. The collision integral depends on the intermolecular forces of the gas molecules and for these intermolecular forces, the Lennard-Jones (6-12) potential is assumed. The collision integrals were obtained from Hirschfelder et al. (1964). So in order to calculate viscosities, σ_{LJ} is needed. This parameter is determined by fitting experimentally obtained viscosity data to equation (22) and for this purpose, a least square technique was used. When looking at the references where the experimentally measured viscosities have been reported, there is a large overlap with the references used in Hirschfelder et al. (1964). An overview of reported kinetic diameters by Svehla (1961) can also be found in Table 23. The difference with the values obtained from viscosity data in Hirschfelder et al. (1964) is only 1.9% and thus minor. The values reported by Svehla (1962) are considered to be appropriate for use and of equal value as the values reported by Hirschfelder et al. (1964).

Table 23: Overview of values for kinetic diameter of gases, obtained from different sources

	Hard sphere model			Lennard-Jones model				
	Viscosity	Viscosity	Viscosity	Lennard-Jones 2nd virial coefficients	Lennard-Jones viscosity	Lennard-Jones Viscosity	Lennard-Jones Viscosity	Stokes-Einstein (in water, at 25°C)
	Haynes (2012)	Hildebrand (1976)	Kaye and Laby (2005)	Hirschfelder et al. (1964)	Poling et al. (2000)	Svehla (1961)	Hirschfelder et al. (1964)	Miller (1924)
He	2.15	1.77	1.21	2.56	2.55	2.551	2.58	0.34
Ne	2.55	2.10	1.44	2.75	2.82	2.820	2.79	0.61
Ar	3.58	2.95	2.02	3.4	3.54	3.542	3.42	1.00
Xe	4.77	3.93	2.69	4.1	4.05	4.047	4.06	1.67
H_2	2.70	2.22	1.52	2.93	2.83	2.827	2.97	0.48
CH_4	4.06	3.35	2.29	3.82	3.76	3.758	3.82	1.33
C_2H_6	5.16	4.25	2.91	3.95	4.44	4.443	4.42	1.78

A1.5 Conclusion and summary

To summarize this annex, one can state that different theoretical approaches exist for calculating the size of a molecule. As the obtained values are used to interprete diffusion data later on, values obtained from diffusion-related equations are not selected because it leads to circular reasoning.

Calculating molecular diameters from viscosity measurements is well known, but it assumes the gas molecules as hard spheres. In literature, different formulas can be found, using a slightly different constant value which leads to differences between the reported values. The highest values can be found in Haynes (2012) while the lowest values can be found in Kaye and Laby (2005), but the difference is up to a factor 1.9.

As discussed above, the hard spheres theory is only an approximation because molecules do interact with each other. Therefore, using the Lennard-Jones interaction potential is a better approach for calculating kinetic diameters. Values obtained from second virial coefficients and from viscosity measurements are both available, but for use with transport properties, it is advised to use the values obtained from viscosity measurements (Hirschfelder et al., 1964). Therefore, these data have been selected for use throughout this manuscript. Two main sources of data can be used: those reported by Hirschfelder et al. (1964) and those reported by Svehla (1961) and we consider them to be of equal

value. As the values of Hirschfelder et al. (1964) have been used in previously written papers and reports, they are also used throughout this manuscript.

Though, some remarks should be made. The selected kinetic diameters are representative for dilute gas mixtures, while we are dealing with gases dissolved in water. However, no data could be found for dissolved gases, except the data derived from the Chapman-Enskog theory and the Stokes-Einstein equation. But the latter uses diffusion data to calculate the kinetic diameter which would in our case lead to circular reasoning. In our opinion, using molecular dynamics could be a good tool to calculate the size of these dissolved gases, but this was not possible within this PhD project. When looking at the effect of the size of molecules on the transport parameters, the relative proportion of the different values is most important. Hence, the values of Hirschfelder et al. (1964) are used, but of course they are only an approximation.

ANNEX 2: Description of used techniques

A2.1 Introduction

One of the main objectives of this PhD was to investigate which petrophysical properties influence the diffusion parameters. Therefore, a detailed petrophysical analysis was performed. After a sample had been removed from the diffusion setup, the diffusion cell was opened and the clay sample was taken out of the diffusion cell. Next, the sample was scanned with computer tomography (CT). The main goal of the CT scan was to look for larger (cm) scale heterogeneities (such as large pyrite inclusions, open fractures, large carbonate inclusions) which could act as preferential pathways for transport. Afterwards, different subsamples have been taken for further analyses.

As a comparison was made between clayey and silty samples, the difference in clay and silt content was verified with grain size analysis (granulometry). As also mineralogy is influenced by differences in clay/silt content, a mineralogical analysis was performed as well.

Differences in mineralogical composition are also reflected in a changed specific surface. An increased clay content is expected to lead to an increased specific surface. Specific surface was measured with N_2-adsorption BET.

Diffusion parameters are strongly influenced by the pore network. Information on the pore size distribution was obtained with mercury intrusion porosimetry (MIP) and with N_2-BET. As zones with higher porosity lead to less attenuation of the X-ray in µ-CT images, µ-CT was used as a tool to visualize these higher porosity zones in 3D.

A very important diffusion parameter is porosity. The water accessible porosity can be calculated from the water content of the sample. One of the input parameters needed is the dry density of the sample. The wet density of the sample was measured by using Archimedes' law and the dry density of the sample was measured by using He-pycnometry.

All used techniques are discussed in the following sections.

A2.2 Granulometry

First, a subsample of ca 5 g is taken (preferably not dried). Next, all cementing and clogging agents are removed by using the "Jackson treatment", named after Jackson (1975). In a first step, carbonates are removed by adding sodium acetate. In a second step, organic matter is removed by adding sodium acetate and hydrogen peroxide. In the last step, iron (hydr)oxides are removed by adding sodium citrate and sodium dithonite. Finally, a peptising solution is added.

Prior to the measurement, the samples are treated with an ultrasonic probe. The grain size distribution of the sample is measured with a SediGraph. The SediGraph method of particle size analysis is based on Stokes' Law: a particle settling in a liquid will achieve a terminal velocity when the gravitational force balances the buoyancy and drag forces on the spherical particle and this is dependent on the size and the density of the particle, and the density and viscosity of the liquid. Simply said, larger particles settle faster than smaller particles and if all other parameters are constant, the settling velocity is proportional to the particle size. In order to detect settling particles, X-rays are used and the law of

Lambert-Beer is applicable: a beam of photons (X-rays, in this case) passing through a medium is attenuated in proportion to the path length through the medium, its concentration, and the extinction coefficient of the medium. So if the other parameters are kept constant, the X-ray attenuation is proportional to mass concentration. In fact the apparatus measures the concentration of particles smaller than or equal to the Stokes' Law predicted size (for a given velocity) at different moments in time and this provides a distribution of concentration for different particle sizes (see Figure 62).

However, clayey samples contain a large amount of platy particles which have a lower settling velocity as their corresponding spheres, which leads to an underestimation the nominal diameter.

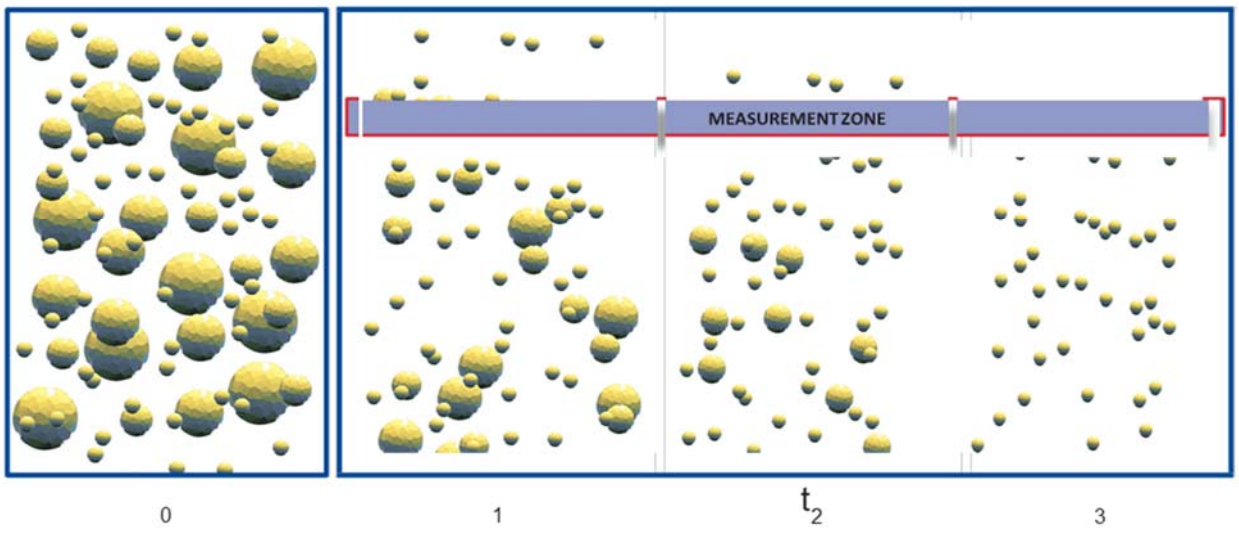

Figure 62: working principle of the SedigGraph (from www.micromeritics.com), based on Stokes' Law.

A2.3 Specific surface (N2-BET)

The specific surface of the samples is measured using a Micromeritics Tristar II 3020 Surface Area Analyser.

Before starting a measurement, the apparatus is thoroughly flushed by using at least 2 cycles of gas filling and vacuum pulling.

Next, a subsample of approximately 5g is taken from the large core and disaggregated with a mortar and pestle. The grinded sample is transferred into an empty sample tube and the exact amount of sample transferred is registered. The filled sample tube is then degassed at room temperature during 30 minutes and at 110°C during 24 hours. Next, the sample tube is packed in an isothermal jacket and placed in a dewar flask, filled with liquid N_2. The system is flushed again and after 5 flushing cycles, the measurement can be started.

The apparatus will measure the amount of adsorbed gas on a sample as a function of the relative pressure of the adsorbate (see Figure 63). By using the theory of Brunauer, Emmett and Teller (BET-theory), the specific surface of the sample can be calculated. More specifically, the adsorption

isotherm (see Figure 64) (based on the BET equation) is plotted and from the slope and the y-intersect of the adsorption isotherm, the quantity of monolayer adsorbed gas (Q_m) and the BET constant can be calculated. From Q_m, the specific surface can be calculated.

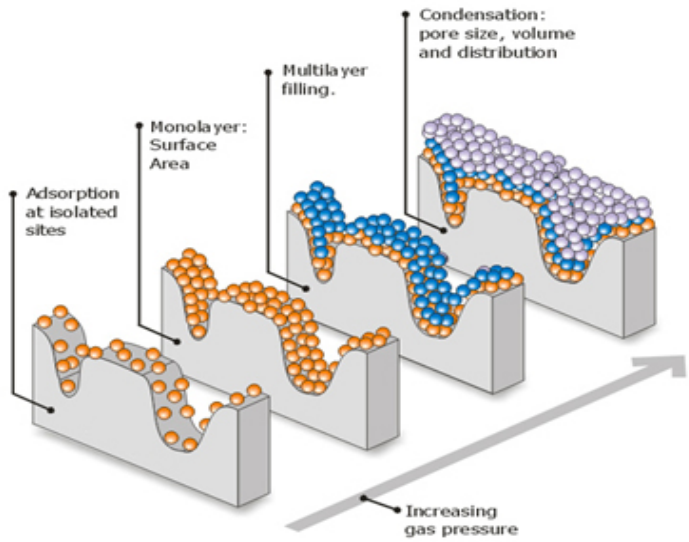

Figure 63: overview of different stages in a N_2-BET measurement (figure from www.micromeritics.com)

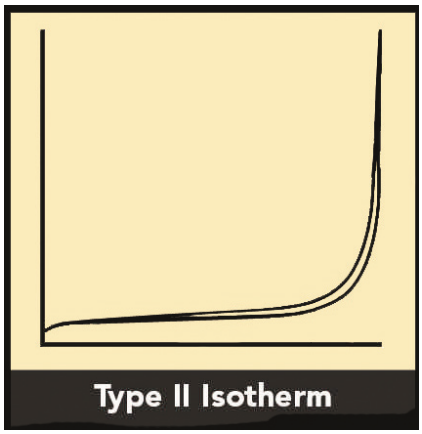

Figure 64: example of an adsorption isotherm (from www.micromeritics.com)

The pore diameter and pore volume can be calculated by using the Barrett, Joyner and Halenda method. However, the BJH theory only applies for mesopores (pore diameter between 2 and 50 nm) and small macropores (pore diameter > 50 nm).

A2.4 Mineralogy

In order to provide enough material for mineralogical analysis, at least 30g of sample was dried at 60°C.

Further preparation of the samples was done either at SCK-CEN, either at KU Leuven and the used procedure is described in detail in Adriaens (2015) and Zeelmaekers (2011). Only a summary is given here.

In the preparation lab, the sample is ground by using a mortar and pestle (until it passes a 500 µm sieve). The homogenized sample is split by coning and quartering.

Next, the sample is further ground in a McCrone Micronizing Mill in order to assure a fine particle size and a narrow grain size distribution. The sample holder is filled with 2.7 g sample, 0.3 g internal standard and 4 ml ethanol. The grinding time is set to 5 minutes.

Afterwards, the sample is dried under a fume hood. The solid residue is crushed using a mortar and pestle (until grain size < 150 µm).

In a last step, the sample is packed into the XRD sample holder, using a side-loading technique. All measurements were performed at KU Leuven, using a Philips PW1050/37 173mm circle goniometer connected with a PW1830 generator and equipped with Cu-Kα-radiation. The detector is a proportional detector type PW3011/00. The diffractometer has a Bragg-Brentano theta-2theta set-up for the source and detector respectively.

Data interpretation and quantitative analysis was performed using QUANTA software.

When a sample is placed in the X-ray diffractometer, a bundle of X-rays will hit the sample which leads to a reflection of the X-rays. In most directions, the reflected waves interfere destructively and cancel out each other. But when parallel X-rays hit the sample under an exact incident angle θ, the interference is constructively and the X-ray can be detected. This is - according to Bragg's law - the case when the difference between two scatterers is d and the pair-length difference 2dsinθ is a multiple of the wavelength ($2d\sin\theta = n\lambda$)(see Figure 65).

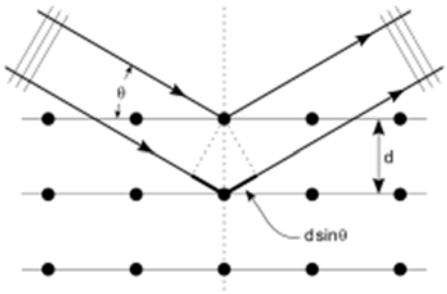

Figure 65: working principle of an X-ray diffractometer. (from www.wikipedia.com)

When measuring a sample, the angle θ is increased progressively. Diffracted X-rays are recorded by a detector and a diffraction pattern is obtained. As each mineral has a unique diffractogram because of a unique d-spacing, different peaks can be attributed to specific different minerals.

A2.5 CT scan

The samples are removed from the stainless steel casing and are wrapped in aluminium foil. Next they are transported to the University Hospital in Leuven.

Scanning occurs in a medical CT (Siemens Somatom Flash Scanner). Samples are scanned at 140kV and a power of 46kW. For reconstruction of the data, filtered back projection is used. A resolution of 0.2 mm is obtained.

In a CT scan, polychromatic X-rays are generated by an X-ray source and pass through the object. Within the object, the X-rays are attenuated and these attenuated X-rays are detected by a detector (see Figure 66). The attenuation of an X-ray is described by Beer's law:

$I=I_0 \cdot e^{(-\mu \cdot x)}$

with I_0 the intensity of the incident beam, I the intensity of the attenuated beam, μ the linear attenuation coefficient (function of the density, atomic number and the energy of the incident beam) and x the length of the X-ray path. Thus, the attenuation of the X-rays is a function of the composition of the object (mineralogy, porosity, …). Therefore, the composition of the object can be reconstructed from X-rays that travelled a different path through the object. As the X-ray source of the used apparatus emits polychromatic X-rays, the occurrence of artefacts such as beam hardening has to be taken into account.

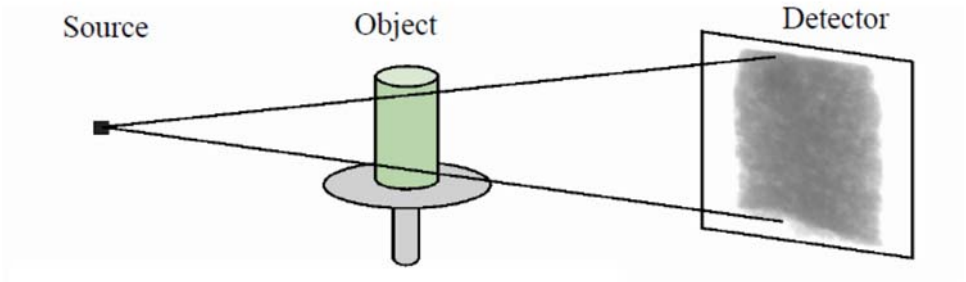

Figure 66: working principle of a CT scan (from Swennen, course on applied sedimentology)

A2.6 µ-CT scan

From the large core, subsamples of 1 cm diameter and 2 cm length are taken by using small aluminium cutting edges. These small subsamples are scanned in a GE Nanotom µ-CT. The plugs are scanned at 132kV with a current of 280 µA, and a resolution of 16µm is obtained.

A2.7 Mercury Intrusion Porosimetry (MIP)

Mercury injection porosimetry (MIP) was performed with a Micromeritics AutoPore IV 9500 instrument at the Institute of Building Materials Research (ibac), RWTH Aachen University.

When using MIP, the sample (about 10g, previously dried at 105°C) is introduced into the MIP instrument in the sample holder. Next, mercury is added. As mercury is a non-wetting fluid, it will not spontaneously intrude the pores by capillary action, but is has to be forced into the pores by applying an external pressure and the required pressure is inversely proportional to the diameter of the pores. So by increasing the external pressure and measuring the amount of mercury that enters the sample, volume and size distribution can be obtained (Figure 67). However, this technique also has some

limitations: only connected porosity is taken into account as mercury is not able to fill unconnected pores. When larger pores have a narrow pore throat, they will only be filled when the pressure is high enough for the mercury to enter the pore throat and this would overestimate the fraction of smaller pores (known as the inkbottle effect). Special precautions have to be taken when dealing with clayey samples as they might crack during drying or under the high injection pressures.

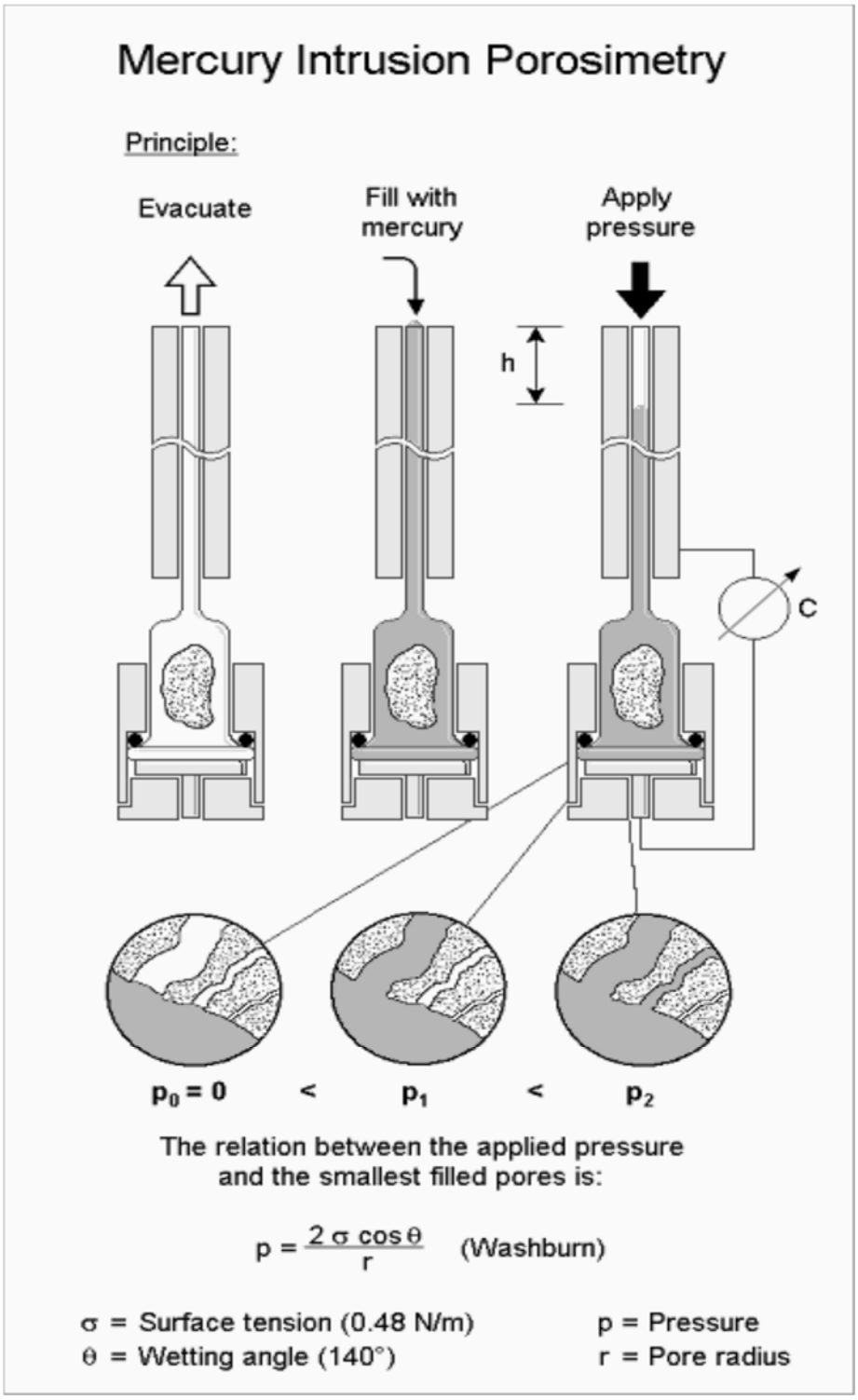

Figure 67: working principle of MIP from Pati (2010)

The raw data were corrected for surface roughness by subtracting injection volumes up to the plateau (see Figure 68). Porosity was calculated from the volume of mercury that had entered the pore system of the sample at maximum injection pressure (before and after correction). Derivation of the intrusion curve (drainage) yields a pore radius distribution.

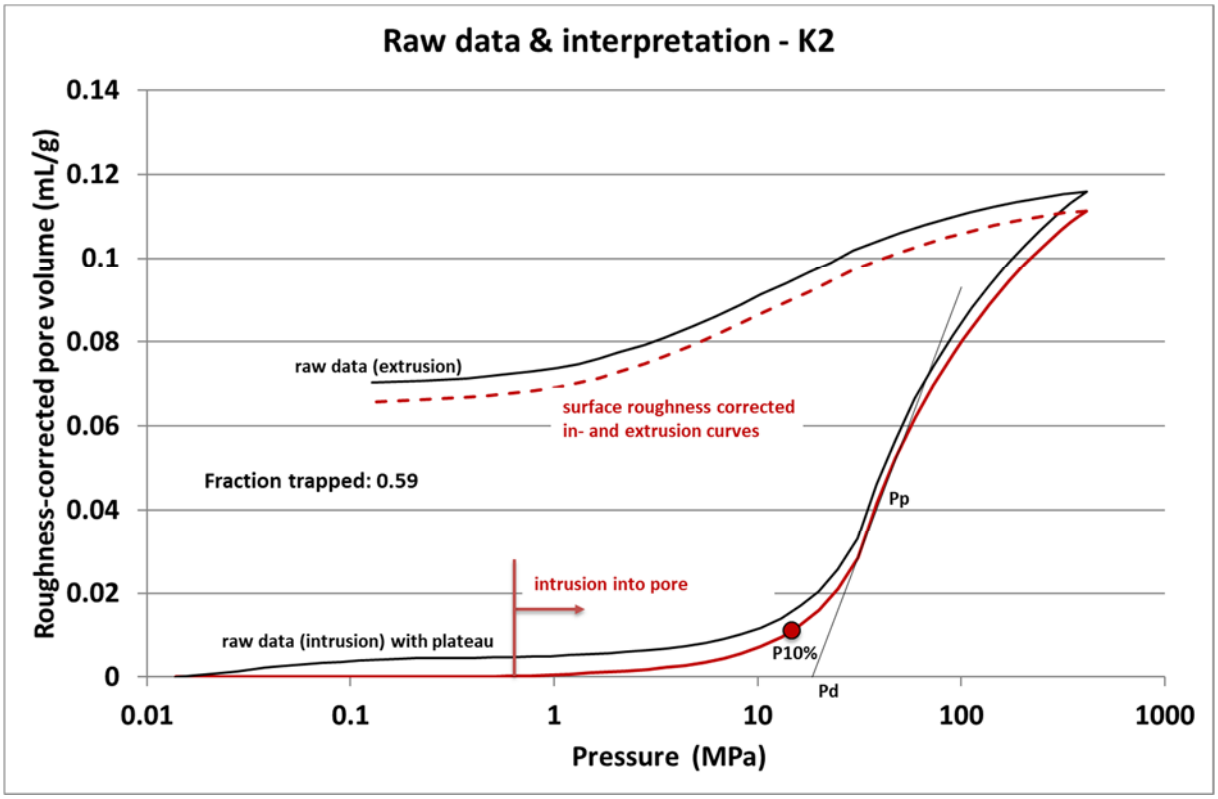

Figure 68: example of a MIP intrusion curve (recorded for sample K2), corrected for surface roughness

A2.8 Soil density determination

Soil density determination is performed according to the Archimedes' principle.

Prior to the measurements, a beaker has to be filled with "Soltrol 130" and temperature equilibrium has to be reached.

Next, per sample 3 solid pieces of approximately 1 cm^3 are cut and the mass of each piece is registered (m_{air}). Next, each sample is placed on the basket, and the mass is registered again (m_{fl}). By using Archimedes' law, the density can now be calculated.

Archimedes stated that "Any object, wholly or partially immersed in a fluid, is buoyed up by a force equal to the weight of the fluid displaced by the object" (see Figure 69).

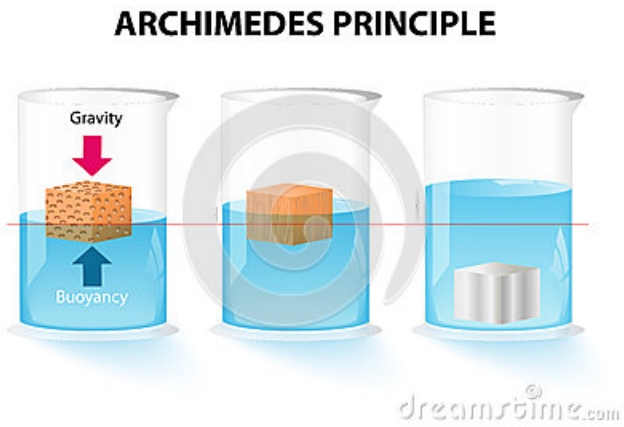

Figure 69: the Archimedes principle (from www.dreamstime.com)

Archimedes' Law can also be written in a different way: if you immerse an object in a liquid, the amount of liquid displaced is equal to the volume of the immersed object.

So:

$V_{liq} = V_{sol}$ with V_{liq} volume of liquid displaced and V_{sol} the volume of the solid. Thus

$m_{liq}/\rho_{liq} = m_{sol}/\rho_{sol}$

So $\rho_{sol} = \rho_{liq}\ m_{sol}/m_{liq}$

With m_{sol} the mass of the solid measured in air which is also written as m_{air}, m_{liq} the difference between the mass measured in air (m_{air}) and in liquid (m_{fl}), ρ_{sol} density of the solid and ρ_{liq} density of the liquid

So $\rho_{sol} = \rho_{liq}\ m_{air}/(m_{air} - m_{fl})$

For the used apparatus, the correct equation is $\rho_{sol} = \rho_{liq}\ m_{air}/(m_{air} - m_{fl}) + 0.0012$

with the density of the Soltrol 130: ρ_{liq} at 20 °C : 0.762

A2.9 Porosity measurement by drying

The total porosity of a saturated clay sample can be calculated from the measured water content. For this purpose, a saturated subsample of approximately 10g fresh clay is taken. The exact mass is registered, and the sample is transferred to an oven at 105°C. The weight is registered regularly and when it is stable, the sample is considered to be dry.

The porosity η can be calculated by using following equation (derivation can be found in Aertsens (2011)) :

$\eta = (m_{wet}-m_{dry})*\rho_{sol} / m_{dry}*\rho_{liq} + (m_{wet}-m_{dry})*\rho_{sol}$

- m_{wet} = mass wet
- m_{dry} = mass dry
- ρ_{sol} = density solid

- ρ_{liq} = density liquid

A2.10 He-pycnometry

The dry density of the samples is measured by using He-pycnometry (AccuPyc II 1340 – Micormeritics). First, samples are dried in a furnace at 105°C. Next, the sample is transferred into one of the available monster cups (1, 3.5 or 10 ml). Then, the monster cup is placed into the apparatus and closed with a screw cap. During the measurement, first the chamber which contains the sample (so a known volume) is filled with helium and the pressure is recorded. Next, the helium is expanded into an adjacent chamber with a well-known internal volume. Based on the pressure in the sample chamber and the pressure in the second chamber after expansion, the solid volume of the sample can be calculated. When also taking into account the weight of the sample, density can be calculated.

$$Vs = Vc + \frac{Vr}{1 - \frac{P1}{P2}}$$

where V_s is the sample volume, V_c is the volume of the empty sample chamber (known from a prior calibration step), V_r is the volume of the reference volume (again known from a prior calibration step), P_1 is the first pressure (i.e. in the sample chamber only) and P_2 is the second (lower) pressure after expansion of the gas into the combined volumes of sample chamber and reference chamber.

ANNEX 3: Measuring the diffusion coefficient of H_2

Applied Geochemistry 61 (2015) 175–184

Contents lists available at ScienceDirect

Applied Geochemistry

journal homepage: www.elsevier.com/locate/apgeochem

Measuring the effective diffusion coefficient of dissolved hydrogen in saturated Boom Clay

E. Jacops [a,b,c,*], K. Wouters [a], G. Volckaert [d], H. Moors [a], N. Maes [a], C. Bruggeman [a], R. Swennen [b], R. Littke [c]

[a] Belgian Nuclear Research Centre (SCK•CEN), Boeretang 200, B-2400 Mol, Belgium
[b] KU Leuven, Dept. of Earth & Environmental Sciences, Celestijnenlaan 200E, 3001 Heverlee, Belgium
[c] EMR|Energy and Mineral Resources Group, Institute of Geology and Geochemistry of Petroleum and Coal, Lochnerstr. 4-20, Haus B, D-52056 Aachen, Germany
[d] Federal Agency for Nuclear Control, AFCN/FANC, B-1000 Brussels, Belgium[1]

ARTICLE INFO

Article history:
Available online 4 June 2015
Editorial handling by Thomas Gimmi

ABSTRACT

Boom Clay is studied as a potential host formation for the disposal of high-and intermediate level long-lived radioactive waste in Belgium. In such a geological repository, generation of gases (mainly H_2 from anaerobic corrosion) will be unavoidable. In order to make a good evaluation of the balance between gas generation vs. gas dissipation for a particular waste form and/or disposal concept, good estimates for gas diffusion coefficients of dissolved gases are essential. In order to obtain an accurate diffusion coefficient for dissolved hydrogen in saturated Boom Clay, diffusion experiments were performed with a recently developed through-diffusion set-up for dissolved gases. Due to microbial activity in the test set-up, conversion of hydrogen into methane was observed within several experiments. A complex sterilisation procedure was therefore developed in order to eliminate microbiological disturbances. Only by a combination of heat sterilisation, gamma irradiation and the use of a microbial inhibitor, reliable, reproducible and accurate $H_2(g)$ diffusion coefficients (measured at 21 °C) for samples oriented parallel ($D_{eff} = 7.25 \times 10^{-10}$ m^2/s and $D_{eff} = 5.51 \times 10^{-10}$ m^2/s) and perpendicular ($D_{eff} = 2.64 \times 10^{-10}$ m^2/s) to the bedding plane were obtained.

1. Introduction

The preferred option adopted by many countries for the long-term management of high- and intermediate level radioactive waste and/or spent fuel is final disposal in a geological repository. In Belgium, no formal decision has been taken yet but for R&D purposes the Belgian radioactive waste management organization ONDRAF/NIRAS considers Boom Clay as a potential host formation for a geological disposal facility. This formation has favourable properties such as a low hydraulic conductivity (Wemaere et al., 2008; Yu et al., 2013), high sorption capacity for many radionuclides (Maes et al., 2004) and self-sealing properties due to its elasto-plastic behaviour (Van Geet et al., 2008).

The production of gas would be unavoidable within a geological repository. Gas is produced by different mechanisms: anaerobic corrosion of metals in waste and packaging, radiolysis of water and organic materials in the packages and microbial degradation of various organic wastes. Anaerobic corrosion and radiolysis yield mainly hydrogen while microbial degradation leads to methane and carbon dioxide (Perko and Weetjens, 2011; Rodwell et al., 1999). In a geological repository, anaerobic corrosion is considered to be the dominant gas production mechanism and consequently hydrogen will be the main gas component. In case of Boom Clay, it is important to note that at the time of hydrogen gas generation, the repository near field is considered to be saturated with pore water (Perko and Weetjens, 2011; Yu et al., 2011).

A part of the generated gas will dissolve in the pore water and will migrate away from the repository by diffusion as dissolved species. If the rate of gas generation is larger than the diffusive flux into the Boom Clay, the pore water within the disposal gallery will become oversaturated and a free gas phase will form. For Boom Clay, tests indicate that the gas entry pressure (e.g. the fluid pressure difference required to overcome capillary forces at the interface between the gas and liquid phases so that the gas can displace the pore water – estimated at approximately 5 MPa) is comparable to the lithostatic pressure (pressure imposed by the weight of the overlying material – 4.5 MPa) at a depth of 225 m. This depth is comparable to the level of HADES URL (High Activity Disposal Experimental Site, underground Research Laboratory) in Mol, Belgium. (Le et al., 2008; Lima et al., 2012). Under repository conditions, evidence by Harrington et al. (2012)

* Corresponding author at: Belgian Nuclear Research Centre (SCK•CEN), Boeretang 200, B-2400 Mol, Belgium. Tel.: +32 14333222.
E-mail address: ejacops@sckcen.be (E. Jacops).
[1] Present address.

http://dx.doi.org/10.1016/j.apgeochem.2015.05.022
0883-2927/

suggests that gas flow will happen through dilatant pathways, corresponding to newly formed porosity. Whether Boom Clay will ever be subject to such high gas pressures depends on many factors: i.e. the gas generation source term, capillary properties and porosity of the repository materials and the (dissolved) gas diffusion coefficient in repository materials and host rock.

The currently available gas diffusion parameters for hydrogen in Boom Clay were obtained from the MEGAS project (Modelling and Experiments on Gas Migration in Repository Host Rocks) (Volckaert et al., 1994). Due to experimental problems like outgassing of the clay, occurrence of a $H_2(g)$ leak and a too short duration of the experiment compared to the length of the samples, only the lumped parameter $\eta R\sqrt{D_{app}}$ (η: diffusion accessible porosity, R: retardation factor, D_{app}: apparent diffusion coefficient) could be obtained from the experimental results and thus only estimations of D_{app} (with a high uncertainty) could be made.

Re-evaluation of the MEGAS data by Aertsens (2009) lead to estimated D_{app} values varying over a wide range: 5×10^{-12} m^2/s and 4×10^{-10} m^2/s.

Sensitivity calculations by Weetjens and Sillen (2006) showed that with this uncertainty on the value of the diffusion coefficient, combined with the uncertainty on the gas source term, the formation of a free gas phase could not be excluded for several waste types. In order to obtain more accurate calculations on the formation of a free gas phase, it is therefore important to provide an accurate diffusion coefficient for dissolved hydrogen. For this purpose, SCK•CEN developed a versatile technique to measure the diffusion coefficient of dissolved gases in low-permeability materials (Jacops et al., 2013) and the accurate measurement of the diffusion coefficient of hydrogen in Boom Clay is the key topic of this study.

2. Hydrogen reactivity and sorption

When performing experiments with hydrogen, one has to take into account that H_2 cannot always be considered as an inert species. In experiments with clayey materials, H_2 can react in an abiotic way, in a biotic way and it can also be sorbed to clay minerals.

Abiotic reactivity is the occurrence of redox reactions in which hydrogen is consumed. In these reactions, hydrogen serves as an electron donor. The reactions which are investigated within the framework of geological disposal in deep clay layers are the reduction of nitrate, sulphate, structural Fe(III) in clay minerals and pyrite (FeS_2) by hydrogen gas. The reduction of nitrate and sulphate by hydrogen is described by Truche et al. (2013) but it is important to consider that both reactions require high temperature (>90 °C) and high H_2 partial pressure (>30 bar). Truche et al. (2010) observed also abiotic reduction of pyrite (FeS_2) to pyrrhotite in the temperature range of 90–180 °C. Another possible redox reaction that can take place in an argillaceous environment is the reaction of Fe(III) with H_2. This Fe(III) can be present as structural Fe(III) in the clay fraction and in contact with H_2, Fe(III) can be reduced to Fe(II) (Didier et al., 2012). However, this reaction has not been demonstrated yet to occur at temperatures lower than 90 °C.

H_2 may also be consumed by micro-organisms (biotic reactivity). Hydrogen is considered as one of the most energetic substrates for microbial life (Libert et al., 2011). Microbial organisms can use H_2 for different redox processes, and under anoxic conditions, the most common reactions are the reduction of NO_3^- to N_2 by denitrifying micro-organisms, the reduction of Fe(III) to Fe(II) by iron-reducing micro-organisms, the reduction of SO_4^{2-} to S^{2-} by sulphate reducing micro-organisms, the reduction of CO_2 to CH_4 by methanogenic micro-organisms (CO_2 (aq) + $4H_2 \leftrightarrow CH_4 + 2H_2O$) and the reduction of CO_2 to acetic acid by acetogenic micro-organisms (Libert et al., 2011). Most of the micro-organisms which are able to metabolize H_2 belong to the Archaea and can survive in extreme conditions (Madigan et al., 2000) so they might occupy certain higher-porosity niches in the repository or host formation (but presumably limited to the disturbed zone).

Besides the abiotic and biotic reactivity of hydrogen, hydrogen can also be sorbed to clay minerals. Most of the research on gas sorption focused on the sorption of CO_2 and CH_4, within the framework of CO_2 storage and shale gas research (Gasparik et al., 2013; Gensterblum et al., 2013; Ghanizadeh et al., 2013). Data on the adsorption of hydrogen on pure clay minerals are rather scarce (Didier et al., 2012). Recently, data on the sorption of hydrogen on dried samples of Callovo-Oxfordian Clay, both raw and purified, have been published by Bardelli et al. (2014).

Dedicated research has been performed on the three possible mechanisms (biotic and abiotic reactivity and sorption behaviour) that affect $H_2(g)$ pressure or concentration on three host rocks which are currently considered for the disposal of radioactive waste: the Belgian Boom Clay, the French Callovo-Oxfordian Clay and the Swiss Opalinus Clay. Results of this research are discussed in the next paragraphs.

The abiotic reactivity of hydrogen with Boom Clay has been studied during the MEGAS project (Volckaert et al., 1994). Results indicate that the reaction capacity of Boom Clay with H_2 is relatively low (range of 10^{-6} mol $H_2(g)$ per g clay) and this abiotic reactivity is considered to have no significant effect on the pressure in a repository. As no sterilisation measures were taken, the occurrence of microbial activity in these experiments cannot be excluded and the disappearance of H_2 might have been provoked by microbial activity.

The biotic reactivity has been described by Ortiz et al. (2002) and Volckaert et al. (1994). Volckaert et al. (1994) performed batch experiments with Boom Clay slurries and hydrogen, and experimental results indicated the conversion of H_2 to CH_4 by methanogenic micro-organisms. Equal observations were reported by Ortiz et al. (2002): in experiments with Boom Clay slurries and iron/stainless steel powder: the hydrogen produced by metal corrosion was converted to methane by methanogenic micro-organisms. Microbial-driven gas conversion is thus a known phenomenon in experiments with hydrogen on Boom Clay samples.

The sorption behaviour of hydrogen on Boom Clay has not yet been investigated.

Dedicated experiments to investigate respectively the sorption and reaction of hydrogen with/on Callovo-Oxfordian clay (a clay rock, considered for geological disposal in France) have been performed by Didier et al. (2012). In order to investigate the reactivity of hydrogen with Callovo-Oxfordian clay (COx), experiments have been performed on dry COx samples, COx samples at different levels of relative humidity (RH) and COx-slurries. Besides the state of the sample, temperature and partial hydrogen pressure used in the experiments were varied. For dry COx, the total amount of hydrogen adsorbed was about 0.05–0.06 wt.% purified COx (at 90 °C). Using an extrapolation of these data, the authors stated that 18.3 m^3 of $H_2(g)$ could be adsorbed per m^3 of COx – based on the sorption efficiency of dry COx powder. For the experiments at different RH, sorption of hydrogen decreased with increasing RH, and at RH 98%, no sorption of hydrogen could be measured (experiment at 25–35 °C, P_{H2} = 0.45 bar). For the slurry experiments (at 27 or 90 °C, P_{H2} between 0.1 and 5.2 bar), the obtained adsorption value of 0.057 wt.% is only an approximation due to complications such as a H_2 leak and reactivity with the reactor material. The abiotic reactivity with hydrogen was investigated with ^{57}Fe Mössbauer Spectrometry for dry COx and slurries. For the dry, raw COx sample no significant reduction was noticed. For the slurry experiments, only at P_{H2} = 5 bar and 90 °C, 9 wt.% of the total Fe was reduced. As a general conclusion, Didier (2012) states that under the conditions of a closed repository, $H_2(g)$ sorption will be

limited and a part of the structural Fe(III) present within the COx can be reduced when the P_{H2} is high enough and at a temperature of approximately 90 °C – but the reduced amount is still low (ca. 9% at P_{H2} = 5 bar). The sorption of hydrogen on Callovo-Oxfordian clay was recently also investigated by Bardelli et al. (2014). Samples (dried, both raw and purified COx) were exposed to a H_2 pressure of 60 bar and the sorption of H_2 was measured volumetrically. Results indicate H_2 sorption up to 0.12% wt. for raw, dried COx and 0.3% wt. for purified COx.

Similar experiments have been performed on the Opalinus Clay, which is considered as a potential host rock for the disposal of radioactive waste in Switzerland. Charlet et al. (2013) investigated the sorption of hydrogen and the reduction of structural Fe(III) by hydrogen on samples of Opalinus Clay. Experiments were performed by adding 5% H_2 (at 9 bar and room temperature) to dry (RH < 17%) and saturated (RH 95 and 98%) samples. Based on the change in gas composition, the amount of sorbed H_2 was determined. For the "dry" samples, ca. 0.02% wt. H_2 was sorbed. For the "saturated" samples, sorption values varied between 0.01 and 0.06% wt. H_2. After finishing the sorption experiment, the powders were sampled for ^{57}Fe Mössbauer Spectrometry to investigate the abiotic reactivity. Results of the "dry" and "saturated" samples indicated a reduction of the structural Fe(III) and approximately 3–4% of the total Fe content was reduced in all samples. To exclude the effect of micro-organisms, the gas phases were also analysed for CH_4 but no CH_4 has been measured so methanogenic micro-organisms are considered to be absent or at least inactive.

In order to study the interaction and transfer of hydrogen under in-situ conditions in the Opalinus Clay, Vinsot et al. (2014) performed an in-situ hydrogen injection experiment in the Mont Terri Underground Research Laboratory. Results showed that hydrogen disappeared much faster than He which was injected simultaneously. Analyses of the water gave indications that hydrogen could be consumed in reactions where also sulphate and iron were reduced. As abiotic reactions do not occur under the experimental conditions, micro-organisms should be involved but hydrogenotrophs have not been identified yet (Vinsot et al., 2014).

In our study, we investigated the transport of dissolved hydrogen gas in saturated Boom Clay by a recently developed through-diffusion technique (Jacops et al., 2013). The possible reaction of H_2(g) with the solid phase or with micro-organisms was not studied in separate batch experiments, but was inferred from the observed behaviour during the diffusion experiment with dissolved hydrogen.

3. Materials and methods

3.1. Through-diffusion technique for dissolved gases

The methodology is described in detail in Jacops et al. (2013) and only the main aspects are repeated in this paper. The principal idea consists of a double through-diffusion test (Shackelford, 1991) with two water reservoirs with dissolved gases placed on opposite sides of a saturated Boom Clay test core (diameter 80 mm, length 30 mm) (Fig. 1). The Boom Clay core is sealed in a stainless steel diffusion cell (constant volume) and is connected via stainless steel filter plates (at both sides) to two water vessels. Both water vessels are pressurized each with a different gas at the same pressure (Fig. 1). In this way no advective flux can occur and the clay sample remains fully water saturated. The water at both sides is circulated over the filters which are in contact with the clay core. The dissolved gas that diffuses into the reservoir on the low-concentration side will equilibrate with the gas in the head spaces and the changes in the gas composition can be measured by e.g. gas chromatography.

Both vessels of the set-up are filled with 500 ml oxygen-free water of 0.014 mol/l $NaHCO_3$ and ca. 500 ml gas at 10 bar pressure. One vessel is filled with Ar(g), the other vessel is filled with H_2(g). For safety reasons, experiments with H_2 are not performed with pure H_2(g) but with a gas mixture of 5% H_2 in Ar (called "Hytec"). In a last step, the entire set-up is checked for its leak tightness by pressurising the set-up with 10 bar gas pressure (Ar at one side, 5% H_2 in Ar at the other side) for at least 4 days. If the pressure is stable during this time period, the set-up is considered to be gastight. During this leak-test, the sample is still isolated from the set-up by closing the valves in order to avoid the ingress of dissolved gas in the sample.

Once the test is started, sampling occurs on a regular basis (generally 1/week) until 10 data points are obtained. The gas composition is analysed with a CP4900 micro GC (VARIAN, Palo Alto, USA). The experiment is performed in a temperature controlled room (21 ± 2 °C).

Once the diffusion experiment has been finished, the hydraulic conductivity (K) is measured. This measurement is performed after the diffusion experiment in order to avoid extra microbial contamination. This K-measurement is done to check if the transport properties of the sample are representative for undisturbed Boom Clay at the Mol site. The method to measure this hydraulic conductivity is described by Wemaere et al. (2008) and reference values for K are summarized in Yu et al.(2013).

3.2. Samples

Boom Clay samples were taken from the cores of the Mol-1 drilling (from a drilling campaign in Mol, in the north-east of Belgium) and their parameters are given in Table 1. The samples originate from the clay-rich Putte Member.

The samples were cored in 1997 and have been stored under anoxic conditions at 4 °C. Prior to their use, they are visually inspected for signs of oxidation which is the main quality threat. Samples are considered to be close to full saturation. During the loading of the diffusion cell, the outer rim (1 cm) and the top and

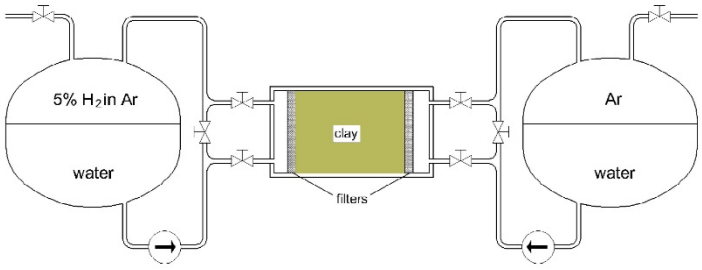

Fig. 1. Schematic design of the set-up to measure the diffusion of dissolved gases.

Table 1
Boom Clay samples used in this study (taken from drill cores from the Mol 1 borehole) orientation is with respect to bedding planes.

Sample n°	86b	87b	91b	95b	96b	100b	127b
Depth (m BDT[a])	235.02–235.12	236.02–236.12	239.99–240.09	243.96–244.06	244.76–244.87	248.78–248.87	275.62–275.72
Orientation	⊥	⊥	⊥	⊥	//	⊥	//

[a] Reference depth is expressed as "meters below drilling table" (BDT). The drilling table was located at 29.73 m T.A.W (Tweede Algemene Waterpassing).

bottom part (3.5 cm) of the clay which might have dried out during storage are removed. After loading in the diffusion cell, the filter chambers at both sides of the clay core are filled with sterile water in order to resaturate the sample.

General mineralogical and physical properties of the Boom Clay are described elsewhere (Maes et al., 2008).

3.3. Measures undertaken to avoid microbial activity in the diffusion experiments

As it is known that microbial activity can complicate the interpretation of diffusion experiments with H_2 in Boom Clay (Volckaert et al., 1994) (Ortiz et al., 2002), several protocols using different (combinations of) sterilisation techniques were followed to avoid microbial activity. In a first attempt, 2 chemicals ($SnCl_2$ and Triclosan) which are known to inhibit microbial activity (Bhargava and Leonard, 1996) were added to the water vessels up to a concentration of 100 mg/l for Triclosan and 0.001 mol/l for $SnCl_2$. During 1 month, the water with inhibitor was circulated over the clay core. Afterwards the water was removed and the set-up was filled with bicarbonate water (0.014 mol/l HCO_3^-) before starting the experiment. In the second attempt, the complete set-up (including the clay sample) was gamma-sterilised with ^{60}Co sources in the RITA irradiation facility, located in Belgian Reactor 2 (BR2) at the site of SCK•CEN (the Belgian Nuclear Research Centre). The total received dose was 39.5 kGy for the set-up with core 87b and 43 kGy for the set-up with core 91b. After irradiation, the gas pressure (Ar and Hytec) was increased from 1 to 10 bar and the experiment was started. In the third attempt, all components of the set-up and the used water were heat-sterilised (15 min at 121 °C). The clay core (95b) was gamma-sterilised before loading into the diffusion cell (43 kGy), and finally (after loading) the complete set-up (without pressure sensors) was again gamma-sterilised for 168 h (received dose: 92.7 kGy). As 2-Bromoethanesulfonate is known as an inhibitor of methanogenesis (Zinder et al., 1984), it was added to the water in the vessels (0.005 mol/l) under sterile conditions. Also the pressure sensors (previously heat sterilised) were installed under sterile conditions. Finally the gas pressure was increased from 1 to 10 bar and to avoid microbial contamination via the gas phase, the gas was injected through a filter (Ultrahigh Purity Gas Filter from Swagelok), which removes all particles >0.003 μm. The same protocol was used for diffusion experiments with samples 127b and 96b.

3.4. Microbial analyses

3.4.1. Analysis of intracellular adenosine triphosphate (ATP)

As an indicator and estimate of microbial metabolic activity, the presence of intracellular adenosine triphosphate (ATP) was analysed in each water sample (water sampled from the water vessels after stopping the diffusion experiment) using the Microbial ATP Kit HS of Biothema (Isogen Life Science, The Netherlands (Lundin 2000)). To neutralize extracellular ATP (e.g. from dead cells), 50 μL of sample was incubated with an equal amount of ATP eliminating reagent for 10 min. Next, 50 μL of a cell lysis solution was added to release the ATP of the viable cells and afterwards the total volume was mixed with 400 μL of ATP reagent HS (containing D-luciferin). Immediately, light intensity (I_{smp}) was measured with a Lumitester C-100 (Kikkoman). Then, 10 μL of 100 nmol L^{-1} ATP standard was added and light intensity was measured again ($I_{smp+std}$). The amount of ATP (pmol) in a sample was calculated as the ratio of I_{smp} to the difference between $I_{smp+std}$ and I_{smp}. Assuming that an average active microbial cell contains 10^{-18} mol ATP, amounts of intracellular ATP were converted to Equivalent Active Cells (EAC), as described by Wouters et al. (2013).

3.4.2. DNA extraction and purification

DNA was extracted from microbial cells using a customised protocol after Tillett and Neilan (2000) and Leuko et al. (2008), and subsequently purified, as described in Wouters et al. (2013). DNA quality and quantity were measured by UV absorbance (Nanodrop).

3.4.3. Polymerase chain reaction (PCR) and agarose gel electrophoresis (AGE)

For polymerase chain reaction (PCR) of the extracted DNA, primers A571F (GCYTAAAGSRICCGTAGC) and UA1204R (TTMGG GGCATRCIKACCT), targeting a region of 836 bp, were selected based on their reported specificity for the Archaea domain (Baker et al., 2003). For all PCR amplifications, approximately 100 ng of DNA was used as a template, mixed with 5 pmol/μL of each primer, and 12.5 μL of GoTaq® Green Master Mix (Promega), completed with molecular grade water to a total reaction volume of 25 μL. PCR comprised of initial denaturation at 94 °C for 2 min, followed by 35 cycles of (1) 94 °C for 1 min, (2) 55 °C for 1 min and (3) 72 °C for 1 min and extension at 72 °C for 10 min.

3.5. Effect of irradiation on the generation of hydrogen within the experimental set-up

It is well known that exposure to ionizing radiation (e.g., gamma irradiation) induces radiolysis of water molecules into H^+ and OH^- radicals. These radicals are chemically reactive and recombine to H_2, O_2 and H_2O_2 (Ershov and Gordeev, 2008). Due to the intensive irradiation of both sample and set-up, H_2 will be generated within the pore water of the sample and in the water phase in the vessels. As the dissolved hydrogen inside the sample will diffuse out of the sample towards the low concentration compartment, this out-diffusion might influence the concentration change in time, and thus the measured diffusion coefficient. In order to investigate the effect of irradiation on the hydrogen diffusion out of the clay core, a blank experiment is performed. In this experiment, the sample and set-up are treated in the same way as in previous diffusion experiments with hydrogen (same preparation and sterilisation procedure), but at both sides an argon gas pressure is applied. Prior to the start of the experiment, the H_2 concentration in both gas phases is measured and during the experiment, the concentration change in time in both vessels is monitored.

3.6. The diffusive transport model

The tests are interpreted with a simple diffusive transport model which is described in detail by Jacops et al. (2013). This

model represents the transport equation in a 1D geometry and it is based on the first and second law of Fick for diffusive transport in porous media. The diffusion-accessible porosity is set at 0.37 (average value derived from migration experiments with the conservative tracer HTO on a series of cores of the Mol-1 drilling (Bruggeman et al., 2013)). The modelling accounts for reduction in pressure in both vessels because of sampling. All calculations are performed with COMSOL Multiphysics® version 3.5a, Earth science module. The diffusion coefficients are obtained by using a least squares fitting procedure to the experimental data with the MATLAB Optimization Toolbox. This toolbox uses a Levenberg–Marquardt method on a Trust region, which is specifically optimised for least square problems. In fact, the model calculates the best fit for 2 products: $D_{pore} \times \eta$ (=D_{eff}) and $R \times \eta$. D_{pore} denotes pore diffusion coefficient, D_{eff} denotes effective diffusion coefficient, R denotes the retardation factor and η denotes porosity. As η is set at 0.37, the values for $D_{eff} = D_{pore} \times \eta$ and R are readily obtained.

The relationship between D_{app} (apparent diffusion coefficient), D_{pore} and D_{eff} is described by Eq. (1).

$$D_{app} = \frac{D_{pore}}{R} = \frac{D_{eff}}{\eta R} \quad (1)$$

The definitions of D_{pore}, D_{eff} and D_{app} can be found in Grathwohl (1998).

4. Results

4.1. Hydraulic conductivity (K)

Measured K-values for the different cores are given in Table 2 and are in line with typical values for Boom Clay (values reported for the Putte and Terhagen Members between 1.5 and 8×10^{-12} m/s (Yu et al., 2013)).

4.2. Diffusion coefficient of H_2

Many attempts were undertaken to measure the diffusion coefficient of H_2(aq). As described in Section 2.3, different procedures to avoid microbial activity (and thus conversion of H_2 into CH_4) were followed. In attempt 1 with core 86b, microbial activity was inhibited by using $SnCl_2$ and Triclosan. After 20 days, CH_4 was measured in the vessel with Hytec gas (5% H_2 and 95% Ar) which indicates microbial activity. As only 2 undisturbed data points (concentration of hydrogen in time) were available, the diffusion coefficient could not be calculated. Before and after the inhibition process, the Sn concentration of the water was measured. For the vessel with hydrogen, 99% of the Sn disappeared from the water phase, for the vessel with Ar, 77% of the Sn disappeared. This can be explained by the sorption of Sn^{2+} on the Boom Clay. The sorption of heavy metals on clay minerals is a known phenomenon which has been described by Bradbury and Baeyens (2005). The concentration of Triclosan was not measured.

In attempt 2 (core 87b and 91b), the set-ups were gamma-irradiated in order to eliminate all micro-organisms. Despite this gamma-irradiation, CH_4 was found in the vessel with hydrogen in both set-ups after 56 days (core 91b) and 76 days (core 87b), respectively. The CH_4 concentration in the vessels with hydrogen increased with time (Fig. 2). The CH_4 concentration in the vessel with Ar was not measured during the experiment.

Considering that 4 mol of H_2 are needed to form 1 mol of CH_4 ($CO_2 + 4\ H_2 \rightarrow CH_4 + 2\ H_2O$) and that the experiments are performed under constant volume conditions, the conversion of H_2 into CH_4 had to lead to a decrease in gas pressure in the vessel where this reaction took place (hydrogen-vessel). In Fig. 3, the pressure of both vessels in the experiment with core 91b is presented as a function of time. Up to approximately day 45, the pressure evolution in the two vessels was similar. Pressure variations are due to small temperature variations and the pressure drops which occur simultaneously in both vessels are due to sampling of the gas phase. After about 45 days, the pressure in the vessel with H_2 decreased more rapidly compared to the pressure in the Ar-vessel.

After dismantling, the water of both set-ups was sampled for microbial investigation: analysis of intracellular ATP gave an indication of the amount of micro-organisms that are metabolically active. Subsequent DNA extraction and PCR indicated which group of micro-organisms were present and might have contributed to the observed activity.

ATP analyses on the water samples (as described by Wouters et al. (2013)) from the experiments with cores 87b and 91b indicated microbial activity in both vessels filled with hydrogen gas (Table 3). Assuming that an equivalent active cell (EAC) contains 10^{-18} mol ATP, microbial cells are present in these cores up to a number of 9.16×10^5 EAC per ml. Extraction and subsequent PCR of the microbial DNA from these water samples suggested that

Table 2
Results for hydraulic conductivity measurements.

	Core 86b	127b	87b	91b	95b	96b
K ($\times 10^{-12}$ m/s)	2.5	3.5	2.3	1.4	2.1	2.6

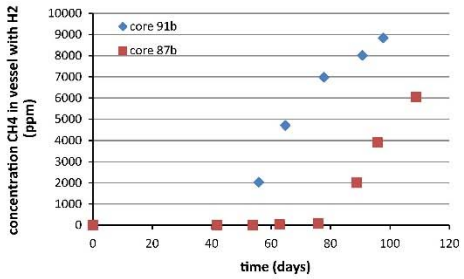

Fig. 2. Evolution of methane concentration for diffusion experiments with cores 87b and 91b.

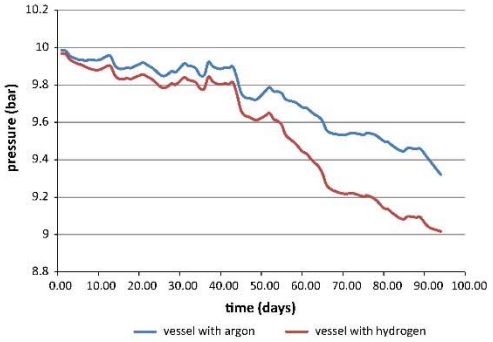

Fig. 3. Pressure evolution (average per day) in the vessels with hydrogen and argon in the experiment with core 91b.

Table 3
ATP measurement of water samples.

Sample	Sterilisation attempt n°	ATP (mol)	Equivalent active cells (cells/ml)
Core 87b vessel with Ar	2	Lower than blank	Lower than blank
Core 87b vessel with H_2	2	4.01×10^{-14}	8.01×10^5
Core 91b vessel with Ar	2	2.50×10^{-15}	5.00×10^4
Core 91b vessel with H_2	2	4.58×10^{-14}	9.16×10^5
Core 95b vessel with Ar	3	Lower than blank	Lower than blank
Core 95b vessel with H_2	3	Lower than blank	Lower than blank
Core 127b vessel with Ar	3	Lower than blank	Lower than blank
Core 127b vessel with H_2	3	Lower than blank	Lower than blank
Core 96b vessel with H_2	3	Lower than blank	Lower than blank

Archaea were present in the vessels with hydrogen and thus presumably responsible for the conversion of H_2 into CH_4 (Thauer, 1998). The microbial presence indicates that the described conversion into CH_4 is likely to be a biotic, and not an abiotic process. In the vessels with Ar, the amount of ATP was about the same value as measured in the blank, so microbes are considered to be inactive or not present in those 2 vessels.

Due to the assumed microbial activity, only 1 undisturbed data point was available in the experiment with core 91b, and 4 undisturbed data points were available in the experiment with core 87b. Based on these 4 data points, the effective diffusion coefficient D_{eff} for dissolved hydrogen for the experiment with core 87b was obtained by curve fitting: $D_{eff} = 1.52 \times 10^{-10}$ m^2/s with a rather large 95% confidence interval between $0.56–4.14 \times 10^{-10}$ m^2/s.

In attempt 3, different measures were undertaken to eliminate all micro-organisms: heat sterilisation, gamma-irradiation, filtration of the gas and addition of an inhibitor. During the experiment, the CH_4 concentration in the vessel with hydrogen was measured weekly.

Experimental results for core 95b are listed in Table 4. The measured data versus the fitted curve are shown in Fig. 4. Only very low background concentrations of CH_4 were measured, probably originating from the irradiation of the Boom Clay (Bonne and Heremans, 1985). For the retardation factor R, a value of = 1.00 was obtained with a 95% confidence interval from 0.79 to 1.28. The larger uncertainty on R can be attributed to the lack of data points during the first days of the experiment.

Experimental results for core 127b are listed in Table 4. The measured data versus the fitted curve are shown in Fig. 5.

Experimental results for core 96b are listed in Table 4. The measured data versus the fitted curve are shown in Fig. 6. The initial concentration of hydrogen in the argon vessel was 49 ppm. This hydrogen was generated during the irradiation process (radiolysis of water) and the background concentration is taken into account in the diffusive model. The effect of irradiation on a diffusion experiment is discussed in the next paragraphs.

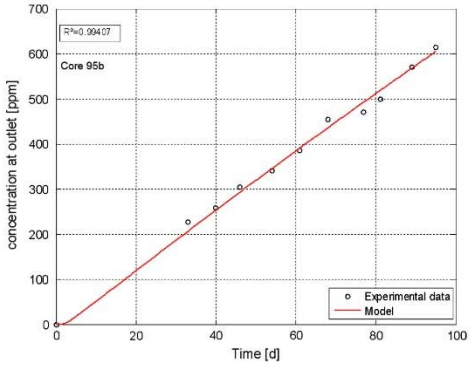

Fig. 4. H_2 concentration evolution in the low concentration vessel, experimental data vs. fitted curve. Best fit of D_{eff} for the H_2 diffusion experiment with core 95b is 2.64×10^{-10} m^2/s.

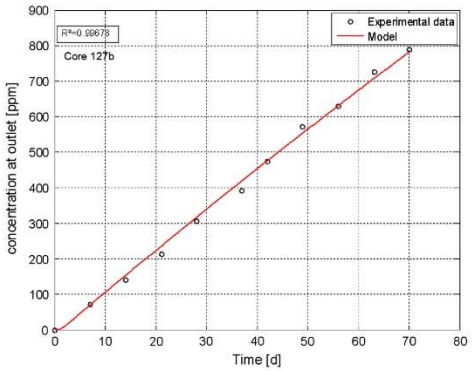

Fig. 5. H_2 concentration evolution in the low concentration vessel, experimental data vs. fitted curve. Best fit of D_{eff} for the H_2 diffusion experiment with core 127b is 5.51×10^{-10} m^2/s.

In order to investigate the effect of irradiation (hydrogen generation) on the diffusion experiments, a blank hydrogen out-diffusion experiment was performed. Initially, the measured concentration of hydrogen in both water vessels was 37 ppm for the left vessel and 54 ppm for the right vessel. After 1 week, a stable value of approximately 59 ppm H_2 was reached in both vessels (Fig. 7). Thus most of the H_2 produced by irradiation originates from radiolysis of the water present in the vessels. The H_2 generated in the clay cores seems to be negligible. As for the diffusion experiments (1) the amount H_2 present in the water vessel before the start of the experiment is known, (2) the data points are obtained at earliest after 7 days and thus in the steady-state phase

Table 4
Overview of measured diffusion coefficients and the 95% confidence interval.

	87b	95b	96b	127b
D_{eff} H_2 ($\times 10^{-10}$ m^2/s)	1.52	2.64	7.25	5.51
95% confidence interval ($\times 10^{-10}$ m^2/s)	0.56–4.14	2.43–2.86	6.99–7.55	5.40–5.62
Methane measured	Yes	Low background concentration	No	No
Microbial activity (based on ATP analyses of water)	Yes	No	No	No

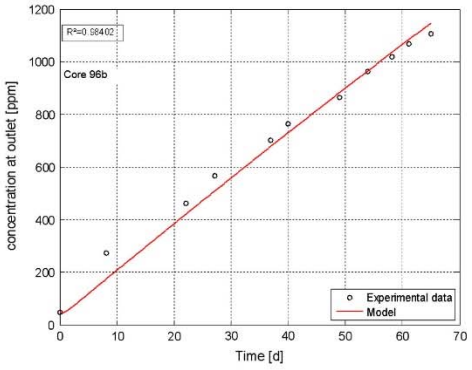

Fig. 6. H_2 concentration evolution in the low concentration vessel, experimental data vs. fitted curve. Best fit of D_{eff} for the H_2 diffusion experiment with core 96b is 7.25×10^{-10} m^2/s.

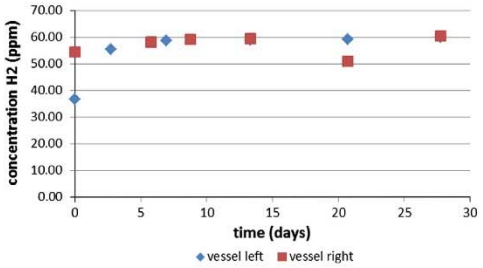

Fig. 7. Out-diffusion of H_2 after irradiation.

and (3) the diffusion coefficient is calculated based on the slope of the data points curve, a reliable diffusion coefficient can be obtained by taking into account the initial concentration of hydrogen.

The concentration of hydrogen in the water vessels could be reduced by replacing the gas phase after irradiation more often than foreseen in the procedure. A good example of the effect of gas phase replacement was the experiment with sample 127b. After replacing the gas phase 30×, the concentration of hydrogen in the Ar vessel was 33 ppm. Due to a leaking pressure sensor, the Ar vessel was opened very shortly and the pressure sensor was replaced. Afterwards, the gas phase of the Ar vessel was replaced for another 40× and the concentration of hydrogen was strongly decreased to 3 ppm. So the background concentration of hydrogen can be reduced by increasing the number of gas replacements, but one should also allow the dissolved hydrogen to equilibrate with the new gas phase.

5. Discussion and conclusions

As reported in literature and summarized in the introduction, hydrogen cannot always be considered as an inert species. Hydrogen can react in an abiotic and biotic way, and it can sorb to clayey materials. The relevance of these different reaction mechanisms for the diffusion experiments with Boom Clay is discussed in the next paragraphs.

Microbial activity in the diffusion experiments with hydrogen was noticed in several lab experiments. But not only lab experiments suffer from microbial conversion of H_2, also in-situ experiments can be disturbed. A good example was reported by Vinsot et al. (2014). Microbial conversion of H_2 was encountered in an in-situ gas injection experiment in the Opalinus Clay. Due to this microbial conversion, they were not able to determine a diffusion coefficient for H_2. In general, microbial conversion of H_2 into CH_4(g) is well noticed in our experiments as it leads to a pressure drop and the production of methane. This has been observed in the experiments with cores 86b (sterilisation attempt 1), 87b and 91b (sterilisation attempt 2). Only after a very thorough sterilisation procedure, microbial H_2(g) conversion could be avoided. ATP analyses of the experiment on cores 95b, 96b and 127b (sterilisation attempt 3) indicated no microbial activity; consequently we consider the diffusion coefficients obtained in these experiments to be undisturbed by microbial reaction.

With respect to abiotic reactivity of hydrogen, mainly redox reactions were noted in previous studies. In literature, information on the abiotic reactivity of hydrogen in Boom Clay is scarce, only Volckaert et al. (1994) reported a low reaction capacity of H_2 with Boom Clay and even this low reaction capacity might be an overestimation because possible H_2 consumption due to microbial activity was not taken into account. Therefore information on possible abiotic reactivity of hydrogen with Boom Clay has to be derived from literature (see Section 2) and in order to determine which abiotic reactions could be possible under the conditions of the diffusion experiments (room temperature, saturated Boom Clay and P_{H2} = 0.5 bar), a comparison is made with the in literature reported conditions. The abiotic reduction of nitrate and sulphate by hydrogen requires high temperature (>90 °C) and high H_2 partial pressures (>30 bar) (Truche et al., 2013, 2009). According to Norris et al. (2013) the in-situ reactivity of hydrogen with nitrate and sulphate can be considered as limited and Didier (2012) states as well that the reaction of sulphate (and also carbonates) with hydrogen is extremely slow. As our diffusion experiments are performed at room temperature and 0.5 bar H_2(g) partial pressure, the described reactivity is also considered to be limited. Hydrogen may also reduce structural Fe(III) as observed for Opalinus Clay (Charlet et al., 2013) and Callovo-Oxfordian Clay (Didier, 2012). Didier (2012) states that for COx, under the conditions of a closed repository, reduction of structural Fe(III) can only occur when the P_{H2} is high enough and temperature reaches values of at least 90 °C. In Opalinus Clay, Charlet et al. (2013) observed reduction of structural Fe(III) in low saturated samples at room temperature and at P_{H2} = 0.45 bar. Given this information, it cannot be excluded that reduction of Fe(III) also takes place in Boom Clay.

But, since no signs of H_2(g) removal were noticed in the current diffusion experiments, (i.e. no unexpected pressure drop in core 95b – Fig. 8), no significant abiotic reactivity should have occurred. However, it cannot be ruled out that the reduction of Fe(III) did happen at trace levels but no spectroscopic analysis was performed to check for the reduction of Fe(III). As abiotic reactivity is considered to be small and probably insignificant, the effect on the diffusion experiment is considered to be negligible.

Concerning the sorption of hydrogen, no information for Boom Clay is available in literature. When looking at the data reported in Section 2, one has to take into account that the reported experiments on Callovo-Oxfordian Clay were performed under dry conditions whereas in our diffusion experiments, the clay sample is completely water-saturated before and during the experiment. It is known from other studies (Gensterblum et al., 2013; Ryan, 2006) that the presence of water (moisture) also influences the sorption capacity of gases. The effect of moisture content on the sorption capacity was investigated in the experiments on Opalinus Clay by conditioning the clay powders at different

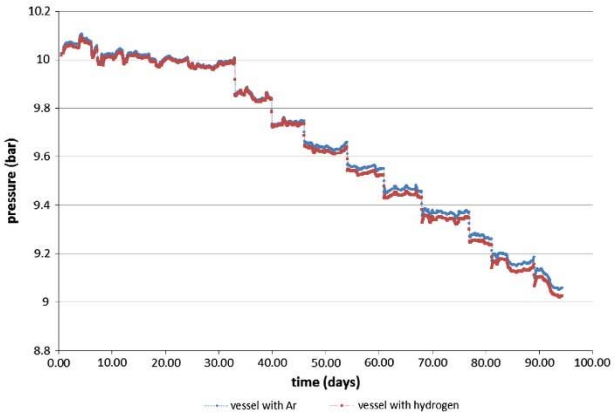

Fig. 8. Pressure evolution (average per hour) in the vessels with hydrogen and argon in the experiment with core 95b. Pressure variations are due to small temperature variations and the pressure drops which occur simultaneously in both vessels are due to sampling.

Table 5
Rock factors for H_2 and HTO for samples 95b, 96b and 127b.

Sample	Orientation	R_f (H_2)	R_f (HTO)
95b	⊥	7.2	9.7[a]
96b	//	2.6	4.1[a]
127b	//	3.4	3.3

[a] As no experimental D_{eff} (HTO) is available for this sample, literature data from Bruggeman et al. (2013) are used.

relative humidity levels but no relationship could be found between the degree of saturation and the sorption of H_2. Another difference with the sorption experiments described by Didier et al. (2012), Charlet et al. (2013) and Bardelli et al. (2014) is the state of the samples: the Boom Clay sample was mounted as bulk core, and not as a reconstituted powdered sample like in the experiments reported for the Callovo-Oxfordian Clay and Opalinus Clay. Due to differences in experimental conditions, no direct extrapolation of H_2 sorption behaviour to Boom Clay can be made, but sorption of H_2 on Boom Clay cannot be excluded. However, as no signs of H_2(g) removal were noticed in the current diffusion experiments, no significant sorption of H_2 is expected in the diffusion experiments and the effect on the diffusion coefficients is considered to be negligible.

For Boom Clay, Jacops et al. (2013) reported diffusion coefficients for dissolved He and CH_4 (Mol-1 drilling; sample 86b; depth 235.02–235.12 m BDT; oriented perpendicular to bedding plane). Considering a fixed porosity of 37%, the reported diffusion coefficients are D_{eff} (He) = 4.51×10^{-10} m^2/s and D_{eff} (CH_4) = 0.90×10^{-10} m^2/s. The diffusion coefficient for H_2 for a sample also oriented perpendicular to bedding plane (sample 95b) is D_{eff} (H_2) = 2.64×10^{-10} m^2/s which is in between the diffusion coefficients of He and CH_4. A similar trend is observed in the D_0 (molecular diffusion coefficient in pure water – in m^2/s) for the considered gases (D_0 (He) = 7.28×10^{-9} m^2/s and D_0 (CH_4) = 1.84×10^{-9} m^2/s) (Boudreau, 1997).

The rock factor is often seen as a characteristic for the porous medium (Grathwohl, 1998) and it provides information on the diffusion pathway geometry. The rock factor (R_f) is calculated according to

$$R_f = \eta \cdot D_0/D_{eff} \quad (2)$$

with η the diffusion accessible porosity and D_0 (molecular diffusion coefficient in pure water – in m^2/s). Values for D_0 (H_2) = 5.11×10^{-9} m^2/s; D_0 (HTO) = 2.22×10^{-9} m^2/s can be found in Boudreau (1997).

For the diffusion of HTO in Boom Clay, Bruggeman et al. (2013) reported values of $D_{eff} = 0.85 \times 10^{-10}$ m^2/s for diffusion perpendicular to bedding plane and $D_{eff} = 2.02 \times 10^{-10}$ m^2/s for diffusion parallel to bedding plane. This leads to $R_f = 9.7$ perpendicular to bedding plane and $R_f = 4.1$ parallel to bedding plane.

Only for sample 127b, the diffusion coefficient for HTO is measured as well ($D_{eff} = 2.53 \times 10^{-10}$ m^2/s), which leads to an $R_f = 3.3$. For the same sample, the R_f for H_2 is 3.4 (Table 5).

For the samples oriented parallel to bedding plane (96b and 127b), the R_f values for H_2 are in line with the value derived from literature for HTO. For sample 95b (⊥ sample) the R_f value compares to the R_f value for HTO as calculated from literature.

The ratio (D_{eff} H_2/D_{eff} HTO)/(D_0 H_2/D_0 HTO) can provide some information on the diffusion characteristics. A large ratio (≫1) is related to surface enhanced diffusion, while a small ratio (between 0.1 and 0.25) is related to anion exclusion. Examples of both phenomena and their effect on the ratio can be found in Jacquier et al. (2013). When calculating the ratio for samples 95b, 96b and 127b, the obtained values are respectively 1.4, 1.6 and 0.9. For samples 95b and 96b for which there is no experimental D_{eff} for HTO available, the literature value from Bruggeman et al. (2013) is used. All ratios are around 1 which points out that there are no clear indications for either anion exclusion or surface enhanced diffusion.

The average anisotropy ratio (=average D_{eff} of samples 96b and 127b/D_{eff} of sample 95b) is 2.39 which is in good agreement with the anisotropy ratio's reported for HTO (2–3) (Bruggeman et al., 2013) and Iodide (2.7) (Bruggeman et al., 2010).

All measured diffusion coefficient are representative for the Putte and Terhagen Members of the Boom Formation which form the most clayey and homogeneous part of the Boom Clay. Bruggeman et al. (2013) reported diffusion coefficients for HTO for the entire Boom Formation. For the section of Boom Clay between 191 and 281 m depth (below drilling table), the diffusion coefficient for HTO shows a very limited variation. This zone comprises the Putte Member, Terhagen Member and the upper part of the Belsele-Waas Member. Diffusion coefficients for HTO for the more silty layers (Voort/Eigenbilzen layer and the lower part of the Belsele-Waas Member) are higher. As HTO and dissolved H_2

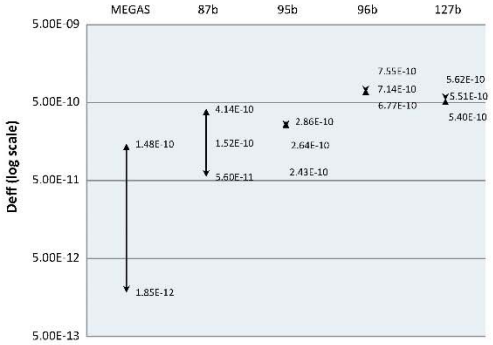

Fig. 9. Comparison of diffusion coefficients for H_2 (triangles) and their uncertainty (arrows) (measured on Boom Clay during different experiments). For "MEGAS" and "87b" only the uncertainty range is shown.

are expected to have a similar diffusive behaviour, the diffusion coefficient for H_2 for these layers might also be higher. The parameter which varies most over the entire Boom Clay formation is the hydraulic conductivity. A difference of more than one order of magnitude exists between the homogeneous clayey and the more silty layers. But large differences in hydraulic conductivity are not reflected in large differences in HTO diffusion coefficients (Bruggeman et al., 2013). To compare: the difference in hydraulic conductivity between sand and compacted clay is 10 orders of magnitude whereas the difference between diffusion in free water (D_0) and diffusion in compacted clay is generally around 10 or even less. The impact of spatial variability of the diffusion coefficient on the flux of dissolved species is limited (up to 25% maximum for the system considered by Huysmans and Dassargues (2006)). By using the diffusion coefficients for H_2 over the entire formation, the removal of gas might be slightly underestimated, which is conservative when studying the impact of potential gas pressure build-up in a repository.

To summarize the results, one can state that major progress has been made with respect to the uncertainty on the diffusion coefficient for dissolved hydrogen in saturated Boom Clay (Fig. 9). By combining the new experimental set-up (Jacops et al., 2013) with a complex sterilisation procedure, an accurate diffusion coefficient with a narrow 95% confidence interval for dissolved hydrogen in saturated Boom Clay was obtained for 3 different samples with different orientation with respect to bedding planes. Within the diffusion experiments, no significant abiotic reactivity or sorption of H_2 was observed and a possible effect on the diffusion coefficient is considered to be negligible. Due to the use of a sterilisation procedure, the experimental results are microbial undisturbed. The obtained diffusion coefficients will be used in future mass balance type screening calculations for relevant radioactive waste types.

Acknowledgements

This work is performed in close cooperation with, and with the financial support of ONDRAF/NIRAS, the Belgian Agency for Radioactive Waste and Fissile Materials, as part of the programme on geological disposal of high-level/long-lived radioactive waste that is carried out by ONDRAF/NIRAS. This work has been performed with the support of Tom Maes, Louis van Ravestyn, Serge Labat, Arno Grade, Joan Govaerts, Eef Weetjens, Andrei Gussarov, Steven Van Looven and Xavier Sillen.

References

Aertsens, M., 2009. Re-evaluation of the experimental data of the MEGAS experiment on gas migration through Boom Clay., SCK-CEN ER-100. SCK-CEN, Mol, Belgium. <http://hdl.handle.net/10038/1182>.
Baker, G., Smith, J., Cowan, D., 2003. Review and re-analysis of domain-specific 16S primers. J. Microbiol. Methods 55, 541–555.
Bardelli, F., Mondelli, C., Didier, M., Vitillo, J.G., Cavicchia, D.R., Robinet, J.-C., Leone, L., Charlet, L., 2014. Hydrogen uptake and diffusion in Callovo-Oxfordian clay rock for nuclear waste disposal technology. Appl. Geochem.
Bhargava, H.N., Leonard, P.A., 1996. Triclosan: applications and safety. Am. J. Infect. Control 24, 209–218.
Bonne, A., Heremans, R., 1985. A decade of research and development studies on the disposal of the high level and alpha-bearing waste in a deep clay formation. Radioactive Waste Manage. Nucl. Fuel Cycle 6 (3–4), 277–291.
Boudreau, B., 1997. Diagenetic Models and their Implementation. Springer, Berlin.
Bradbury, M., Baeyens, B., 2005. Modelling the sorption of Mn(II), Co(II), Ni(II), Zn(II), Cd(II), Eu(III), Am(III), Sn(IV), Th(IV), Np(V) and U(VI) on montmorillonite: linear free energy relationships and estimates of surface binding constants for some selected heavy metals and actinides. Geochim. Cosmochim. Acta 69, 875–892.
Bruggeman, C., Maes, N., Aertsens, M., De Canniere, P., 2013. Tritiated water retention and migration behaviour in Boom Clay – SFC1 level 5 report: First Full Draft. Status 2009., SCK-CEN-ER248. SCK-CEN, Mol, Belgium. <http://hdl.handle.net/10038/8308>.
Bruggeman, C., Aertsens, M., Maes, N., Salah, S., 2010. Iodine retention and migration behaviour in Boom Clay – Topical report, First Full Draft. SCK-CEN ER-119, SCK-CEN, Mol, Belgium.
Charlet, L., Bureau, S., Didier, M., Grenche, J., Vinsot, A., 2013. HT Experiment: Sorption d'hydrogène gazeux sur l' argilite Opalinus de Mont Terri. Mont-Terri project Technical Note 2012-90, Switzerland.
Didier, M., 2012. Etude du transfert réactif de l'hydrogène au sein de l'argilite, l'Ecole Doctorale: ISTerre, Univers, Environnement. Universit de Grenoble, Grenoble, Grenoble.
Didier, M., Leone, L., Greneche, J.M., Giffaut, E., Charlet, L., 2012. Adsorption of hydrogen gas and redox processes in clays. Environ. Sci. Technol. 46, 3574–3579.
Ershov, B., Gordeev, A., 2008. A model for radiolysis of water and aqueous solutions of H_2, H_2O_2 and O_2. Radiat. Phys. Chem. 77, 928–935.
Gasparik, M., Bertier, P., Gensterblum, Y., Ghanizadeh, A., Krooss, B., Littke, R., 2013. Geological controls on the methane storage capacity in organic-rich shales. Int. J. Coal Geol. 123, 34–51.
Gensterblum, Y., Merkel, A., Busch, A., Krooss, B.M., 2013. High-pressure CH_4 and CO_2 sorption isotherms as a function of coal maturity and the influence of moisture. Int. J. Coal Geol. 118, 45–57.
Ghanizadeh, A., Amann-Hildenbrand, A., Gasparik, M., Gensterblum, Y., Krooss, B., Littke, R., 2013. Experimental study of fluid transport processes in the matrix system of the European organic-rich shales: II. Posidonia Shale (Lower Toarcian, northern Germany). Int. J. Coal Geol. 123, 20–33.
Grathwohl, P., 1998. Diffusion in Natural Porous Media: Contaminant Transport, Sorption/desorption and Dissolution Kinetics. Kluwer Academic Publishers.
Harrington, J., Milodowski, A., Graham, C., Rushton, J., Cuss, R., 2012. Evidence for gas-induced pathways in clay using a nanoparticle injection technique. Mineral. Mag. 76, 3327–3336.
Huysmans, M., Dassargues, A., 2006. Stochastic analysis of the effect of spatial variability of diffusion parameters on radionuclide transport in a low permeability clay layer. Hydrogeol. J. 14, 1094–1106.
Jacops, E., Volckaert, G., Maes, N., Weetjens, E., Govaerts, J., 2013. Determination of gas diffusion coefficients in saturated porous media: He and CH_4 diffusion in Boom Clay. Appl. Clay Sci. 83–84, 217–223.
Jacquier, P., Hainos, D., Robinet, J., Herbette, M., Grenut, B., Bouchet, A., Ferry, C., 2013. The influence of mineral variability of Callovo-Oxfordian clay rocks on radionuclide transfer properties. Appl. Clay Sci. 83–84, 129–136.
Le, T., Tang, A., Romero, E., Delage, P., Gens, A., Li, X., Cui, Y., Lima, A., 2008. Water retention properties of Boom clay. In: Toll, D., Augarde, C., Gallipoli, D., Wheeler, S. (Eds.), Unsaturated Soils. Advances in Geo-Engineering. Taylor & Francis, London, pp. 229–234.
Leuko, S., Goh, F., Ibanezz-Peral, R., Burns, B.P., Walter, M.R., Neilan, B.A., 2008. Lysis efficiency of standard DNA extraction methods for *Halococcus* spp. in an organic rich environment. Extremophiles 12, 301–308.
Libert, M., Bildstein, O., Esnault, L., Jullien, M., Sellier, R., 2011. Molecular hydrogen: an abundant energy source for bacterial activity in nuclear waste repositories. Phys. Chem. Earth, Parts A/B/C 36, 1616–1623.
Lima, A., Romero, E., Pina, Y., Gens, A., Li, X., 2012. Water retention properties of two deep belgian clay formations. In: Mancuso, C., Jommi, C., D'Onza, F. (Eds.), Unsaturated Soils: Research and Applications. Springer, Berlin Heidelberg, pp. 179–184.
Madigan, M., Martinko, J., Parker, J., 2000. Brock Biology of Microorganisms, nineth edition. Prentice Hall, New-Jersey.
Maes, N., Salah, S., Jacques, D., Aertsens, M., Van Gompel, M., De Canniere, P., Velitchkova, N., 2008. Retention of Cs in Boom Clay: comparison of data from batch sorption tests and diffusion experiments on intact clay cores. Phys. Chem. Earth 33, S149–S155.
Maes, N., Wang, L., Delcault, G., Beauwens, T., Van Geet, M., Put, M., Weetjens, E., Marivoet, J., Van der Lee, J., Warwick, P., Hall, A., Walker, G., Maes, A.,

Bruggeman, C., Bennett, D., Hicks, T., Higgo, J., Galson, D., 2004. Migration Case Study: Transport of radionuclides in a Reducing Clay Sediment (TRANCOM 2) Contract No FIKW-CT-2000-00008, EUR-21022, Luxembourg. <http://bookshop.europa.eu/en/migration-case-study-pbKINA21022/>.

Norris, S., Lemy, F., del Honeux, C., Volckaert, G., Weetjens, E., Wouters, K., Wendling, J., Dymitrowska, M., Pellegrini, D., Sellin, P., Johnson, L., Sentis, M. and Harrington, J., 2013. Synthesis report: updated treatment of gas generation and migration in the safety case, EC FORGE Project Milestone M68, Luxembourg. <http://www.bgs.ac.uk/forge/docs/reports/D1.5-R.pdf>.

Ortiz, L., Volckaert, G., Mallants, D., 2002. Gas generation and migration in Boom Clay, a potential host rock formation for nuclear waste storage. Eng. Geol. 64, 287–296.

Perko, J., Weetjens, E., 2011. Thermohydraulic analysis of gas generation in a disposal facility for vitrified high-level radioactive waste in Boom Clay. Nucl. Technol. 174, 401–410.

Rodwell, W., Harris, W., Horseman, S., Lalieux, P., Miller, W., Ortiz, L., Pruess, K., 1999. Gas migration and two-phase flow through engineered and geological barriers for a deep repository for radioactive waste, Luxembourg.

Ryan, B., 2006. A discussion on moisture in coal implications for coalbed gas and coal utilization. Summary of Activities: BC Ministry of Energy, Mines and Petroleum Resources pages, 139–149.

Shackelford, C., 1991. Laboratory diffusion testing for waste disposal: a review. J. Contam. Hydrol. 7, 177–217.

Thauer, R., 1998. Biochemistry of methanogenesis: a tribute to Marjory Stephenson. Microbiology 144, 2377–2406.

Tillett, D., Neilan, B., 2000. Xanthogenate nucleic acid isolation from cultured and environmental cyanobacteria. J. Phycol. 36, 251–258.

Truche, L., Berger, G., Albrecht, A., Domergue, L., 2013. Engineered materials as potential geocatalysts in deep geological nuclear waste repositories: a case study of the stainless steel catalytic effect on nitrate reduction by hydrogen. Appl. Geochem.

Truche, L., Berger, G., Destrigneville, C., Guillaume, D., Giffaut, E., 2010. Kinetics of pyrite to pyrrhotite reduction by hydrogen in calcite buffered solutions between 90 and 180C: implications for nuclear waste disposal. Geochim. Cosmochim. Acta 74, 2894–2914.

Truche, L., Berger, G., Destrigneville, C., Pages, A., Guillaume, D., Giffaut, E., Jacquot, E., 2009. Experimental reduction of aqueous sulphate by hydrogen under hydrothermal conditions: implication for the nuclear waste storage. Geochim. Cosmochim. Acta 73, 4824–4835.

Van Geet, M., Bastiaens, W., Ortiz, L., 2008. Self-sealing capacity of argillaceous rocks: review of laboratory results obtained from the SELFRAC project. Phys. Chem. Earth, Parts A/B/C 33 (Supplement 1), S396–S406.

Vinsot, A., Appelo, C.A.J., Lundy, M., Wechner, S., Lettry, Y., Lerouge, C., Fernandez, A.M., Labat, M., Tournassat, C., De Canniere, P., Schwyn, B., Mckelvie, J., Dewonck, S., Bossart, P., Delay, J., 2014. In Situ Diffusion Test of Hydrogen Gas in the Opalinus Clay. Geological Society, London, Special Publications, 400.

Volckaert, G., Ortiz, L., De Cannire, P., Put, M., Horseman, S., Harrington, J., Fioravante, V., Impey, M., 1994. MEGAS modelling and experiments on gas migration in repository host rocks. Final Report Phase 1, Luxembourg. <http://bookshop.europa.eu/en/megas-pbCGNA16235/?CatalogCategoryID=DjYKABstgckAAAEjwpEY4c5L>.

Weetjens, E., Sillen, X., 2006. Gas generation and migration in the near field of a supercontainer-based disposal system for vitrified high-level radioactive waste. 11th International High-level Radioactive Waste Management Conference (IHLRWM), Montpellier.

Wemaere, I., Marivoet, J., Labat, S., 2008. Hydraulic conductivity variability of the Boom Clay in north-east Belgium based on four core drilled boreholes. Phys. Chem. Earth, Parts A/B/C 33 (Supplement 1), S24–S36.

Wouters, K., Moors, H., Boven, P., Leys, N., 2013. Evidence and characteristics of a diverse and metabolically active microbial community in deep subsurface clay borehole water. FEMS Microbiol. Ecol., n/a-n/a

Yu, L., Rogiers, B., Gedeon, M., Marivoet, J., De Craen, M., Mallants, D., 2013. A critical review of laboratory and in-situ hydraulic conductivity measurements for the Boom Clay in Belgium. Appl. Clay Sci. 75–76, 1–12.

Yu, L., Weetjens, E., Perko, J., Mallants, D., 2011. Comparison of numerical tools through thermo-hydro-gas transport modeling for a geological repository in Boom Clay. Nucl. Technol. 174, 411–423.

Zinder, S.H., Anguish, T., Cardwell, S.C., 1984. Selective-inhibition by 2-bromoethanesulfonate of methanogenesis from acetate in a thermophilic anaerobic digester. Appl. Environ. Microbiol. 47, 1343–1345.

ANNEX 4: Detailed petrographical description of the samples of the Boom Clay and the Eigenbilzen Sands.

A4.1 CT imaging (medical CT)

All samples of the Boom Clay and Eigenbilzen Sands have been investigated by CT scanning (medical CT, Siemens Somatom Flash Scanner, located in the University hospital in Leuven). All samples of the Boom Clay contain large amounts of pyrite, which are (due to the large x-ray adsorption capacity of pyrite) coloured in white on the images.

Pyrite is clearly present in all of the samples, but it appears in different forms. Mostly, pyrite is present as individual spots, or as thin, white filaments which is observed in all our samples. Pyrite can also be present in thick, white wires such as in sample K9, or it can be present as aggregates/nodules such as in samples K14 and K4 (Figure 72).

The pyrite filaments are probably pyritised wormholes. When a worm is moving trough the clay, it leaves behind a hole which is covered with mucus. When conditions become reducing, sulphate reducing bacteria will become active and they will use the organic matter of the mucus to convert sulphate to sulphide (in fact H_2S). The wall of these bacteria is negatively charged, so they will attract positively charged cations such as Fe^{2+}. As described earlier, this entire process leads to the production of pyrite and this explains why the occurrence of pyrite is linked to the presence of wormholes.

In some cases, the pyrite observations in the CT images can be linked to visual observations. For instance, the pyrite aggregate, seen in the CT images of sample K4 (Figure 72) was also visually observed in Figure 70.

Figure 70: visual observation of pyrite in sample K4

In sample K10, a pyritised wormhole is running from the top to the bottom of the sample. In Figure 71, it can be observed that a piece of pyrite dropped out of the sample and this was the upper part of the wormhole. The orange rim around the hole points to the presence of iron oxides which were formed due to the exposure to oxidising atmospheric air.

Figure 71: visual observation of sample K10: a piece of pyrite fell out of the sample, leaving a hole. Due to oxidation around that hole a brown zone was left behind, pointing to the presence of iron oxides.

From Figure 72, it is clear that in general, the samples from the Eigenbilzen Sands contain less pyrite, as it is only seen in some local spots, and not spread all over the samples as the case in the Boom Clay samples. Sample K14 containes a very large pyrite nodule, which causes a beam hardening artefact in the CT-images over the rest of the sample.

No distinction can be made between the two main mineral phases (quartz and 2:1 clay minerals) as their size is clearly below the resolution of the applied technique.

In sample K16, pores can be observed (black zones) and they can be found all over the sample. The samples of the Eigenbilzen Sands also show darker patches, which are not present in the Boom Clay samples. Mostly, the shape of these samples is not perfectly round. Due to the increased sand content, the samples are more plastic and have been deformed during the unloading of the diffusion cell and later sample treatment.

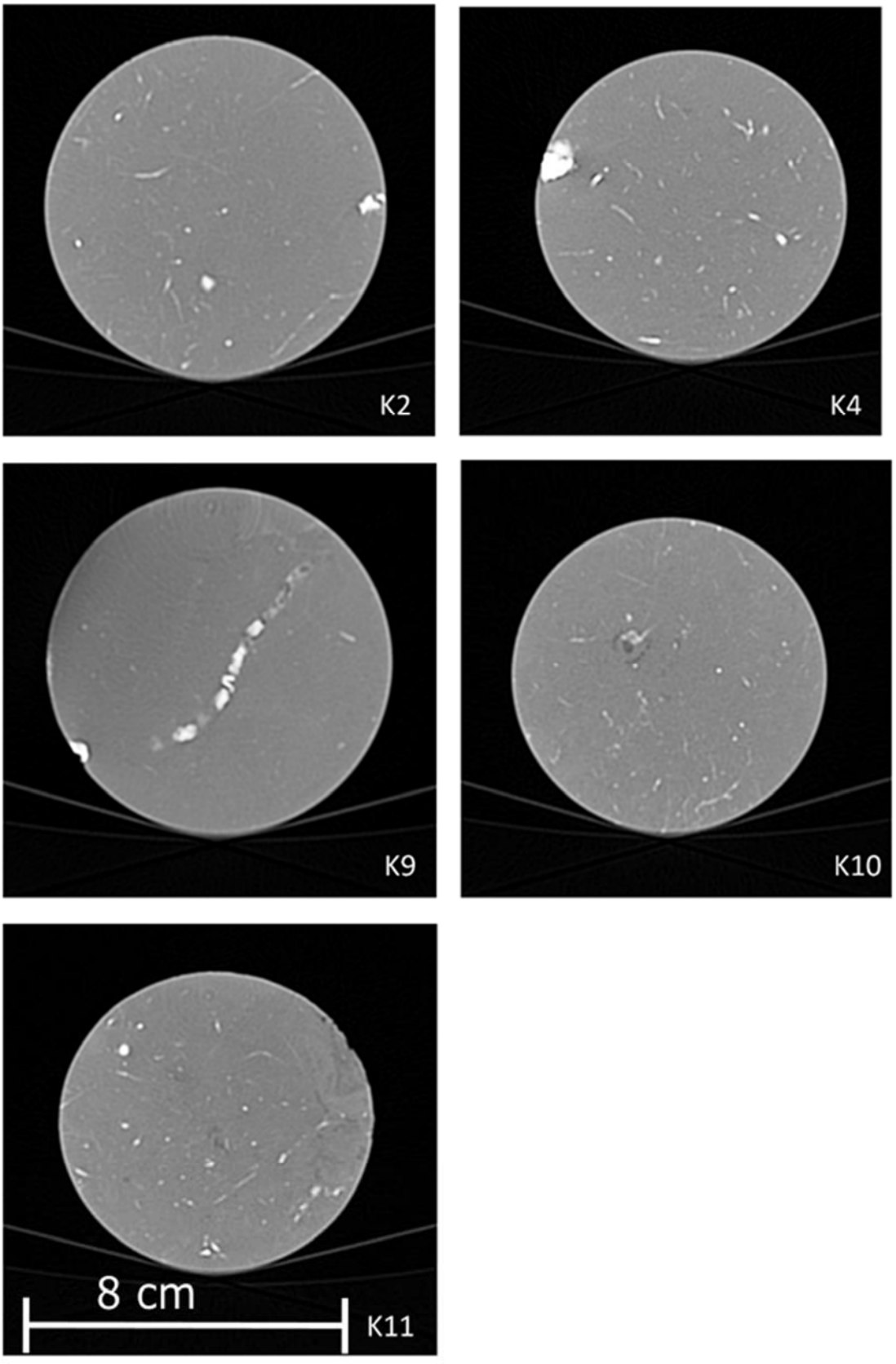
K2
K4
K9
K10
8 cm
K11

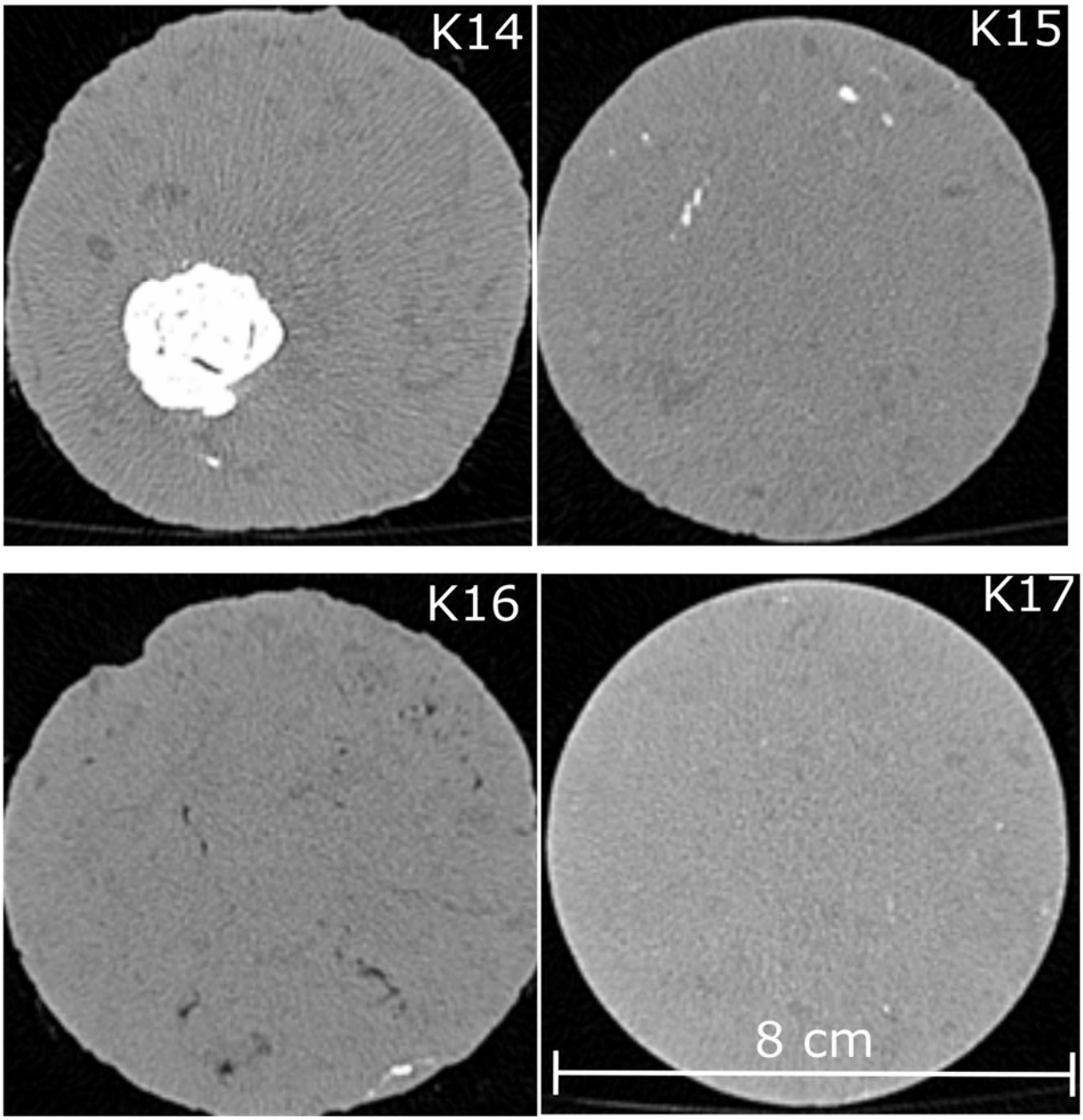

Figure 72: CT images of the Boom Clay samples. Pyrite is shown as white phases due to its high x-ray adsorption capacity (for more details, see text)

A4.2 µ-CT imaging

After CT scan, subsamples of 1 cm diameter and 1 cm length were taken for µ-CT scanning with a GE Nanotom at KU Leuven.

The Boom Clay samples show mainly a clayey background and similar to the medical CT scan, all Boom Clay samples show large amounts of pyrite which is present as filaments or small nodules (Figure 73). Samples K10 and K11 show some other features: within the clay matrix, darker zones can be observed. These darker zones are considered to correspond to zones with a larger porosity, e.g. zones which are enriched in silt/sand with some intergranular porosity. The samples of the Eigenbilzen Sands have a totally different texture. Contrary to the Boom Clay samples, the Eigenbilzen Sands show less pyrite,

and if present it is manifested by very small framboids. Similar observations are made in the CT images shown in Figure 72. Filaments are scarce. The reduced occurrence of pyrite can be explained by the sedimentation conditions: higher concentrations of oxygen due to an increased turbulence, and less organic matter, which is fine grained and easily washed out.

A better view on these samples is obtained in Figure 74 where a projection in both the planar and orthogonal direction is made. Typical for these samples are the fine, grey dots which are spread all over the sample. It are quartz grains, which can – contrary to the Boom Clay samples - be observed as individual phases. They are mainly abundant in sample K14. Also darker grey patches can be seen, which are interpreted as clay rich zones, and their darker colour is attributed to the existence of large amounts of micropores. Probably, these patches still partly have there initial appearance as they have not been completely disturbed by bioturbations. Finally also black spots can be observed, corresponding to large, individual pores. So the features which have been observed in the CT image in Figure 72, are also observed at smaller scale in the µ-CT image of Figure 73 and Figure 74.

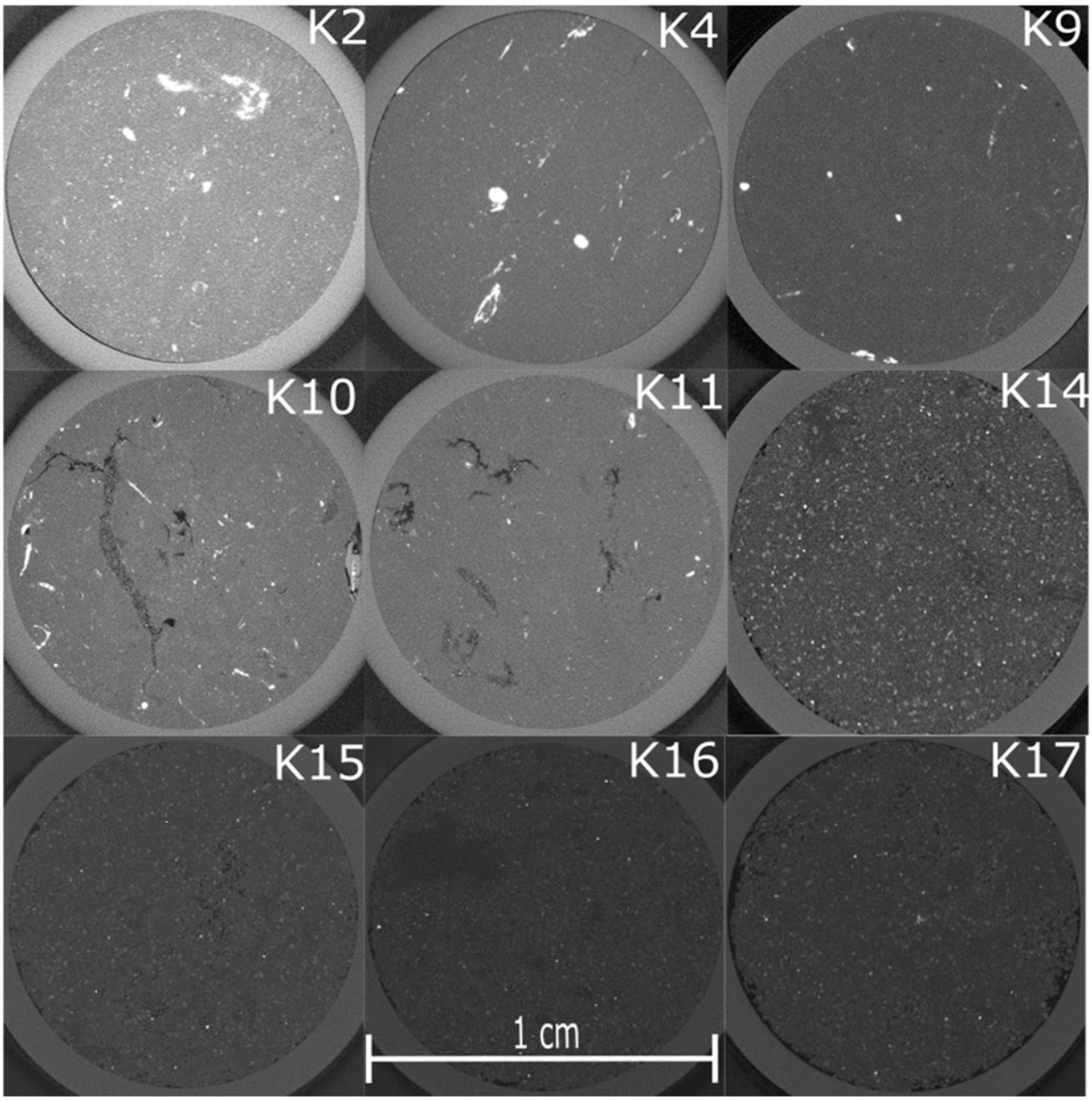

Figure 73: µ-CT images of samples of the samples of the Boom Clay and Eigenbilzen Sands. For more details, see text.

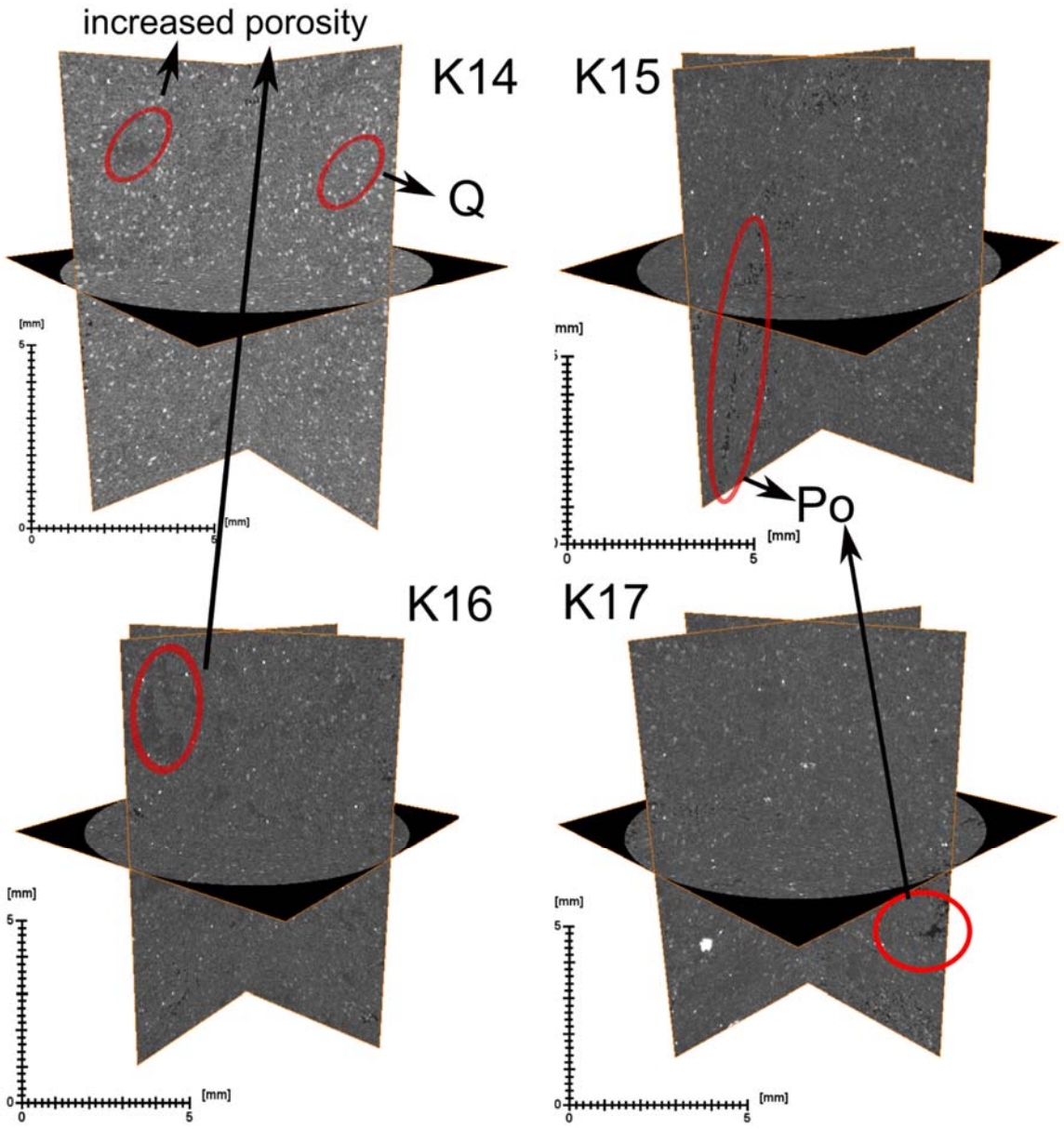

Figure 74: orthogonal projection of the µ-CT scans of sample K14 (top left), K15 (top right), K16 (bottom left) and K17 (bottom right). More information can be found in the text.

As discussed above, Figure 73 also shows that for some Boom Clay samples (K10 and K11), "darker" zones can be observed, which are considered to correspond to areas with a larger porosity. In order to get a better view on the occurrence of these porous zones, they are filtered out and reconstructed in 3D. Figure 75 shows the 3D reconstructed images of samples K10 and K11. Both samples consist of interconnected zones with a higher porosity which are spread all over the sample. To the contrary, for samples K2, K4 and K9, only local spots with higher porosity can be observed and they are not interconnected at all (Figure 75). The planar zones, visible in samples K4 and K9 are drying cracks. Based on the µ-CT images, a clear difference between the samples of the Putte & Terhagen Member and the samples of the Boeretang Member can be observed.

When applying the same technique to the samples of the Eigenbilzen Sands, the result is totally different. In Figure 76, the zones with increased porosity are indicated in blue, and they are mainly located around the quartz grains and within the clayey patches. Notice that only darker zones are indicated in blue, and not the localised black pores. When reconstructing the zones with increased porosity in 3D, it becomes clear that they are abundant and spread all over the sample (Figure 77, left). In order to optimise the visualisation of these zones, a filter is applied and only the larger zones are kept in the figure (Figure 77, right). Despite the fact that both samples are located at a stratigraphic distance of only 3 m – which is small on the scale of a formation – the images look very different. Figure 76 shows for sample K14 mainly increased porosity around the quartz grains with only a few clayey patches while for sample K17 the majority of increased porosity is located in the clayey patches. In the 3D reconstructed images in Figure 77, the same observation can be made with some larger zones of increased porosity in sample K14, while in sample K17 these zones can hardly be distinguished from each other. It is important to note that for these samples a filter has been applied, so the smaller zones of increased porosity which are located e.g. around the quartz grains have been removed. Thus when looking at both samples in Figure 77, one could conclude that sample K14 contains less clayey patches and that the porosity is mainly located next to the quartz grains and less in the clayey patches, while for sample K17 the clayey patches are abundant and contain the majority of the increased porosity. These observations for samples K14 and K17 match with the mineralogical composition of both samples: as shown in Table 6, samples K14 and K17 contain respectively 59% and 54% quartz and resp. 20% and 27% 2:1 clay minerals. With respect to the grain size distribution, both samples contain approximately 35% sand, but the silt and sand fraction are different, i.e. resp. 16 and 49% for K14 and 22 and 43% for K17.

In a last step, the pores which are visible as black spots on the µ-CT images are filtered out and reconstructed in 3D (Figure 78). Both samples K14 and K16 show mainly individual spots and the connectivity is very low. Samples K15 and K17, on the contrary, show a much larger degree of connectivity. For sample K15, this is also visible in Figure 74 (top right), where the black spots run over almost the entire length of the sample.

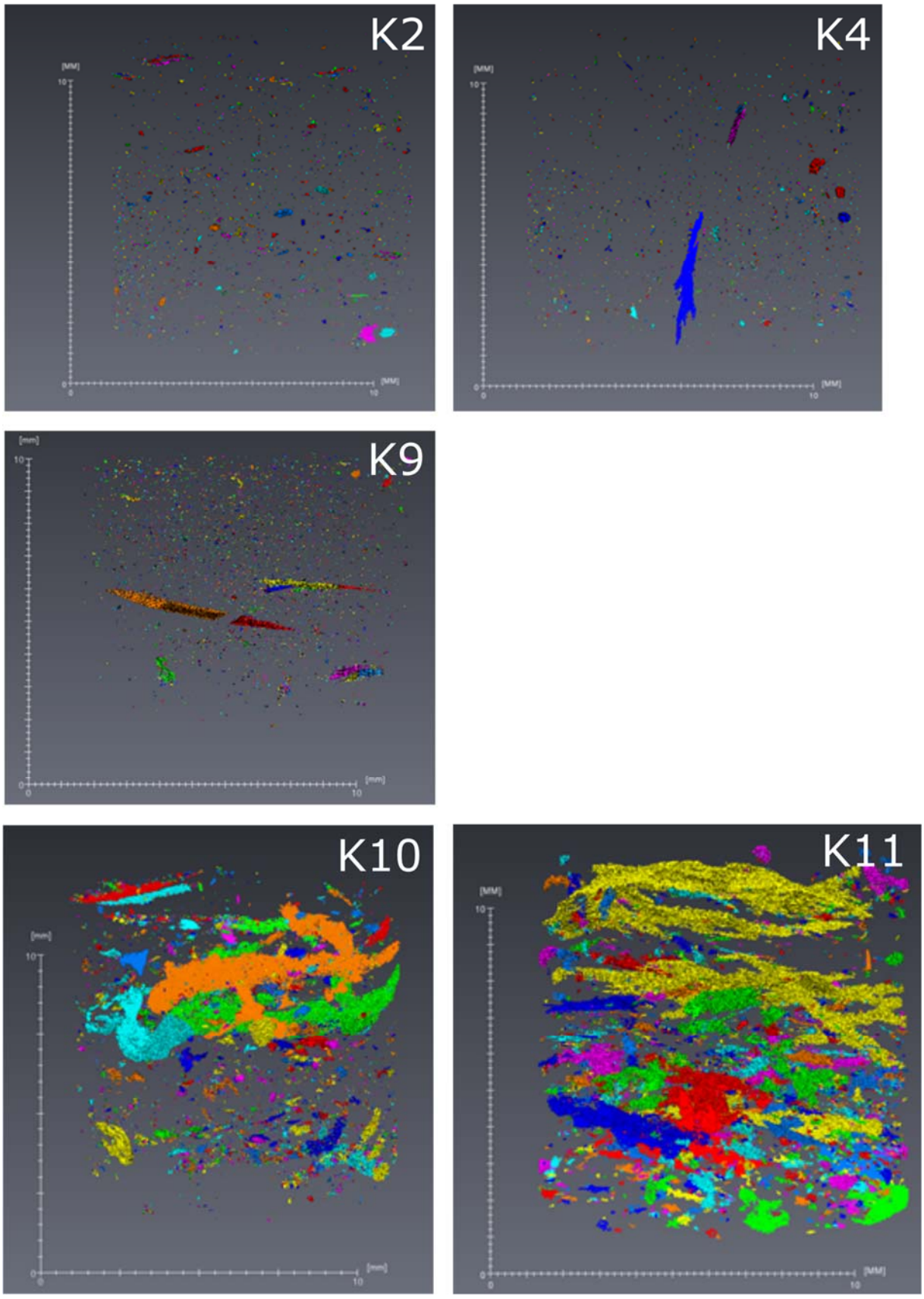

Figure 75: 3D reconstructed µCT image of samples of the Boom Clay. Zones with a higher porosity are indicated in different colours, whereby interconnected pixels received a similar colour.

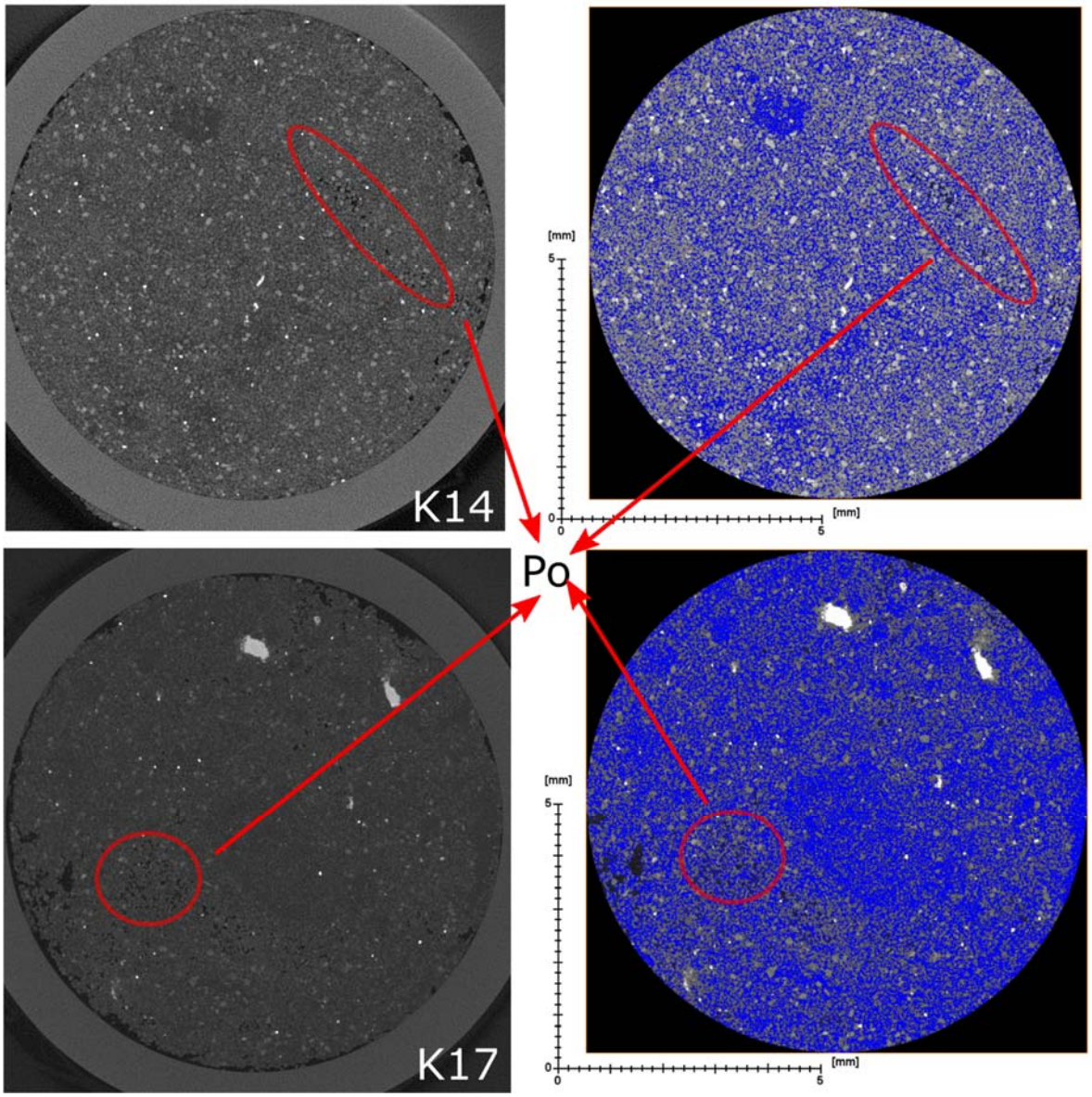

Figure 76: comparison between an unprocessed image, and an image where the darker zones (higher grey value, with increased porosity) are indicated in blue. Top: sample K14, slice 347 and bottom: sample K17, slice 1414. Localised pores (in black) are not taken into account in the processed image.

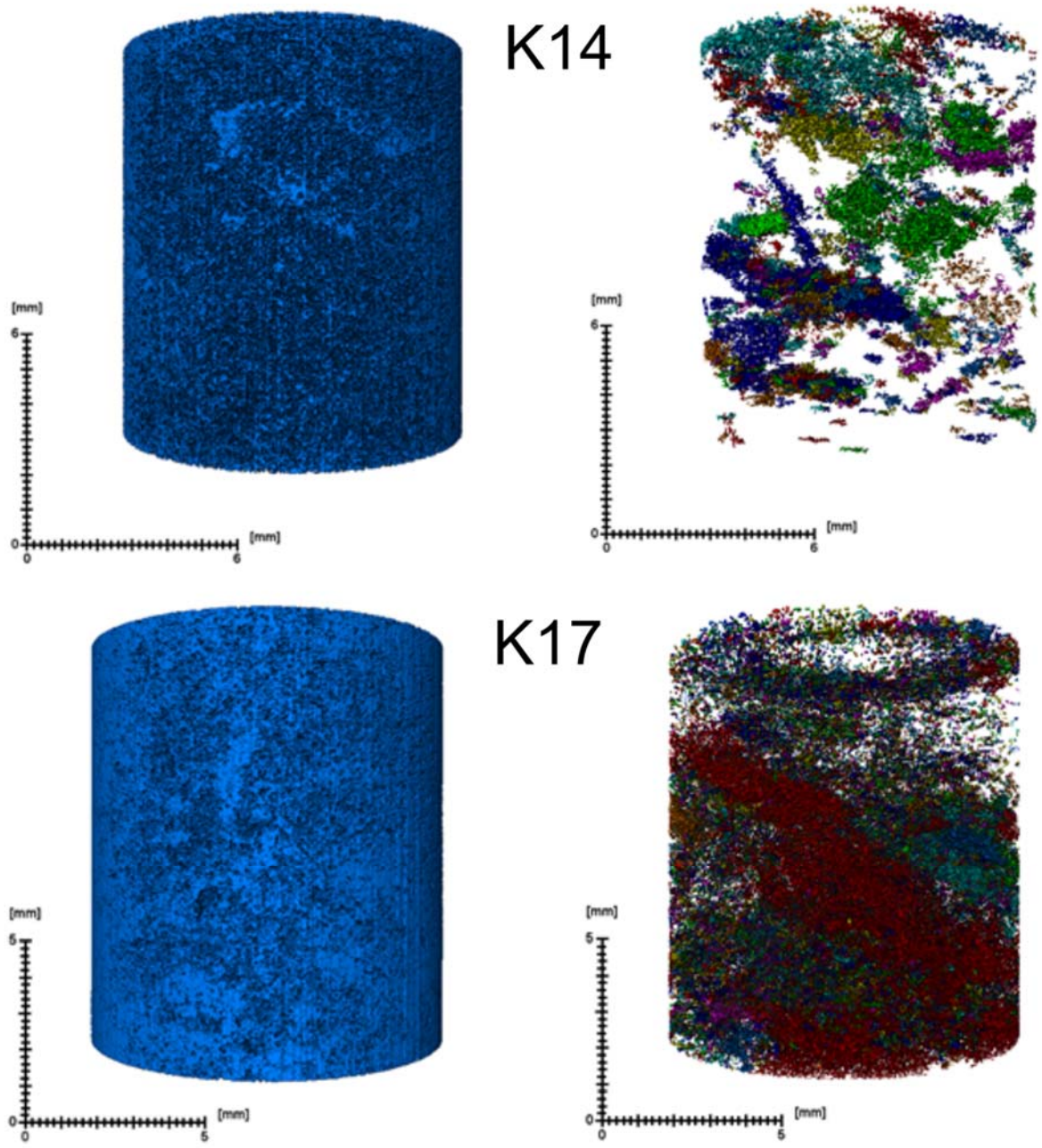

Figure 77: 3D reconstruction of zones with increased porosity in samples K14 (top left) and K17 (bottom left). When applying a filter to remove the smaller connected zones, the image becomes more clear, and in K14 some patchy zones can be observed (top right), while in K17 the zones are still spread all over the sample (bottom right)

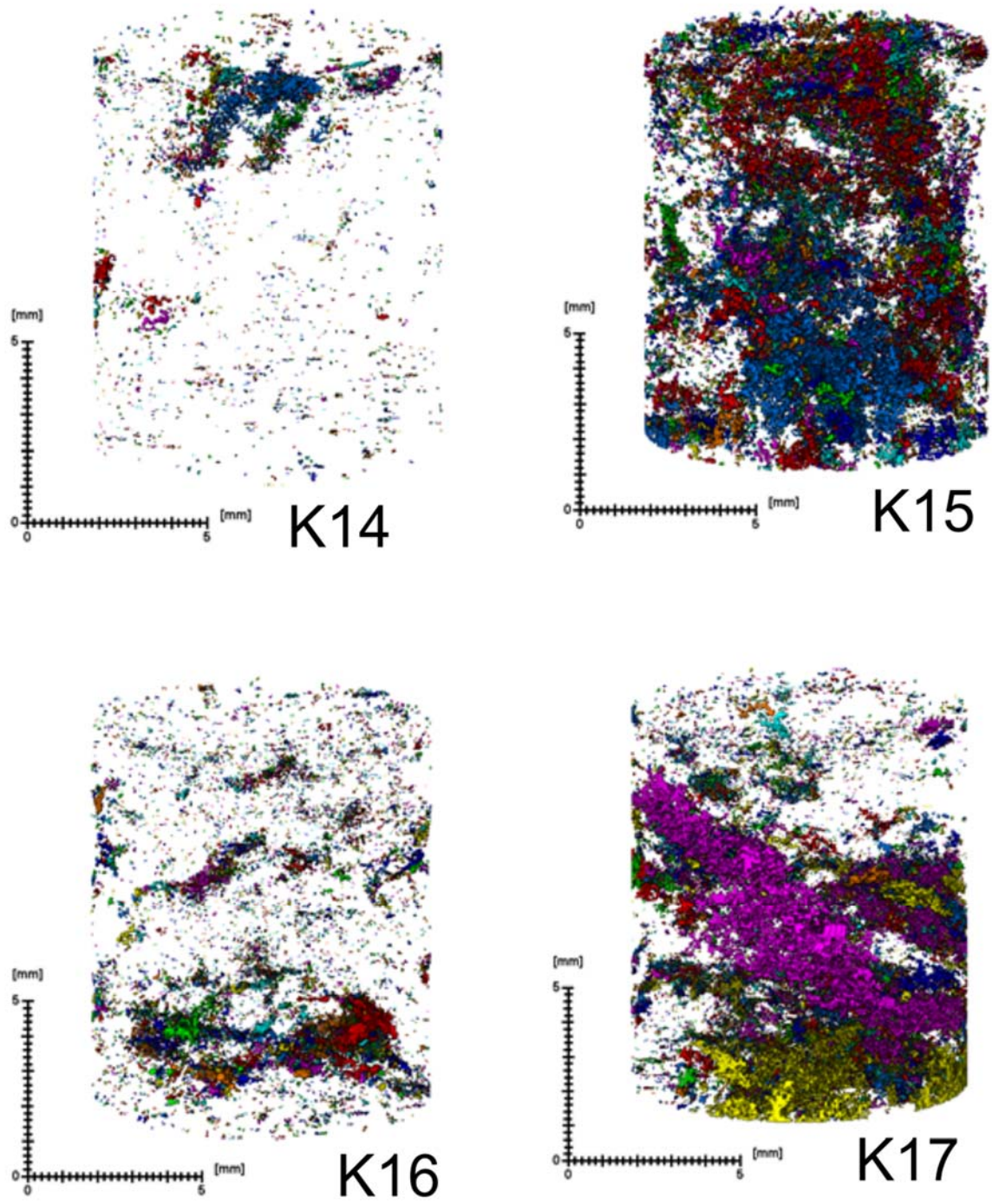

Figure 78: 3D reconstruction of individual pores, observed as black spots in the µ-CT images of samples of the Eigenbilzen Sands. More information is given in the text.

A4.3 Light microscopy of thin sections

All thin sections have been produced by the sample preparation laboratory of the geology section of KU Leuven. Prior to their use, the samples have been impregnated with a resin. The thin sections have been studied with a Carl Zeiss optical microscope, using transmitted light. A description of the lithologies is given below (Table 24), and will not be repeated in the figure captions to avoid duplication of the information provided.

Table 24: Description of the codes used to describe the lithologies

Q	Quartz
Cl	Clay
Gl	Glauconite
Py	Pyrite
Po	Pore

In order to have a fast, visual comparison, all thin sections have been scanned (Figure 79). At first sight, samples K2 and K9 are the most clayey samples (most brown) which contain only few quartz grains, while sample K4 is less clayey but contains more quartz grains. When looking at samples K10 and K11, they seem to be less clayey. However, sample K10 contains less clay and more and larger quartz clusters than K11. For the samples of the Eigenbilzen Sands, K17 contains the largest and K14 the smallest amount of clay, and the two other samples are in between. Sample K17 contains a considerable amount of pyrite.

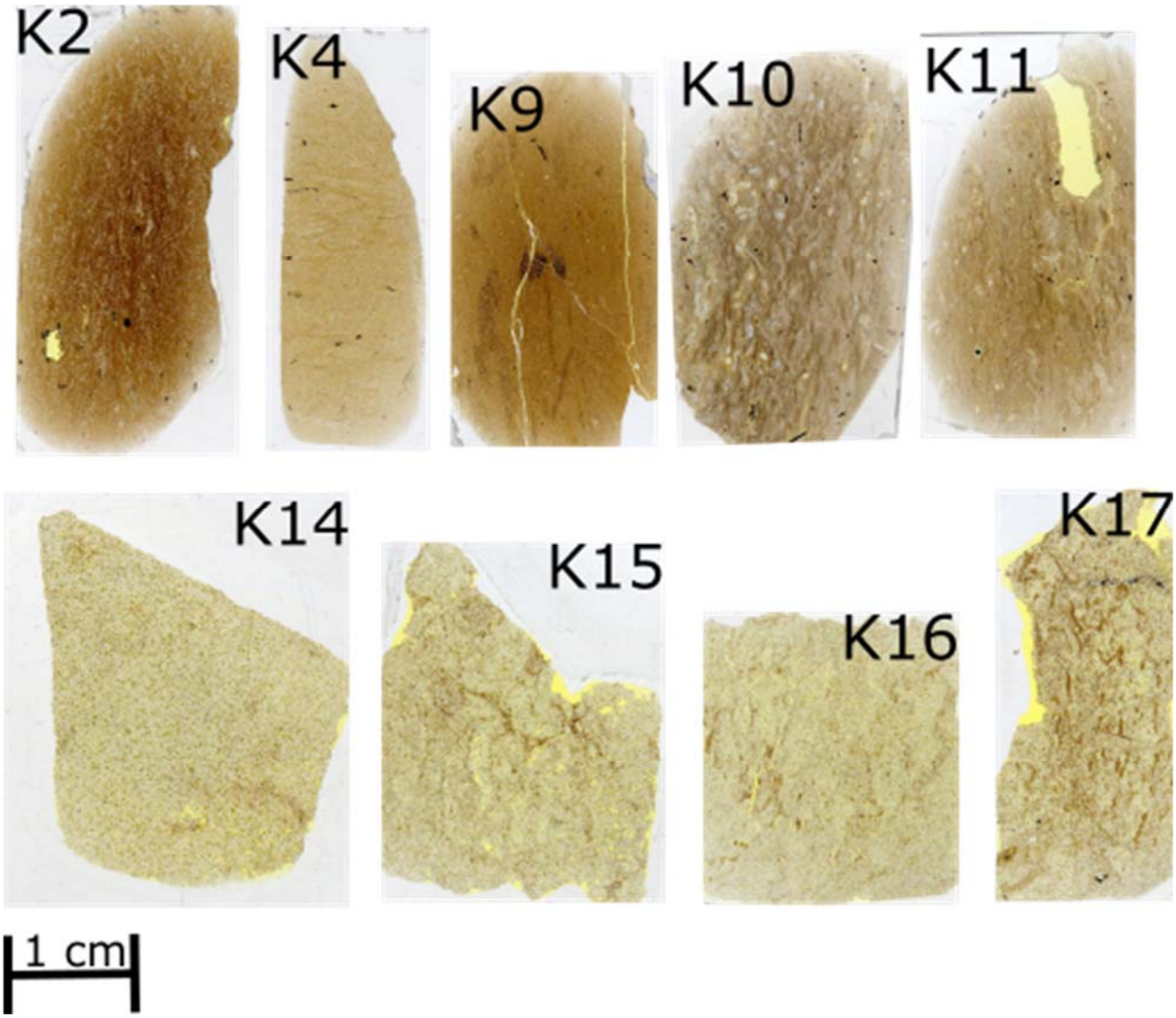

Figure 79: scanned thin sections

In the next section, the observations are discussed, based on their origin.

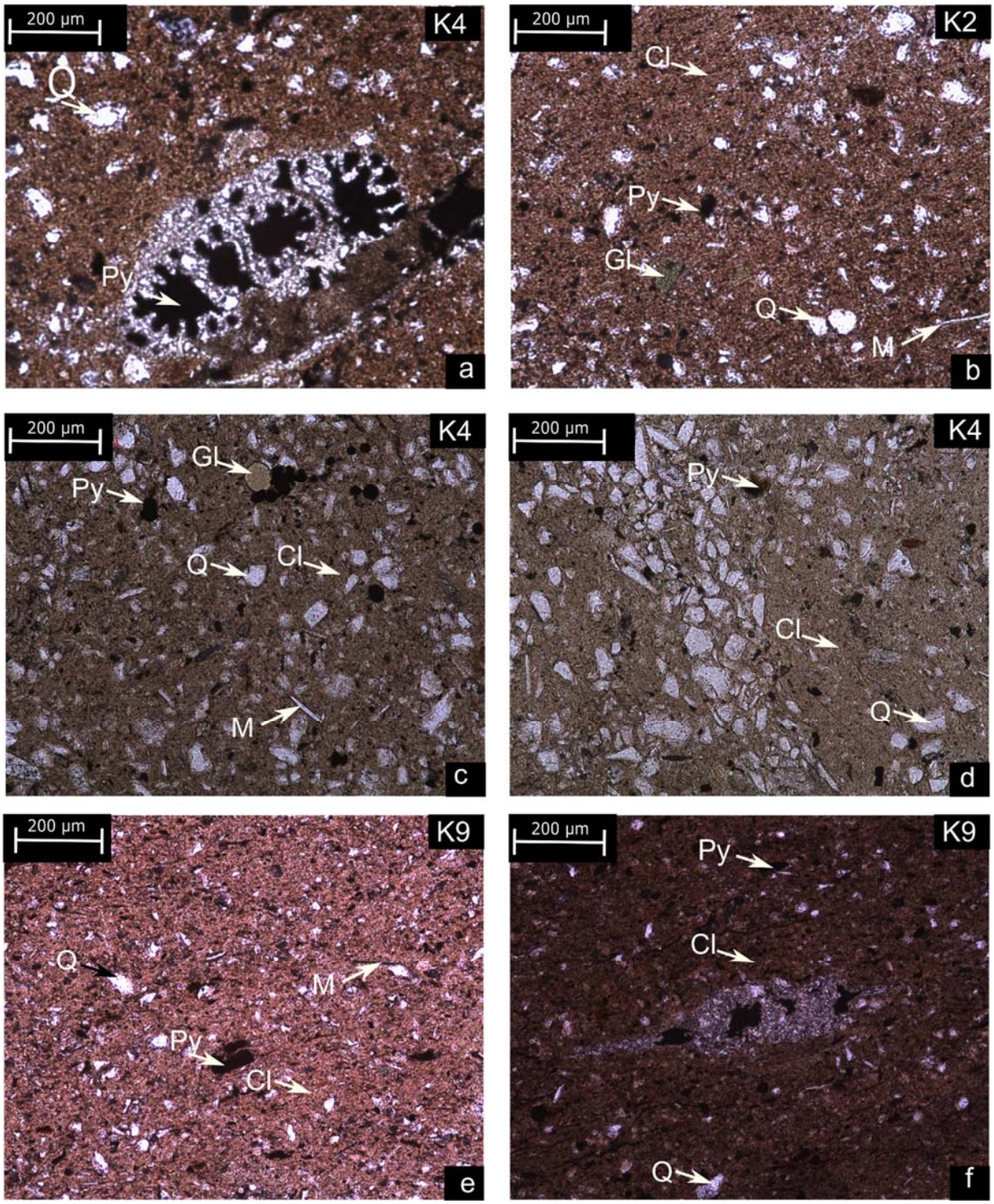

Figure 80: light microscopy images of thin sections of samples K2, K4 and K9

The thin sections of samples K2, K4 and K9 display rather similar constituents (Figure 80). For all samples, we observe a rather homogeneous clay matrix, where quartz grains are regularly distributed. Besides clay minerals and quartz grains, also muscovite and glauconite grains can be observed. In addition, also fossilised and pyritised shells are pesent (Figure 80 a and f).

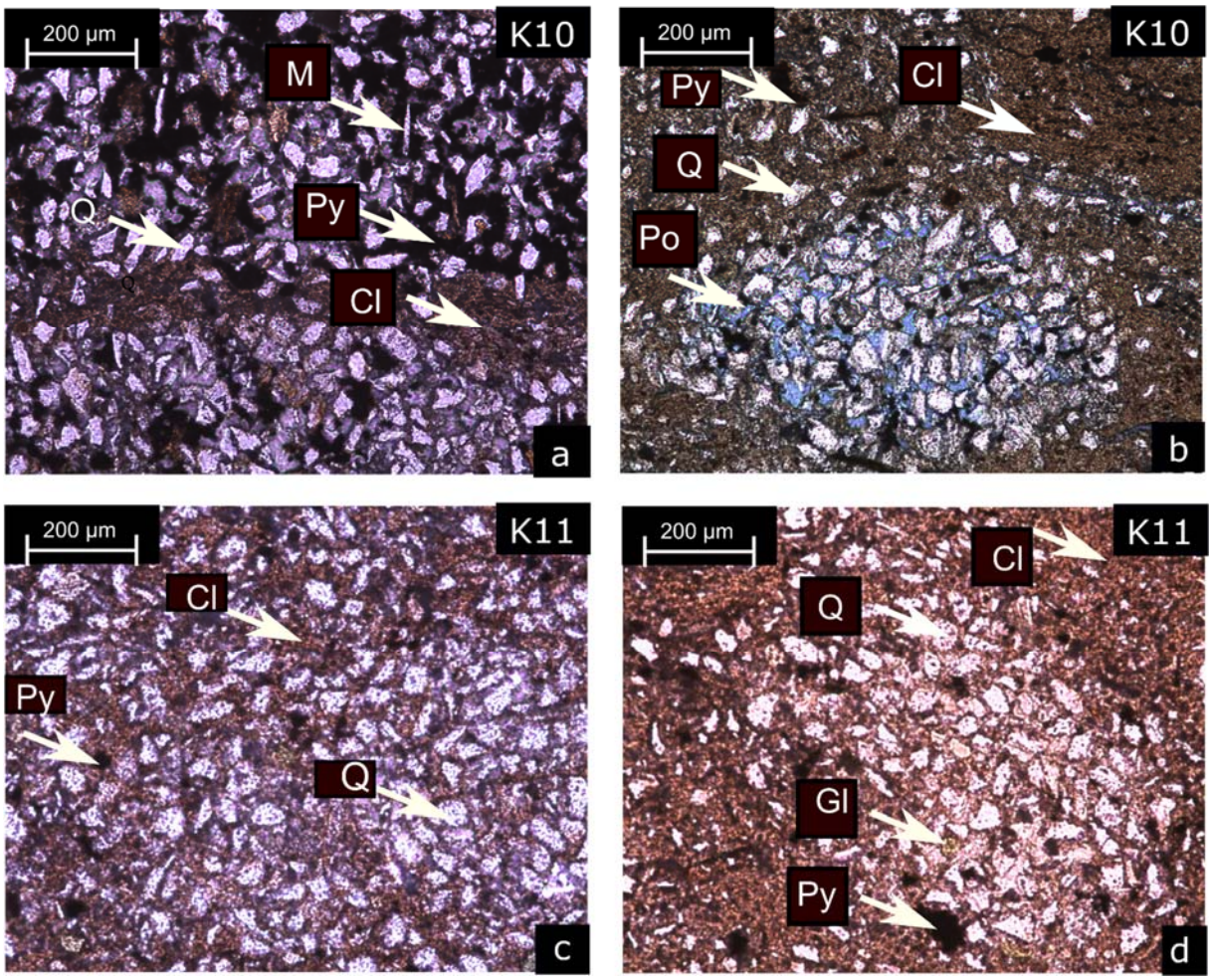

Figure 81: light microscopy images of the thin sections of samples K10 and K11

Figure 81 shows the light microscopy images of the thin sections of the samples of the Boeretang Member: K10 and K11. Contrary to the samples of the Putte & Terhagen Member (Figure 80), the quartz grains are not homogeneously distributed over the clay matrix, but they are grouped into clusters. Within these quartz clusters, pyrite can be observed, but especially in Figure 81b, we observe interparticle porosity: the blue colour is a resin which filled up interparticle pores. The most probable explanation is that these quartz clusters are located along former wormholes, as the quartz grains are often associated with pyrite, and pyrite was often formed within wormholes, as explained before. The wormholes might have collapsed and were filled with quartz grains which were supplied during the sedimentation process.

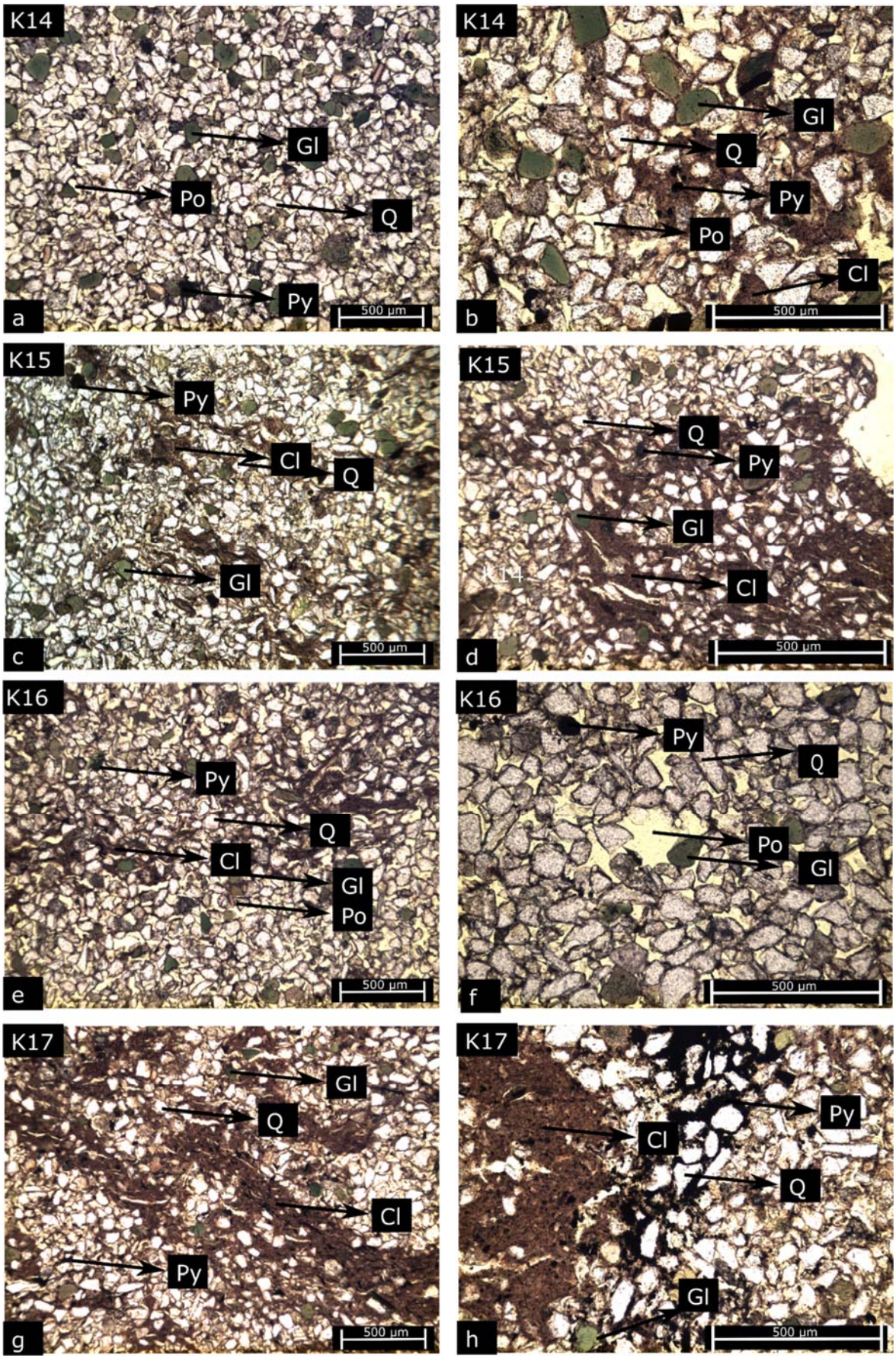

Figure 82: light microscopy images of the thin sections of samples K14 (top), K15 (second row), K16 (third row) and K17 (last row)

Figure 82 shows the light microscopy images of the samples of the Eigenbilzen Sands (K14, K15, K16, K17). All images are dominated by large amounts of quartz grains (transparent) which are considerably larger than the quartz grains of the Boom Clay samples. Besides quartz grains, also patches of clay (brown) are visible, but they are not so abundant. Glauconite (greenish) can also be found in these samples, apart from muscovite (white plates), biotite (brown plates) and pyrite (black). Pyrite is mainly present as framboids. In between the quartz grains, interparticle porosity can be observed (yellow, due to the impregnation of the sample with resin). The interparticle porosity is omnipresent, and some of the pores are large, i.e. they are oversized (e.g. in K16). All samples are strongly bioturbated: after the worm passed through the clayey layer, the hole was filled up with quartz, hence now the clayey layers are disrupted by zones with quartz which can be observed in the thin sections of samples K16 and K17.

A4.4 Point counting and spatial variability

The thin sections have shown large differences in the homogeneity/heterogeneity of the different samples. In order to quantify the homogeneity/heterogeneity, point counting was performed with JMicro Vision, an image analysis toolbox. For each sample, four different categories are used (quartz, porosity, glauconite and other) and 300 points were counted.

One could use the amount of points, needed for a stable result as a measure for the homogeneity/heterogeneity, but this value is also strongly influenced by the amount of quartz. Therefore it is not the best measure. Instead we used a variogram to assess the homogeneity/heterogeneity of the samples. The variogram is defined as the variance of the difference between two variables at two locations. The variogram generally increases with distance and is described by nugget, sill, and range parameters (Figure 83). The nugget is the height of the offset of the variogram at the origin, the sill is the limit of the variogram at infinity and the range is the distance where the difference from the sill becomes negligible, which is often taken as the point where 95% of the sill is reached. When applying this to our example, we should consider that two similar points (e.g. containing quartz) have a variance of 0. If a sample is homogeneous, quartz grains are equally spread it is not likely that two points close to each other both contain quartz, hence the variance in larger and the range is reached at shorter distance. If a sample is heterogeneous (e.g. in K11 which contains quartz clusters), it is more likely to have e.g. two quartz grains next to each other and hence the variance is less and the range is reached at larger distance. So homogeneous and hetergenous samples are expected to show a different variogram, with a variable range. The different variograms were fitted with the gstat package in R, using the “spherical” (Sph) function (Figure 84). Note that the data are normalised for the quartz content, so the difference in quartz content does not influence the plots.

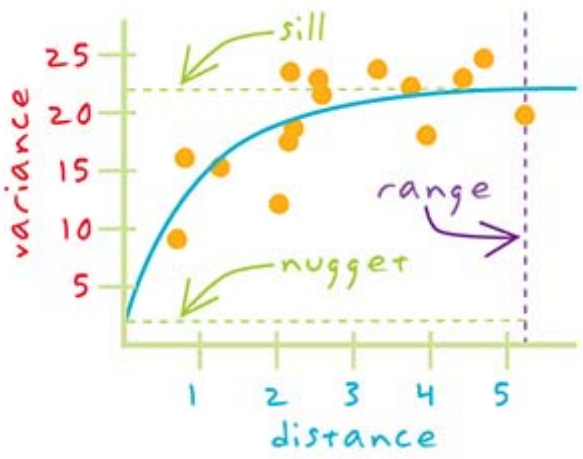

Figure 83: Example of a variogram, from https://support.esri.com/en/other-resources/gis-dictionary/term/variogram

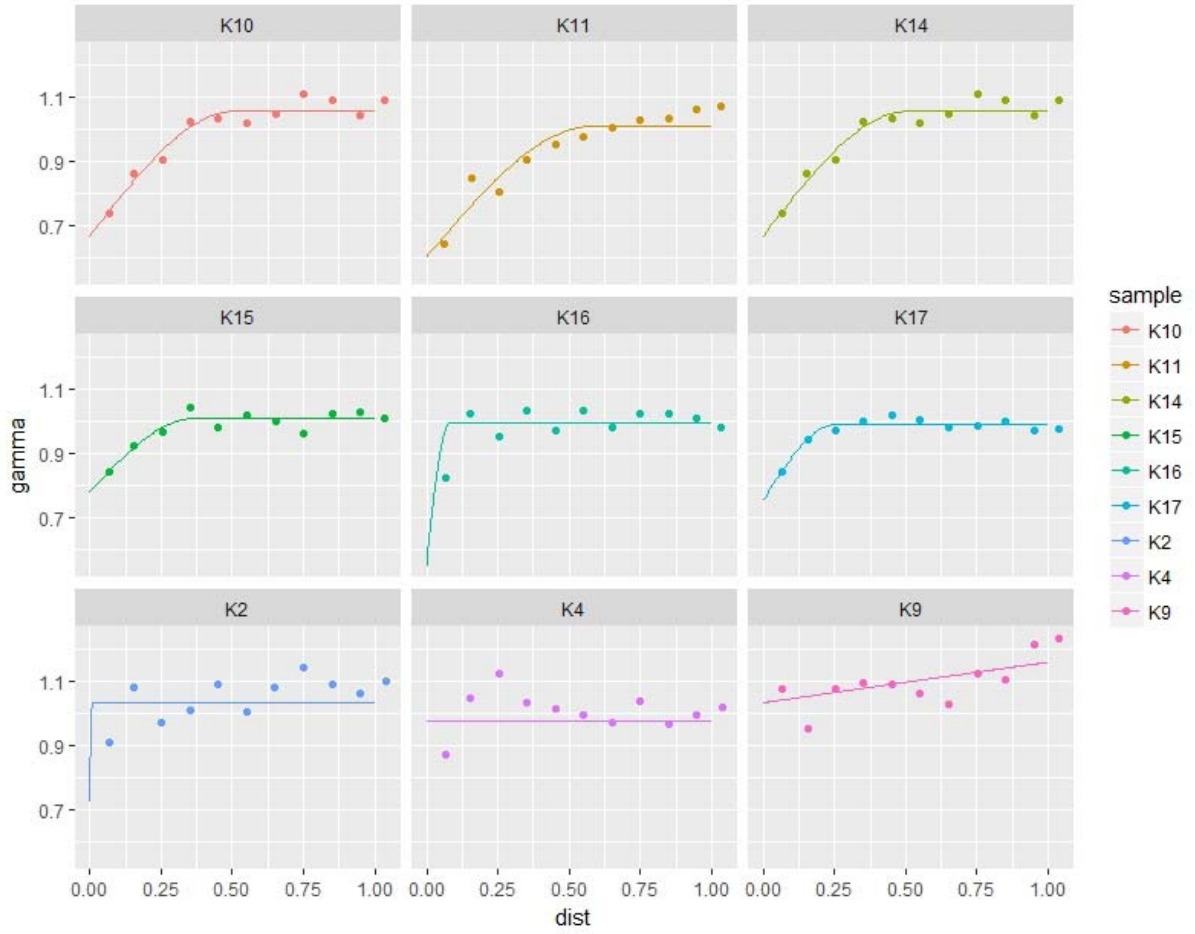

Figure 84: Variograms, representing the variance in the occurrence of quartz in the different samples of the Boom Clay and the Eigenbilzen Sands. The data were fitted with the "Sph" function of the Gstat package in R.

Figure 84 clearly shows differences between the sample types. For the samples of the Putte & Terhagen member (K2, K4 and K9), the sill is almost immediately around 1 and the range is very small (almost 0). This means that in these samples, the quartz grains are homogeneously spread and the variability high everywhere. This matches with the thin sections, were also no spatial correlation was observed. For the samples of the Boeretang Member, the variogram looks totally different: the sill is only reached after 0.5. This means that at a short distance, the spatial variability is low which means

that it is likely that there are two quartz grains close to each other, but at larger distance the variance increases and the spatial correlation is lost. This matches with the observations in the thin sections, where we observed clusters of quartz, which are surrounded by a clay matrix. Within the samples of the Eigenbilzen Sands, we observe some differences. For samples K14, K15 and K17, the spatial correlation of the quartz grains is very clear, though is is a bit less compared to the samples from the Boeretang Member (the sill is reached a bit faster). Samples K16 shows a lower spatial correlation as the sill is reached at small distance, which we cannot explain immediately. When looking back at the pointcounting, we observe that many points were occasionally located in glauconite grains while this was not the case for the other samples. Also the presence of large, oversized pores could influence the spatial variability. Anyhow, in general the observations in the variograms match well with the observations from the thin sections: quartz grains are omnipresent in the samples, but often also pores, glauconite or pyrite can be found between them and these phases increase the spatial variability.

Using variograms to assess the spatial variability of the samples is a suitable way to have an indication on how quartz grains are spread over the samples.

A4.5 Pore size distribution from N2-BET measurements

Pore size distributions have been determined by performing N2-adsorption measurements, using both the Barrett, Joyner and Halenda and the Dubinnin-Astakov theory which allows a reliable determination of the pore size distribution from 1.5 nm up to 250 nm. Please note that due to the limitations of the technique, only information on the micro (< 2nm) and meso (2 – 50 nm) pores can be obtained. Measurements have been performed at the laboratory of clay and interface mineralogy of RWTH Aachen by Pieter Bertier and Timo Seeman.

Figure 85 shows the pore volume distribution of the different samples of the Boom Clay and the Eigenbilzen Sands. A clear difference can be observerd between the two types of samples. For the samples of the Eigenbilzen Sands, the volume of the pores between 1.5 and 250 nm is much smaller compared to the Boom Clay samples. As the total porosity of both types of samples is very similar, the samples of the Eigenbilzen Sands will contain a much larger volume of macro pores. Notice that the latter is clearly observed in CT and µ-CT images, and in the thin sections.

Samples K4 and K9 are the most “clayey” samples. They have the largest amount of 2:1 clay minerals (resp. 41 and 46%) and the smallest amount of quartz (resp. 28 and 26 %) (Table 6). They also show the largest specific surface area (45 m^2/g), and they show the largest pore volume of pores in the 1.5 – 250 nm range. On the CT images, there is no porosity visible (Figure 72) and on the µ-CT images, the 3D reconstruction of zones with increased porosity show only very local spots (Figure 73). In fact these type of pores are clearly below the resolution of the technique. On the thin sections, a homogeneous distribution of clay and quartz grains is visible, showing no interparticle porosity (Figure 80). As the matrix of the samples is very clayey, the porosity consists mainly of micro and meso pores, which is clearly shown in Figure 85.

Sample K14 is a very “sandy” sample. It has a very large amount of quartz constituents (59%), a low amount of 2:1 clay minerals (20%) (Table 6) and a low SSA (15 m^2/g). On Figure 85, a sample is shown

with low volume of pores in the 1.5 – 250 nm range, which indicates that a large volume of pores can be found in the range > 250 nm, which matches with other observations. On the medical CT images, there is no porosity clearly visible (Figure 72), but on the µ-CT images (Figure 73) large quartz grains and macro pores between them can be observed, and the zones with increased porosity are mainly located around the quartz grains and they are spread all over the sample. On thin sections, a heterogeneous distribution of clay and quartz grains is visible, showing widespread interparticle porosity and only some patchy, clayey zones probably containing the meso- and micro-pores (Figure 82). As the matrix of the samples is very sandy, the porosity consists mainly of macro-pores, while the meso- and micro-pores are mainly located in the clayey zones and this is also reflected in the data in Figure 85.

Sample K17 is the most clayey sample of the Eigenbilzen Sands. It has a large amount of quartz (54%), a low amount of 2:1 clay minerals (29%) (Table 6) and a low SSA (20 m^2/g). On Figure 85, this sample shows a larger volume of pores in the 1.5 – 250 nm range compared to the other samples of the Eigenbilzen Sands, which matches with other observations. On the medical CT images, there is no porosity clearly visible (Figure 72), but on the µ-CT images (Figure 73), some macro pores can be observed, but there are less quartz grains (compared to sample K14). For this sample, the zones with increased porosity are located both in the clayey patches and in the pores between the quartz grains. On the thin sections, a heterogeneous distribution of clay and quartz grains is visible, showing some interparticle porosity and clearly more patchy, clayey zones which probably contain the meso and micro pores (Figure 82). This explains why this samples has a higher volume of pores < 250 nm compared to the other samples of the Eigenbilzen Sands. Indeed, this sample contains more clayey zones, which increases the contribution of the meso- and micro-pores.

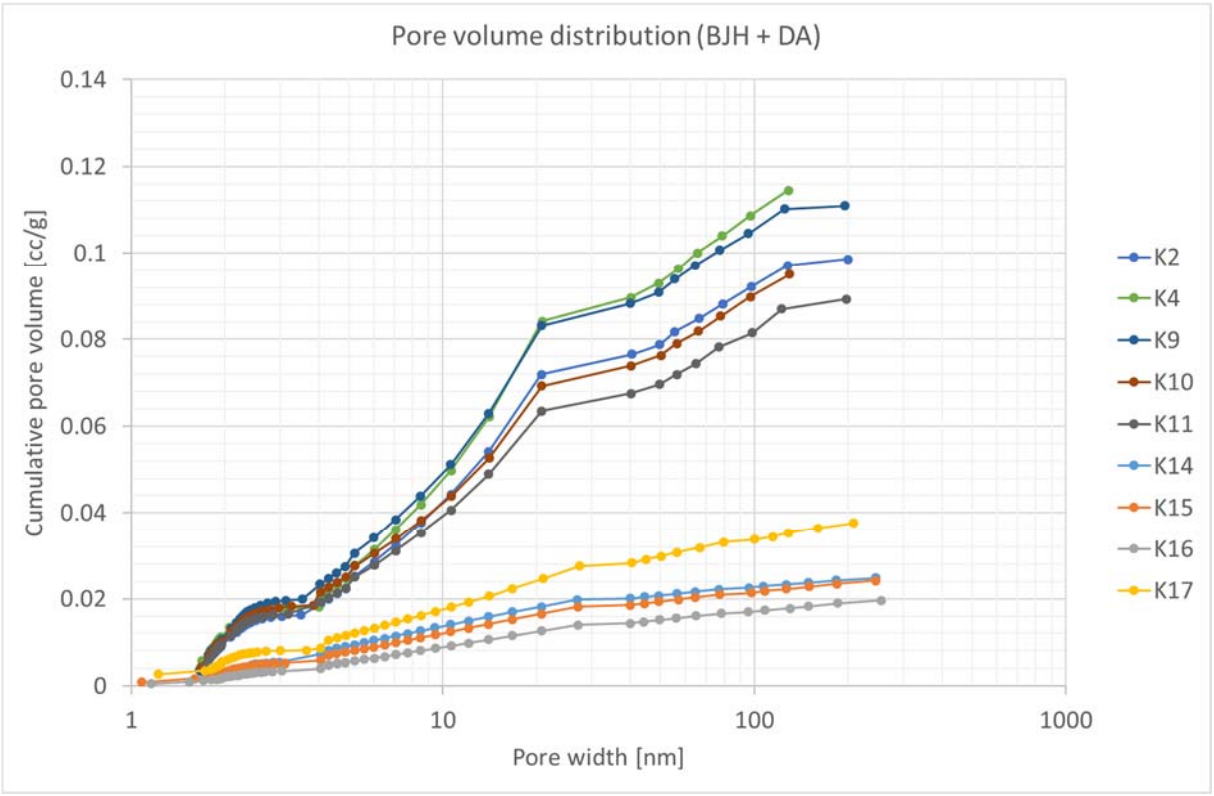

Figure 85: pore volume distribution (based on the Barret-Joyner-Hallenda and the Dubinin-Ashtakov theory) for the samples of the Boom Clay and the Eigenbilzen Sands.

ANNEX 5: Uncertainty propagation and errors

Every measurement is prone to uncertainties. In this thesis, uncertainties are mainly given for the measured diffusion coefficients. Though, these uncertainties represent only the uncertainty on the fit. In order to give a correct estimation, including also the uncertainty on the measurements themselves, this annex is added.

The uncertainty on the measurements should take into account the uncertainty on the calibration gas, on the calibration curve and instrument-related uncertainties (accuracy, stability in time). These data should be available in an instrument validation record. Currently, only a limited version of this document is available at SCK•CEN for both gas chromatographs but in order to proceed the uncertainty propagation, a value of 5% is taken (value similar to the value obtained for another GC). The uncertainty on the repeated measurements (standard deviation of all repeats) is in general low and around 5%. After adding both uncertainties, we consider the global uncertainty in the measurements at 6% maximum.

Another parameter which is taken up into the fit of the diffusion coefficients is the porosity. The porosity is calculated from the water content, the density of the liquid and the density of the solid. For the latter two, standard values from the literature are used for which no uncertainty was given. The used balance has a precision of 0.0004%, hence the error on the weighing is negligible. As the number of significant figures was limited and the uncertainty is in the insignificant figures, the error on the porosity was not taken into account in the calculation of D_{eff}. When calculating the diffusion coefficients, the pressure in the vessels is needed to calculate the total amount of gas. The accuracy of the used pressure sensors is 0.08%, which is maximum 0.008 bar and hence the uncertainty is within the insignificant numbers.

Both the uncertainty on the measurements and the instrument uncertainty have been calculated by using the standard deviation on a series of measurements, and as discussed above the global uncertainty is set at 6%. When the measured data are used to calculate the diffusion coefficient, a least squares fitting is used. When assuming that the errors are normally distributed (hence 0 mean and constant variance), the least square fitting takes into account the errors of the individual points (Mathworks, 2018). Hence, the uncertainty on the fit of the diffusion coefficient includes also the uncertainty on the measurements. The uncertainty on the fitted diffusion coefficients can be used to calculate e.g. the uncertainty on G.

When plotting error bars on the different graphs, it became clear that some of the uncertainties are small. For instance, when plotting the quartz content versus logK for all samples, the error bars are smaller than the datapoints and smaller than the confidence interval of the shown correlation (Figure 86). Hence, the uncertainty is that small that is it not relevant and therefore the error bars for logK vs. mineralogy, grain size distribution and SSA are not shown.

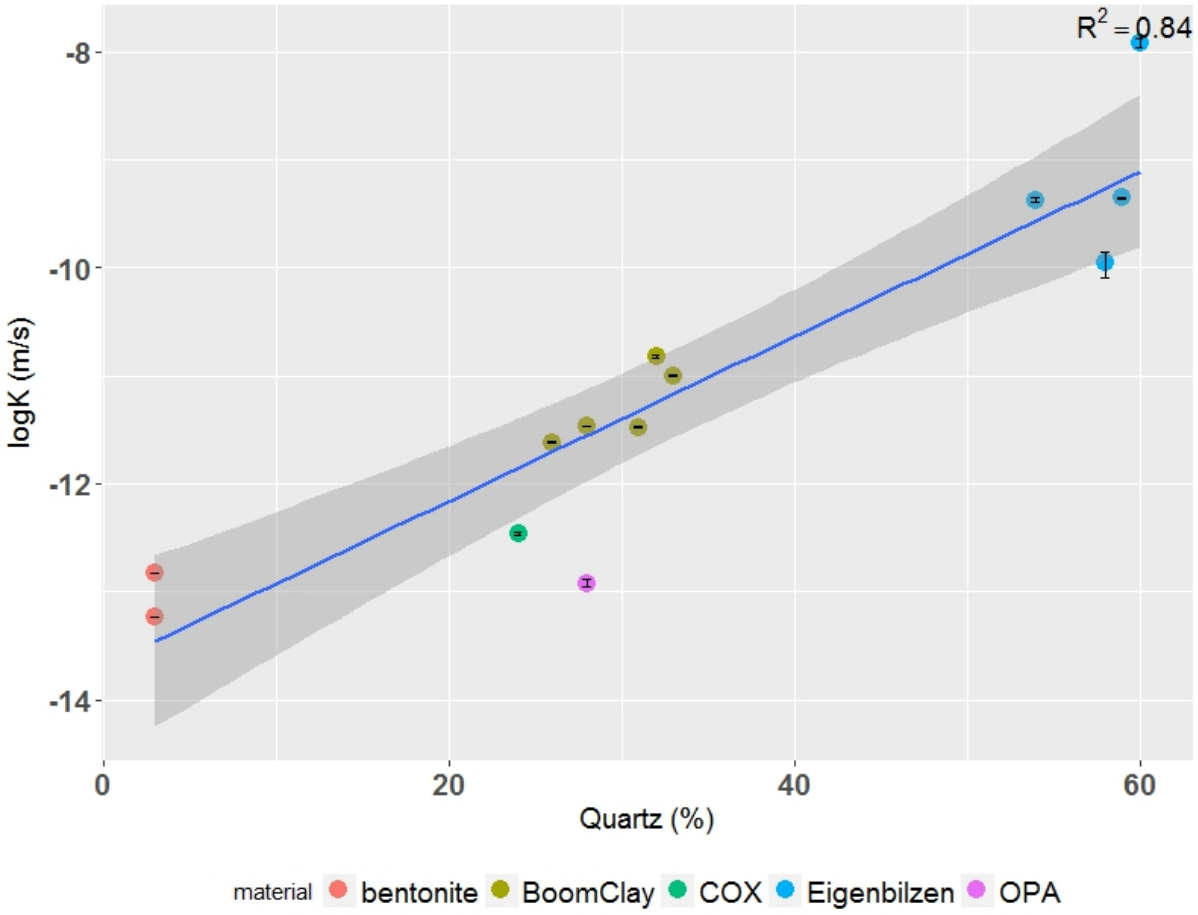

Figure 86: correlation between the quartz content and logK for all samples. The error bars for logK are also shown, but they are mostly smaller than the data points.

ANNEX 6: List of publications

Jacops, E., G. Volckaert, N. Maes, E. Weetjens and J. Govaerts (2013). "Determination of gas diffusion coefficients in saturated porous media: He and CH4 diffusion in Boom Clay." Applied Clay Science 83-84(0): 217-223.

Amann-Hildenbrand, A., B. M. Krooss, J. Harrington, R. Cuss, C. Davy, F. Skoczylas, E. Jacops and N. Maes (2015). Chapter 7 - Gas Transfer Through Clay Barriers. Developments in Clay Science. C. Tournassat, C. I. Steefel, I. C. Bourg and B. Faïza, Elsevier. Volume 6: 227-267.

Jacops, E., K. Wouters, G. Volckaert, H. Moors, N. Maes, C. Bruggeman, R. Swennen and R. Littke (2015). "Measuring the effective diffusion coefficient of dissolved hydrogen in saturated Boom Clay." Applied Geochemistry 61(0): 175-184.

Jacops, E., N. Maes, C. Bruggeman and A. Grade (2016). "Measuring diffusion coefficients of dissolved He and Ar in three potential clay host formations: Boom Clay, Callovo-Oxfordian Clay and Opalinus Clay." Geological Society, London, Special Publications 443.

Jacops, E., M. Aertsens, N. Maes, C. Bruggeman, B. M. Krooss, A. Amann-Hildenbrand, R. Swennen and R. Littke (2017). "Interplay of molecular size and pore network geometry on the diffusion of dissolved gases and HTO in Boom Clay." Applied Geochemistry 76: 182-195.

Jacops, E., M. Aertsens, N. Maes, C. Bruggeman, R. Swennen, B. Krooss, A. Amann-Hildenbrand and R. Littke (2017). "The Dependency of Diffusion Coefficients and Geometric Factor on the Size of the Diffusing Molecule: Observations for Different Clay-Based Materials." Geofluids 2017: 16.

7. References

Adriaens, R., 2015. Neogene and Quaternary clay minerals in the southern North Sea, KU Leuven, Leuven, Belgium, 292 pp.

Adriaens, R., Vandenberghe, N., Elsen, J., 2016. Sedimentary petrology of Ieper Group and Rupel Group Clays. Project report July 2016, KU Leuven, Belgium.

Aertsens, M., 2009. Re-evaluation of the experimental data of the MEGAS experiment on gas migration through Boom Clay. ER-106, SCK-CEN, Mol.

Aertsens, M., 2011. Migration in Clay: experiments and models. SCK-CEN ER-165, Mol, Belgium.

Aertsens, M., De Canniere, P., Lemmens, K., Maes, N., Moors, H., 2008a. Overview and consistency of migration experiments in clay. Physics and Chemistry of the Earth, 33(14-16): 1019-1025.

Aertsens, M., De Cannière, P., Moors, H., Van Gompel, M., 2009. Effect of ionic strength on the transport parameters of tritiated water, iodide and $H^{14}CO_3^-$ in Boom Clay. In: Scientific Basis for Nuclear Waste Management XXXIII. Symposium Proceedings. Volume 1193, St. Petersburg, Russian Federation, 25-29 May 2009 / V.G. Khlopin Radium Institute, Warrendale, PA, United States, Materials Research Society, 2009, p. 497-504.

Aertsens, M. et al., 2005. Determination of the hydraulic conductivity, the product ηR of the porosity η and the retardation factor R, and the apparent diffusion coefficient Dp on Boom Clay cores from the Mol-1 drilling. SCK•CEN-R-3503, Mol, Belgium.

Aertsens, M., Durce, D., Maes, N., Akagi, Y., Ueta, S., 2017. Comparison of HTO and iodide transport parameters in Boom Clay determined by different types of experiments, The 7th International Conference on Clays in Natural and Engineered Barriers for Radioactive Waste Confinement, Davos, Switzerland.

Aertsens, M., Govaerts, J., Maes, N., Van Laer, L., 2011. Consistency of the strontium transport parameters in Boom Clay obtained from different types of experiments: accounting for the filter plates.- In: MRS Symposium Proceedings. Scientific Basis for Nuclear Waste Management XXXV, Buenos Aires, Argentina, 2-7 October 2011 / Materials Research Society, United States, Cambridge University Press, 2012, p. 583-589.

Aertsens, M., Put, M., Dierckx, A., 1999. An analytical model for pulse injection experiments. . In: Feyen, J., Wiyo, K. (Editors), Modelling of transport processes in soils at various scales in time and space, Leuven, Belgium.

Aertsens, M., Put, M., Dierckx, A., 2003. An analytical model for the interpretation of pulse injection experiments performed for testing the spatial variability of clay formations. Journal of Contaminant Hydrology, 61(1-4): 423-436.

Aertsens, M., Van Gompel, M., De Cannière, P., Maes, N., Dierckx, A., 2008b. Vertical distribution of transport parameters in Boom Clay in the Mol-1 borehole (Mol, Belgium). Physics and Chemistry of the Earth, Parts A/B/C, 33, Supplement 1: S61-S66.

Aertsens, M., Wemaere, I., Wouters, L., 2004. Spatial variability of transport parameters in the Boom Clay. Applied Clay Science, 26(1-4): 37-45.

Amann-Hildenbrand, A. et al., 2015. Chapter 7 - Gas Transfer Through Clay Barriers. In: Tournassat, C., Steefel, C.I., Bourg, I.C., Faïza, B. (Eds.), Developments in Clay Science. Elsevier, pp. 227-267.

ANDRA, 2005. La production et le transfert de gaz dans le stockage et la couche du Callovo-Oxfordien, CNTASCM030042, Chatenay-Malabry, France.

Archie, G.E., 1942. The Electrical Resistivity Log as an Aid in Determining Some Reservoir Characteristics. Transactions of the AIME, 146: 54-62.

Atkins, P., de Paula, J., 2006. Physical Chemistry, 8th edition. W.H. Freeman and Company, New York.

Aziz, R.A., 1993. A highly accurate interatomic potential for argon. The Journal of Chemical Physics, 99(6): 4518-4525.

Beattie, J., Barriault, R., Brierley, J., 1951. The Compressibility of Gaseous Xenon. II. The Virial Coefficients and Potential Parameters of Xenon. The Journal of Chemical Physics, 19(10): 1222-1225.

Berner, R.A., 1984. Sedimentary pyrite formation: An update. Geochimica et Cosmochimica Acta, 48(4): 605-615.

Bigler, T., Ilhy, B., Lehmann, B., Waber, H., 2005. Helium Production and Transport in the Low-Permeability Callovo-Oxfordian Shale at the Site Meuse/Haute Marne, France, Helium Production and Transport in the Low-Permeability Callovo-Oxfordian Shale at the Site Meuse/Haute Marne, France. NAGRA, Wettingen.

Birgersson, M., Karnland, O., 2009. Ion equilibrium between montmorillonite interlayer space and an external solution—Consequences for diffusional transport. Geochimica et Cosmochimica Acta, 73(7): 1908-1923.

Boudreau, B., 1996. The diffusive tortuosity of fine-grained unlithified sediments. Geochimica Et Cosmochimica Acta, 60(16): 3139-3142.

Boudreau, B., 1997. Diagenetic models and their implementation. Springer, Berlin, 414 pp.

Bourg, I.C., Tournassat, C., 2015. Chapter 6 - Self-Diffusion of Water and Ions in Clay Barriers. In: Tournassat, C., Steefel, C., Bourg, I., Bergaya, F. (Eds.), Developments in Clay Science. Elsevier, pp. 189-226.

Boving, T., Grathwohl, P., 2001. Tracer diffusion coefficients in sedimentary rocks: correlation to porosity and hydraulic conductivity. Journal of Contaminant Hydrology, 53(1-2): 85-100.

Breck, D.W., 1984. Zeolite molecular sieves: structure, chemistry, and use. R.E. Krieger.

Bruggeman, C., Aertsens, M., Maes, N., Salah, S., 2010. Iodine retention and migration behaviour in Boom Clay – Topical report, First Full Draft. SCK-CEN ER-119. SCK-CEN ER-119, Mol, Belgium.

Bruggeman, C., Maes, N., Aertsens, M., De Canniere, P., 2009. Tritiated water retention and migration behaviour in Boom Clay. SFC1 level 5 report: First full Draft – status 2009. SCK-CEN ER-248. SCK-CEN ER-248, Mol, Belgium.

Capouet, M. et al., 2015. Relevance of gases in the post-closure safety case: An IGSC Position Paper. NEA.

Chapman, S., Cowling, T., 1990. The mathematical theory of non-uniform gases, 3rd edition. Cambridge University Press, Cambridge, UK.

Charlet, L., Bureau, S., Didier, M., Grenèche, J., Vinsot, A., 2013. HT Experiment: Sorption d'hydrogène gazeux sur l' argillite à Opalinus de Mont Terri. Mont-Terri project Technical Note 2012-90, Switzerland.

Chou, H., Wu, L., Zeng, L., Chang, A., 2012. Evaluation of solute diffusion tortuosity factor models for variously saturated soils. Water Resources Research, 48(10): W10539.

Dagnelie, R.V.H. et al., 2014. Sorption and diffusion of organic acids through clayrock: Comparison with inorganic anions. Journal of Hydrology, 511: 619-627.

De Craen, M., 1998. The formation of septarian carbonate concretions in organic-rich argillaceous sediments, KU Leuven, Leuven.

De Craen, M., Van Geet, M., Wang, L., Put, M., 2004a. High sulphate concentrations in squeezed Boom Clay pore water: evidence of oxidation of clay cores. Physics and Chemistry of the Earth, Parts A/B/C, 29(1): 91-103.

De Craen, M., Wang, L., Van Geet, M., Moors, H., 2004b. Geochemistry of Boom Clay pore water at the Mol site. SCK-CEN BLG-990. SCK-CEN BLG-990, Mol, Belgium.

Didier, M., Leone, L., Greneche, J.M., Giffaut, E., Charlet, L., 2012. Adsorption of Hydrogen Gas and Redox Processes in Clays. Environmental Science & Technology, 46(6): 3574-3579.

Dubinin, M.M., Astakhov, V.A., 1971. Development of the concepts of volume filling of micropores in the adsorption of gases and vapors by microporous adsorbents. Bulletin of the Academy of Sciences of the USSR, Division of chemical science, 20(1): 3-7.

Durce, D. et al., 2017. Water-Soluble Organic Matter in Boom Clay: Status report 2012-2016, SCK-CEN ER-XXX, SCK-CEN, Mol, Belgium.

Epstein, N., 1989. On tortuosity and the tortuosity factor in flow and diffusion through porous-media. Chemical Engineering Science, 44(3): 777-779.

Fourre, E. et al., 2011. Dissolved helium distribution in the Oxfordian and Dogger deep aquifers of the Meuse/Haute-Marne area. Physics and Chemistry of the Earth, 36(17-18): 1511-1520.

Franks, F., 1975. Water A Comprehensive Treatise. Springer, United States.

Frederickx, L., 2017. Nitrogen gas physisorption on a selection of Boom Clay samples for the determination of specific surface area and pore size distribution. SCK-CEN I-0576, Mol, Belgium.

Frederickx, L., 2018. The influence of measurement techniques on the grain size distribution of the Boom Clay Formation. SCK-CEN I-0641, Mol, Belgium.

Gasparik, M. et al., 2013. Geological Controls on the Methane Storage Capacity in Organic-Rich Shales. International Journal of Coal Geology(0).

Gaucher, E. et al., 2004. ANDRA underground research laboratory: interpretation of the mineralogical and geochemical data acquired in the Callovian–Oxfordian formation by investigative drilling. Physics and Chemistry of the Earth, Parts A/B/C, 29(1): 55-77.

Gensterblum, Y., Merkel, A., Busch, A., Krooss, B.M., 2013. High-pressure CH4 and CO2 sorption isotherms as a function of coal maturity and the influence of moisture. International Journal of Coal Geology, 118(0): 45-57.

Ghanizadeh, A. et al., 2013. Experimental study of fluid transport processes in the matrix system of the European organic-rich shales: II. Posidonia Shale (Lower Toarcian, northern Germany). International Journal of Coal Geology(0).

Glaus, M.A., Frick, S., Van Loon, L.R., 2017. Diffusion of selected cations and anions in compacted montmorillonite and bentonite. Nagra Technical Report NTB 17-12, Nagra, Wettingen, Switzerland.

Glaus, M.A., Rossé, R., Van Loon, L.R., Yaroshchuk, A.E., 2008. Tracer diffusion in sintered stainless steel filters: Measurement of effective diffusion coefficients and implications for diffusion studies with compacted clays. Clays and Clay Minerals, 56(6): 677-685.

Gómez-Hernández, J.J., 2000. Technical Note 2000-40: FM-C experiment: Part A) Effective diffusivity and accessible porosity derived from in-situ He-4 tests Part B) Prediction of HE-3 concentration in a cross-hole experiment.

Gordon, S., Mc Bride, B., Zeleznik, F.J., 1984. Computer program for calculation of complex chemical equilibrium compositions and applications: supplement I--Transport properties. NASA technical memorandum ; 86885. National Aeronautics and Space Administration, Lewis Research Center, Cleveland, Ohio.

Grathwohl, P., 1998. Diffusion in Natural Porous Media: Contaminant Transport, Sorption/desorption and Dissolution Kinetics. Springer, US.

Haynes, W., 2012. CRC Handbook of Chemistry and Physics, 93rd Edition. CRC Press, Taylor & Francis Group.

Hemes, S., Desbois, G., Urai, J., De Craen, M., Honty, M., 2013. Variations in the morphology of porosity in the Boom Clay Formation: insights from 2D high resolution BIB-SEM imaging and Mercury injection Porosimetry. Netherlands Journal of Geosciences — Geologie en Mijnbouw, 92(4): 275-300.

Hildebrand, J.H., 1976. Viscosity of dilute gases and vapors. Proceedings of the National Academy of Sciences, 73(12): 4302-4303.

Hirschfelder, J., Curtiss, C., Bird, R., 1964. Molecular Theory of Gases and Liquids Wiley, New York, USA.

Holz, M., Heil, S.R., Sacco, A., 2000. Temperature-dependent self-diffusion coefficients of water and six selected molecular liquids for calibration in accurate 1H NMR PFG measurements. Physical Chemistry Chemical Physics, 2(20): 4740-4742.

Horseman, S., Harrington, J., Sellin, P., 1999. Gas migration in clay barriers. Engineering Geology, 54(1-2): 139-149.

IUPAC, 1997. Compendium of Chemical Terminology, 2nd ed. (the "Gold Book"). Compiled by A. D. McNaught and A. Wilkinson. Blackwell Scientific Publications, Oxford (1997). XML on-line corrected version: http://goldbook.iupac.org (2006-) created by M. Nic, J. Jirat, B. Kosata; updates compiled by A. Jenkins. ISBN 0-9678550-9-8. doi:10.1351/goldbook. .

Jackson, M.L., 1975. Soil Chemical Analysis Advanced Course, 2nd edition. Madison, Wisconsin, USA.

Jacops, E. et al., 2017a. Interplay of molecular size and pore network geometry on the diffusion of dissolved gases and HTO in Boom Clay. Applied Geochemistry, 76: 182-195.

Jacops, E. et al., 2016a. Interplay of molecular size and pore network geometry on the diffusion of dissolved gases and HTO in Boom Clay. Applied Geochemistry.

Jacops, E. et al., 2017b. The Dependency of Diffusion Coefficients and Geometric Factor on the Size of the Diffusing Molecule: Observations for Different Clay-Based Materials. Geofluids, 2017: 16.

Jacops, E., Maes, N., Bruggeman, C., Grade, A., 2016b. Measuring diffusion coefficients of dissolved He and Ar in three potential clay host formations: Boom Clay, Callovo-Oxfordian Clay and Opalinus Clay. Geological Society, London, Special Publications, 443.

Jacops, E., Volckaert, G., Maes, N., Weetjens, E., Govaerts, J., 2013. Determination of gas diffusion coefficients in saturated porous media: He and CH4 diffusion in Boom Clay. Applied Clay Science, 83-84(0): 217-223.

Jacops, E. et al., 2015. Measuring the effective diffusion coefficient of dissolved hydrogen in saturated Boom Clay. Applied Geochemistry, 61(0): 175-184.

Johnston, H.L., McCloskey, K.E., 1940. Viscosities of Several Common Gases between 90°K. and Room Temperature. The Journal of Physical Chemistry, 44(9): 1038-1058.

Kaye, Laby, 2005. Tables of Physical & Chemical Constants (16th edition 1995). 2.2.4 Mean velocity, free path and size of molecules. Kaye & Laby Online. Version 1.0 (2005)

Keller, L.M., Hilger, A., Manke, I., 2015. Impact of sand content on solute diffusion in Opalinus Clay. Applied Clay Science, 112–113(0): 134-142.

Keller, L.M., Holzer, L., Schuetz, P., Gasser, P., 2013. Pore space relevant for gas permeability in Opalinus clay: Statistical analysis of homogeneity, percolation, and representative volume element. Journal of Geophysical Research-Solid Earth, 118(6): 2799-2812.

Krooss, B., Schaefer, R.G., 1987. Experimental measurements of the diffusion parameters of light hydrocarbons in water-saturated sedimentary rocks. A new experimental procedure. Organic Geochemistry, 11(3): 193-199.

Libert, M., Bildstein, O., Esnault, L., Jullien, M., Sellier, R., 2011. Molecular hydrogen: An abundant energy source for bacterial activity in nuclear waste repositories. Physics and Chemistry of the Earth, Parts A/B/C, 36(17-18): 1616-1623.

Liu, D. et al., 2013. High-pressure adsorption of methane on montmorillonite, kaolinite and illite. Applied Clay Science, 85: 25-30.

Lojen, S., Ogrinc, N., Dolenec, T., 1999. Decomposition of sedimentary organic matter and methane formation in the recent sediment of Lake Bled (Slovenia). Chemical Geology, 159(1): 223-240.

Macht, F., Totsche, K.U., Eusterhues, K., Pronk, G., 2010. Topography and surface properties of clay minerals analyzed by atomic force microscopy. International Union of Soil Sciences (IUSS), c/o Institut für Bodenforschung, Universität für Bodenkultur, Wien, pp. 206-209.

Madigan, M., Martinko, J., Parker, J., 2000. Brock biology of microorganisms, 9th edition. Prentice Hall, New-Jersey.

Maes, N. et al., 2011. A consistent phenomenological model for natural organic matter linked migration of Tc(IV), Cm(III), Np(IV), Pu(III/IV) and Pa(V) in the Boom Clay. Physics and Chemistry of the Earth, Parts A/B/C, 36(17–18): 1590-1599.

Maes, N. et al., 2004. Migration Case Study : Transport of radionuclides in a Reducing Clay Sediment (TRANCOM 2) Contract No FIKW-CT-2000-00008. EUR-21022, Luxembourg.

Mathworks, 2018. Least-Squares Fitting, https://nl.mathworks.com/help/curvefit/least-squares-fitting.html.

Mazurek, M. et al., 2011. Natural tracer profiles across argillaceous formations. Applied Geochemistry, 26(7): 1035-1064.

Mazurek, M., Hurford, A.J., Leu, W., 2006. Unravelling the multi-stage burial history of the Swiss Molasse Basin: integration of apatite fission track, vitrinite reflectance and biomarker isomerisation analysis. Basin Research, 18(1): 27-50.

Miller, C.C., 1924. The Stokes-Einstein Law for Diffusion in Solution. Proceedings of the Royal Society of London. Series A, Containing Papers of a Mathematical and Physical Character, 106(740): 724-749.

National Commission for Stratigraphy Belgium, 2017. Eigenbilzen Formation.

OECD, N.E.A., 2008. Natural Tracer Profiles Across Argillaceous Formations. OECD Publishing.

Ortiz, L., Volckaert, G., Mallants, D., 2002. Gas generation and migration in Boom Clay, a potential host rock formation for nuclear waste storage. Engineering Geology, 64: 287-296.

Parzen, E., 1962. On Estimation of a Probability Density Function and Mode. Ann. Math. Statist., 33(3): 1065-1076.

Pati, A.R., 2010. Effects of Rebar Temperature and Water to Cement Ratio on Rebar-Concrete Bond Strength of Concrete Containing Fly Ash. Denton, Texas. UNT Digital Library. http://digital.library.unt.edu/ark:/67531/metadc28460/. Accessed September 28, 2016.

Pearson, F. et al., 2002. Geochemistry of Water in the Opalinus Clay Formation at the Mont Terri Laboratory. TR 2003-03, Bern.

Pearson, K., 1901. LIII. On lines and planes of closest fit to systems of points in space. The London, Edinburgh, and Dublin Philosophical Magazine and Journal of Science, 2(11): 559-572.

Perko, J., Weetjens, E., 2011. Thermohydraulic Analysis of Gas Generation in a Disposal Facility for Vitrified High-Level Radioactive Waste in Boom Clay. Nuclear Technology, 174(3): 401-410.

Phung, Q.T., Maes, N., De Schutter, G., Jacques, D., Ye, G., 2013. Determination of water permeability of cementitious materials using a controlled constant flow method. Construction and Building Materials, 47: 1488-1496.

Poling, B., Prausnitz, J., Connell, J.O., 2000. The Properties of Gases and Liquids. McGraw-Hill Education.

Rebour, V., Billiotte, J., Deveughele, M., Jambon, A., le Guen, C., 1997. Molecular diffusion in water-saturated rocks: A new experimental method. Journal of Contaminant Hydrology, 28: 71-93.

Ren, X.W., Santamarina, J.C., 2018. The hydraulic conductivity of sediments: A pore size perspective. Engineering Geology, 233: 48-54.

Robinet, J.-C. et al., 2012. Effects of mineral distribution at mesoscopic scale on solute diffusion in a clay-rich rock: Example of the Callovo-Oxfordian mudstone (Bure, France). Water Resources Research, 48(5): W05554.

Rodwell, W. et al., 1999. Gas migration and two-phase flow through engineered and geological barriers for a deep repository for radioactive waste. EUR19122, Luxembourg.

Rubel, A., Sonntag, C., Lippmann, J., Pearson, F., Gautschi, A., 2002. Solute transport in formations of very low permeability: Profiles of stable isotope and dissolved noble gas contents of pore water in the Opalinus Clay, Mont Terri, Switzerland. Geochimica Et Cosmochimica Acta, 66(8): 1311-1321.

Ryan, B., 2006. A discussion on moisture in coal implications for coalbed gas and coal utilization. Summary of Activities: BC Ministry of Energy, Mines and Petroleum Resources pages 139-149.

Saripalli, K.P., Serne, R.J., Meyer, P.D., McGrail, B.P., 2002. Prediction of Diffusion Coefficients in Porous Media Using Tortuosity Factors Based on Interfacial Areas. Ground Water, 40(4): 346-352.

Savoye, S., Page, J., Puente, C., Imbert, C., Coelho, D., 2010. New Experimental Approach for Studying Diffusion through an Intact and Unsaturated Medium: A Case Study with Callovo-Oxfordian Argillite. Environmental Science & Technology, 44(10): 3698-3704.

Shackelford, C., 1991. Laboratory diffusion testing for waste disposal: A review. Journal of Contaminant Hydrology, 7(3): 177-217.

Shaw, R.P., 2015. The Fate of Repository Gases (FORGE) project. Geological Society, London, Special Publications, 415.

Sneyers, A., 2008. Understanding and Physical and Numerical Modelling of the Key Processes in the Near Field and their Coupling for Different Host Rocks and Repository Strategies (NF-PRO) EUR 23730 Luxembourg.

Stauffer, D., Aharony, A., 1992. Introduction to percolation theory Taylor & Francis, London, UK.

Svehla, R., 1995. Transport Coefficients for the NASA Lewis Chemical Equilibrium Program, Lewis Research Center, Cleveland, Ohio.

Svehla, R.A., 1961. Estimated viscosities and thermal conductivities of gases at high temperatures, NASA, Lewis Research Center; Cleveland, Ohio.

Svehla, R.A., 1962. Estimated Viscosities and Thermal Conductivities of Gases at High Temperatures. National Aeronautics and Space Administration.

Takeda, M., Nakajima, H., Zhang, M., Hiratsuka, T., 2008. Laboratory longitudinal diffusion tests: 1. Dimensionless formulations and validity of simplified solutions. Journal of Contaminant Hydrology, 97(3–4): 117-134.

Thommes, M. et al., 2015. Physisorption of gases, with special reference to the evaluation of surface area and pore size distribution (IUPAC Technical Report), Pure and Applied Chemistry, pp. 1051.

Truche, L., Berger, G., Destrigneville, C., Guillaume, D., Giffaut, E., 2010. Kinetics of pyrite to pyrrhotite reduction by hydrogen in calcite buffered solutions between 90 and 180°C: Implications for nuclear waste disposal. Geochimica Et Cosmochimica Acta, 74(10): 2894-2914.

Truche, L. et al., 2009. Experimental reduction of aqueous sulphate by hydrogen under hydrothermal conditions: Implication for the nuclear waste storage. Geochimica Et Cosmochimica Acta, 73(16): 4824-4835.

Truche, L. et al., 2013. Sulphide mineral reactions in clay-rich rock induced by high hydrogen pressure. Application to disturbed or natural settings up to 250°C and 30bar. Chemical Geology, 351(0): 217-228.

Van Geet, M., Bastiaens, W., Ortiz, L., 2008. Self-sealing capacity of argillaceous rocks: Review of laboratory results obtained from the SELFRAC project. Physics and Chemistry of the Earth, Parts A/B/C, 33, Supplement 1(0): S396-S406.

Van Loon, L., 2015. Effective Diffusion Coefficients and Porosity Values for Argillaceous Rocks and Bentonite: Measured and Estimated Values for the Provisional Safety Analyses for SGT-E2.

Van Loon, L.R., Glaus, M.A., 2008. Mechanical Compaction of Smectite Clays Increases Ion Exchange Selectivity for Cesium. Environmental Science & Technology, 42(5): 1600-1604.

Van Loon, L.R., Mibus, J., 2015. A modified version of Archie's law to estimate effective diffusion coefficients of radionuclides in argillaceous rocks and its application in safety analysis studies. Applied Geochemistry, 59(0): 85-94.

Van Loon, L.R., Soler, J.M., Muller, W., Bradbury, M.H., 2004. Anisotropic diffusion in layered argillaceous rocks: A case study with opalinus clay. Environmental Science & Technology, 38(21): 5721-5728.

Van Marcke, P. et al., 2014. Installation of the PRACLAY Seal and Heater. In: Norris, S. et al. (Eds.), Clays in Natural and Engineered Barriers for Radioactive Waste Confinement. Geological Society Special Publication. Geological Soc Publishing House, Bath, pp. 107-115.

Vandenberghe, N., De Craen, M., Wouters, L., 2014. The Boom Clay Geology. From sedimentation to present-day occurrence: a review. Memoirs of the Geological Survey of Belgium, 60. Royal Belgian Institute of Natural Sciences, Geological Survey of Belgium, Brussels, Belgium, 76 pp.

Volckaert, G. et al., 1994. MEGAS Modelling and experiments on gas migration in repository host rocks. Final Report Phase 1. . EUR16235, Luxembourg.

Wan, Y. et al., 2015. An experimental investigation of diffusivity and porosity anisotropy of a Chinese gas shale. Journal of Natural Gas Science and Engineering, 23: 70-79.

Weissberg, H.L., 1963. Effective Diffusion Coefficient in Porous Media. Journal of Applied Physics, 34(9): 2636-2639.

Wemaere, I., Marivoet, J., Labat, S., 2008. Hydraulic conductivity variability of the Boom Clay in north-east Belgium based on four core drilled boreholes. Physics and Chemistry of the Earth, Parts A/B/C, 33, Supplement 1(0): S24-S36.

Wemaere, I., Marivoet, J., Labat, S., Beaufays, R., Maes, T., 2002. Mol-1 borehole (April-May 1997) Core manipulations and determination of hydraulic conductivities in the laboratory. SCK-CEN R-3590A, Mol, Belgium.

Wenk, H.-R., Voltolini, M., Mazurek, M., Van Loon, L.R., Vinsot, A., 2008. Preferred orientations and anisotropy in shales: Callovo-Oxfordian shale (France) and Opalinus Clay (Switzerland). Clays and Clay Minerals, 56(3): 285-306.

Wersin, P. et al., 2012. Rock and porewater characterisation on drillcores from the Schlattingen borehole. Nagra Arbeitsbericht, Wettingen, Switzerland.

Yampolskii, Y., Freeman, B.D., Pinnau, I., 2006. Transport of Gases and Vapors in Glassy and Rubbery Polymers, Materials Science of Membranes for Gas and Vapor Separation. John Wiley & Sons, Ltd, pp. 1-47.

Yu, L. et al., 2013. A critical review of laboratory and in-situ hydraulic conductivity measurements for the Boom Clay in Belgium. Applied Clay Science, 75-76(0): 1-12.

Yu, L., Weetjens, E., 2009. Summary of Gas Generation and Migration. Current State-of-the-Art. SCK-CEN ER-106, Mol, Belgium.

Yu, L., Weetjens, E., 2012. Estimation of the gas source term for spent fuel,vitrified high-level waste, compacted waste and MOSAIK waste.- Mol, Belgium: SCK•CEN, 2012.- 60 p.- (External Report of the Belgian Nuclear Research Centre; ER-162; CCHO-2009-00940000).- ISSN 1782-2335.

Zeelmaekers, E., 2011. Computerized qualitative and quantitative clay mineralogy: introduction and application to known geological cases. PhD Thesis, K.U. Leuven, Belgium.

Zeelmaekers, E. et al., 2015. Qualitative and quantitative mineralogical composition of the Rupelian Boom Clay in Belgium. Clay Minerals, 50(2): 249-272.

Zhang, J.F. et al., 2016. Methane and Carbon Dioxide Adsorption on Illite. Energy & Fuels, 30(12): 10643-10652.